Unified Machine learning based design of adsorption separation processes

by

Kasturi Nagesh Pai

A thesis submitted in partial fulfillment of the requirements for the degree of

Doctor of Philosophy

in

Chemical Engineering

Department of Chemical and Materials Engineering
University of Alberta

Abstract

Pressure swing adsorption (PSA) processes are an industrially mature low energy consumption pathway for gas separations. Due to their performance being linked to the separation media, they provide an additional degree of freedom for process design. They are difficult to accurately model due to the propagation of sharp heat and mass transfer fronts. These are unsteady-state processes and, as such, have to be run cyclically till a cyclic steady state to measure performance. The highly multivariate nature of the process inputs also makes them hard to optimize and control. With the advent of metal-organic chemistry and the almost infinite number of possible adsorbents, and the possibility of tailor-made adsorbents already being highlighted in the literature, there is a need for fast and accurate means there is a need for fast and accurate models. Industrial gas separations such as CO_2 capture and O_2 concentration can significantly benefit from finding the suitable adsorbent in an optimized process. The traditional process design and optimization frameworks require considerable computation resources, and thus primary screening of adsorbents is performed using simplified metrics. There is no explicit agreement over the link between process performance and separation media. In this thesis, the modelling, simulation, optimization, screening and experimental validation of pressure swing adsorption processes are investigated using machine learning. The CoRE database of adsorbents is screened in a multi-scale framework for post-combustion CO_2 capture. The GCMC simulations are used to predict CO_2 and N_2 equilibria. Using this data, a detailed process model was used to evaluate over 1500 adsorbents, and the results showed no statistical correlation to common screening metrics. A machine learning model

generated using a decision tree algorithm was also presented to screen adsorbents for CO_2 capture. Various machine learning algorithms are investigated for their ability to accelerate the optimization of PSA processes. Two optimization frameworks, Surrogate Opt. and CSS Opt., were presented to speed up PSA optimization. A neural network model was trained to learn from the final cyclic steady-state profiles, and the detailed model was used to initialize at CSS. The models were validated using lab-scale experimental data. A general adsorbent agnostic machine-assisted process learner and emulator (MAPLE) was developed to simulate the detailed process model. The unique aspect of this model is that adsorbent-specific parameters were inputs to the model along with process inputs. This means that once trained; the model can predict the performance of any type 1 adsorbent for a given process. The trained model had high accuracy with $R^2_{ADJ} \geq 0.99$ for all the outputs, such as CO_2 purity, recovery. The modelling and optimization framework (MAPLE Opt.) was validated for a CO_2 capture case study using data from the scholastic literature. The question of process performance limits for PVSA based CO_2 capture was analyzed using the MAPLE model. Various optimization case studies investigated performance limits of real-world as well as hypothetical best adsorbents at different feed compositions. The showed that the innovation gap between real-world materials and the hypothetical best was very conservative. It was also shown that significant energy saving is possible at higher CO_2 feed compositions using PSAs. The experimental validation of the MAPLE model was performed using a O_2 concentration case study. The adsorbent agnostic MAPLE model was used to optimize the performance of LiX and 13X of a Skarstrom cycle. The results from the optimization were used to operate a bench-scale 2-bed lab scale rig to verify the performance. The results show that a model trained with hypothetical adsorbent equilibria can target performance in an experiment. This experimentally validated machine learning framework provides an alternative fast modelling pathway for PVSA process design and optimization.

Preface

This thesis focuses on the holistic design and optimization of both the adsorbent and the adsorption-driven separation processes. The research conducted in this thesis was partly funded by the Canada Foundation for Innovation, Carbon Capture Initiative, Natural Sciences and Engineering Research Council (NSERC), and Alberta Innovates. The computational work conducted in this work was thanks to the resources provided by Compute Canada. A part of this thesis was conducted in collaboration with computational material chemists at the University of Ottawa. The computational modelling of the adsorbents evaluated in this thesis was generated by Sean Collins and Thomas Burns from the Woo Labs at the University of Ottawa. Alberta Innovates provided resources for conducting the vacuum swing adsorption experiments. This thesis is written in a paper-based format; thus, several minor parts might be overlapped between chapters. A. Rajendran and V. Prasad were the supervisory authors, and they were involved in concept formation, analysis and manuscript composition.

Chapter 1 of this thesis introduces the topic of adsorptive separations and contains a literature review of the current state of the art in adsorption and adsorbent modelling. A part of this chapter that details the adsorbent screening and characterization was written by Kasturi Nagesh Pai and is also submitted for publication as Sai Gokul Subraveti, Kasturi Nagesh Pai, Vinay Prasad, Arvind Rajendran, Peter T. Clough *et al.*"Harnessing the power of machine learning for carbon capture, utilization, and storage (CCUS) – A state-of-the-art review" in Energy Environ. Sci. Chapter 2 of this thesis was published by Thomas D Burns, Kasturi Nagesh Pai, Sai Gokul Subraveti, Sean P Collins, Mykhaylo Krykunov, Arvind Rajendran, Tom K

Woo, "Prediction of MOF Performance in Vacuum Swing Adsorption Systems for Post-combustion CO_2 Capture Based on Integrated Molecular Simulations, Process Optimizations, and Machine Learning Models". In this paper, Thomas D Burns and Sean Collins generated material-specific isotherms. Kasturi Nagesh Pai and Sai Gokul Subraveti were responsible for process modelling and simulation. Kasturi Nagesh Pai, Thomas D Burns and Sai Gokul Subraveti were responsible for data generation, collection and analysis. The manuscript was also composed by Kasturi Nagesh Pai and Thomas D Burns, and Sai Gokul Subraveti.

Chapter 3 of this thesis was published by Kasturi Nagesh Pai, Vinay Prasad, Arvind Rajendran, "Experimentally validated machine learning frameworks for accelerated prediction of cyclic steady-state and optimization of pressure swing adsorption processes". In this paper, Kasturi Nagesh Pai was responsible for process modelling and simulation. He was also responsible for the design of experiments and the manuscript composition. The manuscript and analysis were also composed by Kasturi Nagesh Pai, with the guidance of Arvind Rajendran and Vinay Prasad.

Chapter 4 of this thesis was published as Kasturi Nagesh Pai, Vinay Prasad, Arvind Rajendran, "Generalized, Adsorbent-agnostic, artificial neural network framework for rapid simulation, optimization, and adsorbent screening of adsorption processes". In this paper, Kasturi Nagesh Pai was responsible for process modelling and simulation. He was also responsible for the design of experiments and the manuscript composition. The manuscript and analysis were also composed by Kasturi Nagesh Pai, with the guidance of Arvind Rajendran and Vinay Prasad.

Chapter 5 of this thesis was published as Kasturi Nagesh Pai, Vinay Prasad, Arvind Rajendran, "Practically Achievable Process Performance Limits for Pressure-Vacuum Swing Adsorption-Based Post-combustion CO_2 Capture". In this paper, Kasturi Nagesh Pai was responsible for process modelling and simulation. He was also responsible for the design of experiments and the manuscript composition. The manuscript and analysis were also composed by Kasturi Nagesh Pai, with the guidance

of Arvind Rajendran and Vinay Prasad.

Chapter 6 of this thesis is in preparation for publishing as Kasturi Nagesh Pai, Tran Thanh Tai Nguyen, Vinay Prasad, Arvind Rajendran, "Experimental validation of an adsorbent agnostic machine-assisted adsorption process learning and emulation (MAPLE) framework". In this paper, Kasturi Nagesh Pai was responsible for process modelling and simulation. Kasturi Nagesh Pai was also responsible for the design of experiments and the manuscript composition. The experiments were run and analyzed by both Kasturi Nagesh Pai, Tran Thanh Tai Nguyen. The manuscript and analysis were composed by Kasturi Nagesh Pai, with the guidance of Arvind Rajendran and Vinay Prasad.

Owing to the format of the thesis, some level of repetition of topics such as process modelling is unavoidable.

To my Anna and Bappamma

Acknowledgements

I want to express my gratitude to my supervisory committee, Dr. Arvind Rajendran, Dr. Vinay Prasad, and Dr. Zukui Li, for pursuing doctoral studies at the University of Alberta. I want to acknowledge Dr. Arvind Rajendran for his infinite patience and support in helping me improve on aspects I lacked. Arvind, I sincerely appreciate your guidance throughout my Master's and Ph.D. studies at the UofA. The numerous individual and group meetings have been instrumental in expanding my understanding of the adsorption process. I will always be grateful for your excellent inputs regarding the direction you have provided me for my research projects. I would again like to thank you for your patience when it comes to my various eccentricities. I would like to extend my gratitude to Dr. Vinay Prasad. Thank you for letting me know not to restrict myself to a box and try new things. I would also like to thank Marnie Jamieson, for whom I was the TA for multiple design courses. I have learnt a great deal as a simulator TA, and I would like to thank you again for the opportunity. Many sudden unplanned events have occurred during my time at the UofA. I would like to thank you all for being accommodating, especially the 5 months of remote workings during the COVID-19 pandemic.

I would like to extend my thanks to my group-mates, new and old. Ali, Ashwin, Libardo, Gokul, Nick, Vishal, Tai, Rafael, Bhubesh, Yoga, Gwen, Lauren, Jim have made my days at the 3-336.34, DICE building, the University of Alberta highly enjoyable. I want to extend my gratitude to Sanjula, Yashas, Ananthan, and all my other peers on the 3^{rd} and 4^{th} floor of DICE. I will keep the conversations in the hallway and during breaks very dear to me. I appreciate your support, patience,

collaboration, and an ear whenever I needed one. A part of this thesis was written in my hometown of Mangalore, where I was residing during the COVID 19 pandemic. I would like to thank Prajwal and Nithan, who made this time productive with their support and help. Finally, I would like to thank my mother, brother and girlfriend for their constant support at every moment in my life. None of this would have been possible without your love, affection, and understanding.

"If I have seen further than others, it is by standing on the shoulders of giants"

-Sir Isaac Newton

Table of Contents

1 Introduction **1**

1.1 Case Study 4

1.1.1 Carbon Dioxide Capture 4

1.1.2 Oxygen Generation 4

1.2 Gaps in Research 5

1.3 Traditional adsorptive process design 6

1.4 Structure of the thesis 9

2 Prediction of MOF performance in vacuum swing adsorption systems for post-combustion CO_2 capture based on integrated molecular simulations, process optimizations, and machine learning models **12**

2.1 Introduction 12

2.2 Computations Methods 15

2.3 Results and Discussion 20

3 Experimentally validated machine learning frameworks for accelerated prediction of cyclic steady state and optimization of pressure swing adsorption processes. **30**

3.1 Introduction 30

3.2 Experimental System, Process and Machine-learning Models 33

3.2.1 Experimental System 33

3.2.2 Process Cycle 34

3.2.3 Detailed Process Modeling 35
3.2.4 Process Optimization 38
3.2.5 Machine Learning Models 39
3.3 Surrogate Models: Training and Validation 41
3.3.1 Surrogate Model for Performance Indicators 43
3.3.2 Surrogate Model for CSS Profiles 45
3.4 Process Optimization 50
3.4.1 Computational Advantage 55
3.5 Experimental Validation of the Surrogates 57
3.6 Conclusions 60

4 Generalized, Adsorbent-agnostic, artificial neural network framework for rapid simulation, optimization, and adsorbent screening of adsorption processes 63

4.1 Introduction 63
4.2 Machine-assisted Adsorption Process Learning and Emulation (MAPLE) framework 66
4.2.1 Detailed model 66
4.2.2 Machine-learning training and validation 69
4.2.3 Process Optimization 75
4.3 Performance evaluation of MAPLE 77
4.3.1 Simulation of a VSA process 77
4.3.2 VSA optimization 78
4.3.3 Adsorbent screening through process optimization 81
4.4 Conclusions 86

5 Practically Achievable Process Performance Limits for Pressure-Vacuum Swing Adsorption-Based Post-combustion CO_2 Capture. 88

5.1 Introduction 88

5.2 Methodology 91
5.2.1 Separation System and Performance Metrics: 91
5.2.2 PVSA Process Modelling: 91
5.2.3 Process Cycles: 93
5.2.4 The MAPLE Framework and Process Optimization: 94
5.3 Results and discussions 96
5.3.1 Limits for US-DOE targets: 96
5.3.2 Process limits: 99
5.3.3 Adsorbent limits: 104
5.3.4 Perspective: 108

6 Experimental validation of MAPLE: an adsorbent agnostic neural network VSA model 113

6.1 Introduction 113
6.2 Adsorbent Equilibria 115
6.3 Experimental System and process cycle 117
6.4 Process cycle 118
6.5 Performance Indicators 120
6.6 VSA Process Modelling 121
6.7 MAPLE Sampling and Training 122
6.8 Results and Discussion 124
6.8.1 Purity-Recovery Optimization 125
6.8.2 Purity-Productivity Optimization 126
6.8.3 Experimental Validation 128
6.9 Conclusions 133

7 Conclusions, Recommendations, & Future Work 134

7.1 Conclusions 134
7.2 Future Work 137

Bibliography **139**

Appendix A: Supporting information for: Prediction of MOF performance in vacuum swing adsorption systems for post-combustion CO_2 capture based on integrated molecular simulations, process optimizations, and machine learning models. **153**

A.1 Grand Canonical Monte Carlo Simulations 153

A.2 Validation of Competitive Isotherm Model 154

A.3 Removal of Toxic and Rare Atom Types 154

A.4 Geometric Property Calculations 156

A.5 VSA Simulator 156

A.6 Parasitic Energy 158

A.6.1 VSA Energy 158

A.6.2 Compression Energy Contribution 158

A.7 Simulation Methodology 159

A.7.1 Validation of VSA model 161

A.7.2 Grid-Search of Process Conditions 161

A.7.3 Genetic Algorithm (GA) 163

A.7.4 Objective Function 164

A.7.5 Top 12 Materials 166

A.7.6 Random Forest Decision Tree Modelling 166

A.7.7 Univariate Analysis 168

A.7.8 Linear Discriminant Analysis (LDA) 170

A.7.9 Principal Component Analysis (PCA) 171

A.7.10 Machine Learning Models for Parasitic Energy and Productivity 175

A.8 Vacuum Pump Efficiencies 178

Appendix B: Supporting information for: Experimentally validated machine learning frameworks for accelerated prediction of cyclic steady

state and optimization of pressure swing adsorption processes. 179

B.1 Process Modeling 179

B.1.1 Model Equations 179

B.1.2 Boundary Conditions 180

B.1.3 Simulation Parameters 181

Appendix C: Supporting information for: Generalized, Adsorbent-agnostic, artificial neural network framework for rapid simulation, optimization, and adsorbent screening of adsorption processes 187

C.1 Process Modeling 187

C.1.1 Model Equations 187

C.1.2 Boundary Conditions 188

C.1.3 Key process performance indicators (PIs) 189

Appendix D: Supporting information for: Practically Achievable Process Performance Limits for Pressure-Vacuum Swing Adsorption-Based Post-combustion CO_2 Capture. 200

D.1 Process Modeling 200

D.1.1 Model Equations 200

D.1.2 Boundary Conditions 201

D.1.3 Key process performance indicators (PIs) 201

Appendix E: Supporting information for: Experimental validation of MAPLE: an adsorbent agnostic neural network VSA mode 206

E.1 Process Modeling 206

E.1.1 Model Equations 206

E.1.2 Boundary Conditions 207

E.1.3 Key process performance indicators (PIs) 207

List of Tables

2.1 List of the 12 high-performing materials which simultaneously achieve a parasitic energy less than 250 kWh_e /MT CO_2 and a productivity greater than Zeolite-13X (4.2 TPD CO_2 /m^3). PE and productivities are given for a single process point that meets the aforementioned criteria while also meeting the 95/90-PRT. [a]CCDC identifier for MOFs in the Cambridge Structural Database. [45] 18

2.2 List of sorbent metrics and the correlation coefficients of the metrics to the productivity and parasitic energy for all MOFs that meet the 95/90-PRT and whose process conditions have been fully optimized (392 materials). 22

3.1 Parameters used for simulations. 38

3.2 Optimal operating conditions and the measured performance of the VSA experiments [36], shown alongside the surrogate model predictions for the same conditions. 59

4.1 Parameters used for detailed model simulations. Those indicated as variable are used for training the MAPLE framework and used as decision variables. 72

5.1 Parameters used for detailed model simulations. Those indicated as variable are used for training the MAPLE framework and used as decision variables. 111

5.2 The data from the fitting of the various optimizations cases discussed in Fig. 5.3 to performance indicator (PI), PI = $\alpha e^{\beta y_F}$. Energy values are in (kWh_e/tonne CO_2 cap) and productivity values are in (mol_{CO_2}/m^3 ads s). These fits are valid for values of y_F between 0.05 and 0.45. However for the cases of E11, E12, E13, P11, P12, P13, the applicable ranges are provided in Fig. 5.3 112

6.1 Single site Langmuir isotherm model fitting parameters for three gases, namely, N_2, O_2, and Ar along with the 95% confidence interval from the isotherm fitting. 119

6.2 Parameters used for detailed model simulations. Those indicated as variable are used for training the air separation MAPLE framework and used as decision variables. 123

6.3 Optimal operating conditions and the measured performance of the VSA experiments, shown alongside the MAPLE model predictions for the same conditions. * the units of productivity are mol_{O_2} / m^3 ads /s. 130

A.1 N_2 potential parameters used in GCMC simulations. ^{a}bl is the distance of the atom to the molecular centre of mass (COM) 154

A.2 Equations for modeling adsorption column dynamics. 156

A.3 Boundary conditions for the typical steps in a cyclic adsorption process. 157

A.4 Equations for the key performance indicators. 158

A.5 Simulation parameters for VSA simulations 160

A.6 Values and ranges used in the grid-search 162

A.7 Process parameter ranges allowed during the GA optimization. 163

A.8 Values used in the fitness function to scale the performance parameters. 165

A.9 Values used in the fitness function to scale the performance parameters. 166

A.10 List of all geometric descriptors used in decision tree fittings. 168

B.1 Equations for modeling adsorption column dynamics. 179

B.2 Boundary conditions for the typical steps in a cyclic adsorption process. 180
B.3 Dual-site Langmuir isotherm parameters for CO_2 and N_2 on Zeochem Zeolite 13X [36] 181
C.1 Equations for modeling adsorption column dynamics. 187
C.2 Boundary conditions for the typical steps in a cyclic adsorption process. 188
C.3 Equations for the key performance indicators. 189
C.4 Single Site Langmuir (SSL) isotherm parameters for the adsorbents in the literature [15]. Only those adsorbents that met the criteria for representation by an SSL isotherm are provided here. Some duplicate occurences refer to different data sources reported in the original paper. 189
C.5 Comparison of DOE classification and minimum energy calculations of MAPLE with those from Khurana and Farooq . [15]. A flag of "1" represents that the material can satisfy DOE target, while a"0" indicates that it cannot. Note that the Detailed model results from Khurana and Farooq use a dual-site Langmuir isotherm to describe the equilibria, whereas the MAPLE-Opt. uses a single-site Langmuir fitted to the the data generated using the dual-site Langmuir parameters provided by Khurana and Farooq. 191
D.1 Boundary conditions for the typical steps in a cyclic adsorption process. 201
D.2 Single site Langmuir (SSL) isotherm parameters for the adsorbents used in this study. 205
E.1 Boundary conditions for the typical steps in a cyclic adsorption process. 207

List of Figures

1.1 a) Qualitative adsorption equilibrium isotherm b) Basic cyclic adsorption process [1]. 2

1.2 Adsorption process simulation from material properties, a) the traditional approach to adsorption process simulation alongside the proposed machine learning approach b) a qualitative indication of time and computational effort is shown against accuracy for different modeling schemes. 10

2.1 a) Process schematic of the 4-step VSA cycle simulated. b) Pressure profile of the VSA cycle. The times of the adsorption, blowdown and extraction steps (t_{ADS}, t_{BLOW}, t_{EXTRACT}) and the blowdown and extraction pressures (P_{LOW},P_{EXTRACT}) shown are 5 of the 7 variables used in the process optimization. 16

2.2 (a) Lowest PEs resulting from process optimization of the top 150 materials (circles) as a function of the CO_2/N_2 selectivity. The right-hand vertical axis is the energy penalty, which is the percentage of the power plant's energy output that must be diverted for CO_2 capture and compression. (b) The highest productivity of the same top 150 materials (in units of tonnes of CO_2 captured per day per m^3 of sorbent) as a function of the single component working capacity. For IISERP-MOF2, highlighted in yellow, the productivity is shown for the process conditions that give the best productivity (circle), best PE (diamond) and a balance of the two (triangle). All points shown in (a) and (b) meet the 95/90-PRT. Well known materials are highlighted in red including those that are not part of the top 150 materials (squares). The PE of a state-of-the-art liquid amine scrubber was taken from reference [78] while the thermodynamic separation limit + compression was calculated from Ruthven *et al.*[79] 19

2.3 Univariate probability distributions for (a) the CO_2/N_2 single component selectivity, (b) the fitted N_2 dual-site Langmuir isotherm parameter for the stronger site, (c) the working capacity, and (d) the N_2 saturation uptake for the stronger DSL site. Shown in the four plots is the probability distribution for the MOFs which pass the 95/90-PRT (blue), fail the 95/90-PRT (red), and the top 150 MOFs by PE (black). These distributions have been normalized so that the sum areas under the curve of the pass and fail distributions equals 1. 24

2.4 CO_2 (a) and N_2 (b) isotherms of all MOFs studied that do not meet the 95/90 PRT. CO_2 (c) andN_2 (d) isotherms of all MOFs that do meet the 95/90-PRT, and CO_2 (e) and N_2 (f) isotherms of the top 150 MOFs. The bold lines correspond to an 'average' isotherm constructed by using the average uptake of all isotherms at discrete pressure points with red corresponding to MOFs that don't meet the 95/90-PRT, blue corresponding to those that do meet the 95/90-PRT and black representing the top 150. The bottom figures compare the averaged CO_2 (g) and N_2 (h) isotherms from each class of MOFs where the shaded regions cover 1 standard deviation in each class. 26

3.1 Experimental set-up and cycle studied (a) Schematic diagram of the bench-scale VSA test apparatus. (b) Illustration of the 4-step cycle with LPP. Note that the thermocouples TC-1, TC-2, and TC-3 are at 8, 16, and 24 cm from the column inlet. 41

3.2 Impact of the size of training set on the accuracy of the surrogate models. a) Evolution of the R^2_{ADJ} for CO_2 purity and CO_2 recovery from an initial training sample size of 100 points (shown as a filled symbol) upto 800 points, each symbol depicts the addition of 100 more points. b) Evolution of the R^2_{ADJ} for energy consumption and productivity from an initial training sample size of 100 points (shown as a filled symbol) upto 800 points.The R^2_{ADJ} values for Energy and Productivity for SVM (Linear) are outside the range plotted. The shaded region represents the sample standard deviation in model prediction for 10 different randomly sampled runs. 46

3.3 The average total L_1 norm for each cycle step as a function of the different training sample sizes. Note that the results shown are the sample mean and the shaded area represents the sample standard deviation from the test-set (n =200). 47

3.4 Cyclic steady state profiles of the intensive variables at the end of the steps for are a sample VSA simulation. The dashed lines are predictions from the ANN surrogate model and the solid lines are the detailed model simulations. CSS profiles of a) the gas phase composition of CO_2. b) the bed temperature. c) the solid phase loading for CO_2 d) the solid phase loading for N_2. 48

3.5 Convergence to cyclic steady state as a function of number of cycles of the detailed model for two cases, namely, cycle initialised with feed conditions (15 mol% CO_2) shown as solid lines, and the dashed lines are the result for the cycle initialised with ANN-based CSS predictor trained with 400 samples. The L_1 norms and the mass balance errors are the average values from the test-set comprising of 200 samples. a) the variation of the average L_1 norm for both cases. b) the average mass balance error for both cases, the horizontal dotted line shown the 0.5% error line and the vertical dotted lines indicating the average CSS criteria for the test set. Note that criterion for CSS requires a mass balance error of <0.5% for 5 consecutive cycles. 51

3.6 Optimization approaches considered in this study. DV and IC stand for decision variables and initial conditions, respectively. 53

3.7 Process optimization for the two scenarios (a) the Pareto curves obtained from the multi-objective maximization of purity and recovery for the three optimization approaches. b) Variation of P_{INT} for the Pareto points shown in (a); and (c) Variation of $t_{\mathrm{ADS}} \times v_{\mathrm{FEED}}$ for the Pareto points shown in (a); (d) the Pareto curves obtained from the multi-objective maximization of productivity and minimization of energy for the three optimization approaches, subject to constraints of CO_2 purity $\geq 95\%$ and CO_2 recovery $\geq 80\%$; e) Variation of P_{INT} for the Pareto points shown in (d); and (f) Variation of $t_{\mathrm{ADS}} \times v_{\mathrm{FEED}}$ for the Pareto points shown in (c). The Surrogate Opt. and the CSS Opt, used a GPR(Matern) kernel(trained with 400 samples) and an ANN model (trained with 400 samples), respectively. 56

3.8 a) The normalized area under the Pareto curve obtained from a maximization of purity and recovery, is shown as a function of computational time for all three optimization approaches. The results of Detailed Opt. are shown as black symbols, the Surrogate Opt. is shown as red symbols, and the CSS Opt. shown in blue symbols. b) Computational effort for optimization using the three optimization approaches. 58

3.9 Cyclic steady state profiles of the intensive variables at the end of the cycle steps for the experimental run A from Table 3.2; the dashed lines are predictions from the ANN surrogate model and the solid lines are the detailed model simulations. CSS profiles of a) the gas phase composition of CO_2, the symbols are the CO_2 concentrations measured at the $Z = 0$ and $Z = L$ end of the column at the end of each cycle step. b) the bed temperature, the symbols in a) and b) represent the average of experimental measurements from the last 5 cycles. 61

4.1 The 4-step with light-product pressurization (LPP) process used in this study. 69
4.2 Key components of the MAPLE framework. 71
4.3 The effect of neural network architecture on model prediction accuracy: Average test R^2_{Adj} is shown as a function of the training-set size a) The effect of number of neurons and training samples on R^2_{Adj} b) The effect of number of hidden layers; ten neurons were used in each hidden layer. The test-set contains 1000 samples. 74
4.4 Parity plot of the detailed model and MAPLE surrogate results for a test-set of 1000 samples shown for the four key performance indicators a) Purity, b) Recovery, c) Productivity, d) Energy. 76
4.5 Parametric study showing the variation of key performance indicators a) CO_2 Purity b) CO_2 Recovery c) Productivity d) Energy, for Zeolite 13X as a function of intermediate pressure P_{INT}. Solid lines show the results from MAPLE and symbols correspond to the detailed model results. The shaded area represents a 2% error band. 79
4.6 Pareto curves resulting from the multi-objective optimization of the 4-step cycle with LPP process employing Zeolite 13X. Symbols are from the Detailed-Opt. and solid line from MAPLE-Opt. a) Pareto curve resulting from the unconstrained maximization of purity and recovery. b) Pareto curve resulting from the minimization of Energy and maximization of recovery subject to a CO_2 purity $\geq$95% c) Pareto curve resulting from the maximization of productivity and recovery subject to a CO_2 purity $\geq$95%. 80

4.7 Results from the unconstrained multi-objective maximization of purity and recovery for Zeolite 13X, UTSA-16, and Mg MOF-74 a) Pareto resulting from the unconstrained maximization of purity and recovery. b) The variation of $t_{\mathrm{Ads}} \times v_{\mathrm{F}}$ vs Purity. Lines denote results from MAPLE-Opt. and symbols are from Detailed-Opt. 82

4.8 Comparison of screening results from MAPLE with those reported by Khurana and Farooq [15]. a) Confusion matrix showing the classification results for the DOE Purity-Recovery requirements. b) Comparison of minimum energy values, subject to constraints of CO_2 purity $\geq 95\%$ and recovery $\geq 90\%$ calculated by MAPLE and those from the literature. 85

5.1 Process cycles used in this study a) 4-step with feed pressurization (FP), b) 4-step with light-product pressurization (LPP). c) The key components of the MAPLE framework. 97

5.2 Pareto curves obtained from a multi-objective optimization for maximizing low-pressure (P_{L}) and minimizing high-pressure (P_{H}) to achieve US-DOE targets (CO_2 purity $> 95\%$ and recovery $\geq 90\%$)for various feed compositions using the 4-step with LPP cycle. Both operating and isotherm parameters were used as decision variables. The region to the right of each curve is infeasible. 98

5.3 Practically achievable performance limits for a variety of case studies. The figures in the left column refer to minimum energy, while those on the right indicate maximum productivity case studies. a) and b) are results from case study 1, where both isotherm and process operating parameters are used as decision variables. c) and d) are results from case study 2, where the aim was to evaluate the performance of some real adsorbents with the 4-step LPP process. Here only operating parameters are used as decision variables. e) and f) are results from case study 3 that explored the impact of CO_2 recovery on the achievable limits with the 4-step LPP process. Here both isotherm and operating parameters were treated as decision variables. g) and h) are results from case study 4 that explored the impact of the low pressure with the 4-step LPP process. Here both isotherm and operating parameters were treated as decision variables. The reboiler duty for adsorption was obtained from the literature [148] and a 40% efficiency was used to convert from thermal to electrical units. Note: 100 kWh_e/tonne CO_2 cap = 0.36 GJ/tonne, 10 mol_{CO_2}/m^3 ads s = 38 tonne CO_2/m^3 ads day 105

5.4 Mapping of decision variables corresponding to curves E3 and P3in Fig. 5.3. a) Radar plot of decision variables corresponding to minimum energy (i.e., curve E3 in Fig 5.3), and b) Radar plot of decision variables corresponding to maximum productivity (i.e., curve P3 in Fig 5.3). c) and d) show the isotherms of CO_2 (and N_2, its very low) corresponding to isotherm parameters shown in a) and b). The plot of the isotherms shown in a) and b) along with those of the three real adsorbents studied are shown in sub-figures c) and d), respectively. 109

5.5 The impact of adsorption isotherm on process performance. The subplots a) and c) show minimized energy, while b) and d) show maximized productivity of the 4-step with LPP cycle. For each combination of H_{CO_2} and H_{N_2}, the process operating conditions are optimized to either minimize energy or maximize productivity. The diagonal lines on the plot represent the lines of constant selectivity, the symbols correspond to the adsorbents used in this study as a reference. Note that the isotherm parameters for these materials are provided in the supporting information. The results are shown for two different feed compositions $y_F = 0.15$ (top row), $y_F = 0.25$ (bottom row) 110

6.1 Characterization of adsorption equilibria. The left column are the isotherms for LiX, and the right column are the isotherms for 13X. The symbols are experimentally measured values and the lines are the SSL fit. 116

6.2 Experimental set-up and cycle studied (a) Schematic diagram of the bench-scale VSA test apparatus. (b) Illustration of the 4-step cycle with LPP. Note that the thermocouple TC-1 is at 17 cm from the column inlet. 120

6.3 The parity plots of the prediction from MAPLE for different performance indicators against those obtained from the detailed model for a test-set of 1000 samples as inputs for the Skarstrom cycle. a) Purity, b) Recovery, c) Productivity. The shaded area indicates a 5% deviation from the diagonal. 125

6.4 Pareto fronts for the multi-objective optimization of purity and recovery of the four-step Skarstrom VSA cycle for the two adsorbents. The solid blue line corresponds to LiX, and the red line corresponds to 13X. The closed symbols represent the purity and recovery obtained from running operating conditions in the experimental rig, and the open symbols the results from the same operating conditions in the MAPLE model. The dashed lines indicate the 95% confidence interval for isotherm parameters. 126

6.5 Pareto fronts for the multi-objective optimization of purity and productivity of the Skarstrom VSA cycle for the two adsorbents are shown. The solid blue line corresponds to LiX, and the solid red line corresponds to 13X. The closed markers represent the purity and productivity and the open markers the results from the same operating conditions in the MAPLE model. The dashed lines indicate the 95% confidence interval for isotherm parameters 127

6.6 Comparison of experimental and simulated transients for the experimental runs. The pressure history for one cycle is shown along with the detailed model results for the same inputs. The middle row and bottom row in each sub figure shows the outlet flow rate of the raffinate and extract product step, respectively. The symbols are from the experimental measurement and the line is obtained from the detailed simulations. 131

6.7 Comparison of experimental and simulated values of purity and recovery over 100 cycles for the Skarstrom cycle from dry air. Open markers represent the experimental purity and recovery at each cycle, and solid lines is from the detailed model simulation. 132

A.1 Loading as a function of the total pressure for a 15% CO2/85% N2 mixture for binary GCMC simulations (circles) and the competitive dual-site Langmuir isotherms (lines) fit using single component GCMC for a. PESTUD, b. LABGAY, c. OPENON, and d. UFUMUD02. . . 155
A.2 Typical operating configurations of the constituent steps in a P/VSA cycle 157
A.3 Fitted plot of the average fluid density of CO_2/N_2 mixture as a function of the mole fraction of CO_2. Points represent the NIST values and the dotted line represents the fit. 159
A.4 Effect of (a) adsorption step time (b) blowdown pressure on purity and recovery. Symbols represent the pilot plant experiments while the lines represent the model predictions. [75] 161
A.5 Convergence of (a) mass balance error (b) CO_2 purity and recovery after the VSA process has reached CSS. LABGAY MOF with isotherm shown in Fig.A.1 (b) was used for this case study. 161
A.6 Axial profiles of (a) CO_2 solid phase concentration (b) CO_2 gas phase concentration (c) Temperature across the column at the end of each step in the VSA process after the system reached CSS. LABGAY MOF with isotherm shown in Fig. A.1 (b) was used for this case study. . . 162
A.7 CO_2 purity vs recovery obtained for LABGAY MOF during grid-search simulations. 163
A.8 CO_2 recovery vs purity obtained for LABGAY MOF for 5 generations of a genetic algorithm optimization. 164
A.9 The average population fitness value (green circles) and the best candidate solution fitness values (blue diamonds) as a function of generation over the course of a single optimization of LABGAY MOF. 166
A.10 Single component a) CO_2 isotherms and b) N_2 isotherms for the 12 materials in Table 2.1. 167

A.11 Comparison of univariate probability distributions of different metrics for three classes of materials, i.e. 1) Top 150 (shaded in black) 2) DOE (shaded in blue) 3) Non-DOE (shaded in red) 169
A.12 Comparison of univariate probability distributions of structural properties for three classes of materials, i.e. 1) Top 150 (shaded in black), 2) DOE (shaded in blue), 3) Non-DOE (shaded in red) 170
A.13 Best accuracy points from LDA analysis for all 22 performance metrics, with the numbers on the axes corresponding to the metrics in Table1. The diagonal on these matrices contain the 1-dimensional LDA results for each parameter and the off-diagonal entries contain the 2-dimensional LDA model results. 171
A.14 Best MCC points from LDA analysis for all 22 performance metrics, with the numbers on the axes corresponding to the metrics in Table1. The diagonal on these matrices contain the 1-dimensional LDA results for each parameter and the off-diagonal entries contain the 2-dimensional LDA model results. 172
A.15 Precision for the best MCC points from LDA analysis for all 22 performance metrics, with the numbers on the axes corresponding to the metrics in Table1. The diagonal on these matrices contain the 1-dimensional LDA results for each parameter and the off-diagonal entries contain the 2-dimensional LDA model results. 172
A.16 Number of 95/90-PRT MOFs identified out of 392 for the best MCC points from LDA analysis for all 22 performance metrics, with the numbers on the axes corresponding to the metrics in Table1. The diagonal on these matrices contain the 1-dimensional LDA results for each parameter and the off-diagonal entries contain the 2-dimensional LDA model results. 173

A.17 Results from the 1 and 2-dimensional LDA analysis for the 6 structural properties. The metric numbers correspond to the metrics in Table 1. These plots present a) the overall accuracy [%] of the models, b) the MCC × 100 values of the models, c) the precision [%] of the models, and d) the recall [%] of the models. The diagonal on these matrices contain the 1-dimensional LDA results for each parameter and the off-diagonal entries contain the 2-dimensional LDA model results. 173

A.18 Results from the 1 and 2-dimensional LDA analysis for isotherm parameters showing a) the overall accuracy of the models, b) the MCC of the models, c) the Precision of the models, and d) the number of 95/90 PRT MOFs identified by the models. The diagonal on these matrices contain the 1-dimensional LDA results for each parameter and the off-diagonal entries contain the 2-dimensional LDA model results. 174

A.19 Kernel PCA plots for materials separated by a) parasitic energy, and b) productivity where blue points represent MOFs which failed the DoE PRT, red points are materials which meet the PRT and the best points are worse than the Pe/Prod median value, and green are materials which meet the PRT and whose best points outperform the median value. 175

A.20 Kernel PCA plots for materials separated by productivity where red points are materials which meet the PRT and the best points are worse than the Pe/Prod median value, and green are materials which meet the PRT and whose best points outperform the median value. 176

A.21 The GBR performance results showing the 5-fold cross-validation Pearson R2 (green), the test set R^2 values (blue), and the Training Set R^2 (red) for a) the Parasitic Energy using a min sample size of 4 and a learning rate of 0.01, and b) the productivity using the min sample size of 4 and a learning rate of 0.1. 177

A.22 Plots of the a) Productivity, b) Parasitic Energy, c) Purity, and d) Recovery as a function of feed velocity for different orders of magnitude of the macropore diffusion coefficient. 178

B.1 Typical operating configurations of the constituent steps in a PSA cycle 180

B.2 Characterization of adsorption equilibria. a) CO_2 isotherms with symbols representing experimentally measured values and the lines showing the DSL fit. b) N_2 isotherms with symbols being experimentally measured values and the lines showing the DSL-EES fit. c)Competitive equilibria of CO_2 and N_2 at 1.01 bar and 22°C. The symbols were measured from DCB experiments. The lines show the calculated values from the DSL-EES isotherm. Reproduced from Perez *et al.* [36] . 182

B.3 The input sample distribution of the different unique operating conditions, namely, t_{ADS}, P_{INT}, P_{LOW}, and v_{FEED}, for the 4-step cycle with LPP 183

B.4 The output distribution of the key performance indicators for the 4-step cycle with LPP obtained from the LHC sampling from Fig. B.3, i.e. Purity, Recovery, Productivity, and Energy. Note that the sub-plots in the diagonal are the univariate distributions for the key performance indicators. 184

B.5 Cyclic steady state profiles of the state variables at the end of the cycle steps for the experimental run B from Table 3; the dashed lines are predictions from the ANN surrogate model and the solid lines are the detailed model simulations. a) CSS profiles of the gas phase composition of CO_2, the symbols are the CO_2 concentrations measured at the$Z = 0$ and $Z = L$ end of the column at the end of each cycle step. b) CSS profiles for the solid state loading for CO_2 d) CSS profiles for the solid state loading for N_2. d) CSS profiles for the bed temperature, the symbols are the temperatures measured at TC-1, TC-2, TC-3 along the column at the end of each step averaged over the last 5 cycles. 185

B.6 Cyclic steady state profiles of the state variables at the end of the cycle steps for the experimental run C from Table 3; the dashed lines are predictions from the ANN surrogate model and the solid lines are the detailed model simulations. a) CSS profiles of the gas phase composition of CO_2, the symbols are the CO_2 concentrations measured at the$Z = 0$ and $Z = L$ end of the column at the end of each cycle step. b) CSS profiles for the solid state loading for CO_2 d) CSS profiles for the solid state loading for N_2. d) CSS profiles for the bed temperature, the symbols are the temperatures measured at TC-1, TC-2, TC-3 along the column at the end of each step averaged over the last 5 cycles. 186

C.1 Typical operating configurations of the constituent steps in a P/VSA cycle 188

C.2 Parametric study showing the variation of key performance indicators a) CO_2 Purity b) CO_2 Recovery c) Productivity d) Energy for Zeolite 13X as a function of intermediate pressure y_F. Operating parameters t_{ADS}[s]: 92.4, P_{INT}[bar]: 0.08, P_L[bar]: 0.03, v_F[$m\,s^{-1}$]: 0.64. Solid lines show the results from MAPLE surrogate framework and symbols correspond to the detailed model results, the shaded area represents a 2% error band. 193

C.3 Distribution of operating conditions used in the training set. A total of 21000 sample's are shown here. 194

C.4 Distribution of CO_2 (top) and N_2 (bottom) isotherms used in the training set. 195

C.5 The effect of neural network architecture on model prediction accuracy: Test R^2_{Adj} for Purity is shown as a function of the training-set size a) The effect of number of neurons and training samples on R^2_{Adj} b) The effect of number of hidden layers. Ten neurons were used in each hidden layer. The test-set contains 1000 samples. 196

C.6 The effect of neural network architecture on model prediction accuracy: Test R^2_{Adj} for Recovery is shown as a function of the training-set size a) The effect of number of neurons and training samples on R^2_{Adj} b) The effect of number of hidden layers. Ten neurons were used in each hidden layer. The test-set contains 1000 samples. 197

C.7 The effect of neural network architecture on model prediction accuracy: Test R^2_{Adj} for Energy is shown as a function of the training-set size a) The effect of number of neurons and training samples on R^2_{Adj} b) The effect of number of hidden layers. Ten neurons were used in each hidden layer. The test-set contains 1000 samples. 198

C.8 The effect of neural network architecture on model prediction accuracy: Test R^2_{Adj} for Productivity is shown as a function of the training-set size a) The effect of number of neurons and training samples on R^2_{Adj} b) The effect of number of hidden layers. Ten neurons were used in each hidden layer. The test-set contains 1000 samples. 199

D.1 Typical operating configurations of the constituent steps in a P/VSA cycle 201

D.2 Training sample distributions of the SSL isotherm parameters. A total of 50000 sample's are shown here. 202

D.3 Training sample distributions of the cycle specific operating parameters. A total of 50000 sample's are shown here. 203

D.4 The parity plots of the prediction from MAPLE for different performance indicator against those obtained from the detailed model for a test-set of 1000 samples as inputs for the 4 step with LPP cycle. a) Purity, b) Recovery, c) Energy, d) Productivity. The shaded area indicates a 5% deviation from the diagonal. 204

E.1 Typical operating configurations of the constituent steps in a P/VSA cycle 207

Chapter 1

Introduction

Physical adsorption is a surface phenomenon in which gas molecules adhere to the surface of certain solids and is based on weak physical bonds. The materials that can reversibly adsorb gases on their surface are called adsorbents. Adsorbents are usually porous solids, and their ability to adsorb varies from one to another and is dependent on the temperature and pressure of the system. This phenomenon of differential adsorbent-adsorbate gas affinity can be used in a cleverly designed process to separate or purify gas mixtures [1, 2]. Adsorption processes separate gas mixtures by using packed beds filled with porous adsorbents. When a gas mixture is sent through the bed of the adsorbent, one of them strongly adsorbs to the adsorbent when compared to the other one. Hence, the less adsorbed gas passes through the bed with a higher velocity compared to the other. The product rich in the unadsorbed gas is called the light product or raffinate, while the other is called the heavy product or extract. After a certain period of operation, the bed is regenerated. The process of adsorption and regeneration is repeated cyclically to achieve gas separation [1, 2].

Usually, as the system temperature increases or the pressure decreases, the ability of the material to adsorb decreases [1]. This can be understood further by examining the equilibrium loading at different temperatures and pressures. The adsorption equilibria quantify the amount of gas adsorbed onto the adsorbent when the gas system is brought to a state of equilibrium. The visual representation of this is

(a)

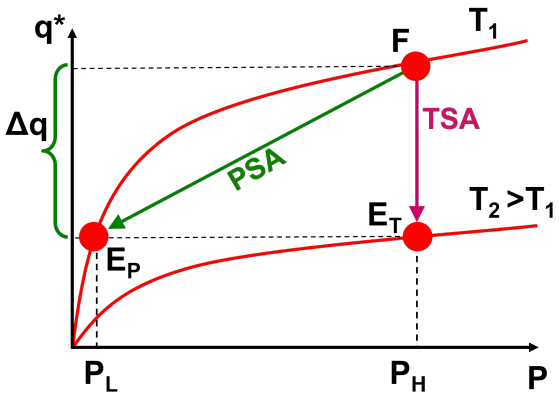

(b)

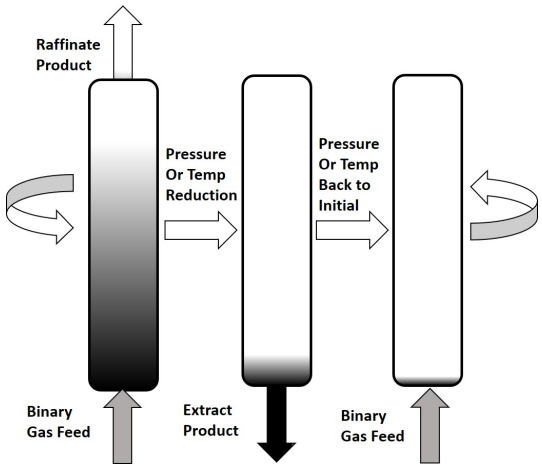

Figure 1.1: a) Qualitative adsorption equilibrium isotherm b) Basic cyclic adsorption process [1].

generally made in the form of an "isotherm". This plot shows the equilibrium gas loading as a function of pressure at constant temperature [2–4]. In Fig. 1.1 a) a qualitative isotherm of gas A is shown of an adsorbent material as a function of pressure, X-axis represents a changing pressure. The Y-axis represents an equilibrium gas loading on the adsorbent.

For a given pressure and temperature condition, the solid equilibrium loading can be quantified using the isotherm. For example in Fig. 1.1 a) F is the equilibrium loading at feed conditions. F represents the amount of gas adsorbed on the solid adsorbent at pressure= P_H, and temperature = T_1. If we apply a temperature change

to $T_2 \geq T_1$ or change the pressure to P_L, we release part of the adsorbed gas Δq. This phenomenon is used to construct separation processes such as the one shown in Fig. 1.1 b). Here a basic cyclic adsorption process is shown, with an adsorption step. The gas is adsorbed at equilibrium conditions, followed by a regeneration step. The adsorbent can be regenerated in many ways. Two of them, namely, varying the temperature or the pressure, are standard modes of operation. When a pressure change is applied, the process cycle is referred to as a Pressure Swing Adsorption (PSA) process, depending on the range of pressure swings. When a temperature change is applied, the process is referred to as Temperature or Thermal Swing Adsorption (TSA). The pressure reduction is generally achieved either by naturally depressuring a column or by using a vacuum pump. The working principle of a TSA process is similar to a PSA process. However, temperature reduction is achieved by the use of a cooling and heating stream [1, 2]. This step is followed by a re-initialization step, where the condition of the bed is brought back to initial adsorption conditions. This is done by bringing the temperature and pressurization back to the initial conditions [1].

Beyond the regeneration and adsorption steps, reflux steps (analogous to distillation) can be added to a process cycle to obtain desired process performance [1, 2, 4]. PSA processes are used mainly in the industry for the purification of H_2, O_2, N_2 and TSA processes are widely used in the industry for applications such as drying of natural gas, etc [5, 6]. They are less understood for applications such as extract/ heavy product purification [7, 8]. These cyclic adsorption processes can be used as an alternative to conventional separation processes like distillation and absorption. In small and medium scales, these processes are energy efficient when compared to the conventional separation techniques [2–4].

1.1 Case Study

1.1.1 Carbon Dioxide Capture

Today, the conversation relating to climate change and the future of the world's energy infrastructure is predominantly focused on renewable sources. However, globally we are far from breaking our dependence on fossil fuels [9–11]. Greenhouse gases such as CO_2 and methane are the main contributors to manufactured climate change, and their effects are mitigated. The world is looking to shift to a low-carbon, high-energy efficiency infrastructure, and there is a need to find low energy and highly productive technologies to facilitate this change [12].

Carbon Capture and Storage (CCS) is a field of study dedicated to the capture and utilization of anthropogenic CO_2. It has been projected that CCS, along with other low carbon emission technologies, is essential for sustained yet sustainable growth [13]. The majority of the CO_2 generated is through large point sources of energy such as fossil fuel-based power plants. The CO_2 stream at the outlet of these plants is very dilute and thus, is energy-intensive to separate and capture effectively [12]. The current state-of-the-art technology, which is based on a liquid amine-driven absorption process, is energy-intensive, consuming about 25% of the plants' energy, and is also inherently deleterious to the environment [14]. Adsorption technologies are considered viable option to compete with the absorption-based CO_2 capture [15, 16].

1.1.2 Oxygen Generation

Industrial oxygen generation from the air is produced by cryogenic distillation at a high production rate and using pressure swing adsorption (PSA) at lower production rates. The product quality of 99% from cryogenic separation and 90+5% is typically expected from PSAs for various applications. Large industrial-scale PSA plants for oxygen production have been developed to replace air with 90% oxygen in aquaculture, water treatment, steel, etc. [17]. The main motivation for using PSAs for oxygen

generation over cryogenic distillation is the lower capital and operational cost at relatively lower scales, with PSAs being cost-competitive at scales below 300 tonnes per day of oxygen (TPDO). [17]

With the advent of the COVID 19 pandemic and the shortage of O_2 it has caused in many parts of the world, there is a real and immediate need for innovation in low-cost O_2 production. PSA technology, which is industrially mature, is an exciting candidate for such an application. Especially with the different production scales and modularity of these units make them easy and quick to deploy without massive infrastructural investments. The recent innovations in metal-organic chemistry and our ability to identify and synthesize tailor-made adsorbents for this separation make this a fascinating and relevant case study, currently and for the future. PSA-based O_2 generation is highly researched and commercially available. However, designing an optimal operation of such systems is very challenging. The need of the hour is to democratize this technology and simplify the operation of this process to aid in remote deployment.

1.2 Gaps in Research

"Many PSA process paths can be designed for the same separation objectives."- Sircar et al. [2].

"There are an almost unlimited number of Metal Organic Framework (MOF) adsorbents."- R. Snurr et al. [18].

These two statements, made on adsorbent and adsorption process design, bring up whether there exists an optimum process and magic adsorbent for a given separation objective. If true, should the two be designed in a collaborative or unified manner?

Many microporous and mesoporous adsorbents exhibit vastly different adsorption properties, which changes their ability to separate a given gas mixture. The separation potential of the adsorbents needs to be fully understood before an appropriate process can be developed around it. Therefore, the best material for a separation process

should have an accompanying process cycle that can exploit its properties for the separation goal. This is selected based on the adsorbent's isotherms or physical properties, so these properties need to be identified.

Conversely, for a process cycle with a general separation objective, the adsorbent must have a specific gas adsorption isotherm and physical properties best suited to the separation objective. Marrying these two procedures with the optimization of the process and material conditions can, thus, lead to a more productive outcome with a corresponding reduction in the time for development [4].

Many possible process cycles can be designed. The cycle design is currently based on a heuristical approach that varies for different separations with little agreement on the best process cycles [4, 19–21]. Both raffinate and extract purification cycles are studies to a large extent in the literature. [22–25].

1.3 Traditional adsorptive process design

The existing literature surrounding adsorption process development can be separated into two main categories—the first consists of studies performed on an atomistic scale. Chemists and materials engineers perform *in-silico* or experimental screenings of material. This involves either simulating or experimentally testing adsorbents for a specific gas separation process [26–28]. There is currently no consensus on the definition of a high-performing material in this area. In the literature, different performance metrics are used in the material discovery process [15, 29]. Metrics include the gas uptakes, the selectivity of the material, the heats of adsorption, and the working capacities. Using the information provided by these, simple models can be applied to provide rough estimates of the separation potential of these materials [26, 30]. Although much can be learned about these materials using these techniques, very little information can be obtained concerning the actual performance of the material in the industrial gas separation process, such as the purity of the captured product or the volumes of the materials which would be required to run the separation

continuously.

The second category focuses on the process design and optimization of the adsorbents in the process. These studies aim to determine how an adsorbent will perform if placed in an industrial process [15, 19, 31–33]. In Fig. 1.2 a), the schematic of a traditional process design and optimization scheme is provided. The selected adsorbent material is evaluated with a specified process cycle. These studies have relied on the researchers synthesizing promising material and testing its performance on a bench scale setup or modelling the performance based on experimental isotherm data found in the literature. The adsorbents are screened by optimizing the performance of each adsorbent using the detailed model coupled with an optimization routine. Optimization of any adsorbent-based separation process is non-trivial as it involves multiple inputs, and the outputs are highly non-linear by nature [31, 34, 35]. This, coupled with the vast number of available materials and the slow convergence of the optimal solution, makes the hunt for a global optimum solution challenging. Recent studies have also validated the use of the technique in directing experimental campaigns [36]. The results from this type of study are specific to each separation and the process constraints [19, 29, 35].

Fig. 1.2 b) shows a qualitative plot of the various methods to model and predict adsorption processes. The x-axis shows the computational time, and the y-axis shows the accuracy of these models. Generally, material screening in the literature uses simplified metrics [37] that can be calculated quickly but have no significant statistical correlation to real-world performance [29, 38]. Reduced-order models [39] and batch adsorber analogues [38] are better at the overall performance of the system but are lacking in the prediction of process dynamics. Full adsorption models based on first principles, as explained in the modelling section in the appendix, are accurate but slow, making optimization of the process difficult. The main bottleneck in this adsorbent screening and evaluation process is the time it takes to accurately screen and evaluates the adsorbents, both computationally and experimentally.

The literature is thus segregated into two views, a material perspective and a process perspective. Large databases with over 1 million such real and *in-silico* hypothetical porous structures are available to process designers that are already partially characterized for the application of CO_2 capture [40–47]. The Cambridge Structural Database (CSD) is one of the many available adsorbent databases and contains thousands of adsorbent structures that can be evaluated for various applications [18, 41]. To screen these in an adsorption process, their gas adsorption needs to be quantified and characterized. This is done either by using *in-silico* techniques or by using gravimetric or volumetric adsorption measurements. Grand Canonical Monte Carlo (GCMC) is one proposed avenue to estimate gas adsorption of thousands of structures as they are quicker than physical experiments. The adsorption predictions can then be fitted to functional isotherm forms, which allowed for preliminary screening of the materials [41, 48, 49]. Other databases like the National Institute of Standards and Technology (NIST) and literature are available to use with a large data-set of experimental and theoretical materials that can also be used for process design. Recent development in the ability to create, tune, and tailor-make adsorbents has garnered much attention in both the scientific and engineering communities [18, 37]. This means that by performing large-scale screening of adsorbents, faster modelling techniques need to be developed. With thousands of new materials and hundreds of cyclic processes possible, the design of an optimum adsorbent-based separation process and screening adsorbents is an exciting problem to study [18, 37]. A combined approach is necessary as this would lead to a more accurate understanding.

This thesis will implement a unified material and process design approach to understand process design better. The goal of this proposal is to map processes and relevant material properties to the final process outcomes. The developed models need to be fast and should emulate the detailed model accurately. This model should be generalizable over physically relevant input conditions, after which it can be used as a proxy for the slow, detailed model. This would allow for faster optimizations,

material screening, and the investigation of the structure to performance relationship.

1.4 Structure of the thesis

The thesis is divided into five sections and is summarized below:

In chapter 2, atomistic simulations were fully integrated with a detailed VSA simulator to screen 1632 experimentally characterized MOFs for CO_2 capture using detailed process models. A total of 482 materials were found to meet the US DOE specifications for carbon capture, i.e., 95% CO_2 purity and 90% CO_2 recovery targets (95/90-PRTs). 365 of the screened adsorbents have parasitic energies below that of solvent-based capture (*approx*290 kWh_e/MT CO_2) with a low value of 217 kWh_e/MT CO_2. Machine learning models were also developed using common adsorption metrics to predict a material's ability to meet the 95/90-PRT with an overall prediction accuracy of 91%. It was also found that accurate parasitic energy and productivity estimates of a VSA process require full simulations.

In chapter 3, machine learning-based surrogate models were developed to accelerate the process models and optimization. Various supervised machine learning algorithms, such as decision trees, random forests, support vector machines, Gaussian process regression, and artificial neural networks, were tested for their ability to predict key performance indicators for a given set of operating conditions. Experiments performed on a lab-scale two-column rig, for the concentration of CO_2 from a mixture of CO_2+N_2 on Zeolite-13X, confirm performance indicators such as purity, recovery and axial profiles predicted by the surrogate models.

In chapter 4, a generalized data-driven surrogate model that fully emulates the operation of an adsorption process at the cyclic steady state is studied. This framework is called machine-assisted adsorption process learning and emulation (MAPLE). This model is generalized for various inputs, including adsorbent properties, the Langmuir adsorption isotherm parameters, and operating conditions. The ability of this framework for rapid screening of adsorbents for post-combustion CO_2 capture was also

(a)

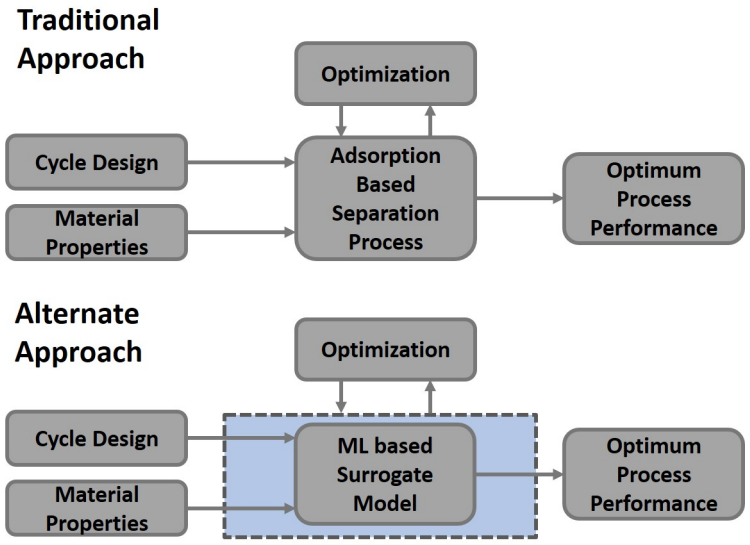

(b)

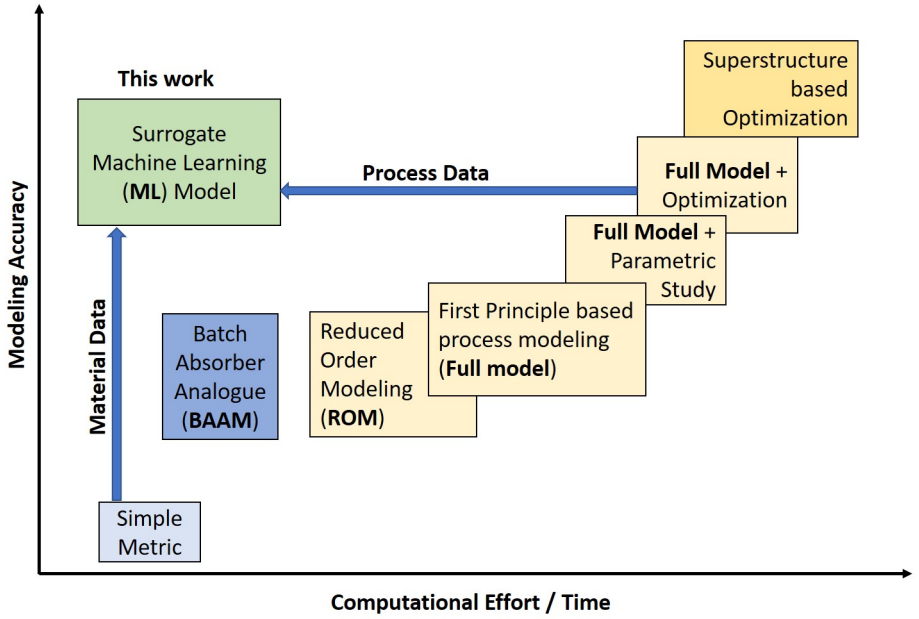

Figure 1.2: Adsorption process simulation from material properties, a) the traditional approach to adsorption process simulation alongside the proposed machine learning approach b) a qualitative indication of time and computational effort is shown against accuracy for different modeling schemes.

illustrated.

In chapter 5, the practically achievable limits for a PVSA-based carbon capture were evaluated. Two low-energy process cycles are considered, and a machine learning surrogate model is trained with inputs from a detailed PVSA model. Several case studies were considered to evaluate two critical performance indicators: minimum energy and maximum productivity. The genetic algorithm optimizer coupled to the machine learning surrogate model searches tens of thousands of combinations of isotherms and process operating conditions for each case study.

Chapter 6 involves the experimental validation of the adsorbent agnostic MAPLE model using cyclic adsorption experiments. In this work, data obtained from a detailed model using hypothetical inputs for isotherm parameters were used to train a multi-layer neural network to predict process performance. The system used to validate this methodology was O_2 separation from air. The process cycle used was a 4 step Skarstrom cycle with feed pressurization. The optimized process conditions for both adsorbents were used to run lab-scale cyclic experiments. The results showed good agreement between the detailed and MAPLE model and translated on a real-world physical experiment.

Chapter 2

Prediction of MOF performance in vacuum swing adsorption systems for post-combustion CO_2 capture based on integrated molecular simulations, process optimizations, and machine learning models

2.1 Introduction

[1] Global warming caused by greenhouse gases, primarily CO_2, represents one of the greatest challenges faced by our generation. Yet, fossil fuels are expected to play an important role in global energy systems for decades to come. For this reason, most serious climate assessment models include carbon capture and storage (CCS) as a route to reduce CO_2 emissions. Since ≈35% of the world's anthropogenic CO_2 emissions arise from fossil fuel based power plants, there has been substantial interest in technology to capture CO_2 from the combustion flue gases of such point sources [50, 51]. Although several industrial scale CCS projects exist that capture and store more than a million tons of CO_2 per year, the solvent-based CO_2 scrubbing technologies

[1]This chapter appears as- Burns, T. D., Pai, K. N., Subraveti, S. G., Collins, S. P., Krykunov, M., Rajendran, A., and Woo, T. K. (2020). Prediction of MOF performance in vacuum swing adsorption systems for post-combustion CO_2 capture based on integrated molecular simulations, process optimizations, and machine learning models. Environmental science and technology, 54(7), 4536-4544.

used in these projects are considered too energetically expensive for wide-scale deployment [52].

Several technologies are being explored as energy efficient alternatives to current solvent based CO_2 scrubbing systems. At the forefront, are solid sorbent-based technologies that use porous materials within pressure and/or temperature swing adsorption (P/TSA) systems. Techno-economic studies suggest that P/TSA technologies have the potential to substantially reduce the cost of carbon capture, if the right solid sorbents can be found [13]. Metal organic Frameworks (MOFs), which are crystalline nano-porous materials that are constructed from inorganic and organic building units, [53, 54] have attracted significant attention as possible sorbents. Due to the seemingly endless combination of building units that can be combined to construct them, a dizzying range of MOFs is possible such that they can potentially be tuned for any given application. Indeed, it is estimated that nearly 70,000 different MOFs have been synthesized and characterized to date [42]. MOFs are often introduced as outstanding materials for post-combustion CO_2 capture by highlighting a few targeted adsorption properties, such as high CO_2 uptake capacity or CO_2/N_2selectivity, [55–59], without a clear understanding of how these properties affect their performance in a real industrial P/TSA process. Large databases, some containing millions of hypothetical materials, [18] have been screened computationally via detailed atomistic simulations for their potential to be used as solid sorbents for post-combustion CO_2 capture. [26, 41, 60, 61] Again, in most instances, a few targeted adsorption properties or related figures of merit (FOM) have been used to rank the materials. In a limited number of cases the parasitic energy (PE) of CO_2 capture has been used as a metric for screening [26, 62, 63]. The PE is the energy required to regenerate the sorbent during the gas separation process and to compress the CO_2 to 150 bar for transport and storage. In other words, the PE provides an estimate for how much energy is needed to run a CCS unit on a coal fired-power plant, which is a critical component in determining its feasibility. Although the PE is a more holistic and

pragmatic metric, [64] the PEs used in previous most screening studies [62] are based on simplistic equations using equilibrium adsorption data. As a result, these calculations cannot determine if the materials can meet the US-DoE targets of achieving 95% CO_2 purity while recovering 90% of CO_2 from the flue gas. [65] Thus, while valuable insights have been inferred from these various screening studies, it is still unclear how the reported metrics relate to the actual performance of a full-scale P/TSA system. In the 2018 Mission Innovation report "Accelerating Breakthrough Innovation in Carbon Capture, Utilization and Storage", one major research challenge identified for solid sorbents was to "Understand the relationship between material and process integration to produce optimal capture designs for flexible operation – bridging the gap between process engineering and materials science." [66] The goal of this work is to perform a large-scale screening of MOFs using sophisticated process simulations integrated with molecular simulations to examine the performance of MOFs in an industrial vacuum swing adsorption (VSA) system - thus bridging the gap between materials design and process engineering. Although full process simulations have been previously performed on solid sorbents, including MOFs, generally only a limited number and diversity of sorbents have been studied in this way, [15, 29, 31, 67–71] due in part to the computational intensity of such simulations. Snurr and coworkers used a multi-scale approach to study a group of 369 MOFS using a 4-stage flue gas re-pressurization cycle. [72] In that work, the parasitic energy and CAPEX were used in the costing analysis. However, the estimates of the capital costs in that work are simplistic compared to those generally reported in the literature [73] and therefore have particularly large uncertainties associated with them. It is notable, however, that they found that the N_2 adsorption behaviour is the most important factor in determining if a material will meet the US-DoE 95/90 purity/recovery targets (95/90-PRT). This is rather non-intuitive since the CO_2 adsorption behaviour most often discussed in evaluating the performance of a MOF. In this work we have screened 1632 MOFs and related materials with an advanced PSA process simulator

that has been experimentally validated at the pilot scale using a 4-step light-product pressurization (LPP) cycle shown in Figure 2.1. This cycle has been shown to be the most energy efficient cycle for post-combustion CO_2 capture. [19] While a costing algorithm could be used as the objective function, there are large uncertainties in the costing of MOFs in order to estimate the capital expenditures. Hence, the goal here was to obtain high reliability results at a scale where our models have been validated. Therefore, the process conditions have been optimized for each material to minimize the PE or to maximize the productivity while meeting the 95/90 purity-recovery targets (PRT). The productivity of a material or how much CO_2 the sorbent can extract per unit volume of the material per unit time is not only important for determining how much material is required for CO_2 capture, it is also vital for determining the complexity of the VSA system required, and more suitable but essential considerations such as the capacity of the vacuum pumps that are required.

The screening also provides a unique opportunity to compare the effectiveness of various metrics that have been used by researchers to evaluate solid sorbents for post-combustion CO_2 capture against actual VSA performance.

2.2 Computations Methods

The CoRE database of materials, containing over 5000 experimentally characterized MOFs, was used as a starting point for this work. [74] Due to the high computational costs involved in the simulations, a series of heuristic filters were applied to remove materials that would not be suitable for a large-scale industrial process, such as MOFs containing rare or toxic metals. This left 1,584 MOFs from the CoRE database, for which the CO_2 and N_2 adsorption isotherms were predicted using atomistic Grand Canonical Monte Carlo (GCMC) simulations. In addition to materials from the CoRE database, an additional 32 well-known MOFs, 8 zeolites, and 8 porous polymer network materials with experimental adsorption properties available at the conditions of interest were added to the screening for a total of 1632 materials (collectively

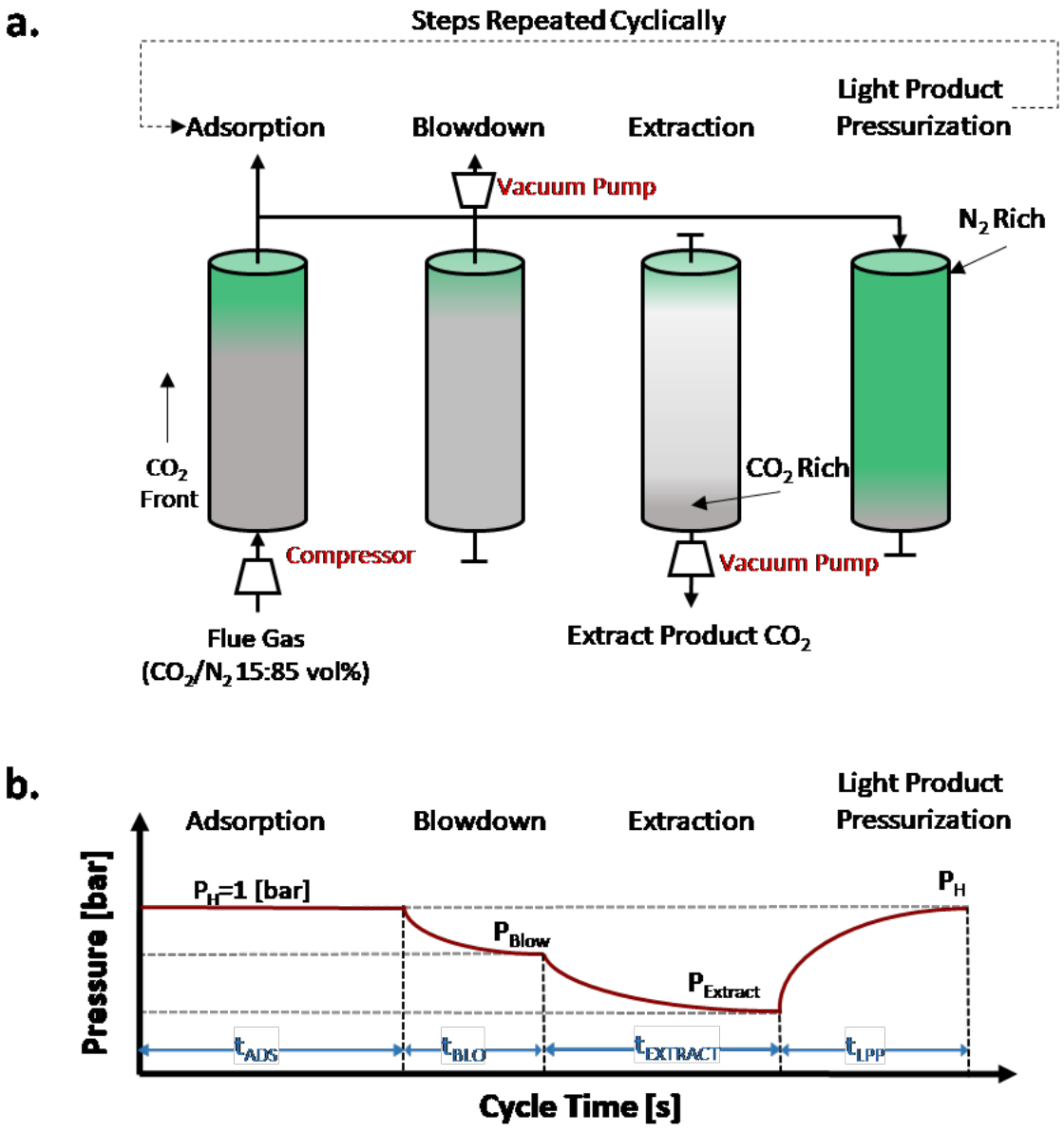

Figure 2.1: a) Process schematic of the 4-step VSA cycle simulated. b) Pressure profile of the VSA cycle. The times of the adsorption, blowdown and extraction steps (t_{ADS}, t_{BLOW}, t_{EXTRACT}) and the blowdown and extraction pressures (P_{LOW},P_{EXTRACT}) shown are 5 of the 7 variables used in the process optimization.

referred to as MOFs for simplicity). In this work, a dry flue gas composed of 15% CO_2 and 85% N_2 was used. The process simulation model used in this work has been shown to reproduce experimental results (both transient and steady-state) from a pilot-scale column packed with 80 kg of Zeolite-13X pellets. [75] The MOF crystals are considered to be formed into 1mm diameter spheres using a structuring agent and uniformly packed in a column of length 1 m and 0.3 m diameter, in order to be consistent with the scale of the pilot-plant. The model accounts for the dynamics of heat transfer within the column and across the column walls, mass transfer including diffusion of gas into the sorbent particles, frictional pressure drops, and the concentration and temperature changes due to adsorption/desorption. PEs were calculated using well established efficiencies for vacuum pumps, blowers, and compressors. To summarize, the model captures the entire physics and the dynamics of the process without any significant simplifications.

The VSA cycle can be optimized for a given material by varying the following process variables: the flue gas flow rate, the inlet gas temperature, the times of the blow-down, adsorption, and extraction steps, and the extraction and blow-down pressures. For each of the 1632 materials, a grid search of 1000 unique combinations of the process variables that cover a wide range of operating conditions were run. From this grid search, materials were ranked by their ability to meet the 95/90-PRT and their parasitic energies. The process conditions for the top 1022 materials from this ranking were then fully optimized using a genetic algorithm (GA) to find the best process conditions that minimizes an objective function that combines both PE and productivity while maintaining the 95/90-PRT. A minimum of 3 GA optimizations were performed on each material to provide a robust sampling of the search space and ensure that a reasonable estimate for the global minimum was found.

Material	Parasitic Energy [kWh_e / MT CO_2]	Productivity [TPD CO_2/ m^3]
IISERP-MOF-2 [63]	241	5.39
UTSA-16 [76]	249.1	5.15
zif-36-frl [62]	248.9	4.37
Zeolite NaA [77]	248.4	4.76
GAYFOD[a]	249.9	5.53
HUTTIA[a]	249.4	4.5
IGAHED02[a]	244.3	4.89
QIFLUO[a]	249.6	4.29
WUNSII[a]	249.9	5.51
XAVQIU01[a]	246.8	4.78
YEZFIU[a]	247.7	5.01
ZEGSUB[a]	250	4.45

Table 2.1: List of the 12 high-performing materials which simultaneously achieve a parasitic energy less than 250 kWh_e /MT CO_2 and a productivity greater than Zeolite-13X (4.2 TPD CO_2 /m^3). PE and productivities are given for a single process point that meets the aforementioned criteria while also meeting the 95/90-PRT. [a]CCDC identifier for MOFs in the Cambridge Structural Database. [45]

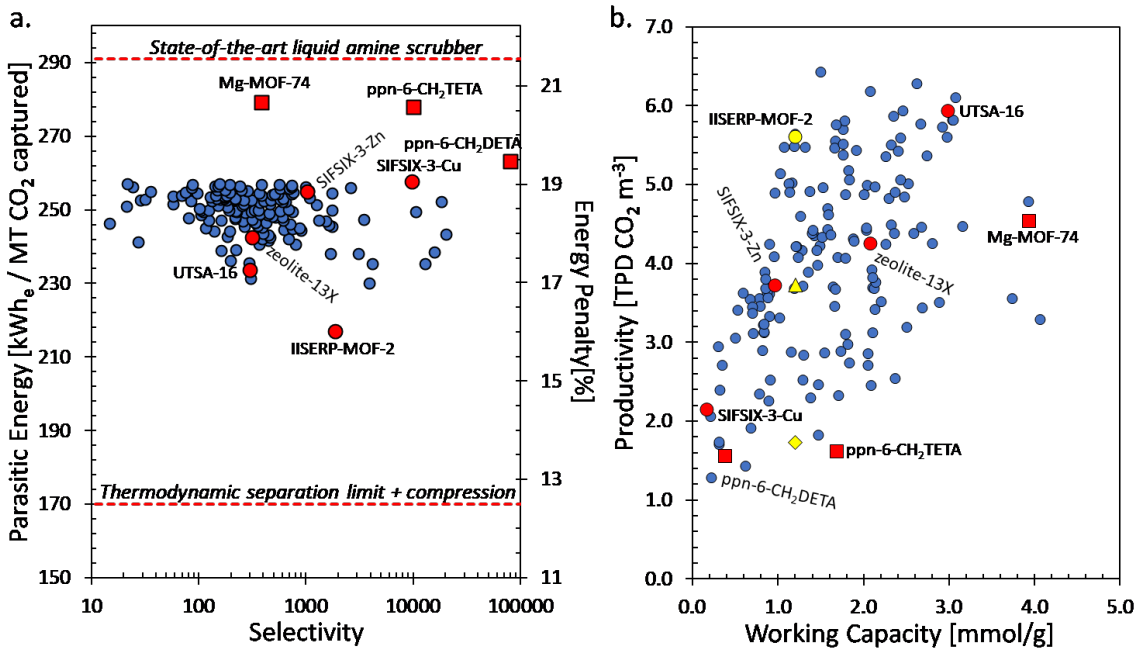

Figure 2.2: (a) Lowest PEs resulting from process optimization of the top 150 materials (circles) as a function of the CO_2/N_2 selectivity. The right-hand vertical axis is the energy penalty, which is the percentage of the power plant's energy output that must be diverted for CO_2 capture and compression. (b) The highest productivity of the same top 150 materials (in units of tonnes of CO_2 captured per day per m^3 of sorbent) as a function of the single component working capacity. For IISERP-MOF2, highlighted in yellow, the productivity is shown for the process conditions that give the best productivity (circle), best PE (diamond) and a balance of the two (triangle). All points shown in (a) and (b) meet the 95/90-PRT. Well known materials are highlighted in red including those that are not part of the top 150 materials (squares). The PE of a state-of-the-art liquid amine scrubber was taken from reference [78] while the thermodynamic separation limit + compression was calculated from Ruthven *et al.*[79]

2.3 Results and Discussion

Over the course of this study, over 5 million unique process simulations were performed where 392 materials were found to meet the 95/90 purity-recovery target using a 4-step VSA cycle. Figure 2.2 a) shows the genetic algorithm-optimized PEs from the top 150 materials that meet the 95/90-PRT plotted against the CO_2/N_2 selectivity of the material. We will refer to these 150 materials ranked in terms of the PE as the 'top 150'. All top 150 materials out-perform the state-of-the-art liquid amine system in terms of PE with the best material, IISERP-MOF2, having a PE of 217 kWh_e/MT CO_2 or 781 $kJ_e/kgCO_2$. This is a 25% improvement over the state-of-the-art liquid amine scrubbing system. [78] Another essential quantity in assessing the operational performance of a solid sorbent is the productivity. The productivity can be used to determine the size and complexity of a VSA plant and full process simulations are one of the few ways to estimate it aside from pilot scale experiments. Figure 2.2 b) shows the best productivities of the top 150 materials plotted against the CO_2working capacity of the material. For reference, we highlight the maximized productivity of Zeolite-13X (4.2 tonnes CO_2captured per day/m^3 of sorbent), which is a sorbent currently used in industrial VSA systems for capturing CO_2in methane rich streams. [77] 67 MOFs that are part of the top 150 have maximum productivities that are better than Zeolite-13X. It is important to note that Figures 2a and 2b show the same materials but at different process conditions where the 95/90-PRT can be achieved. In Figure 2.2a, the conditions have been optimized to give the lowest PE, while in Figure 2.2b, they have been optimized for the productivity. For example, when the process conditions for IISERP-MOF2 are optimized for the productivity, its PE increases to 250 kWh_e/MT CO_2 (yellow circle in Figure 2.2b) from its minimum of 217 $kWh_e/MTCO_2$. Conversely, when the conditions are optimized for the PE (yellow diamond), the productivity of IISERP-MOF2 is reduced by approximately 70% from its maximum value. A balanced process point on the PE/productivity

Pareto front for IISERP-MOF2 is shown as a yellow triangle in Figure 2.2b, where the productivity is more than double the minimum value, but whose parasitic energy of 222 kWh_e/MT $CO_2$is only slightly higher than the best value.

Given in Table 2.1 is a list of materials which are able to simultaneously achieve parasitic energies below 250 kWh_e/MT $CO_2$and productivities greater than Zeolite-13X (4.2 TPD CO_2/ m^3) with a single process point (or single set of process conditions). The value of 250 kWh_e/MT CO_2 is chosen since the materials would still outperform solvent based capture systems with room to spare once the energetic cost of drying the flue gas is added (drying to less than 100 ppm has been estimated to be as low as 24 kWh_e/MT CO_2 [87]). Interestingly the list includes NaA, a Linde Type A (LTA) zeolite with a 1:1 Al:Si ratio. [88] This is a significant result since industrial scale synthesis of LTA zeolites is common [76, 89] and therefore could be used as a low cost CCS sorbent if the flue gas is dried. It is also notable that the best performing material, IISERP-MOF2, is stable in moist, acid gas environments and its CO_2adsorption properties are nearly unchanged in high humidity conditions. [63, 90] IISERP-MOF-2 was identified as having the lowest parasitic energy without the constraints imposed on the PE and productivity with a PE of 217 kWh_e/MTCO_2. This value which is remarkably close to the best possible hypothetical minimum-energy material predicted by Khurana and Farooq, which has a parasitic energy of 213 kWh_e/MT CO_2 meeting identical CO_2 purity and recovery. [91] The process conditions can also be adjusted with IISERP-MOF-2 such that the productivity can be relatively large while still maintaining a low parasitic energy. IISERP-MOF-2 is therefore an ideal candidate material for the post-combustion carbon capture process and should be considered for future materials research to provide a pathway for scale up and implementation.

Highlighted in Figure 2.2 as red data points are the optimized PE's and productivities some well known materials. Mg-MOF-74 and the porous polymer network PPN-6-CH_2TETA have previously been determined to have amongst the lowest PE's based on equilibrium adsorption properties for a P/TSA system. However, for VSA

Metric number	Adsorbent Metric	Correlation R^2	
		Productivity	PE
1	CO_2 uptake capacity [mmol g^{-1}]	0.07	0.01
2	competitive CO_2 uptake capacity [mmol g^{-1}]	0.06	0.02
3	CO_2 work capacity [mmol g^{-1}]	0.17	0.01
4	competitive CO_2 working capacity [mmol g^{-1}]	0.17	0.01
5	N_2 uptake capacity [mmol g^{-1}]	0	0.02
6	competitive N_2 uptake capacity [mmol g^{-1}]	0	0.1
7	N_2 working capacity [mmol g^{-1}]	0	0.02
8	N_2 competitive working capacity [mmol g^{-1}]	0	0.1
9	single component CO_2/N_2 selectivity CO_2 [-]	0.01	0.02
10	competitive CO_2/N_2 selectivity [-]	0.03	0
11	Henry's selectivity [-]	0.01	0
12	CO_2 heat of adsorption [kJ mol^{-1}]	0	0.06
13	N_2 heat of adsorption [kJ mol^{-1}]	0	0.03
14	Sorbent Selection Parameter [80] [mmol g^{-1}]	0.01	0
15	Adsorbent Performance Score [81] [mmol g^{-1}]	0.02	0.01
16	Separation Potential [82] [mmol g^{-1}]	0.06	0.02
17	Percentage Regenerability [83] [%]	0.04	0.02
18	Yang's FOM [80] [-]	0.01	0.01
19	Wiersum's FOM [84] [mol^3 J^{-1} kg^-2]	0.1	0.03
20	Notaro's FOM [85] [mmol g^{-1}]	0.01	0
21	Ackley's FOM [86] [mmol g^{-1}]	0.01	0
22	Huck's PE [62] [kWh_e/t CO_2]	0	0
23	Generalize Evaluation Metric (GEM) [-]	0.02	0.03
24	maximum accessible pore diameter [Å]	0.03	0
25	maximum channel diameter [Å]	0.02	0
26	maximum pore diameter [Å]	0.03	0
27	gravimetric surface area [m^2 g^{-1}]	0.07	0.01
28	volumetric surface area [m^2 g^{-1}]	0.1	0.01
29	void fraction [-]	0.04	0

Table 2.2: List of sorbent metrics and the correlation coefficients of the metrics to the productivity and parasitic energy for all MOFs that meet the 95/90-PRT and whose process conditions have been fully optimized (392 materials).

separations we find are not even part of the top 150 in terms of PE. Further, Figure 2.2a shows that materials with a wide range of selectivities (12 to 20145) can achieve the 95/90-PRT and that there is no strong correlation between the selectivity and the PE. Similarly, Figure 2.2b suggests there is not a strong correlation between the CO_2working capacity and the productivity as one might intuitively expect. For example, Mg-MOF-74 which possesses amongst the highest CO_2working capacities known, does not even rank in the top 20% of materials examined in terms of productivity. Indeed, this screening allows for an examination of which metrics commonly used to evaluate MOFs (see Table 2.2) are good predictors of a material's PE, productivity, or whether it will meet the 95/90-PRT. We have considered the fitted isotherm parameters for both $CO_2$and N_2, 13 conventional adsorption metrics, such as the CO_2working capacity, 9 composite metrics, such as the Adsorption Performance Score (APS), [92] and 6 geometric features of the MOF, such as the maximum pore diameter.

We first examine the PRT of the 1632 materials that were subjected to a grid search and GA optimization of process conditions. Provided in Figure 2.3 are probability distribution plots of four common metrics and the N_2isotherm parameters for materials split into three categories: all materials which pass the 95/90-PRT (blue), those that fail the 95/90-PRT (red), and the Top 150 (black). These distributions are normalized such that the sum of the pass and fail distributions is 1, which means that when the lines intersect, the two outcomes are equally probable. Interestingly, no distinctions can be made between materials that meet or fail the 95/90-PRT for any of the tested metrics (See Fig. S9-S10 for all metrics) with the exception of the N_2isotherm parameters (Figure 2.3c and d). The absence of this same behaviour (Figure 2.3a-b) in the CO_2isotherm parameters is somewhat surprising given that the state of materials discovery for CO_2separations is largely focused on a material's ability to adsorbCO_2, with the N_2behaviour often only considered implicitly through a material's selectivity. We note that that although there is some separation in the

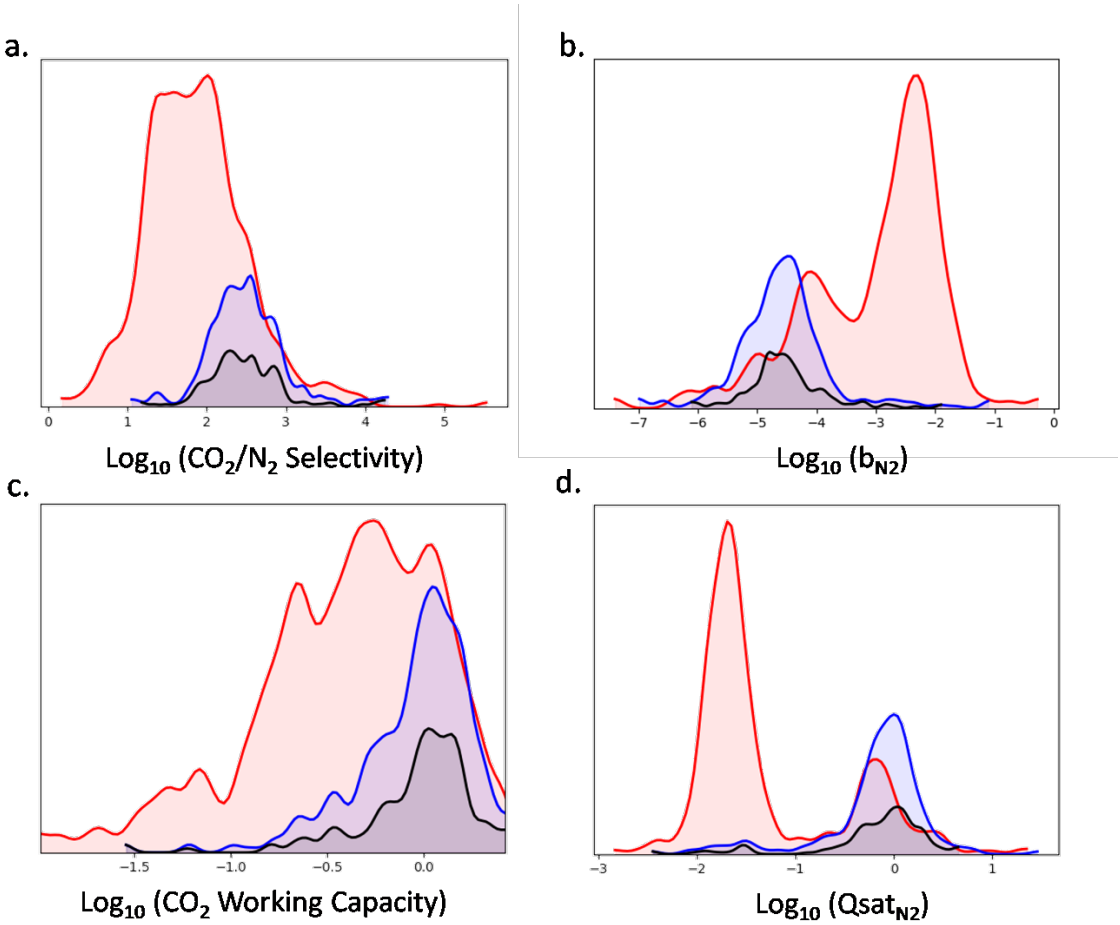

Figure 2.3: Univariate probability distributions for (a) the CO_2/N_2 single component selectivity, (b) the fitted N_2 dual-site Langmuir isotherm parameter for the stronger site, (c) the working capacity, and (d) the N_2 saturation uptake for the stronger DSL site. Shown in the four plots is the probability distribution for the MOFs which pass the 95/90-PRT (blue), fail the 95/90-PRT (red), and the top 150 MOFs by PE (black). These distributions have been normalized so that the sum areas under the curve of the pass and fail distributions equals 1.

N_2isotherm parameters probability plots between MOFs that meet the 95/90-PRT and those that do not, there is still significant overlap meaning a simple cut-off value would be insufficient to distinguish between materials.

The relationship between the VSA performance of a material and its gas adsorption isotherms are further explored in Figure 2.4, which shows a superposition of the CO_2(left) and N_2(right) isotherms of all the 1632 MOFs screened, grouped into different categories. The bold lines in Figure 2.4 are the averaged isotherms for each group, while the shaded regions in Figures 4g and 4h correspond to the first standard deviation of each group. It is clear that a wide range of CO_2isotherm shapes (linear to strongly non-linear) are seen in all three categories of MOFs, including the top 150 materials. The behaviour observed between the materials which do and do not meet the 95/90-PRT demonstrates that there is no clear distinction between the isotherm behaviour, indicating that MOFs possessing similar CO_2isotherms can provide vastly differing process performance. On the other hand, the range of N_2isotherms for materials which do meet the 95/90-PRT is much narrower, showing a distinct region of high performance. These "good" MOFs all have comparable N_2uptakes and have very linear isotherms, whereas the MOFs which fail the PRT show a much wider spread of uptakes with highly non-linear isotherms. Although significant overlap exists between the sets, these visible trends reinforce that the potential for predicting the 95/90-PRT based on N_2 isotherm behaviour exists.

To explore whether a predictive model can be constructed to determine a material's ability to meet the 95/90-PRT, machine learning classifiers were trained on all the metrics listed in Table 2.2 using a 90%/10% training/validation set split. Random Forrest models were found to be the most successful with a overall prediction accuracy of 91% determined with the validation set. More specifically, the best model (available upon request) was able to recover 85% of the MOFs in the validation set known to meet the PRT and had a positive predictive rate of 86%. In other words, 86% of the MOFs predicted to meet the 95/90-PRT actually meet the PRT. Thorough

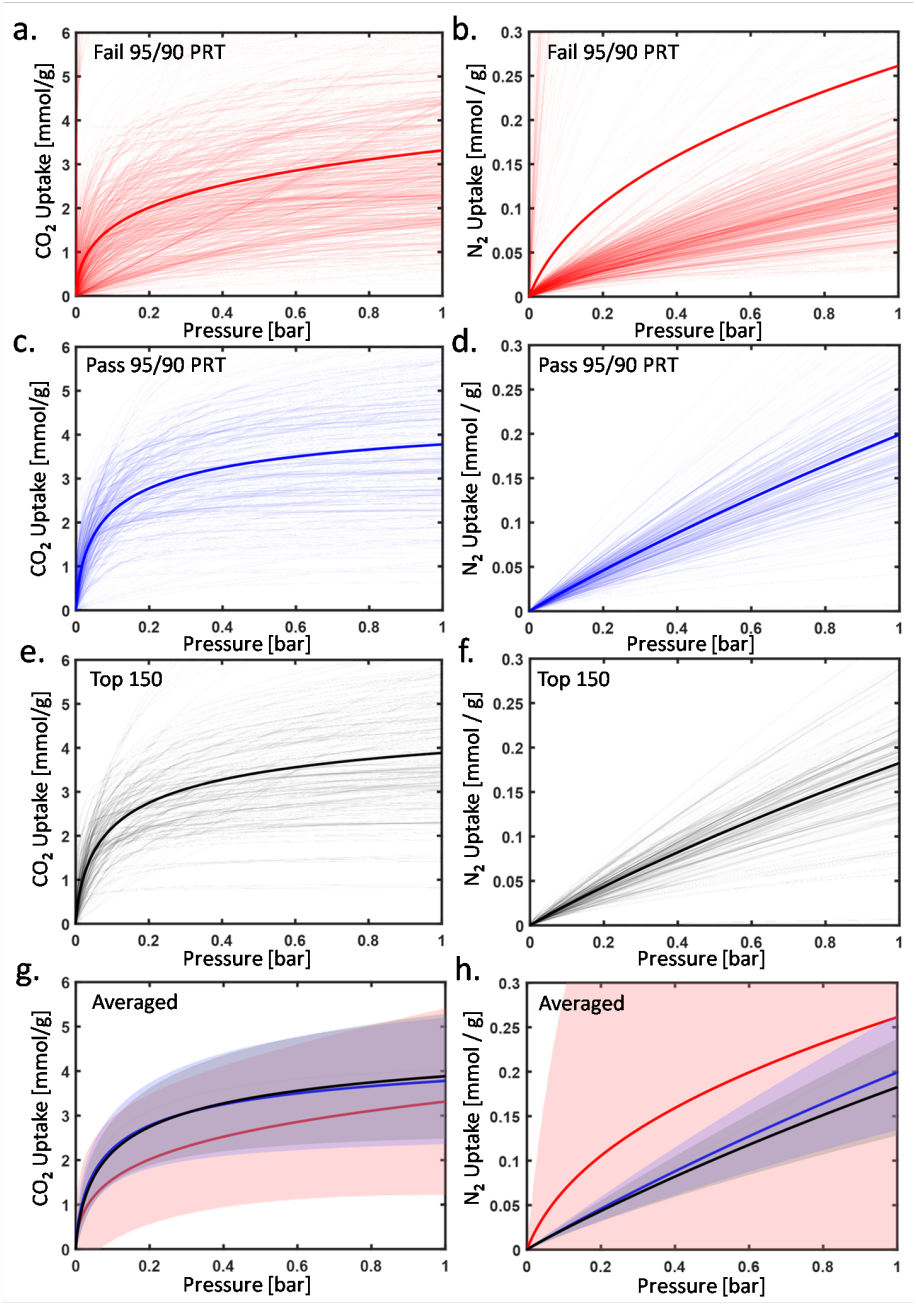

Figure 2.4: CO_2 (a) and N_2 (b) isotherms of all MOFs studied that do not meet the 95/90 PRT. CO_2 (c) andN_2 (d) isotherms of all MOFs that do meet the 95/90-PRT, and CO_2 (e) and N_2 (f) isotherms of the top 150 MOFs. The bold lines correspond to an 'average' isotherm constructed by using the average uptake of all isotherms at discrete pressure points with red corresponding to MOFs that don't meet the 95/90-PRT, blue corresponding to those that do meet the 95/90-PRT and black representing the top 150. The bottom figures compare the averaged CO_2 (g) and N_2 (h) isotherms from each class of MOFs where the shaded regions cover 1 standard deviation in each class.

investigation of the metrics utilized by the model reveals that the most important metrics, present across all 21 decision trees in the random forest, are the Langmuir isotherm parameters for N_2adsorption. For example, the first node in all 21 trees of the random forest rely on either the N_2 Langmuir constant or the N_2saturation uptake of the stronger of the two DSL sites, indicating that nitrogen isotherm behaviour is the most important predictor of a material's ability to meet the 95/90-PRT. To corroborate the importance of the N_2isotherm parameters, random forest classifiers were built where they were omitted from the model. Without the N_2isotherm parameters, overall prediction accuracy and positive predictive rate of the best model dropped to 78% and 63%, respectively, demonstrating the importance of the N_2parameters for constructing an accurate model.

We also explored whether the PE or the productivity of a material can be predicted from any of the common metrics used to characterize solid sorbents. Here it is important to note that the PE and productivity are only meaningful at process points that meet the 95/90-PRT constraint since low PE's or high productivities can always be achieved without the constraint. For materials that meet the 95/90-PRT, the third and fourth columns of Table 2.2 show the correlation R^2 between 29 metrics and the productivity and PE, respectively. All metrics show poor linear correlations with Pearson R^2 values of 0.17 or less for either the productivity or PE. To examine if more complex relationships exist between the PE or productivity and the 29 metrics including the N_2isotherm parameters, we built a series of different machine learning regression models using data from 435 materials that were able to meet the 95/90-PRT. The best model, a gradient boosted decision tree model, possessed correlation R^2 values (on the validation set) of only 0.41 for predicting the productivity and 0.18 for predicting the PE. Overall, these results suggest that the most common metrics used to evaluate MOFs are poor predictors of the material's PE and productivity. This indicates that full process simulations are necessary to evaluate PE and productivity performance of a material for VSA gas separations and likely related P/TSA

separations. Advanced process simulations of a 4-step VSA system, which have been validated at the pilot scale, have been integrated with atomistic simulations allowing for the screening of 1632 experimentally characterized MOFs for post-combustion CO_2capture. 392 MOFs were found to meet the 95/90 purity-recovery targets, while a dozen materials, including IISERP-MOF2, UTSA-16 and zeolite NaA, were able to simultaneously achieve PE's ¡250 kWh_e/MT $CO_2$and productivities greater than that of Zeolite-13X. Although we have assumed a dry flue gas, a handful of MOFs have been reported, whose CO_2adsorption properties are nearly unchanged in high humidity conditions. [63, 90] In those cases, the results of these simulations remain applicable. For MOFs whose adsorption properties are substantially changed in humid conditions, the flue gas stream can be dried at an energetic cost estimated to be as low as 24 $kWh_e/MTCO_2$ [93]. In total, 97 MOFs were found to have PE's ¡250 $kWh_e/MTCO_2$, which makes them highly competitive with advanced solvent based scrubbing systems even when the cost of drying the flue gas is included. This screening suggests that IISERP-MOF-2 is close to an ideal candidate material for a VSA post-combustion carbon capture process, since it is stable in moist, acid gas environments, made from an earth abundant metal (Ni), whose CO_2adsorption properties are minimally effected by humidity and whose PE of CO_2capture is close to the theoretical minimum.

Twenty-nine adsorption metrics and geometric parameters were examined to see if they are good predictors of a material's performance in a VSA gas separation system. N_2 rather than CO_2 adsorption behaviour is found to be the key metric to predict whether a material can meet the 95/90 purity-recovery requirements for post-combustion CO_2capture. This contradicts the current consensus in the field, but is in agreement with the results of other process simulations [29] and the recent screening study by Snurr and co-workers [32] Machine learning models can be built using the adsorption metrics that can predict whether a material can meet the 95/90-PRT with overall prediction accuracies of up to 91%. Analysis of the models corroborates

that the N_2isotherm parameters are the key predictors of whether a material meets the 95/90-PRT. On the other hand, predicting the PE or productivity based on the 29 metrics (including the N_2isotherm parameters) was found to be much more difficult with the best machine learning regression models giving correlation R^2s of only 0.41 for predicting the productivity and 0.29 for predicting the PE. Thus, the PE or productivity of CO_2capture with solid sorbents within a VSA system cannot be accurately predicted from equilibrium adsorption metrics alone - here full process simulations are required.

Chapter 3

Experimentally validated machine learning frameworks for accelerated prediction of cyclic steady state and optimization of pressure swing adsorption processes.

3.1 Introduction

[1] Traditional separation processes such as distillation account for 10-15% of the world's energy consumption [12]. Hence, there is a need to explore alternative separation pathways with the potential to reduce energy consumption. Adsorption-based processes are one such low energy alternative separation pathway [1, 3]. Adsorption processes are versatile and flexible for the separation of gases and have been widely used in the industry for applications such as gas drying, air fractionation [94], hydrogen purification [95], etc. [1, 96]. Furthermore, the ability to synthesize a variety of processes by combining a set of constituent steps is an additional degree of freedom that can be exploited [2].

Advances in organometallic chemistry have led to the development of thousands

[1]This chapter has appeared as- Pai, K. N., Prasad, V., and Rajendran, A. (2020). Experimentally validated machine learning frameworks for accelerated prediction of cyclic steady state and optimization of pressure swing adsorption processes. Separation and Purification Technology, 241, 116651.

of new adsorbents and have thus brought about a critical need for faster modeling and optimization of adsorption processes [18]. Most of these metal-organic framework (MOF) adsorbents are tunable and their properties are being increasingly computed *in-silico* [18, 97, 98]. Recent investigations have shown that most commonly used adsorption screening metrics, which use simple equilibrium data, can be unreliable, and hence screening should be combined with process design and optimization [29, 32, 38]. This implies that rapid and reliable process optimization tools should be developed for the screening of very large adsorbent databases. Furthermore, addressing this problem would contribute to a better understanding of how adsorbent properties impact process performance [2].

The simulation and optimization of adsorption processes are challenging as they are operated under cyclic and unsteady state conditions [1, 96]. The models describing adsorption process consist of a system of coupled partial differential equations along with nonlinear algebraic equations (together referred here as NLPDEs). Due to the propagation of sharp temperature and concentration fronts in the process, obtaining the numerical solution of these systems is challenging [31]. The application of advanced numerical schemes, such as finite volume methods (FVM), has enabled robust and accurate simulations [31, 99]. However, the inherent unsteady state nature of these processes requires solution of the NLPDEs repetitively until a cyclic steady state (CSS) is reached [100, 101]. This increases computational effort significantly [39, 100]. The presence of many design parameters such as the number of steps, pressure levels, feed rates, step times, and column dimension, leads to a large set of possible combinations, and thus makes the adsorption process optimization challenging [39, 100].

Various methods have been proposed in the literature to reduce the computational effort for PSA optimization, including reduced order models and meta-models [15, 38, 73, 102, 103]. Data-driven surrogate modeling has been proposed as a potential solution, as these models are trained using data obtained from validated detailed math-

ematical models or even experiments. The main advantage of these models is their ability to reduce computational load without compromising accuracy [104]. Hasan *et al.* [105] and Beck *et al.* [106] presented surrogate-assisted optimization frameworks and tested successfully with detailed models for the ability to perform multi-objective optimizations. Recently, Subraveti *et al.* showed that a surrogate-assisted framework can reduce the computational time for the optimization of a PSA process by an order of magnitude, using dimension reduction techniques and by training data derived from the generations of an evolutionary algorithm [107]. On the one hand this approach can be very advantageous for problems that involves a large number of design variables. On the other hand, if the objective functions are changed, then the detailed model should be evaluated again resulting in additional computational burden. Leperi *et al.* showed that the data from the detailed model can also be used to train artificial neural network (ANN)-based surrogate models for process optimization and the prediction of bed profiles at cyclic steady state [72]. In order to improve the confidence in using machine-learning tools routinely in process design and optimization experimental validation is a critical step and to the best of our knowledge, this has not be reported in the literature. The development, evaluation and experimental validation of machine-learning models to accelerate the optimization of cyclic adsorption processes is the core objective of the current work. Further, we also demonstrate how the prediction of cyclic steady state profiles can be used to accelerate detailed PSA simulations.

In this work, the separation of CO_2 from a mixture containing 15 mol% CO_2 and 85 mol% N_2 on zeolite 13X using a 4-step vacuum swing adsorption (VSA) process cycle is considered. This system is well studied, both theoretically [29, 39, 71, 108, 109] and experimentally, [36, 110, 111] with some work being carried out at pilot plant scales [75, 112, 113]. This work follows up a recent work from our group, where the reliability of process optimization techniques was validated experimentally [36]. The objective of this study is to demonstrate the ability of machine learning (ML)-based surrogate

models to predict key process indicators, such as purity, recovery, productivity, and energy consumption, as well as to predict CSS profiles. Various ML-based algorithms are trained as surrogates using the data from a detailed model generated using Latin Hypercube (LHC) sampling strategy. The trade-off between training effort and prediction accuracy is used to select the best surrogate model for process optimization. The ability of the surrogate models to predict Pareto curves for both constrained and unconstrained multi-objective optimization problems is compared with the results from a traditional detailed model-based optimization. The ANN-based CSS profile predictor is also tested for its ability to accelerate the detailed model simulations in a novel optimization framework. The predictions of the surrogate models are validated with experimental data from a two-column lab-scale VSA rig.

3.2 Experimental System, Process and Machine-learning Models

3.2.1 Experimental System

In this work, the experimental results reported by Perez *et al.* [36] were used and no additional experiments were performed. Since all the details have been provided earlier, only a brief description of the unit is provided here. The three experiments conducted using the 4-step cycle with light product pressurization (LPP) were considered in this study. The cycle was chosen for its simplicity of implementation and its effectiveness in concentrating the CO_2 from the dilute feed mixture [19]. The VSA experiments were carried out in a two-bed lab-scale system, the process schematic of which is shown in Fig. 3.1 a). It consists of two stainless steel columns (30 cm length and 3.2 cm diameter). Each column was packed with 162 g of Zeolite 13X (Z10-02) pellets from Zeochem AG, Switzerland. Two vacuum pumps were used to operate the unit at sub-ambient pressures. Suitable flow controllers and flow meters were used. The CO_2 and N_2 isotherms on Zeolite 13X were measured using volumetry

and confirmed using dynamic column experiments [36]. The VSA experiments were conducted using certified premixed cylinders containing 15 mol% CO_2 and 85 mol% N_2. The VSA experimental rig includes CO_2 sensors to collect CO_2 composition at the extract ($Z = 0$) and raffinate ($Z = L$) end of the column. Three thermocouples located at 8, 16, and 24 cm from the column inlet were used to obtain the transient temperature histories. All cycles were run until cyclic steady state was reached, which was ≈ 70 cycles.

3.2.2 Process Cycle

The schematic of the VSA process cycle is provided in Fig. 3.1 b). The cycle has an adsorption step performed at atmospheric conditions. The feed containing 15 mol% CO_2 and 85 mol% N_2 enters the column at the feed end ($Z = 0$) at a fixed flowrate. The CO_2 is preferentially adsorbed in the bed while the light component, N_2, is removed at the outlet of the bed ($Z = L$). This is followed by a co-current blowdown step to remove the N_2 impurity present in the bed voids. In this step, vacuum is applied at the $Z = L$ end to reduce the pressure to sub-atmospheric conditions. This intermediate pressure level, referred to as P_{INT}, has a major influence on the CO_2 product purity. The blowdown step is followed by the main product collection step, referred to as the evacuation step. The counter-current evacuation step is performed by reducing the pressure of the bed at the feed end to a low pressure (P_{LOW}). The pressurization step is carried out using the light product from the adsorption step from the $Z = L$ end. The gas from the adsorption step is predominantly N_2 and this step is referred to as light product pressurization (LPP). Note that the 4-step cycle with LPP has been shown in earlier studies to be effective for CO_2 capture a variety of adsorbent materials [19, 29, 71].

3.2.3 Detailed Process Modeling

The detailed mathematical modeling of the VSA process used in this study employs a uni-bed modeling approach provided in the work presented by Hagpahnah *et al.* [31]. Here, an adsorbent-filled bed is assumed to undergo all the individual cycle steps in a cyclic sequence with the final condition of the preceding step being the initial condition for the next. The flow through the bed is modeled as a one-dimensional axially dispersed plug flow. The gas phase is assumed to obey the ideal gas law. Mass transfer kinetics within the solid phase are described by the linear driving force (LDF) model, with the LDF coefficient being calculated with the understanding that molecular diffusion in the macropore controls the mass transfer resistance [114]. Darcy's law was found to adequately describe pressure drop in the axial direction. Note that longer columns would require the Ergun equation for an accurate estimation of the pressure drop. Bed voidage and particle size are assumed to be uniform across the column. The fluid and adsorbent are assumed to be in thermal equilibrium. Temperature, pressure, and concentration gradients in the radial direction are neglected. The outer column wall is assumed to be in equilibrium with the ambient temperature. Under these assumptions, mass, energy, and other transport equations can be obtained and are provided in Table S1 of the supporting information. Danckwerts's boundary conditions as shown in Table S2 of the supporting information are used to simulate the individual steps.

A dual-site Langmuir (DSL) model, is used to describe the equilibrium loading. The DSL model is given by:

$$q_i^* = \frac{q_{\mathrm{sb},i} b_i C_i}{1 + \Sigma b_i C_i} + \frac{q_{\mathrm{sd},i} d_i C_i}{1 + \Sigma d_i C_i} \tag{3.1}$$

where C_i and q_i^* are the fluid phase concentration and the equilibrium solid phase loading, respectively, $q_{\mathrm{sb},i}$ and $q_{\mathrm{sd},i}$ are the saturation capacities, and b_i and d_i are the affinity parameters for the first and second site, respectively. The temperature

dependence of the affinity parameters are described by the following relationships:

$$b_i = b_{0,i} e^{-\Delta U_{\mathrm{b},i}/RT} \tag{3.2}$$

$$d_i = d_{0,i} e^{-\Delta U_{\mathrm{d},i}/RT} \tag{3.3}$$

$b_{0,i}$ and $d_{0,i}$ are the pre-exponential factors while $\Delta U_{\mathrm{b},i}$ and $\Delta U_{\mathrm{d},i}$ are the internal energies of adsorption of the two sites. The isotherms are shown in Fig. S2, while the DSL isotherm parameters are provided in Table S3. The other simulation parameters are provided in Table 3.1. The equations are discretized in space and solved using a finite volume method (FVM) with a van Leer flux limiter. The system of coupled equations is solved in MATLAB 2017b using the *ode*23*s* solver until cyclic steady state (CSS) is reached. In this work, attainment of cyclic steady state is determined when the mass balance error on CO_2 is below 0.5% for 5 consecutive cycles. Beyond this condition, the key performance indicators did not show much variation. In addition to the key performance indicators (PIs), the axial profiles of the intensive variables, namely, bed temperature, fluid and solid phase CO_2 and N_2 loadings at the end of the different steps are collected at CSS. The key process performance indicators (PI) are defined as follows:

$$\text{Purity, } Pu_{\,\mathrm{CO_2}}[\%] = \frac{n_{\mathrm{CO_2}}^{\mathrm{EVAC}}}{n_{\mathrm{CO_2}}^{\mathrm{EVAC}} + n_{\mathrm{N_2}}^{\mathrm{EVAC}}} \times 100 \tag{3.4}$$

$$\text{Recovery, } Re_{\,\mathrm{CO_2}}[\%] = \frac{n_{\mathrm{CO_2}}^{\mathrm{EVAC}}}{n_{\mathrm{CO_2}}^{\mathrm{FEED}}} \times 100 \tag{3.5}$$

where $n_{\mathrm{i}}^{\mathrm{EVAC}}$ is the number of moles of component i collected in a single evacuation step, while $n_{\mathrm{i}}^{\mathrm{FEED}}$ is the number of moles of component i in the feed. The energy consumption of the process is defined below:

$$\text{Energy, } En \left[\frac{\mathrm{kWh_e}}{\text{tonne } \mathrm{CO_2} \text{ captured}}\right] = \frac{E_{\mathrm{ADS}} + E_{\mathrm{BLO}} + E_{\mathrm{EVAC}}}{\text{Mass of } \mathrm{CO_2} \text{ in evacuation product}} \tag{3.6}$$

Energy consumption, which is indicative of the operational cost, is defined as the electrical energy equivalent required to capture one tonne of CO_2. The terms E_{ADS}, E_{BLO} and E_{EVAC} refer to energy consumption in the adsorption step, co-current blow-down, and counter-current evacuation steps, respectively. In the above expression, E_{ADS} is the energy spent in overcoming the pressure drop during the adsorption step and is evaluated as

$$E_{\mathrm{ADS}} = \frac{1}{\eta}\epsilon\pi r_{\mathrm{in}}^2 \frac{\gamma}{\gamma-1}\int_{t=0}^{t=t_{\mathrm{ADS}}} (vP)\left[\left(\frac{\Delta P}{P_{\mathrm{atm}}}\right)^{\frac{\gamma-1}{\gamma}} - 1\right] dt \tag{3.7}$$

The equations for the energy consumption for the other two steps is given by

$$E_{\mathrm{step}} = \frac{1}{\eta}\epsilon\pi r_{\mathrm{in}}^2 \frac{\gamma}{\gamma-1}\int_{t=0}^{t=t_{\mathrm{step}}} (vP)\left[\left(\frac{P_{\mathrm{atm}}}{P}\right)^{\frac{\gamma-1}{\gamma}} - 1\right] dt \tag{3.8}$$

where P_{atm} is 1 bar, η represents the efficiency of the vacuum pumps/blower, which is considered to be 72%, γ is the adiabatic constant, P is the Pressure, v is the interstitial velocity and r_{in} is the inside diameter of the column. Note that industrial-scale vacuum pumps that operate at very low pressures are known to provide lower efficiency [115]. In the experimental study, the vacuum pumps were oversized and did not show any variation in power consumption over the steps. Hence,in this study the efficiency of 72% was used merely to demonstrate the efficacy of the ML-based surrogates to predict the energy consumption calculated by the detailed model. The productivity of the process is defined as:

$$\text{Productivity, } Pr \ \left[\frac{\text{mol }_{\mathrm{CO_2}}}{\mathrm{m^3\ ads\ s}}\right] = \frac{n_{\mathrm{CO_2}}^{\mathrm{EVAC}}}{(\text{ Vol of ads })\ (\text{Cycle time })} \tag{3.9}$$

The cycle time in the Eq. 3.9 is the sum of the duration of the different steps in the cycle. It is important to note that certain simplifying model assumptions, e.g. the use of Darcy's equation, requirement of scheduling, etc., that hold for small scale adsorbent beds, may need to be revisited if scale-up is necessary. However, the framework for developing the surrogate models will remain essentially the same.

Parameter	Symbol	Value	Units
Column length	L	0.3	[m]
Inner column radius	r_{in}	0.014	[m]
Outer column radius	r_{out}	0.016	[m]
Column void fraction	ε	0.41	[-]
Particle voidage	ε_{p}	0.35	[-]
Particle radius	r_{p}	0.75×10^{-03}	[m]
Tortuosity	τ	3	[-]
Column wall density	ρ_{s}	7800	$[\text{kg m}^{-3}]$
Molecular diffusivity	D_{m}	1.53×10^{-05}	$[\text{m}^2\,\text{s}^{-1}]$
Adiabatic constant	γ	1.4	[-]
Thermal conductivity of column wall	K_{w}	16	$[\text{J m}^{-1}\,\text{K}^{-1}\,\text{s}^{-1}]$
Inside heat transfer coefficient	h_{in}	8.6	$[\text{J m}^{-2}\,\text{K}^{-1}\,\text{s}^{-1}]$
Outside heat transfer coefficient	h_{out}	10	$[\text{J m}^{-2}\,\text{K}^{-1}\,\text{s}^{-1}]$
Solid phase specific heat capacity	C_{ps}	900	$[\text{J kg}^{-1}\ \text{K}^{-1}]$
Universal gas constant	R	8.314	$[\text{m}^3\,\text{Pa mol}^{-1}\,\text{K}^{-1}]$
Ambient temperature	T_{a}	298.15	[K]
Vacuum pump efficiency	η	0.72	[-]
Parameter for blowdown pressure profile	α_{BLOW}	0.174	$[\text{s}^{-1}]$
Parameter for evacuation pressure profile	α_{EVAC}	0.027	$[\text{s}^{-1}]$

Table 3.1: Parameters used for simulations.

3.2.4 Process Optimization

Owing to the transient nature of adsorption process and the complex relationship of operating conditions, optimization of the PSA process is challenging. In previous studies, it has been shown that the non-dominated sorting genetic algorithm-II

(NSGA-II) can be used to optimize the process conditions. It is robust at optimizing this system for various multi-objective problems [19, 31, 106, 116]. The algorithm can escape local minima and can be parallelized easily for multi-core processing [116]. This method of optimizing the VSA process has been reported in earlier studies [19, 29, 31] and has also successfully been verified using experiments [75]. In a recent study by Perez *et al.*, the authors have also shown that this optimization technique can help guide the design of experiments to obtain the optimum performance [36].

3.2.5 Machine Learning Models

In the absence of knowledge of the specific input-output(I/O) relations, supervised machine learning (ML) can be used to construct predictive models using sufficient training data. Improvements in ML algorithms, especially for function approximation via supervised machine learning-based regression, now enable the modeling of complex multivariate phenomena as simple input-output relations [104]. A computationally expensive model, $y = f(X)$, where $f(X)$ can be any continuous quantity, e.g. a key performance indicator of a process, which is defined by a k-vector of design variables $X \in D \subset \mathbb{R}^k$, can be emulated as a "*surrogate*" $\hat{f}$. The output data $y_1, y_2, y_3, \cdots, y_n$ that result from inputs $X_1, X_2, X_3, \cdots, X_n$ can be mapped as $y = f(X_i)$, where $X_i = \{x_j^{(1)}, x_j^{(2)}, x_j^{(3)}, \cdots, x_j^{(n)}\}$ is the matrix of inputs [104]. In this paper, supervised machine learning techniques were used to generate approximate models $\hat{y} = \hat{f}(X)$ for the data obtained from the detailed VSA model. Many machine learning methods are available to develop regression relationships. In this paper, the following were evaluated: decision trees (DT) [117], ensemble bagged trees (EBTs), which employ a random forest algorithm [118, 119], support vector machines (SVMs) [120], ANNs [121] and Gaussian process regression (GPR) [122]. All ML studies were implemented using MATLAB's machine-learning toolbox.

Decision trees are simple prediction models that are used to classify based on a tree or graph structure of conditions. They can also be used as regression models

for cases where the outputs are numerical responses. Random forest models such as EBTs use multiple learner DTs that are trained to solve the same problem. In classification, the mode of the DTs, and in regression, the mean of the DTs, are used for prediction. They, therefore, become versatile in developing regression models for large complex data-sets that may involve many different trends. Support vector machines are another type of classification model that can also be used to build multivariate input-output regression relationships. The objective of this method is to find a hyperplane that can segregate the multidimensional data into classes. The algorithm tries to maximize the distance between this hyperplane and the data-set. In classification tasks, the SVM attempts to find the hyperplane that provides the maximum margin, i.e. the distance between the hyperplane and the nearest point in each class is maximized. Support vector regression attempts to constrain all predictions of the response variable y to be within an epsilon-threshold of the data. Various kernel functions such as linear, quadratic, cubic, Gaussian, etc. can be used for the classification or regression of nonlinear data-sets. Gaussian process regression is a powerful regression tool for complex functions that can be trained with a relatively small amount of data [104]. Gaussian process regression uses a non-parametric kernel-based probabilistic model. Here, a probability distribution is defined over the entire function space; inferences taken from the model are thus based on the local probability distribution [122]. Artificial neural networks use multiple layers of "*neurons*" to build nonlinear models between inputs and outputs. Each neuron performs a nonlinear transformation on the weighted sum of its inputs from the neurons in the previous layer. In training of the ANN, the weights in the network are adjusted to minimize the error between the ANNs outputs and the corresponding training data.

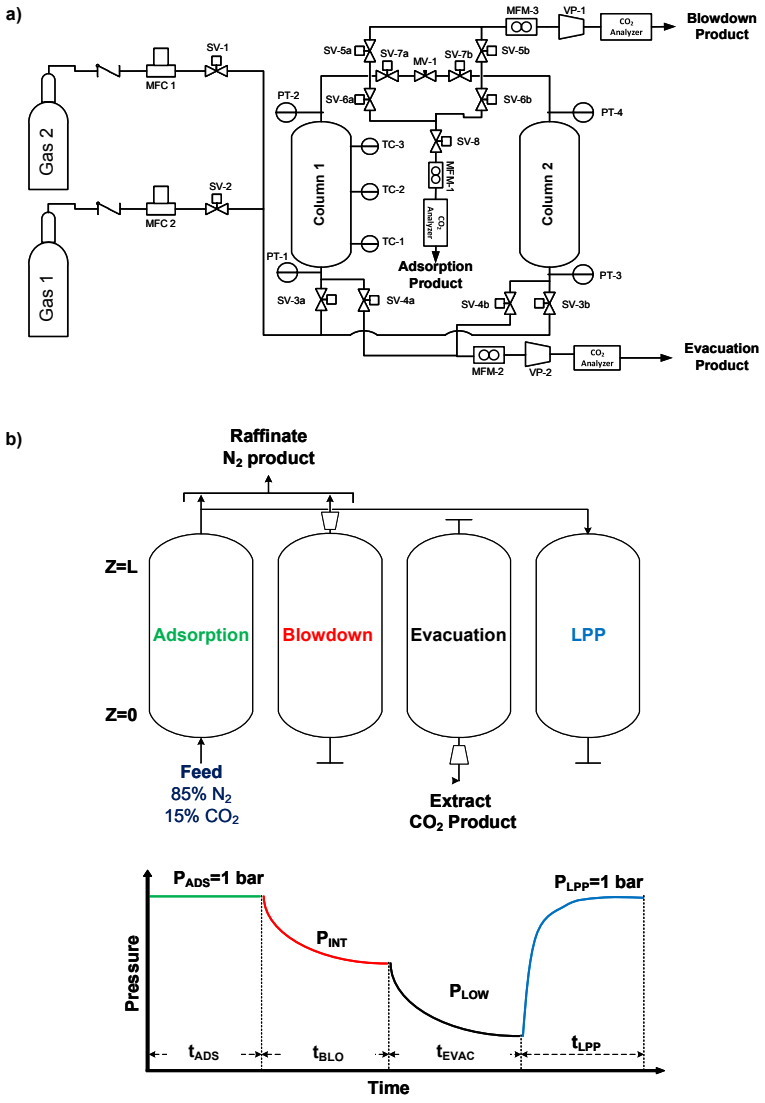

Figure 3.1: Experimental set-up and cycle studied (a) Schematic diagram of the bench-scale VSA test apparatus. (b) Illustration of the 4-step cycle with LPP. Note that the thermocouples TC-1, TC-2, and TC-3 are at 8, 16, and 24 cm from the column inlet.

3.3 Surrogate Models: Training and Validation

Surrogate models should be trained using data that is representative of the entire input space. A Latin Hypercube (LHC) design was used to generate a set of operational inputs. The range of the input space were as follows: $t_{\mathrm{ADS}}[\mathrm{s}]$: $20-200$, $P_{\mathrm{INT}}[\mathrm{bar}]$: $0.03-0.3$, $P_{\mathrm{LOW}}[\mathrm{bar}]$: $0.03-0.1$, and $v_{\mathrm{FEED}}[\mathrm{ms}^{-1}]$: $0.05-1$. A physical constraint of

$P_{\mathrm{INT}} \geq P_{\mathrm{LOW}} + 0.01$ [bar] was imposed while generating the data-set. A set of 800 samples was evaluated using the detailed VSA model and the outputs; namely the four performance indicators, viz., Pu_{CO_2}, Re_{CO_2}, E, and Pr. The input and output data-set distributions are provided in Figs. S3 and S4 of the supporting information. The two sets of data obtained from the detailed model that are used in this paper include the scalar key performance indicators (purity, recovery, energy, productivity) and vectors of CSS axial profiles (gas phase and solid phase compositions of CO_2 and N_2, and the internal bed temperature). All the above-mentioned machine learning models can be used to develop surrogates to predict the scalar performance indicators. The training of the surrogate models is performed using a five-fold cross validation technique, to ensure that over-fitting the data is avoided. A test-set (number of samples = 200) was also obtained using the detailed model and was used to test all the trained models.

To compare the predictive capabilities of the surrogate models for key performance indicators, the adjusted coefficient of determination is used as the evaluation metric:

$$\mathrm{R}^2 = 1 - \frac{\Sigma_{j=1}^{n}(y_j - \hat{y_i})^2}{\Sigma_{j=1}^{n}(y_j - \bar{y_j})^2} \tag{3.10}$$

$$\mathrm{R^2}_{\mathrm{ADJ}} = 1 - \frac{(1 - \mathrm{R}^2)(\mathrm{n} - 1)}{(n - k - 1)} \tag{3.11}$$

where n is the number of training or testing samples and k is the number of input descriptors, y_j is the actual observed output, $\hat{y_j}$ is the predicted output, and $\bar{y_j}$ is the mean of the set of actual outputs. Although other metrics are available for model evaluation, $\mathrm{R^2_{ADJ}}$ is chosen because it was independent of the scale of the output and number of samples. The magnitude of the output data does not matter in computing the $\mathrm{R^2_{ADJ}}$ value, and it varies between -∞ and 1. An $\mathrm{R^2_{ADJ}}$ of 1 would mean perfect prediction and negative $\mathrm{R^2_{ADJ}}$ would imply the predictions are worse than the actual mean of the data-set. Evaluating the surrogate models using an independently generated test-set is important, because models that may have high

training accuracy may not predict the outputs for new inputs accurately.

To evaluate this surrogate model for CSS profiles, the predictions of the ANN-based surrogate model for the CSS profile is evaluated using a L_1 norm of the intensive variables. The L_1 for a intensive variable is defined as

$$L_{1,f} = \frac{\sum_{m=1}^{30} |f_{\mathrm{ref,m}} - f_m|}{\sum_{m=1}^{m} f_{\mathrm{ref,m}}} \tag{3.12}$$

where f is an intensive variable (temperature, gas composition and solid phase loadings) at node m. Here, the f_{ref} reference state is the CSS profiles obtained from detailed model simulations of the test-set simulated to CSS conditions. The denominator ensures that all the compared quantities are on the same scale, and the total of the 4 intensive variables gives the total L_1 norm, $L_{1,Tot}$:

$$L_{1,Tot} = L_{1,y_{\mathrm{CO_2}}} + L_{1,q_{\mathrm{CO_2}}} + L_{1,q_{\mathrm{N_2}}} + L_{1,\mathrm{T}} \tag{3.13}$$

3.3.1 Surrogate Model for Performance Indicators

Each key performance indicator was trained independently with a surrogate model to maintain accuracy, i.e. the surrogate models for purity, recovery, energy, and productivity are trained independently. The main goal of this work is to reduce computational load for the design and optimization of the VSA process, the largest contribution to which is the solution of the detailed model. This means the ability of the ML algorithm to correctly map the input to the corresponding output needs to be as good as possible with the least training effort. The training data-set which consists of 800 samples was randomly divided into 8 data-sets of increasing sample size (100, 200, 300, $\cdots$, 800). The data-sets were then used to train surrogate models. This process was repeated 10 times, each time with a new set of randomly selected data-sets.

The sampled means and one standard deviation of the test $\mathrm{R^2_{ADJ}}$ from all the trained models is shown in Fig. 3.2. In Fig. 3.2 a), the $\mathrm{R^2_{ADJ}}$ of CO_2 purity surrogate model

is plotted against the R^2_{ADJ} of CO_2 recovery for the different sample sizes starting from N=100 (closed symbol) moving upto 800. Note that the shaded areas represent one sample standard deviation based on the 10 repeat training runs. As expected, a general upward trend in model predictive capability was observed for increasing training sample size for all the models. The linear SVM regression model performed poorly with the highest R^2_{ADJ} for purity and recovery being less than 0.9, indicating that the output data had nonlinear trends. The higher order polynomial and Gaussian kernel-based SVM performed better than the linear case. The DT model performed better than the linear models in predicting the CO_2 recovery as the sample size is increased. The EBT model performed better than the DT model with the $R^2_{ADJ} = 0.95$ for the best case. The performance of the SVM model with a cubic kernel was also found to be good with a test $R^2_{ADJ} > 0.95$. The ANN model for the purity did not improve with increasing sample size for the chosen shallow network. The GPR model had the highest predictive capability for even small data-sets. Purity and recovery of the VSA process are usually the primary design objectives and the surrogate models need to be accurate in predicting these quantities. All the kernel functions tested for the GPR model gave good predictive results. Note that in Fig. 3.2 a) the results obtained from the marginally better GPR model with the Matern kernel is plotted. The models that showed $R^2_{ADJ} > 0.95$, were the SVM model with cubic and Gaussian kernels, the EBT model, and the GPR model. Note that with just small (100 samples) training data-set, the GPR (Matern) provides a $R^2_{ADJ} > 0.98$.

In Fig. 3.2 b), the R^2_{ADJ} of surrogate model for the energy consumption is plotted against the R^2_{ADJ} of productivity for the different sample sizes. Of the seven algorithms tested to model the energy and productivity of the VSA process, the GPR performed the best, followed by the SVM and ANN models. The SVM model with the Gaussian kernel, which worked well in predicting the purity and recovery of the process, did not predict the energy of the process well with ($R^2_{ADJ} < 0.9$). The GPR model performed well in predicting both energy and productivity ($R^2_{ADJ} > 0.95$). The minimum number

of samples that are required to train the GPR model for an $R^2_{ADJ} > 0.98$ for all cases was 400. This was considered as the least training effort required while maintaining a high model prediction accuracy. It should be noted that even though the training time for these models are insignificant in a computational sense, as we increase the training sample size, training ML models like GPR to screen large databases could become computationally restrictive.

3.3.2 Surrogate Model for CSS Profiles

Unlike the case of the key performance indicators, the CSS profiles are vectors, while surrogate models such as SVM and GPR provide only scalar outputs. Hence, an ANN-based method is used to predict CSS profiles. It is worth noting that Leperi *et al.* have reported a similar approach to predict the CSS profiles recently [72]. The ANN-based CSS profile predictor is trained using the samples generated from the previous section. MATLAB 2017b Neural Network Toolbox is used for the model training and the trained model is used to predict the CSS profiles for new inputs. In this study, Bayesian regularization technique is used to train the model [107]. The ANN-based CSS profile predictors are trained individually with four operational conditions as inputs in order to predict the CSS profiles for four intensive variables, namely, gas phase CO_2 composition; bed temperature; and the solid phase CO_2 and N_2 loading for the various cycle steps. Physical constraints such as the gas composition should be between 0 and 1, and solid loadings should be positive are imposed. This means that each model has 4 inputs and the output contains 30 scalar values of the intensive variables for the 30 finite volume discretization. Note that this means a total of 16 individual surrogate models are trained, each one to predict one intensive variable for each of the 4 different steps at the CSS conditions.

The algorithm was used to train the ANN-based CSS prediction model for different number of neurons, varying from 5 to 100, and the error between the test-set and the model predictions was calculated. Of the different number of nodes that were tested

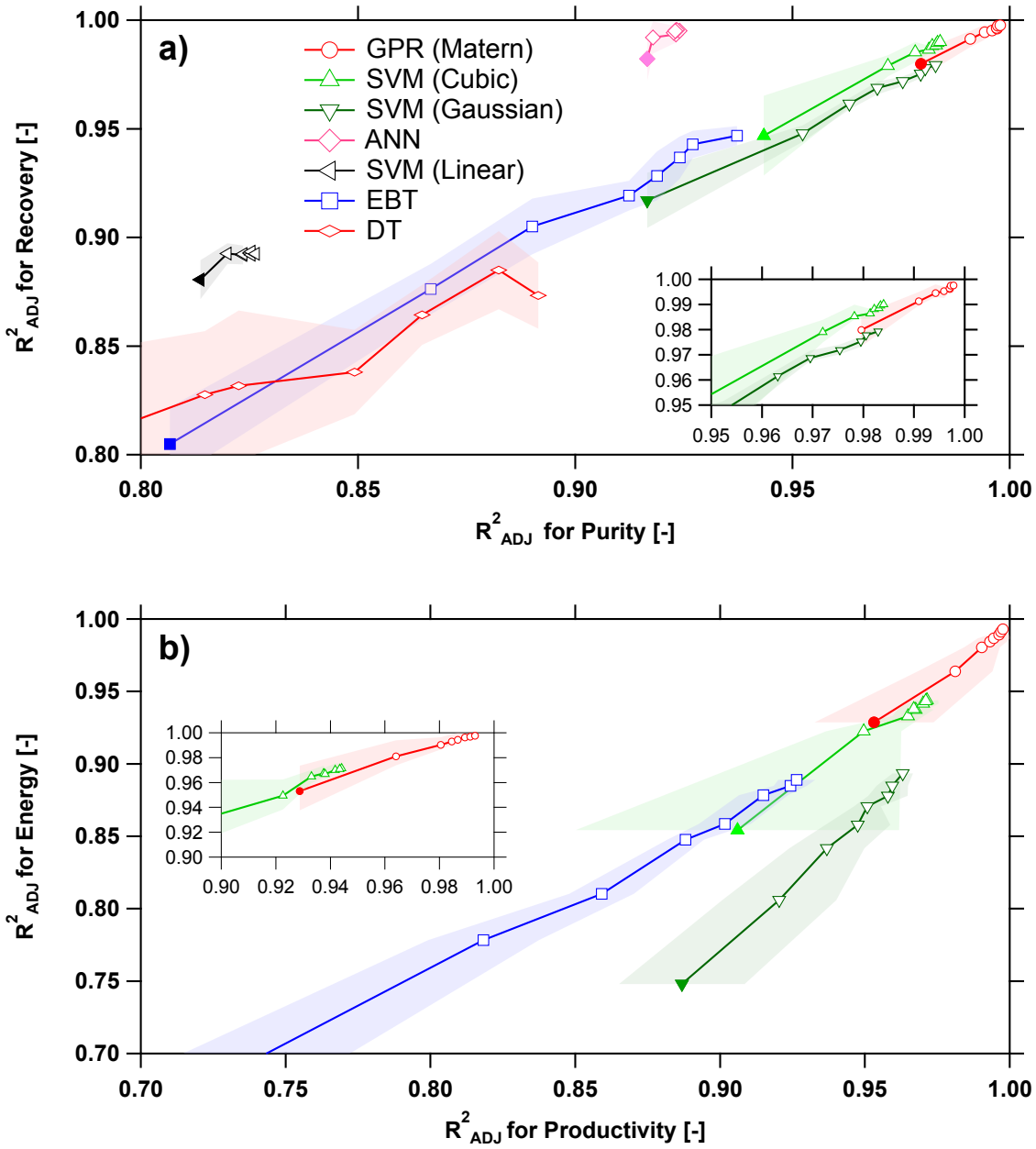

Figure 3.2: Impact of the size of training set on the accuracy of the surrogate models. a) Evolution of the R^2_{ADJ} for CO_2 purity and CO_2 recovery from an initial training sample size of 100 points (shown as a filled symbol) upto 800 points, each symbol depicts the addition of 100 more points. b) Evolution of the R^2_{ADJ} for energy consumption and productivity from an initial training sample size of 100 points (shown as a filled symbol) upto 800 points.The R^2_{ADJ} values for Energy and Productivity for SVM (Linear) are outside the range plotted. The shaded region represents the sample standard deviation in model prediction for 10 different randomly sampled runs.

during ANN training, it was found that the best performance was obtained with a hidden layer containing 30 neurons to predict the 30 nodes of the adsorption bed. Note that only one hidden layer was sufficient in fitting the profile data. To understand the trade-off between training effort and accuracy of predictions, the training data was randomly divided into 8 data-sets of increasing sample size (100, 200, 300, $\cdots$, 800). These data-sets were used to train the ANN-based surrogate models for the different steps and intensive variables. Like in the previous section, the standard test-set (n=200) was used to predict the CSS profiles using the trained models. Figure 3.3 shows the variation of the average $L_{1,Tot}$ norm of the test-set for each cycle step as a function of the different training sample sizes. The L_1 norm for the test-set tends to reduce with increase of training samples, but the rate of reduction in the L_1 norm plateaus after models trained with 400 samples. This means that a model trained with sample size of 400 can adequately predict the CSS profiles, with the least training effort.

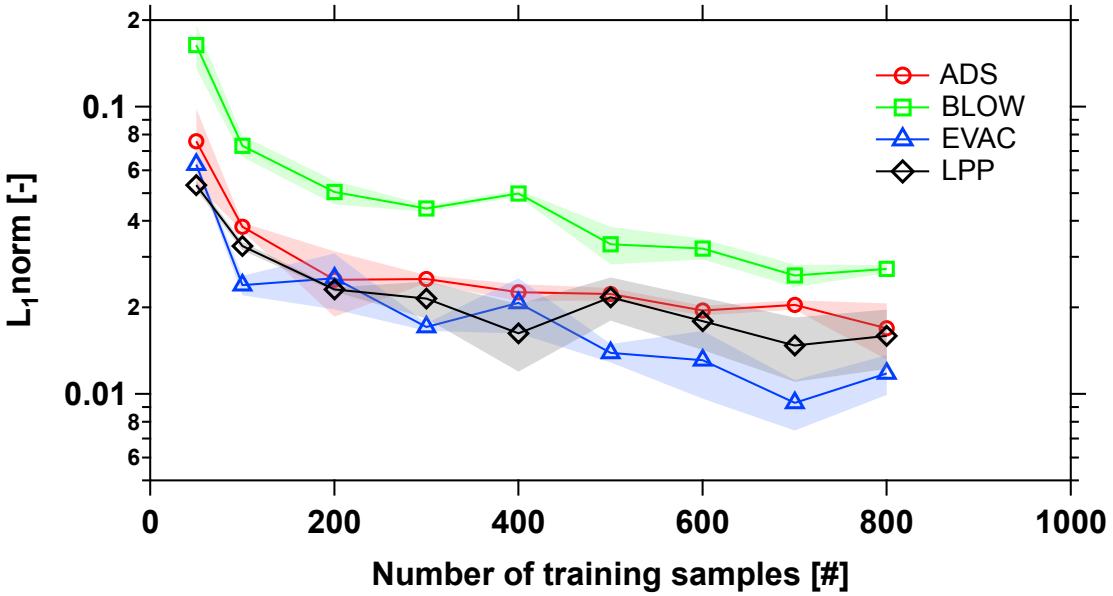

Figure 3.3: The average total L_1 norm for each cycle step as a function of the different training sample sizes. Note that the results shown are the sample mean and the shaded area represents the sample standard deviation from the test-set (n =200).

To highlight the accuracy of the predictions from the surrogate, an operating con-

dition from the test-set is shown in Fig. 3.4. The solid lines show the results from the detailed model and the dashed lines represent the results from the ANN-based surrogate model. Fig. 3.4 c) and d) shows the variation of the solid phase profiles for CO_2 and N_2 loadings along the adsorption bed. Note that the time required to solve the detailed model for the operating conditions plotted in Fig. 3.4 was $\approx$ 15 minutes while for ANN model produced an instantaneous solution. Note that in Fig. 3.3, the blowdown step has the highest $L_{1,Tot}$ norm among all the cycle steps; this is because the blowdown step has the most irregular profile for the intensive variables. The evacuation and LPP steps have the least $L_{1,Tot}$ norm and this is because the profiles of the intensive variables in these steps are simpler as observed in Fig. 3.4. The trained and validated ANN-based surrogate CSS profile predictor can be used to predict CSS profiles for new operating conditions.

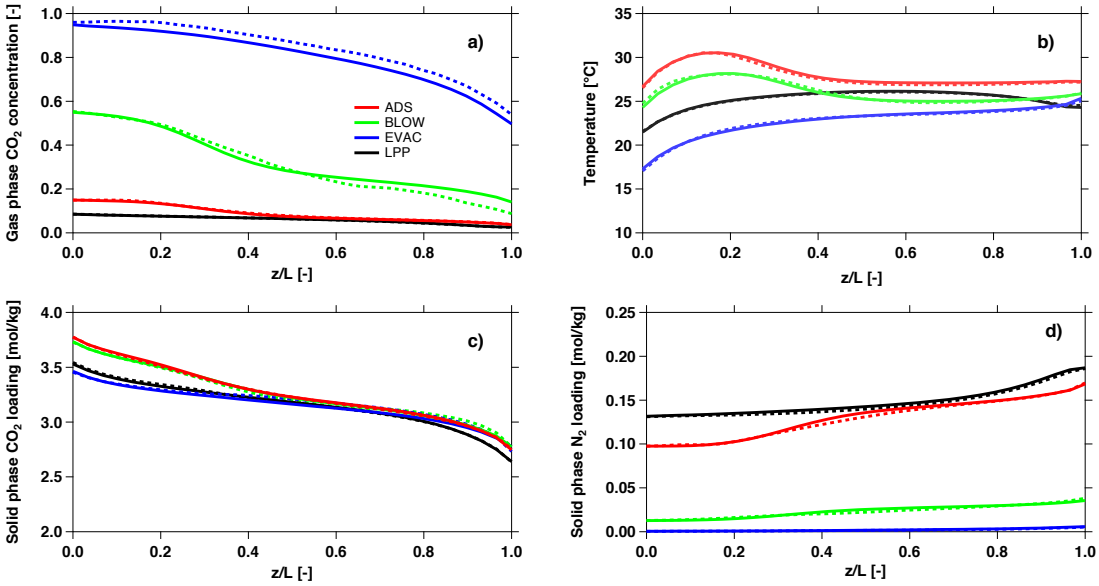

Figure 3.4: Cyclic steady state profiles of the intensive variables at the end of the steps for are a sample VSA simulation. The dashed lines are predictions from the ANN surrogate model and the solid lines are the detailed model simulations. CSS profiles of a) the gas phase composition of CO_2. b) the bed temperature. c) the solid phase loading for CO_2 d) the solid phase loading for N_2.

Accelerated CSS Identification

Due to the cyclic nature of the VSA process, the process performance is evaluated at CSS. The solution of the detailed model is computationally demanding and it can be argued that the most computational effort results from the repeated computation of the constituent steps until the attainment of CSS. Hence, if this computational effort devoted to the calculation of CSS can be reduced, PSA design and optimization can be accelerated. Having said that, it is also illustrative to consider that ANN-based CSS predictions are only an approximation of the actual profiles. In rare cases it is possible that the predicted profiles are not representative of the actual CSS profiles. In such cases it would be pertinent to not rely on these profiles, but instead treat them as initial conditions and simulate the detailed model until CSS criterion is satisfied. This approach provides two key advantages. First, it irons out unrealistic profiles that could be predicted by the ANN model. Second, the results that will be obtained are from a detailed model, significantly improving reliability. Depending on the accuracy of the surrogate profile predictions, this methodology could significantly reduce the solution time of the detailed model.

To understand the advantage in convergence, the operating conditions from the test-set were run in the detailed model initialized with the ANN-based CSS predictions. The results were than compared to the results obtained from the detailed model initialized with feed conditions. Figure 3.5 shows the average convergence of the detailed model to cyclic steady state for a test-set consisting of 200 samples (See Fig. S5, for the contributions of the various intensive variables towards the total L_1 norm). The results from the detailed model initialized with the feed (15 mol% CO_2) shown as solid lines and the ANN-based CSS accelerated detailed model shown as dashed lines. Fig. 3.5 a) shows the variation of the $L1$. A lower value of L_1 norm indicates that the profiles are closer to the actual CSS conditions. In the case of the ANN-based CSS accelerated detailed model the L_1 norm is always lower when compared to the

detailed model initialized with feed conditions. Since the mass balance error is used in this study to estimate CSS conditions, the variation of average mass balance error of the test-set is shown as a function of the number of cycles in Fig. 3.5 b). The horizontal dotted line indicates the 0.5% error, which is the criterion for CSS in this study. The vertical dashed line indicates the average of the number of cycles to reach CSS conditions for the two approaches. We can observe that the process has reached the mass balance criteria for CSS, the condition is measured only after 5 cycles, hence the average number of cycles for the CSS accelerated detailed model case is 6. In the case where the detailed model was initialized with the feed, the average number of cycles to reach CSS was 24. This highlights the effectiveness of the surrogate profile predictor in accelerating the detailed model convergence. Although this methodology can be used in accelerating the identification of the CSS profiles, the real application of this methodology would be in optimizing systems that are slow to converge to the CSS conditions.

3.4 Process Optimization

Separation processes like CO_2 capture must satisfy certain process targets for product purity and recovery. Along with achieving the minimum product purity and recovery stipulations, it is also necessary to optimize the process energy consumption and the process productivity for the minimum stipulated process purity and recovery. The schematic of the genetic algorithm framework is shown in Fig. 3.6, and is implemented as follows: a set of decision variables such as step times, pressure levels, feed velocities, are chosen using a Latin Hypercube (LHC) sampling technique. This is called the initial population. For this study, the initial population consisted of a set of 96 unique operating conditions. The objective functions are calculated by running either the detailed model or the surrogate model. Based on the objective functions for each individual simulation, the next "generation" is chosen. In order to avoid convergence to local minima, operations such as mutations and cross over ensure that sufficient

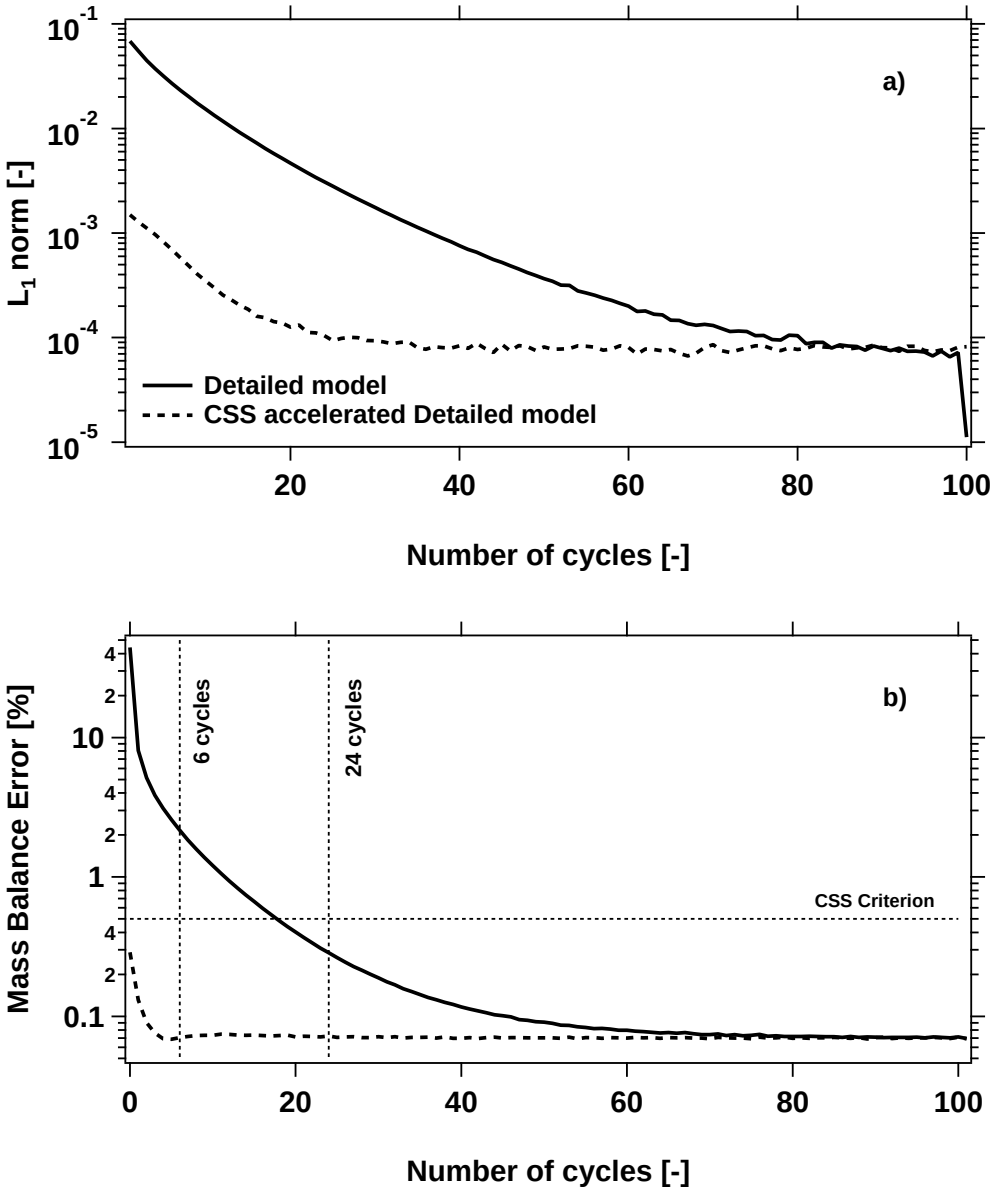

Figure 3.5: Convergence to cyclic steady state as a function of number of cycles of the detailed model for two cases, namely, cycle initialised with feed conditions (15 mol% CO_2) shown as solid lines, and the dashed lines are the result for the cycle initialised with ANN-based CSS predictor trained with 400 samples. The L_1 norms and the mass balance errors are the average values from the test-set comprising of 200 samples. a) the variation of the average L_1 norm for both cases. b) the average mass balance error for both cases, the horizontal dotted line shown the 0.5% error line and the vertical dotted lines indicating the average CSS criteria for the test set. Note that criterion for CSS requires a mass balance error of <0.5% for 5 consecutive cycles.

diversity is maintained in the population. The stopping criteria for the algorithm is set at 50 generations, which means that 4800 unique operating conditions are evaluated in total. The Pareto curve is obtained by choosing the best trade-off between the multiple objectives. In this work, three different optimization approaches are considered and are shown in Fig. 3.6.

- Detailed Opt.: In this approach, the multi-objective optimization is coupled with the detailed model. For a given set of operating conditions, the detailed model is run until CSS is reached and the performance indicators are returned to the optimizer.

- Surrogate Opt.: In this approach, the multi-objective optimization is coupled with the GPR-based surrogate model for the key performance indicators instead of the detailed model.

- CSS-Opt.: In this approach, the optimizer provides the set of decision variables to the CSS predictor that estimates the profiles of the intensive variables at the end of the LPP step. This profile is then used as the initial conditions(ICs) for the detailed model, which is then solved until the CSS condition is reached. In essence, this is identical to Detailed Opt. with one exception, i.e., the detailed model is initialized with profiles obtained from the CSS predictor.

Note that the results of the Detailed Opt. were considered as the reference. All other optimization parameters were kept the same for the various optimization approaches. To identify the optimum operating conditions that achieve all the stipulated targets, two scenarios were tested in this section.

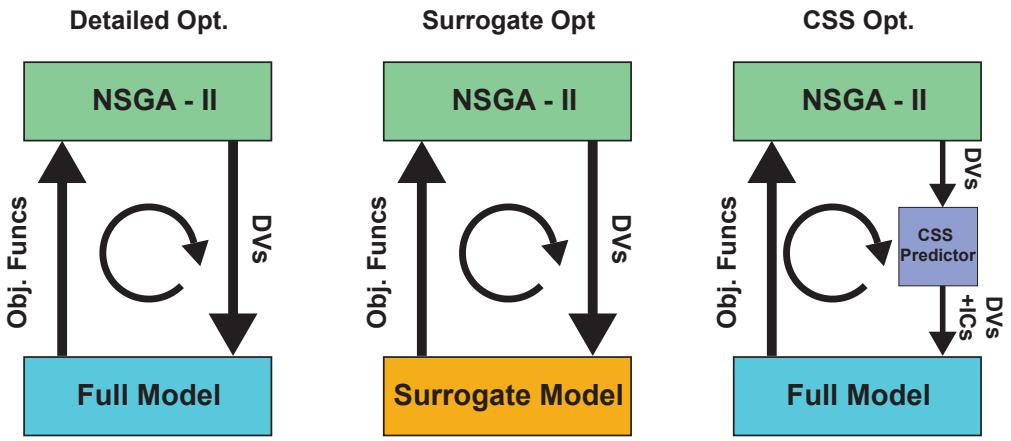

Figure 3.6: Optimization approaches considered in this study. DV and IC stand for decision variables and initial conditions, respectively.

- Unconstrained optimization of purity and recovery
- Constrained optimization of energy and productivity

For the first scenario, a multi-objective optimization was carried out to improve the CO_2 purity and CO_2 recovery of the system by reducing the following objectives simultaneously.

$$\min J_1 = \frac{100}{Pu_{CO_2}} \tag{3.14}$$

$$\min J_2 = \frac{100}{Re_{CO_2}} \tag{3.15}$$

For the second scenario, to check the ability of the surrogate optimization frameworks to perform multi-objective optimization with constraints, a multi-objective optimization for the minimization of energy and the maximization of productivity was carried out, with purity and recovery requirements set as constraints. The CO_2 purity constraint was set $\geq 95\%$. This target was chosen as it is necessary for sequestration of the captured CO_2. The CO_2 recovery constraint was chosen to be 80% for the 4-step cycle with LPP. Note that a low value of recovery was chosen to merely

test the efficacy of the optimizer. Any other achievable value can indeed be chosen. The objective functions are defined as

$$\min J_3 = \frac{En}{100} + 500 * [max(0, Pu_{\text{tgt}} - Pu_{\text{CO}_2})]^2 + 500 * [max(0, Re_{\text{tgt}} - Re_{\text{CO}_2})]^2 \tag{3.16}$$

$$\min J_4 = \frac{1}{Pr} + 500 * [max(0, Pu_{\text{tgt}} - Pu_{\text{CO}_2})]^2 + 500 * max[(0, Re_{\text{tgt}} - Re_{\text{CO}_2})]^2 \tag{3.17}$$

where Pu_{tgt} is 95% and Re_{tgt} is 80%.

The Pareto curves from the maximization of purity-recovery from the three optimization approaches are shown in Fig. 3.7 a). The solid line, red dashed line, and the blue dashed line represent the Pareto obtained with the Detailed Opt., Surrogate Opt. (trained with a sample size 400), and CSS Opt. (trained with a sample size 400). The surrogate predictions are all within a 3% difference of the detailed model predictions (shown as a shaded region on the Detailed Opt. Pareto curve). Figures. 3.7 b) and c) show the variation of the decision variables with respect to an objective function from the three optimization approaches. Note that these points correspond to the Pareto curve shown in Fig. 3.7 a). It is indeed encouraging that all the three approaches not only yield similar Pareto curves but also identify similar optimal operating conditions.

Figure 3.7 d) shows the results of the multi-objective optimization to minimize energy and maximize productivity. It should be noted that these constrained optimizations take longer to converge. The Pareto curve with the solid lines shows the results from the Detailed Opt. The Pareto curve with the dashed line represent the results from the Surrogate Opt. Both approaches provide similar results and the results are again in good agreement. The surrogate prediction for the second optimization scenario is also within the 3% difference of the detailed model prediction (shown as a shaded region on the Detailed Opt. Figs. 3.7 e) and f) show the variation

of the decision variables with respect to an objective function from the three optimization approaches. Note that these points correspond to the Pareto curve shown in Fig. 3.7 d). It is worth noting that not only are the Pareto curves predicted accurately, but the decision variables are also predicted well. This indicates that the Surrogate Opt. and CSS Opt. can be used with confidence to design experimental campaigns. These results are also significant because the surrogate is trained using data from a large input range, but the optimum conditions occupy a small range of decision variables. This implies that the surrogate model developed for the larger input range is sufficiently accurate in the neighbourhood of the optimum.

3.4.1 Computational Advantage

The main reason to use a surrogate model for optimization is to reduce the computational load. A direct substitution of the detailed model with the trained surrogate model reduces the computational load considerably. Additionally, once the samples are generated and the models trained, the surrogate model approach can be used in multiple optimization runs for different objectives. A considerable amount of computation is required to solve the detailed model repetitively to reach CSS. Initializing the detailed model with a very close approximation of the CSS would reduce computational load. In this section, the three optimization approaches tried in this work, namely the Detailed Opt., CSS Opt. and Surrogate Opt., are compared for their computational load. Since the Detailed Opt. is run iteratively through 50 generations the accounting of computational time for the optimization was analysed by using the Purity-Recovery Pareto curves. The Pareto curves were evaluated using a normalized area metric (A [%]), which is defined as

$$A[\%] = \frac{AUP_{Detailed\,Opt.} - AUP}{AUP_{\text{Detailed Opt.}}} \tag{3.18}$$

where $AUP_{\text{DetailedOpt.}}$ corresponds to the area under the Pareto obtained from the Detailed Opt. shown in Fig. 3.7 a) and AUP corresponds to the area under the Pareto

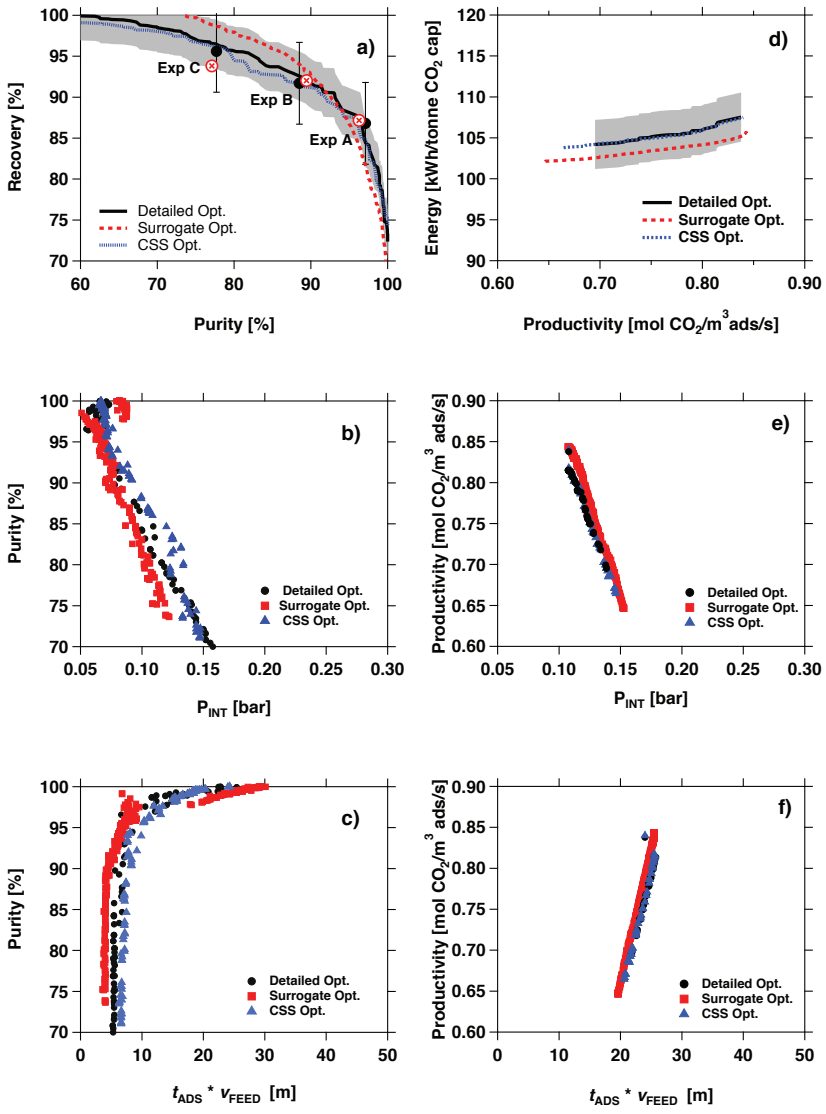

Figure 3.7: Process optimization for the two scenarios (a) the Pareto curves obtained from the multi-objective maximization of purity and recovery for the three optimization approaches. b) Variation of P_{INT} for the Pareto points shown in (a); and (c) Variation of $t_{\mathrm{ADS}} \times v_{\mathrm{FEED}}$ for the Pareto points shown in (a); (d) the Pareto curves obtained from the multi-objective maximization of productivity and minimization of energy for the three optimization approaches, subject to constraints of CO_2 purity $\geq 95\%$ and CO_2 recovery $\geq 80\%$; e) Variation of P_{INT} for the Pareto points shown in (d); and (f) Variation of $t_{\mathrm{ADS}} \times v_{\mathrm{FEED}}$ for the Pareto points shown in (c). The Surrogate Opt. and the CSS Opt, used a GPR(Matern) kernel(trained with 400 samples) and an ANN model (trained with 400 samples), respectively.

obtained from Surrogate Opt. and CSS Opt., where n is the training sample size. The area under the Pareto is evaluated in the region $Pu \geq 70\%$ and $Re \geq 70\%$, which covers the region of interest. Figure 3.8 a) shows the variation of the normalized area A versus the computational effort shown interms of core hours. The closed black symbols show the progression of the Detailed model Pareto through the generations of the purity-recovery optimization. The red symbol show the normalized area A for the Surrogate Opt. trained with 400 samples. The blue symbol show the normalized area obtained from running the CSS Opt. using a CSS profile predictor trained with 400 samples. It can be observed that both the surrogate-assisted optimization frameworks required less computational time to achieve comparable accuracies with the Detailed Opt. In Fig. 3.8 b), the computational time for the three tested optimization frameworks is shown. The Detailed Opt. results in 1550 core-hours, with the unconstrained purity-recovery optimization accounting for 550 core-hours and the energy-productivity optimizations accounting for the rest. The CSS Opt. accounts for 260 core-hours, with the sample training accounting for 70 core-hours, the unconstrained purity-recovery optimization accounting for 75 core-hours and the rest for the energy-productivity optimization. In the case of Surrogate Opt., the time taken to simulate the training data-set was 64 core-hours, and the training and surrogate optimization together consumed less than 1 core hour. A large computational saving was observed for both surrogate-assisted frameworks. Compared to Detailed Opt., the CSS Opt. and Surrogate Opt showed a $\approx 6\times$ and $\approx 23\times$ reduction in computational load, respectively, while providing identical Pareto curves.

3.5 Experimental Validation of the Surrogates

It is important to validate the surrogate model predictions with independently obtained experimental data. The experimental data is obtained from the work of Perez *et al.* [36] performed for the same system. The specific details of experimental runs and the surrogate model for purity and recovery are also tabulated in Table 3.2 and

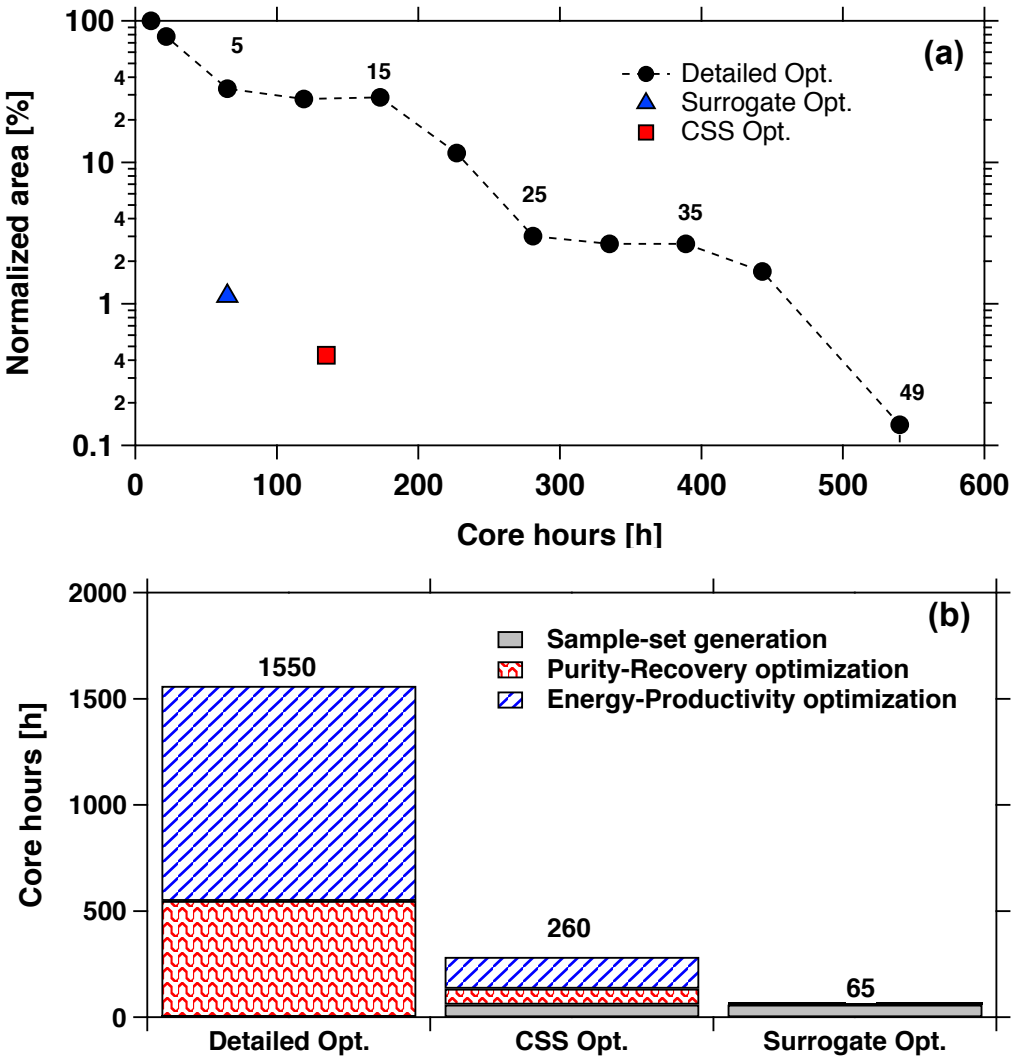

Figure 3.8: a) The normalized area under the Pareto curve obtained from a maximization of purity and recovery, is shown as a function of computational time for all three optimization approaches. The results of Detailed Opt. are shown as black symbols, the Surrogate Opt. is shown as red symbols, and the CSS Opt. shown in blue symbols. b) Computational effort for optimization using the three optimization approaches.

are also plotted in Fig. 3.7 a) as symbols. Note that the closed black symbols correspond to the experimentally measured purity and recovery, and the red symbols correspond to the results for the same operating conditions obtained from the GPR-based surrogate model. The surrogate purity and recovery predictions are well within the 5% error that is associated with the experimental runs.

Experiment	t_{ADS}	P_{INT}	P_{LOW}	v_{FEED}	Experimental		Surrogate Model	
	[s]	[bar]	[bar]	[m s^{-1}]	Purity [%]	Recovery [%]	Purity [%]	Recovery [%]
A	142	0.0720	0.0300	0.0799	97.10	86.10	96.28	87.16
B	140	0.0912	0.0308	0.0588	88.50	91.70	89.44	92.03
C	117	0.1335	0.0318	0.0611	77.70	95.60	77.10	93.80

Table 3.2: Optimal operating conditions and the measured performance of the VSA experiments [36], shown alongside the surrogate model predictions for the same conditions.

The CSS profile predictions from the ANN model were also validated by comparing them with those from the detailed model and experimentally measured values. The results from experiment A are shown in Fig. 3.9. The dashed lines represent the ANN-based surrogate profile predictions (trained with a sample size 400) and the solid lines represent the profiles from the detailed model simulations for the same conditions. Figure 3.9 a) and b) shows the gas phase CO_2 and temperature profiles of each cycle step at the CSS conditions, respectively. It is worth noting that only the temperature profile is measured experimentally. In order to verify the gas phase composition, it is possible to extract values from the composition histories. For the case of solid phase loading, there was no way to experimentally obtain these values either directly or indirectly. The CO_2 analyser histories at the two ends of the column as well as the temperature histories from the three thermocouples were compared with the surrogate profile predictions. In Fig. 3.9 a), the CO_2 concentration at the $Z = 0$ and $Z = L$ end of the column at the end of each step are plotted as symbols. In Fig. 3.9 b), the

temperatures measured at the three thermocouples in the experimental setup at the end of each process step are plotted against the axial CSS predictions as symbols. It can be observed that the CSS predictions from the ANN model and the detailed model are within 5% error from the experimentally measured CO_2 concentration, and the three temperature measurements along the axial are also in good agreement, with the detailed model and surrogate profile predictions. The surrogate models trained with sampled training data can predict the performance indicators as well as the CSS profiles of optimized operating conditions. Note that the profile predictions for the other two experiments can be found in the supporting information. (Figs.S6 and S7)

3.6 Conclusions

Fast and robust surrogate models were developed using supervised machine learning algorithms to model a VSA process for a CO_2 capture case-study. The surrogates were trained using sampled data obtained from a computationally expensive detailed model and acted as fast function approximations of the process performance indicators. Various machine learning algorithms were tested for their ability to predict the performance indicators of the VSA process, such as purity, recovery, energy, and productivity. The effect of training sample size on predictive performance of the various machine learning algorithms were tested. The Gaussian process regression (GPR) model was found to be the best at approximating the above-mentioned quantities with the least number of training data points. An ANN-based model was also trained to emulate the detailed model by predicting the internal cyclic steady state (CSS) profiles from the same sampled data. The trained ANN-based CSS profile predictor was tested, and the predictions were compared to the detailed model predictions. The CSS profile predictor showed good agreement with the detailed model predictions for all the concentration and temperature profiles. The surrogate model results were validated experimentally using data obtained from a bench-scale VSA set-up from a previous study for the same system. The resulting surrogate predictions for purity

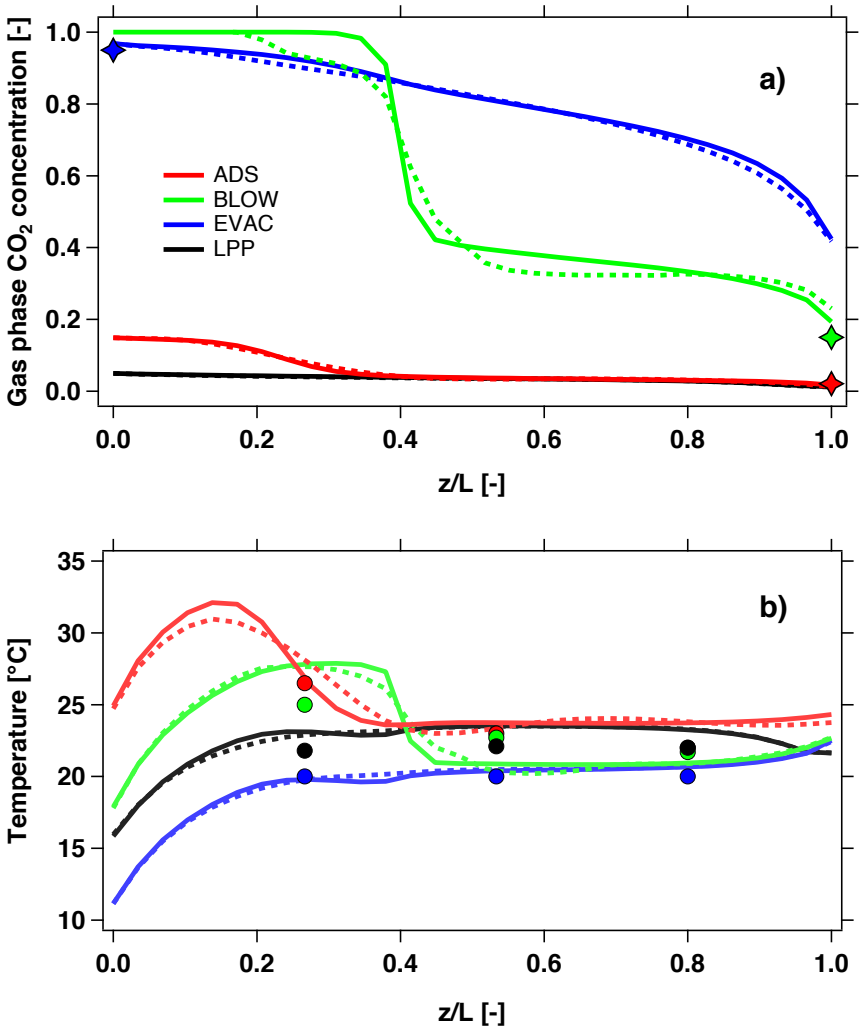

Figure 3.9: Cyclic steady state profiles of the intensive variables at the end of the cycle steps for the experimental run A from Table 3.2; the dashed lines are predictions from the ANN surrogate model and the solid lines are the detailed model simulations. CSS profiles of a) the gas phase composition of CO_2, the symbols are the CO_2 concentrations measured at the $Z = 0$ and $Z = L$ end of the column at the end of each cycle step. b) the bed temperature, the symbols in a) and b) represent the average of experimental measurements from the last 5 cycles.

and recovery were in good agreement with the experimental results. The ANN CSS predictions were also validated using the experimental temperature and concentration histories for the same experimental case. A 4 times reduction in the number of cycles to reach CSS was observed by using the ANN-based CSS predictor as the initial conditions for the detailed model. The ability of the surrogates to handle different optimization objectives was tested using two cases, a) purity/recovery maximization and b) energy minimization and productivity maximization, under constraints of purity and recovery. Two new surrogate assisted optimization frameworks, namely the Surrogate Opt. and the CSS Opt. were tested. These optimization frameworks were tested, and the results compared with the traditional Detailed Opt. The CSS Opt. showed a $\approx 6\times$ reduction in computational load. There was a $\approx 23\times$ reduction in computational load for optimization using the Surrogate Opt.

The main challenge with rigorous optimization of a cyclic adsorption process is the large computational load associated with it, two major contributors of which are: the need to solve many unique operating condition combinations over a multivariable design space, and the computation required to accurately estimate the cyclic steady state for each of these cases. In this work, we addressed these problems using machine learning, by reducing a dynamic process to a static surrogate, and by using an estimated cyclic steady state to accelerate the convergence of the simulation. Overall, the observations and findings from this study can be used to develop static surrogate models to assist and replace computationally expensive detailed dynamic adsorption process models, as these models have been validated against both simulation and experimental cases and in regions of optimal operation. This framework can now be extended for computational screening of adsorbent and process cycles to better understand the process and material linkage in performance. It can also be extended to design optimal adsorbent-based processes for the separation of various gas mixtures that involve computationally costly cyclic adsorption process simulations.

Chapter 4

Generalized, Adsorbent-agnostic, artificial neural network framework for rapid simulation, optimization, and adsorbent screening of adsorption processes

4.1 Introduction

[1] Cyclic adsorption processes such as pressure/vacuum/temperature swing adsorption (P/V/T-SA) are used extensively for a variety of gas separation applications [2, 3, 96]. In their simplest manifestation, an adsorbent capable of selectively retaining one of the components in a gas mixture is packed in a column and the gas is routed in a variety of ways to perform a separation. The ability to configure a variety of "cycles" by altering the sequence of steps is a particularly attractive feature of cyclic adsorption processes. The processes are rather complex owing to the simultaneous propagation of heat and mass transfer fronts. Hence, designing these processes invariably requires numerical simulations. The numerical simulations require the solution of coupled partial differential equations with non-linear algebraic equations until a cyclic steady state (CSS) is reached. Depending on the nature of the system, it is quite possible

[1] Pai, K. N., Prasad, V., and Rajendran, A. (2020). Generalized, Adsorbent-agnostic, artificial neural network framework for rapid simulation, optimization, and adsorbent screening of adsorption processes. Industrial and Engineering Chemistry Research, 59(38), 16730-16740.

that hundreds of cycles need to be simulated to in order to determine the performance indicators for a single operating condition [101]. This makes P/V/T-SA simulations computationally intensive and prohibits their use for many practical applications that have presented themselves in recent years.

In recent years, the development of advanced numerical techniques [99, 123] and the availability of inexpensive computing power have allowed researchers to solve optimization problems that explore thousands of possible operating conditions using detailed simulations [71, 123–126]. The explosive growth in metal-organic chemistry and molecular simulations have led to the synthesis of hundreds of thousands of both real and hypothetical adsorbents [26, 41]. Further, many research groups now confirm that potential of adsorbents cannot be evaluated by simple metrics such as selectivity, working capacity, etc., and process simulations combined with optimization is essential [20, 30, 33, 127, 128]. This means that future efforts in adsorbent screening will require process optimization tools that are reliable and fast.

Current simulation tools are time consuming and the computational effort to screen large databases is still substantial. Leperi, *et al.* [32] and Burns, *et al.* [129] used detailed process models and optimization to screen > 560, and > 1500 metal organic frameworks (MOFs), respectively. These represent evaluating millions of unique operating conditions. From our own experience, large-scale screening requires several hundred (possibly thousand) core-years of computational power. Several approaches, including the development of simplified analogue models [130–133] and surrogate models [134] have been used to overcome these challenges.

Advances in machine-learning have opened up an exciting opportunity to significantly reduce computational times associated with P/V/T-SA simulations. This topic has been recently explored by several research groups. Khurana and Farooq developed an artificial neural network (ANN) model to relate adsorbent characteristics with the minimum energy and maximum productivity achievable for a VSA process [20]. Using this model, they were able to evaluate the performance of 75 adsorbents for

post-combustion CO_2 capture. Subraveti, *et al.* developed an optimization technique where an ANN model is trained for one specific adsorbent internally in an optimization framework to reduce the dimensionality of the problem and to aid the speed-up of the optimization [107]. Leperi, *et al.* developed an ANN model to emulate a PSA process for a given set of operating conditions [72]. Pai, *et al.* developed a variety of regression models to predict the performance indicator and axial profiles of intensive variables of a VSA process that employs Zeolite 13X and proposed a novel optimization framework that enables rapid identification of cyclic steady state performance [135]. They also validated the ANN predictions against experiments thereby confirming that these approaches can be used reliably. All of these models were trained for a combination of specific cycle and an adsorbent.

The above summary indicates that supervised machine-learning models have been developed to predict the performance of a specific process using a specific adsorbent. However, using such models for adsorbent screening is a rather insurmountable task since the number of adsorbents that are being developed are in the order of hundreds of thousands. Hence, there is a clear need to develop generalizable surrogate models that can predict the performance of an arbitrary adsorbent when subject to a specific operating condition (without being trained for that specific adsorbent). The development of such a model will provide a powerful tool that could enable not only the optimization of a process for a specific adsorbent, but also the screening of large databases in a more reliable manner. This is the central goal of the current work. This is referred to as the machine assisted adsorption process learning and emulation (MAPLE) framework. First, we discuss the development of the MAPLE framework. The trade-off between training effort and accuracy is evaluated and the ability of the framework to predict the performance of an arbitrary adsorbent is evaluated by comparing the results to a detailed mathematical model. The ability of the framework for is illustrated by first evaluating it for the optimization of the industrial benchmark Zeolite 13X for different conditions and objectives. The framework is then used to

screen a host of adsorbents presented in the literature [15].

4.2 Machine-assisted Adsorption Process Learning and Emulation (MAPLE) framework

The MAPLE framework consists of three stages: 1. Development of a detailed mathematical model; 2. Training and validation of an ANN model; 3. Deployment of the ANN model for simulation, optimization, and adsorbent screening. Each of these stages are described below. The goal of the current work is to describe the development of the data-driven surrogate framework and prove its effectiveness. To do so, the case of post-combustion CO_2 from dry flue gas is considered. Specifically, a 4-step VSA process with light-product pressurization (4-step with LPP), a simple yet effective process that has been demonstrated in both lab-scale [36] and pilot-scale [75] is considered. A similar framework can be extended to other cycles and separations.

4.2.1 Detailed model

The simulation of any cyclic adsorption process requires a robust mathematical model that describes the key physical phenomena that occur within the column. In this study, the column dimensions and other key simulation parameters are provided in Table 4.1. This study does not aim to design a new process, but considers the question: if a laboratory-scale VSA system of a fixed dimension and a given range of operating conditions is available, how could different adsorbents perform when deployed in the rig ? The entire framework is designed with this objective in mind.

The detailed model used in this study has been described in several of our previous works [123]. The key assumptions being: 1. The gas phase is ideal; 2. The flow in the column is described by an axially dispersed plug flow model; 3. The fluid and solid phases are in thermal equilibrium and the column is adiabatic; 4. The mass transfer between the gas and solid phase can be described by a linear-driving force (LDF) model, with the molecular diffusion in macropores controlling the mass transfer; 5.

The pressure drop in column is described by Darcy's law (for the column dimensions chosen and the operating conditions encountered here, this assumption was found to be sufficient). The models thus obtained, along with the suitable boundary conditions, are provided in the supporting information.

The competitive adsorption equilibrium is assumed to be described by the single-site Langmuir (SSL) isotherm:

$$q_i^* = \frac{q_{\text{sat}} b_i C_i}{1 + b_{\text{CO}_2} C_{\text{CO}_2} + b_{\text{N}_2} C_{\text{N}_2}}, \; i = \text{CO}_2, \text{N}_2 \tag{4.1}$$

where q_i^* is the equilibrium solid phase loading, b_i and is the equilibrium constant for component i, and q_{sat} is the saturation capacity. The temperature dependence of the equilibrium constant is described by

$$b_i = b_{0,i} e^{\frac{-\Delta U_i}{RT}} \tag{4.2}$$

It is worth noting that the equilibrium of CO_2 and N_2 cannot be accurately described by the Langmuir isotherm for all the adsorbents; often more complex forms such as the dual-site Langmuir (DSL) would be needed [110, 136]. The main reason for choosing the SSL isotherm is that it is generic enough to capture the behaviour of many practical systems with a small set of parameters namely, q_{sat}, b_{0,CO_2}, b_{0,N_2}, ΔU_{CO_2}, and ΔU_{N_2}. It is worth noting that including more complex isotherm descriptions, e.g., DSL, is likely to increase the training effort significantly and were not considered at this moment. In addition to the equilibrium, the other key aspect to consider is the mass transfer within the adsorbent particle. In this study, we assume that the adsorbent is prepared in a pelletized form and that the diffusion within the crystals is fast. However, during the pelletization process, the diffusional resistance that will arise in the macropores cannot be avoided. Hence, the current description of the mass transfer depicts the minimum resistance that would be seen. Further within the range of velocities chosen for this study, the macropore resistance is expected to stronger than the film resistance.

The specific process used in this study is shown in Fig. 4.1. The cycle consists of four steps: 1. The feed step, in which the feed mixture containing y_F mole-fraction of CO_2, and the rest being N_2, is fed from the bottom of the column with an interstitial velocity v_F. The product leaving from the top of the column is predominantly N_2. The feed step is carried out at a fixed pressure of P_H =1 bar for a duration of t_{ADS}. 2. The blowdown step, in which vacuum is applied from the top of the column and the column pressure is reduced to P_{INT}. The aim of this step is to remove as much N_2 as possible, while reducing CO_2 loss. 3. The evacuation step, in which vacuum is applied from the bottom of the column reduces the pressure to P_L. The CO_2 product is collected in this step. 4. The LPP step, in which the product from the feed step is used to pressurize the column to bring it back to P_H. This step has been shown to improve CO_2 recovery [36]. Each step in the cycle is simulated assuming that one column undergoes all the steps in the given sequence. The partial differential equations arising from the mass and energy balances are discretized in the axial direction using a finite-volume scheme and the ordinary differential equations obtained are solved using *ode23s*, an inbuilt solver in MATLAB. Four key performance indicators are calculated, viz., CO_2 Purity, CO_2 Recovery, Energy consumption and Productivity. These are defined in the supporting information and briefly described here. The purity (in %) represents the ratio of the moles of CO_2 to the moles of CO_2+N_2 recovered in the product stream while the recovery represents (in %) the ratio of CO_2 obtained in the product stream and in the amount feed stream. The energy consumption for the process comes from three steps: In the feed-step, the energy required to pressurize the gas in order to overcome the pressure drop in the column; In the blowdown and evacuation, the energy consumption relates to the energy spent for evacuating the column. In all these steps, the isentropic efficiency of the prime mover is assumed to be 72%. The productivity is defined as the moles of CO_2 collected in the product step per unit volume of the adsorbent per unit cycle time. The cycle time in this case is the sum of the duration of the four steps. In all the

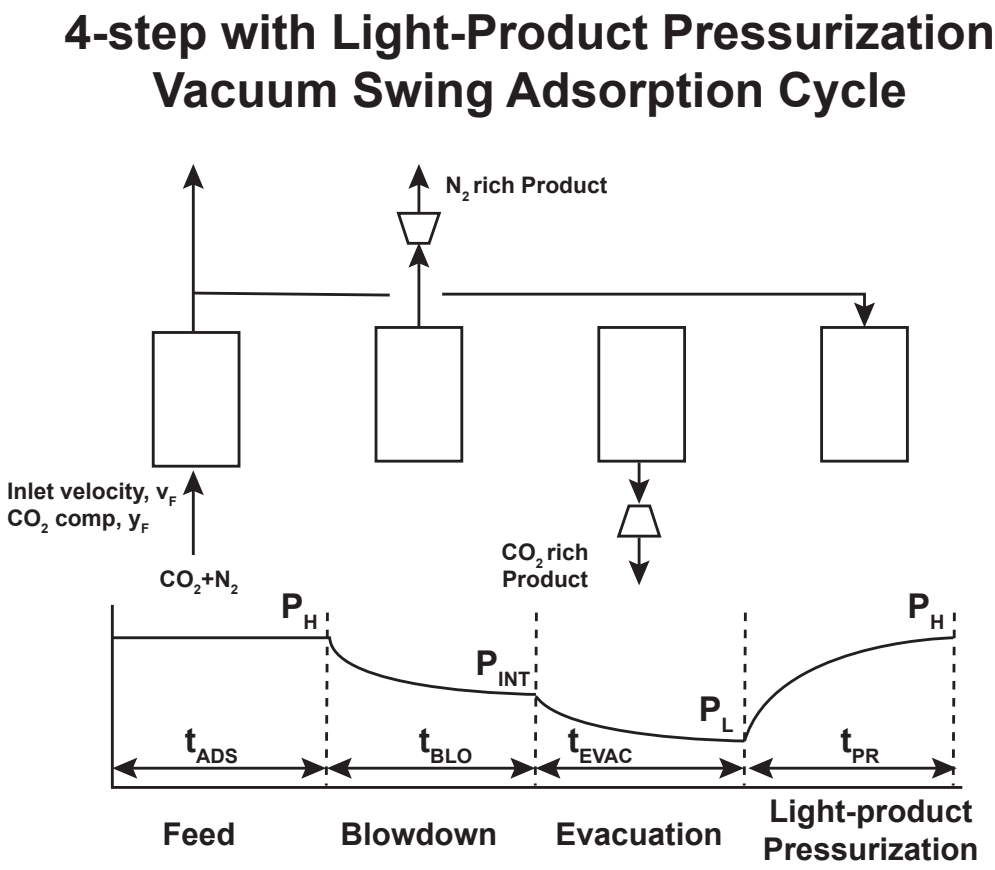

Figure 4.1: The 4-step with light-product pressurization (LPP) process used in this study.

simulations, a single-bed is allowed to transition from one-step to the other until cyclic steady state (CSS) is reached, The efficiency of this model to describe experimental measurements has been demonstrated in many of our previous studies [36].

4.2.2 Machine-learning training and validation

The machine-learning framework is shown in Fig. 4.2. The framework comprises of three blocks: the inputs; the neural network; and the outputs. Three steps are typically involved in developing neural network models, namely training, validation and testing. The input block consists of key inputs comprising of operating conditions shown in Fig. 4.2 and adsorption isotherm parameters of CO_2 and N_2. The neural

network block consists of a set of ANN models whose architecture is described below. The output block consists of key process indicators. In the training step a large enough dataset comprising of the inputs and the corresponding outputs are used to train the ANN model. In the testing step the ability of ANN to predict purity, recovery, energy, and productivity is evaluated. Each of these features is described below.

In this work, four independent neural networks were used to predict the key performance indicators, viz. Purity, Recovery, Energy, and Productivity. Each neural network model has ten inputs, including five isotherm parameters and five process operating conditions. The specific variables are shown in Figure 4.2 and their ranges are provided in Table 4.1. The range for the training variables have been chosen based on experience from previous studies where meaningful process performance was observed for a wide range of adsorption isotherm parameters [129]. A latin Hypercube sampling technique was used to generate 21,000 unique combinations of the input variables; and for each set, the detailed process model was run until CSS was reached and the performance indicators at CSS were used to train the ANN models. These values at CSS were used for training, i.e., no transients are considered. A total of 1,000 randomly selected data-points were removed from this set and used as a test-set. Note that this data was not used in training the model. The distributions of the various variables used for the training set is provided in the supporting information.

A deep neural network is made up of an input layer followed by a series of hidden layers with different number of nodes/ neurons followed by an output layer. A sigmoidal activation function was used in the hidden layers and a linear activation function was used for the output layer. The neural networks were trained with a Bayesian regularization with backpropogation technique *trainbr*, implemented in MATLAB 2019b [107, 121, 135]. The algorithm was run for 200 epochs with 5% of the training set randomly selected in the algorithm as a validation set (referred in the *trainbr* documentation as the test-set) to observe the training and validation loss

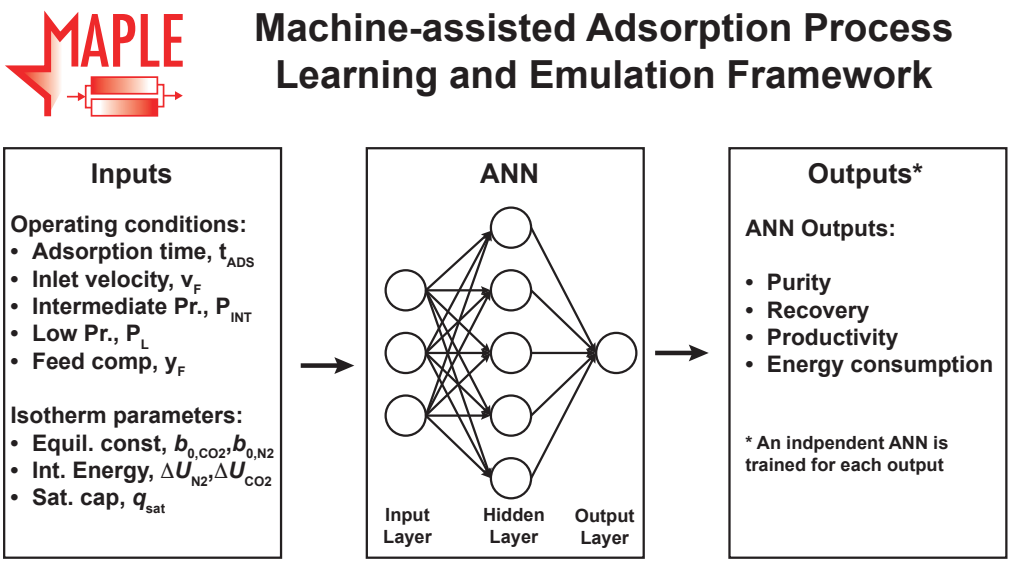

Figure 4.2: Key components of the MAPLE framework.

to avoid over-fitting. Note that the mean squared error between the predicted and measured outputs was treated as the loss function. All the computation required for data generation was carried out in Compute Canada advanced research computing systems and the training and validation of the neural network models was performed on desktop workstation with a dual 18 core Intel Xeon 2.7 GHz processors and 128 gigabytes of RAM.

Training effort vs model accuracy

It is important to note that neural network models are highly parametrizable and very flexible, which also makes them prone to over-fitting and over-parametrizing [137]. Over-fitting can be avoided by techniques such as cross-validation and measuring the accuracy against the test-set that has not been included in model training. In this work, the difference between the validation and training losses was taken as an indication of over-fitting. It is well known that the most computational effort in training machine learning models for PSA processes is spent in generating the training data-set [135]. A parametric study was performed to evaluate the trade-off between

Parameter	Type	Value
Column properties		
Bed length, L [m]	Fixed	1.0
Column inner radius, r_{in} [m]	Fixed	0.1445
Column outer radius, r_{out} [m]	Fixed	0.1620
Particle voidage, ϵ_{p} [-]	Fixed	0.35
Particle radius, r_{p} [m]	Fixed	1×10^{-3}
Density of the column wall, ρ_{w} [kg m^{-3}]	Fixed	7,800
Bed voidage, ϵ [-]	Fixed	0.37
Tortuosity factor, τ [-]	Fixed	3.0
Fluid properties		
Effective heat conduction coefficient, K_{z} [J m^{-1} s^{-1} K^{-1}]	Fixed	0.0903
Thermal conductivity of the wall, K_{w} [W m^{-1} K^{-1}]	Fixed	16.0
Inside heat transfer coefficient, h_{in} [W m^{-2} K^{-1}]	Fixed	0
Outside heat transfer coefficient, h_{out} [W m^{-2} K^{-1}]	Fixed	0
Gas specific heat capacity, $C_{\text{p,g}}$[J kg^{-1} K^{-1}]	Fixed	1010.6
Adsorbed phase specific heat capacity, $C_{\text{p,a}}$ [J kg^{-1} K^{-1}]	Fixed	1010.6
Wall specific heat capacity, $C_{\text{p,w}}$ [J kg^{-1} K^{-1}]	Fixed	502.0
Adiabatic constant, γ [-]	Fixed	1.4
Universal gas constant, R [m^3 Pa mol^{-1} K^{-1}]	Fixed	8.314
Fluid viscosity, μ [kg m^{-1} s^{-1}]	Fixed	1.72×10^{-5}
Molecular diffusivity, D_{M} [m^2 s^{-1}]	Fixed	1.60×10^{-5}
Adsorbent properties		
Density of the solid particle, ρ_{s} [kg m^{-3}]	Fixed	1130
Adsorbent specific heat capacity, $C_{\text{p,s}}$ [J kg^{-1} K^{-1}]	Fixed	1070
Adsorption saturation capacity, q_{sat} [mol kg^{-1}]	Variable	0.8 to 1.2
Adsorption equilibrium constant of CO_2, b_{0,CO_2} [m^3 mol^{-1}]	Variable	10^{-12} to 10^{1}
Adsorption equilibrium constant of N_2, b_{0,N_2} [m^3 mol^{-1}]	Variable	10^{-9} to 10^{3}
Heat of adsorption of CO_2, ΔU_{CO_2} [kJ mol^{-1}]	Variable	-20 to -42
Heat of adsorption of N_2, ΔU_{N_2} [kJ mol^{-1}]	Variable	-5 to -18
Process properties		
Ambient temperature, T_{a} [K]	Fixed	298.15
Feed temperature, T_{F} [K]	Fixed	298.15
Compression/evacuation pump efficiency, η [-]	Fixed	0.72
Blowdown step exponential pressure history term, α_{BLO} [s]	Fixed	0.5
Evacuation step exponential pressure history term, α_{Evac} [s]	Fixed	0.5
Pressurization step exponential pressure history term, α_{PRESS} [s]	Fixed	0.5
High pressure, P_{H} [bar]	Fixed	1
Adsorption step time, t_{ADS} [s]	Variable	10 to 110
Intermediate pressure, P_{INT} [bar]	Variable	0.05 to 0.45
Evacuation pressure, P_{L} [bar]	Variable	0.01 to 0.05
Feed rate, v_{F} [m s^{-1}]	Variable	0.1 to 2
CO_2 feed composition, y_{F} [-]	Variable	0.05 to 0.7

Table 4.1: Parameters used for detailed model simulations. Those indicated as variable are used for training the MAPLE framework and used as decision variables.

training effort and model accuracy. The impact of the ANN architecture was also studied. In this work, the training effort was quantified as the total time required for sample generation and the neural network training time. However, in all cases the sample generation using the detailed model required a substantially large time when compared to neural network model training time. The corresponding training accuracy was quantified using a R^2_{Adj} metric, the adjusted coefficient of determination:

$$R^2{}_{\text{Adj}} = 1 - \frac{(1 - R^2)(n - 1)}{(n - k - 1)} \tag{4.3}$$

where

$$R^2 = 1 - \frac{\Sigma^{\text{n}}_{j=1}(f_j - \hat{f}_j)^2}{\Sigma^{\text{n}}_{j=1}(f_j - \bar{f})^2} \tag{4.4}$$

where n is the number of testing samples and k is the number of input descriptors, which in this work is 1000 and 10, respectively. f_j is the actual observed output, $\hat{f}_j$ is the predicted output, and $\bar{f}$ is the mean of the set of actual outputs. Note that the R^2_{Adj} value was obtained using a independent test-set consisting of 1,000 simulated VSA data samples. These data-points where unique and was not included in the training of the ANN models.

The basic neural network model, in this study, made up of one input layer and one hidden layer with 10 neurons. Progressively, the complexity of the model was increased by using additional neurons. The 20,000 samples were randomized and smaller sets were formed. The distribution of the various inputs in the training set is provided in the supporting information. Figure 4.3 a) shows the resulting average R^2_{Adj} of all the predicted quantities as a function of training sample size for different number of neurons. It can be observed from the figure that increasing the number of neurons improves the overall predictive capability of the neural network for all sample sizes. It is interesting to note that even with a relatively small number of training samples (7,500) the network can achieve a R^2_{Adj} as high as 0.98. Further, it can be

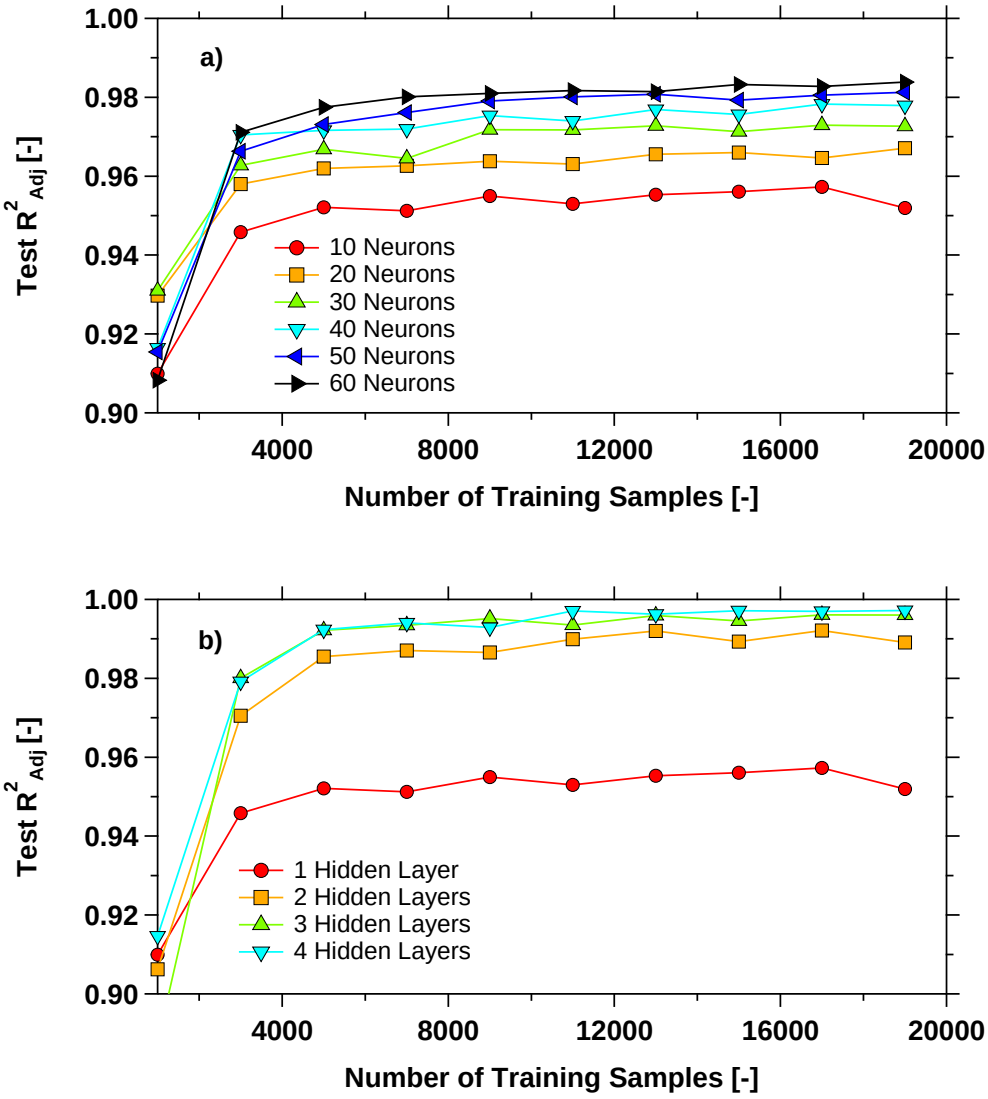

Figure 4.3: The effect of neural network architecture on model prediction accuracy: Average test R^2_{Adj} is shown as a function of the training-set size a) The effect of number of neurons and training samples on R^2_{Adj} b) The effect of number of hidden layers; ten neurons were used in each hidden layer. The test-set contains 1000 samples.

seen that for a given number of training samples the addition of neurons in the hidden layer increases the predictions accuracy from an R^2_{Adj}. However, beyond 30 neurons, no significant gain in accuracy can be obtained. The other neural network component that can help improve predictive capability is the number of hidden layers. So again, keeping the base case as one hidden layer with 10 neurons, the number of hidden layers was progressively increased. Figure 4.3 b) shows the resulting average test R^2_{Adj} of all the predicted quantities as a function of training sample size for different number of hidden layers. The addition of hidden layers improves the predictive capability of the neural network. The number of sample points that are needed to achieve an average test $R^2_{\text{Adj}} \geq 0.99$ is as low as 10,000 with just 2 hidden layers. There is no significant improvement in model accuracy beyond 2 hidden layers. Note that the variation of the R^2_{Adj} for the individual performance indicator models are provided in the supporting information.

Following the procedure as above it was found that a neural network with 2 hidden layers with 20 neurons in each hidden layer reduces the number of parameters while keeping a high test $R^2_{\text{Adj}} \geq 0.995$ with just 10,000 points. The four performance indicators corresponding to the test set, calculated from the ANN model and the detailed model are compared in Figure 4.4. The results show an excellent correlation, thus confirming accuracy of the surrogate model.

4.2.3 Process Optimization

The transient nature of adsorption process and the numerous possible operating conditions makes the optimization of the P/VSA process challenging. In this work, an evolutionary algorithm, non-dominated sorting genetic algorithm-II (NSGA-II), is used to optimize the process conditions. It is been shown in the literature to optimize PVSA systems for various multi-objective problems [70, 106]. In this study, two optimization approaches were considered. In the first one, called "Detailed-Opt.", the genetic algorithm optimizer is coupled with the detailed model. The optimizer

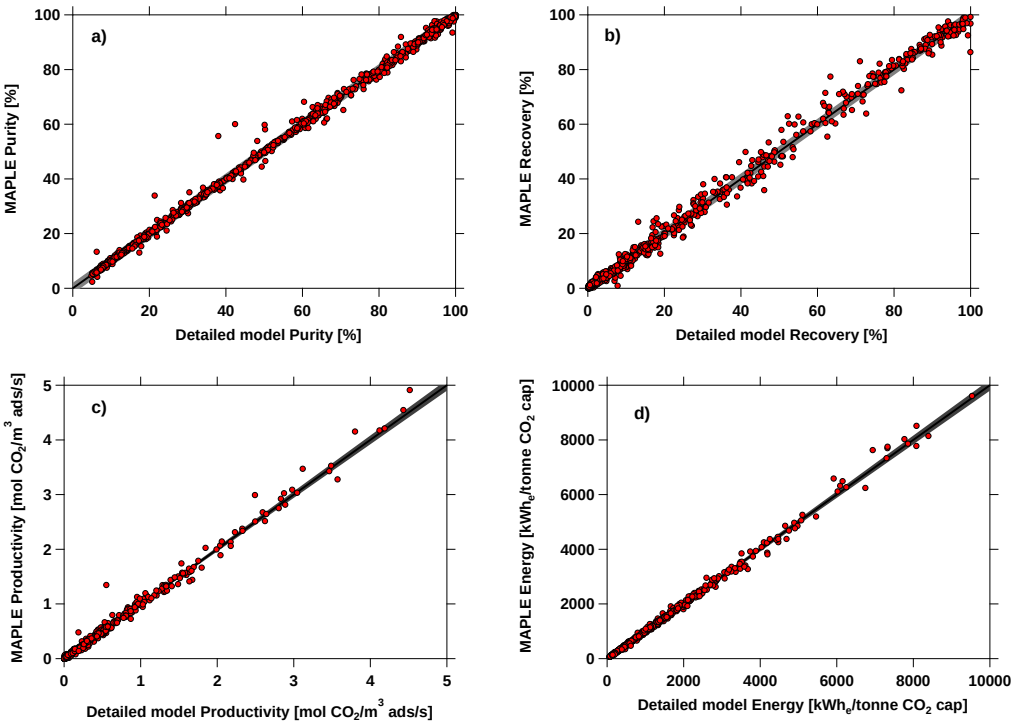

Figure 4.4: Parity plot of the detailed model and MAPLE surrogate results for a test-set of 1000 samples shown for the four key performance indicators a) Purity, b) Recovery, c) Productivity, d) Energy.

chooses an initial population that comprises of a set of decision variables. These are sent to the detailed model, which simulates each step of the VSA process until CSS is reached. At this point, the performance indicators are returned to the optimizer where the objective functions are calculated. If constraints are present, a suitable penalty function is applied and the objective function values are re-calculated. Based on the objective function values the next generation is generated and the process is repeated. This technique has been shown to be very effective for VSA simulations and has also been shown to compare well with experiments [36]. The second optimization approach is called "MAPLE-Opt.". In this case, the detailed model in the Detailed-Opt. is replaced by the MAPLE model. Instead of computing each step in the adsorption cycle, the MAPLE model directly estimates the CSS performance indicators and returns them to the optimizer. As expected, this significantly reduces the computational time.

4.3 Performance evaluation of MAPLE

The trained and validated neural network models obtained with MAPLE framework can, in principle, now be used to predict the performance of any adsorbent-adsorbate system that can be described by a Langmuir isotherm. To highlight this feature, a series of case studies were performed. The first case study relates to testing the ability of the MAPLE framework for simulating specific operating conditions when the VSA process is operated using an adsorbent that was hitherto not present in the training set. The second case study extends the first by considering multi-objective optimization of the process, and screening adsorbents screened in the literature.

4.3.1 Simulation of a VSA process

Among the several potential applications of the MAPLE framework is the simulation of a process for a given adsorbent and operating conditions. Although the high accuracy of the predictive capability has been demonstrated above, it is necessary

to verify its performance for an adsorbent that was not "seen" by the model in the training set. For this purpose, the isotherms of CO_2 and N_2 on Zeolite 13X were considered. While the isotherm of this system, strictly requires a DSL model, for the purpose of this study, a SSL model was fitted to the data. The SSL isotherm parameters are provided in the supporting information. For this study, the cycle specific inputs were fixed as follows: $t_{\mathrm{ADS}} = 92.4$ s, $P_{\mathrm{INT}} = 0.08$ bar, $P_{\mathrm{L}} = 0.03$ bar, $v_{\mathrm{F}} = 0.64$ ms^{-1}, and $y_{\mathrm{F}} = 0.15$. For the first case, the intermediate pressure (P_{INT}) was varied from 0.08 to 0.18 bar. For each value of P_{INT}, both the detailed model and MAPLE were run using the SSL isotherm parameters and the resulting performance indicators are compared in Figure 4.5 a) - d). The results confirm the predictive capability of MAPLE where each performance indicator was predicted within 2% of the detailed model. As expected, an increase in P_{INT} results in the reduction of CO_2 product purity as N_2 is not sufficiently removed in the blowdown steps. A second parametric study was performed by varying the feed composition of CO_2 (y_{F}) from 0.05 to 0.18 and the results are shown in the supporting information. Again, the MAPLE framework is able to predict every performance indicators with an error less than 2%.

4.3.2 VSA optimization

One of the key understanding from large scale screening studies has been that measuring key performance indicators such as energy consumption or cost of separation, etc., cannot be accurately predicted without full process simulation coupled with robust multivariate optimization [129]. While this represents a computationally challenging proposition, MAPLE has the potential to overcome this bottleneck. This feature of MAPLE needs to be evaluated in order to confirm its suitability for use in robust multi-objective optimizations. A series of optimization case-studies were performed to examine this claim using the detailed model. In order to illustrate this capability we employ two optimization approaches, viz., "Detailed-Opt.", and "MAPLE-Opt.",

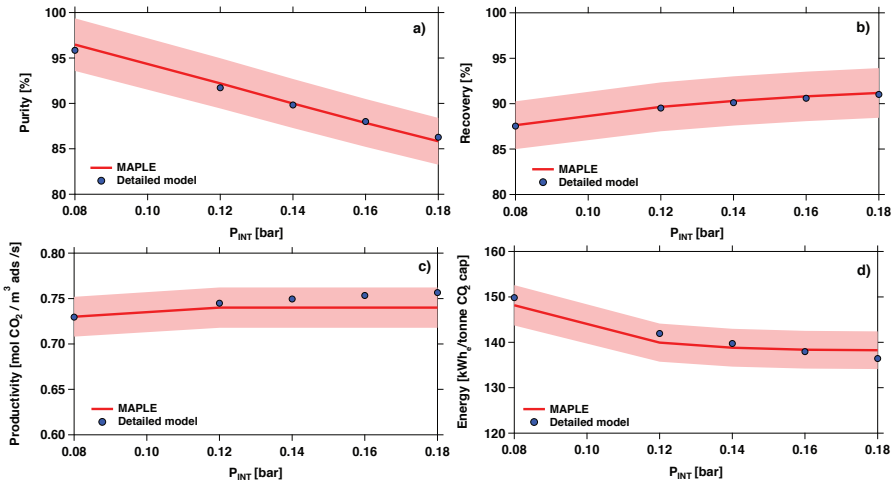

Figure 4.5: Parametric study showing the variation of key performance indicators a) CO_2 Purity b) CO_2 Recovery c) Productivity d) Energy, for Zeolite 13X as a function of intermediate pressure P_{INT}. Solid lines show the results from MAPLE and symbols correspond to the detailed model results. The shaded area represents a 2% error band.

both of which have been explained earlier. Three cases were chosen to highlight the ability of MAPLE to achieve the above-mentioned requirements. The first case study considered the unconstrained simultaneous maximization of CO_2 purity and recovery for four different feed composition of 10, 12, 15, 18% with the balance being N_2. In this case, the isotherm inputs were fixed to SSL parameters of Zeolite 13X.

Figure 4.6 a) shows the optimized Pareto curves for the different feed composition. The solid lines represent the Pareto predicted by MAPLE-Opt. framework, with the shaded area representing a 2% error bar on the abscissa and the symbols the Pareto curve obtained with the Detailed-Opt. Both the optimization frameworks result in essentially the same Pareto curves. For the case of constrained optimizations, two case studies were considered. The first case involved minimizing the energy consumption while maximizing the recovery of CO_2 of Zeolite 13X for at different feed compositions for a CO_2 purity constraint of 95%. Similar to the previous study, the cycle specific operating conditions such as adsorption time, pressure levels, and feed velocity were the decision variables and these bounds are shown in Table 4.1.

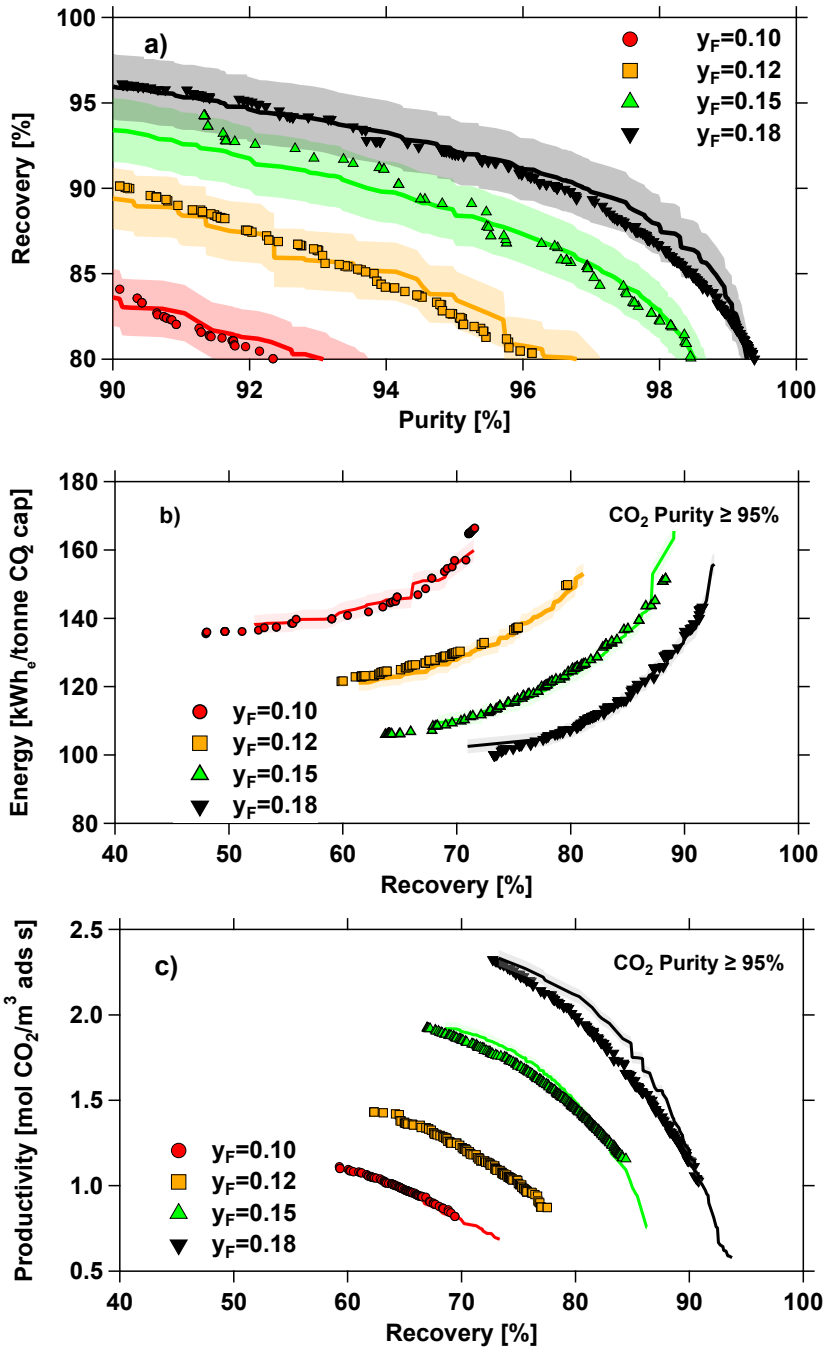

Figure 4.6: Pareto curves resulting from the multi-objective optimization of the 4-step cycle with LPP process employing Zeolite 13X. Symbols are from the Detailed-Opt. and solid line from MAPLE-Opt. a) Pareto curve resulting from the unconstrained maximization of purity and recovery. b) Pareto curve resulting from the minimization of Energy and maximization of recovery subject to a CO_2 purity $\geq$95% c) Pareto curve resulting from the maximization of productivity and recovery subject to a CO_2 purity $\geq$95%.

Figure 4.6 b) shows the optimized Pareto curves for the different feed composition provided in the legend. The solid lines represent the Pareto predicted by MAPLE-Opt., with the shaded area representing a 2% error bar on the abscissa. The symbols represent the Pareto curve obtained from Detailed-Opt. As expected, the Pareto curve move towards the bottom right of the plot with increasing feed composition. This indicates that better recovery at a lower energy consumption can be achieved at higher feed compositions. The plot illustrates the ability of MAPLE to accurately predict the results of the constrained multi-objective optimization problems. In the second case of the constrained optimization, the simultaneous maximization of productivity and recovery is carried out for a purity $\geq 95\%$. The results shown in Figure 4.6 c). shows the optimized Pareto curves for the different feed compositions. The solid lines represent the Pareto predicted by optimizing the MAPLE-Opt., with the shaded area representing a 2% error bar on the abscissa. The symbols represent the Pareto curve obtained with the Detailed-Opt. As expected with the increase in feed composition of CO_2, the Pareto curve moves to the top right. Finally, it is also worth noting that the Pareto curves obtained from MAPLE-Opt. and Detailed-Opt. are nearly identical, indicating the high model accuracy achievable using the MAPLE framework. It should be noted that it took less than 2.4 core-mins to generate one Pareto curve using MAPLE-Opt., while Detailed-Opt. required ≈ 500 core hours for the same. This simple comparison illustrates the significant savings in computational effort that can be achieved by using MAPLE.

4.3.3 Adsorbent screening through process optimization

One of the key applications of the MAPLE framework is anticipated to be in screening adsorbents for specific separations. In order to illustrate this potential we consider two illustrative examples. In the first example, we consider the detailed optimization of three materials. Such a detailed optimization is essential as each adsorbent is expected to perform at its best for a unique set of operating conditions. Hence, any

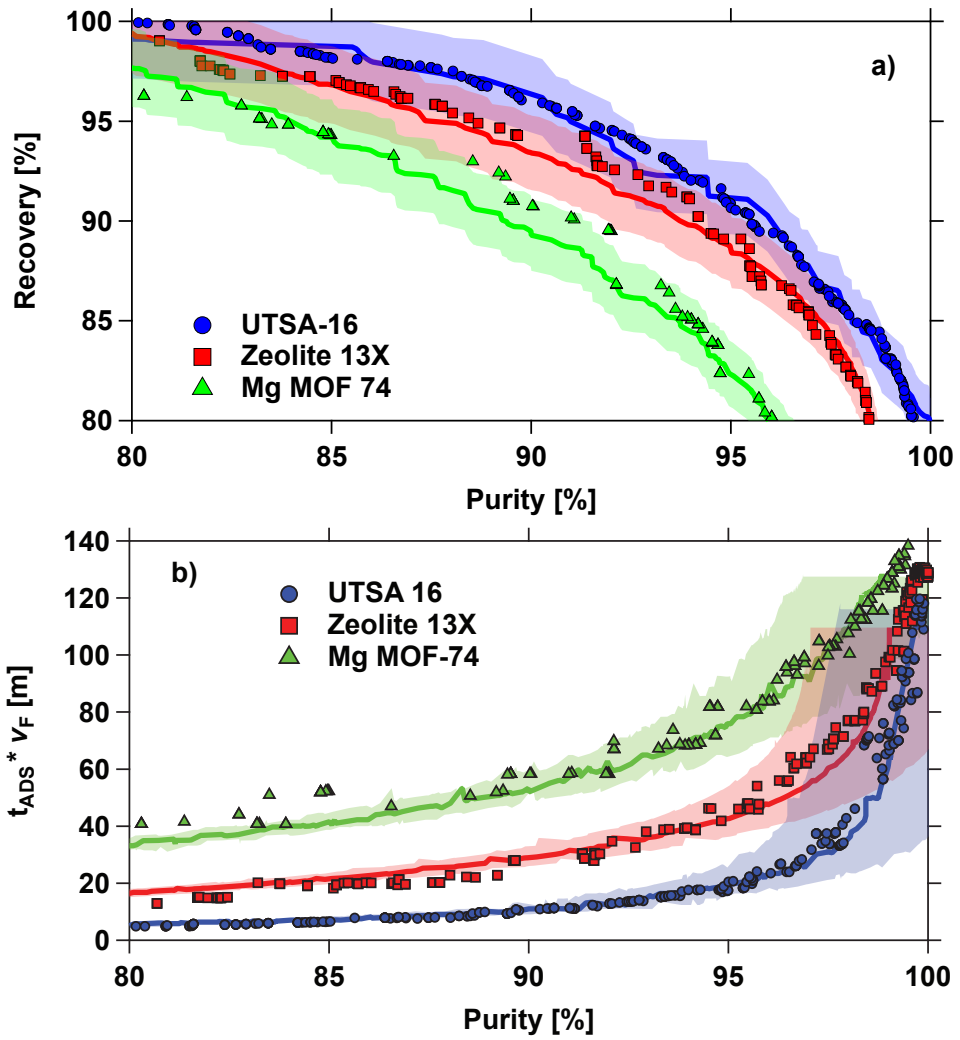

Figure 4.7: Results from the unconstrained multi-objective maximization of purity and recovery for Zeolite 13X, UTSA-16, and Mg MOF-74 a) Pareto resulting from the unconstrained maximization of purity and recovery. b) The variation of $t_{\mathrm{Ads}} \times v_{\mathrm{F}}$ vs Purity. Lines denote results from MAPLE-Opt. and symbols are from Detailed-Opt.

meaningful screening should consider the entire range of operating conditions. To illustrate this aspect, three adsorbents, namely Zeolite 13X and two MOFs (UTSA-16 and Mg-MOF-16) are considered [29]. The SSL isotherm parameters are provided in the Supporting information. For each of these adsorbents, both the MAPLE-Opt. and Detailed-Opt. were run in order to maximize CO_2 purity and recovery. The cycle specific operating conditions such as adsorption time, pressure levels, and feed velocity were the decision variables and were allowed to vary within bounds provided in Table 4.1. The resulting Pareto curves for both Detailed-Opt. and MAPLE-Opt. are compared in Figure 4.7 a). The solid lines represent the Pareto predicted by optimizing the MAPLE-Opt., with the shaded area representing a 2% error bar on the abscissa. The symbols represent the Pareto curve obtained with the Detailed-Opt. Among the three adsorbents, UTSA-16 has the best potential for separation followed by Zeolite 13X and Mg-MOF-74. The trends and the absolute values are consistent between MAPLE-Opt. and Detailed-Opt. Figure 4.7 b) shows the variation of the decision variables, $t_{\mathrm{ADS}} \times v_{\mathrm{F}}$, which is a estimate of the bed utilization vs purity of the CO_2 product. The optimization results clearly indicate a larger bed utilization favours higher purity (at the cost of lower recovery). Further, both MAPLE-Opt. and Detailed-Opt. show identical values of bed utilization, confirming that the MAPLE-Opt. not only predicts the performance indicators correctly but also provides an exact mapping to the decision variable space. This is an important confirmation that increases the confidence in using MAPLE for routine process optimization-based adsorbent screening.

In the final illustration, MAPLE-Opt. was used to screen a group of 75 adsorbents that were reported by Khurana and Farooq [15]. It is worth noting that the original data provided by the authors described the CO_2 and N_2 equilibrium using a DSL isotherm. It is well-known that competitive adsorption has a major impact on process calculations [33, 110]. Hence, in order to adopt the data reported by the authors within this current framework, it was important to identify those materials that can

be adequately represented by the SSL. In order to do this, the isotherms of both CO_2 and N_2 were generated upto 1 bar pressure using the DSL parameters reported in the original paper. Using these points, the SSL isotherm was fitted at 3 different temperatures. Those materials that yielded a R^2 of less than 0.95 were removed. This yielded 53 materials. Then the competitive loadings of both CO_2 and N_2 were calculated at 1 bar total pressure and a CO_2 composition of 0.15, using both the DSL and SSL parameters. If the absolute difference between the two loadings was greater than 30%, then those materials were also eliminated. This ensured that only those materials whose single and competitive isotherms can be reasonably described by the SSL isotherm are considered. This resulted in a total of 36 materials. The SSL parameters can be found in the supporting information. These adsorbents were optimized first to verify if they achieve the United States Department of Energy (DOE) guidelines for post-combustion carbon capture, i.e, $\geq$ 95% CO_2 purity and $\geq$ 90% CO_2 recovery. This screening was carried out by running the unconstrained MAPLE-Opt. The confusion matrix comparing the results of classification from this study and the original one is shown in Fig. 4.8 a). A high classification accuracy of 97.22% was achieved, with no false negatives. Additionally, the adsorbents that met the DOE target were further considered to identify the minimum energy at which the DOE targets can be achieved. The minimum energy from MAPLE-Opt. is tabulated against the results from the detailed model optimization reported by Khurana and Farooq in the supporting information. Figure 4.8 b) shows the parity plot between the two results as blue squares. As shown, it is clear that the minimum energy calculated by MAPLE-Opt. correlates well with an independent source confirming its accuracy. The outliers in the plot are to due to the characterization of the dual site behaviour using a SSL. Although the single component isotherms for both SSL and DSL forms are comparable, there was a higher degree of mismatch in the competitive loadings of CO_2 and N_2. This points to the importance of an accurate description of competitive adsorption equilibria.

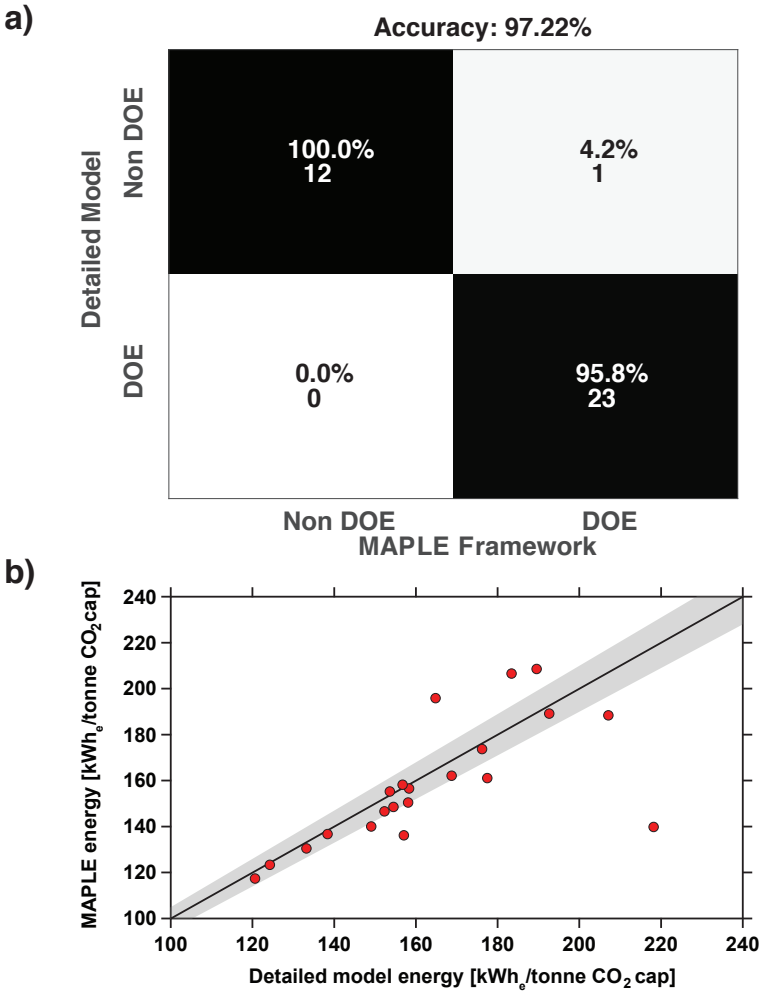

Figure 4.8: Comparison of screening results from MAPLE with those reported by Khurana and Farooq [15]. a) Confusion matrix showing the classification results for the DOE Purity-Recovery requirements. b) Comparison of minimum energy values, subject to constraints of CO_2 purity $\geq 95\%$ and recovery $\geq 90\%$ calculated by MAPLE and those from the literature.

4.4 Conclusions

In this paper, the development of a material-agnostic machine-learning model for the rapid simulation of VSA processes was presented. The key difference between this study and the ones in the literature is the inclusion of the adsorption isotherm parameters. The model is trained not using properties of real adsorbents, but rather by parametrizing the Langmuir adsorption isotherm of the two components. It is important to highlight that the current machine-learning model has been trained for a limited set of variables over a specific range. For instance, the column size and cycle are fixed; only a selected number of operating parameters are varied over a certain range; the feed temperature is fixed; the description of the adsorption isotherm is limited to single-site Langmuir function; the mass transfer resistance is considered to be confined to the macropores; the adsorbent properties, e.g., density, specific heat are held constant. Barring these few properties, the model can be considered as being agnostic even to the two species to be separated. It was further shown that the framework can be reliably used for calculating the performance of adsorbents that were not used in the training set. This means that such a model can be used for describing the process performance of any arbitrary adsorbent as long as the equilibrium data can be adequately represented by the SSL. This was demonstrated by calculating the performance of over 40 adsorbents. It is important to caution that the optimal conditions for a specific material can indeed lie beyond the range of conditions that the model is trained for. Further modeling and optimization might be required to fully understand the potential of the material.

MAPLE can be used in a variety of ways: design/describe experimental campaigns, perform parametric studies, perform screening of large adsorbent databases for any arbitrary set of constraints and objective functions. The most important advantage of this approach lies in the ability to screen large databases. Experimental and hypothetical materials are rapidly increasing and databases that contain hundreds of

thousands of such material are now common and there is an increasing urge to mine them to identify adsorbents for further development. Many research groups have now confirmed that the process configuration has a major impact on the material performance. Hence, tools such as MAPLE are expected to provide researchers the ability to optimized the process for each adsorbent before a more meaningful evaluation can be made. Further, for the process considered in this study, the entire training effort for generating 10,000 training sets and training the framework costed $\approx$ 1,700 core-hours. Once trained, the MAPLE-Opt. takes $\approx$ 0.04 core hours to optimize one adsorbent. Hence, for a database consisting of 10,000 materials, assuming about 3,000 unique simulations are required to identify the optimum condition per adsorbent, a detailed model would take a total of 5,125,000 core-hours to screen, while MAPLE would be completed (including the time for training) in 2,100 core-hours. This is a significant computational advantage, especially when very large databases are considered. Naturally, there are many other advances that are required in order to be able to perform a thorough optimization of any arbitrary adsorbent. We highlight two here: Developing frameworks for systems that require more complex description of the equilibrium and/or kinetics; and developing superstructures that not just optimize the operating conditions but also the cycle configuration. This study also clearly demonstrates that machine-learning approaches have the potential to tackle such computationally intensive problems and should be explored further.

Chapter 5

Practically Achievable Process Performance Limits for Pressure-Vacuum Swing Adsorption-Based Post-combustion CO_2 Capture.

[1]

5.1 Introduction

Carbon capture and storage (CCS) is a critical component of the suite of technologies needed to fulfill the goals of the Paris agreement [138]. Carbon capture, i.e., concentrating CO_2 from flue gas or other intermediate streams, is the most expensive step in the CCS chain. Reducing the cost of capture is critical to the large-scale deployment of CCS [13]. Post-combustion CO_2 capture refers to the concentration of CO_2 from flue gas that contains N_2, CO_2 and other impurities. Absorption using liquid solvents, typically amines and their derivatives, is currently the preferred industrial technology for large-scale CO_2 capture. High regeneration costs, degradation of the solvent, and equipment corrosion are significant bottlenecks that have motivated researchers to

[1]Pai, K. N., Prasad, V., and Rajendran, A. (2021). Practically Achievable Process Performance Limits for Pressure-Vacuum Swing Adsorption-Based Postcombustion CO2 Capture. ACS Sustainable Chemistry and Engineering, 9(10), 3838-3849.

look for alternatives [13]. Carbon capture using solid adsorbents is one such promising alternative. These adsorbents can be deployed in both pressure-vacuum swing adsorption (PVSA) or temperature swing adsorption (TSA) processes [13, 108]. The advent of novel adsorbents, such as metal-organic frameworks (MOFs), and covalent organic frameworks (COFs), has intensified the search for suitable capture materials [13, 139].

Traditionally, the selection of adsorbents has heavily relied on simplified process metrics that are calculated from simple equilibrium measurements/ calculations. However, in recent years, there seems to be a consensus that these metrics are not reliable and that detailed process simulations and optimization essential to reliably evaluate the true separation potential of adsorbents [29, 30, 32, 33, 40, 129]. Exploring this adsorbent-process relationship can be classified into two approaches: screening and process inversion. In screening, the critical question is, *"If we know the characteristics of an adsorbent, what is the best process outcome that can be achieved?"*. Both simple and detailed process models have been used for screening, and a variety of studies have been published [15, 32, 129, 131, 140]. In process inversion, the central question is: *"What should be the characteristic of the adsorbent that produces the best process outcome?"*. A few studies have explored this *"inverse"* problem. Maring and Webley used a simplified batch-adsorber model to vary adsorbent-specific properties such as Henry's constant and heat of adsorption to explore the features of an adsorbent that minimizes energy [130]. Rajagopalan and Rajendran used detailed models to explore how the competitive nature of CO_2 and N_2 impacts the separation and identified regions where low energy consumption can be achieved [141]. Danaci extended the Maring-Webley model and explored adsorbent features that would minimize the cost of capture [132]. Khurana and Farooq used detailed process models and examined the characteristics of the CO_2 and N_2 isotherms that enhance process performance [15] and cost [73] for the case of post-combustion CO_2 capture from coal plants.

The above-mentioned studies have allowed the scientific community to make progress in understanding the relationship between adsorbent characteristics and process performance. While this pursuit is far from over, [40] the question *"What are the best performance indicators, namely energy consumption and productivity, that are practically achievable by using adsorption processes?"* remains open. While the (technology-agnostic) thermodynamic minimum energy consumption, based on the free-energy of mixing, is undoubtedly helpful, it is well known that practical separation processes consume significantly higher energy compared to these values. It is, in fact, the practically achievable minimum energy and maximum productivity values that will permit objective technology evaluation. These limits also indicate the *"innovation potential"* that is possible, thereby providing useful information to both materials chemists and process engineers. It is worth noting that such limits, for the case of adsorption, are currently not known. In this work, we restrict ourselves to the case of pressure-vacuum swing adsorption (PVSA) applied to post-combustion CO_2 capture, a class of adsorption process that has been extensively studied. Accordingly, the critical question that we seek to answer in this work is *"If we can design the ideal adsorbent(s), what are the practically achievable limits of minimum energy and maximum productivity for PVSA?"*. It is well known that adsorption process simulations are time-consuming, and hence deploying them for large-scale optimization and screening remains a challenge [40, 135]. In this work, we exploit recent innovations in machine learning to accelerate adsorption process simulations [72]. Specifically, we employ the machine-assisted process learning and evaluation (MAPLE) framework, a data-driven modelling framework trained using a detailed process model suitable for accepting both process operating conditions and adsorbent properties as inputs [142]. Several case studies are presented to explore the operation, performance, and material limits.

5.2 Methodology

5.2.1 Separation System and Performance Metrics:

CO_2 capture is modelled as the separation and concentration of CO_2 from a binary gas mixture of CO_2 and N_2. While most flue gas contains impurities including, water, we assume that they are removed upstream of the capture unit. This seems reasonable since most adsorbents, barring a few exceptions, adsorb water strongly, and their performance is likely to deteriorate in the presence of water. The CO_2 purity, Pu_{CO_2}= (moles of CO_2 in the product)/(moles of CO_2 + N_2 in the product) $\times$ 100 [%] and CO_2 recovery, Re_{CO_2}=(moles of CO_2 in the product)/(moles of CO_2 in the feed) $\times$ 100 [%] are important metrics to evaluate CO_2 capture performance. The US-Department of Energy (US-DOE) targets require $Pu_{CO_2} \geq 95\%$ and Re_{CO_2} $\geq 90\%$. The key performance metrics that are used to evaluate the process include energy consumption, En =(energy consumption / tonne CO_2 captured) the process productivity, Pr =(moles of CO_2 captured/ unit volume of adsorbent/second). It is worth noting that a proper scale-up and techno-economic analysis is required to evaluate the potential of any capture technology [73, 143]. However, since the cost of many novel adsorbents is not known, full-scale costing may not be feasible without making assumptions. Under such circumstances, energy and productivity estimates are valuable in making critical decisions about technology selection and evaluation.

5.2.2 PVSA Process Modelling:

The accurate modelling of an adsorbent-based separation process requires a detailed description of mass and heat transfer and fluid dynamics. Since adsorptive processes are inherently cyclic, the equations describing each step are iteratively solved until a cyclic steady state. In this study, we keep the column dimensions and the sizes of fluid movers fixed to match the scale of a PVSA-based CO_2 capture pilot plant described Krishnamurthy et al.[75]. The model is based on the following key assumptions: 1.

The ideal gas law is obeyed; 2. An axially dispersed plug flow model describes the flow in the column; 3. The solid and fluid phases are in thermal equilibrium, and that the column is assumed to be adiabatic; 4. The adsorbent is assumed to be particles of 2 mm in diameter. Mass transfer is described by a linear-driving force (LDF) model, assuming that the molecular diffusion in macropores controls the mass transfer; 5. Darcy's law is used to describe the pressure drop in the column (It has been shown that for the current process scale under investigation and the operating conditions studied, this assumption is satisfactory). The column mass and energy balances result in a system of partial differential equations (PDEs). The PDEs are reduced to ordinary differential equations (ODEs) system using a finite-volume scheme. They are solved using *ode23s*, an inbuilt solver in MATLAB. Appropriate boundary conditions are applied for the specific step. Model equations and boundary conditions are provided in the supporting information. Properties associated with the column are provided in Table 5.1. The entire simulation strategy is detailed in a previous work [19] and validated experimentally both at lab-scale [36] and pilot-scales [75].

In this study, we use a constant-selectivity single-site Langmuir (SSL) isotherm to describe the competitive adsorption equilibrium:

$$q_i^* = \frac{q_{\text{sat}} b_i C_i}{1 + b_{\text{CO}_2} C_{\text{CO}_2} + b_{\text{N}_2} C_{\text{N}_2}} = \frac{H_i C_i}{1 + b_{\text{CO}_2} C_{\text{CO}_2} + b_{\text{N}_2} C_{\text{N}_2}}, , \ i = \text{CO}_2, \text{N}_2 \tag{5.1}$$

where q_{sat} is the saturation capacity, b_i is the equilibrium constant for component i, and q_i^* is the equilibrium solid phase loading. The product of q_{sat} and b_i is the Henry constant, H_i. The temperature dependence of the equilibrium constant is described by

$$b_i = b_{0,i} e^{\frac{-\Delta U_i}{R_g T}} \tag{5.2}$$

where ΔU_i is the internal energy of adsorption for component i, R_g is the universal gas constant and, T is the temperature. The SSL isotherm comprises of five parameters, *viz.*, q_{sat}, b_{0,CO_2}, b_{0,N_2}, ΔU_{CO_2}, and ΔU_{N_2}. It is worth noting that in many cases, more

complicated forms of the isotherm, e.g., dual-site Langmuir, are needed to describe the equilibrium loading [136], and the use of an SSL can limit the range of isotherm behaviours that can be studied. While we acknowledge that this can be considered a limitation, it is worth pointing out that the SSL isotherm does provide a simple and elegant formulation to describe competitive behaviour for several systems of practical interest [26, 129]. Further, since the isotherm uses just five parameters, it allows for the understanding and visualization of the interplay between material properties and process configurations.

5.2.3 Process Cycles:

The PVSA processes used in this study are shown in Fig. 5.1. A 4-step cycle with light product pressurization (LPP) is shown in Fig. 5.1 a), and a 4-step cycle with feed pressurization (FP) is shown in Fig. 5.1 b). Both cycles consist of four steps: 1. An adsorption step, where the feed mixture consisting of y_{F} mole-fraction of CO_2, with the balance being N_2, is introduced at the feed end ($z = 0$) of the column with an interstitial feed velocity v_{F} and pressure P_{H}, for a period of t_{ADS}. The light product, which is predominantly N_2, is collected at the outlet end ($z = L$). 2. A blowdown step, where a vacuum pump removes gas from the top of the column and the column pressure is reduced to an intermediate value, P_{I}. This step aims to remove the N_2 while reducing CO_2 loss. 3. An evacuation step, where another vacuum pump further reduces the pressure to a low value, P_{L} and high purity CO_2 product is collected at the feed end ($z = 0$). 4. A pressurization step, where the pressure of the column is brought back from the P_{L} to P_{H} using either the feed stream (F) or the light-product (LP). The cycles are called 4-step with LPP and 4-step with FP depending on how the pressurization step is performed. Although the two differ in just one step, they are known to show measurably different performances [19, 36]. While it is certainly possible to construct more complex cycles, we limit ourselves to these two cycles, as they have been used by several research groups as a benchmark [33, 73, 128, 129],

and they have been demonstrated in lab-scale [36] and pilot-scale experiments [75].

At a process scale, four performance indicators, Pu_{CO_2}, Re_{CO_2}, En, and Pr, are considered and have been defined earlier. The energy consumption for the process comes from four steps: the energy required to pressurize the gas from atmospheric pressure to the P_H and to overcome the pressure-drop in the column during the pressurization and adsorption steps; and the energy consumption of the vacuum pumps in the blowdown and evacuation steps. The vacuum pump efficiency, while in many process studies were fixed to $\approx 70-80\%$, is now assumed to vary with pressure according to the expression given in Table 5.1. The cycle-time used to calculate productivity is the sum of the duration of the four steps. Each of the pressure reduction steps has a dedicated vacuum pump that operates at a constant volumetric flow rate. This means that the duration of the blowdown (t_{BLO}) and evacuation (t_{BLO}) steps are dependent on the flow rate. Naturally, using a pump with a higher flow rate will reduce the duration but could result in a higher cost. This study considers the vacuum pump, and the column dimensions are fixed. Finally, the pressure drops in the lines can be detrimental for energy consumption for systems working under vacuum conditions. The pressure drop can result in increased energy consumption and slower evacuation, both of which will worsen the process performance. In this study, such pressure drops, external to the columns, are considered to be negligible. It is important to consider the results in light of these assumptions.

5.2.4 The MAPLE Framework and Process Optimization:

The MAPLE framework, is a data-driven surrogate model trained to emulate an adsorbent process using supervised machine learning [142]. The main advantage of this framework lies in its ability to have both adsorbent and process-related inputs. Compared to the full models, MAPLE is orders of magnitude faster to train and deploy [142]. The operating conditions and their training ranges for the two process cycles are shown in Fig: 5.1 a) and b). The adsorbent and operationally related trained

input space is shown in Figs. S2 and S3 of the supporting information and in Table 5.1. Physically meaningful constraints were applied while generating the samples. For instance, CO_2 is always the strongly adsorbed gas, i.e. $b_{CO_2} \geq b_{N_2} + 3.1$ [m^3/mol]. The heat of adsorption of CO_2 is always greater than N_2, i.e., $|\Delta U_{CO_2}| \geq |\Delta U_{N_2}| + 2$ [kJ/mol]. The ranges for the isotherm parameters were selected to cover the range of adsorbents from the carbon capture materials database [26, 131]. The high pressure is always greater than the intermediate pressure ($P_H \geq P_I + 0.5$[bar]). The intermediate pressure is always greater than the low pressure ($P_I \geq P_L + 0.05$[bar]). The selectivity of the adsorbent, $\alpha = H_{CO_2}/H_{N_2}$, is in the range of $3 \leq \alpha \leq 10^7$. It is worth pointing out that the equilibrium constant b_i and ΔU are (at least weakly) correlated. However, in this study, no such constraints are imposed, implying that a hypothetical adsorbent can be defined by any random combination of the five SSL parameters. The training variables are shown along with a visual representation of the MAPLE framework in Fig: 5.1 c). The trained variables consist of five SSL parameters, three pressure levels (P_H, P_I, P_L), the duration of the adsorption step (t_{ADS}), feed velocity (v_F), feed concentration (y_F) and adsorbent particle density (ρ_{ADS}). Recent studies have pointed out that performance gains can be obtained by also varying particle sizes and porosities [33, 128]. In this study, we settle for conservative values of these parameters that are based on commercially available materials. The dataset consisting of 50,000 samples was run in the detailed model. This data was then split into a training and testing ratio of 90:10 and the model accuracy was evaluated using the R^2_{Adj} of the test-set. A network consisting of 3 hidden layers with 30 neuron layers was chosen. A test $R^2_{Adj} \geq 0.99$ was obtained for all the performance indicators, signifying high prediction accuracy. The testing and validation results can be found in Fig S4 of the supporting information. The MAPLE model is then coupled with a genetic algorithm optimization tool non-dominated sorting genetic algorithm-2 (NSGA-2) available in MATLAB for performing all the case studies described below. We call this optimization framework MAPLE-Opt. [142, 144]. For each optimization, an ini-

tial population of 96× [Number of decision variables] is chosen, and MAPLE-Opt. is run for 60 generations. MAPLE-Opt. is run multiple times with varying the initial populations to avoid local minima and or stochastic variations in the final result. The optimized decision variables obtained from MAPLE-Opt. are then re-run in the detailed model until cyclic steady state (CSS) is reached to increase the certainty of prediction. Summarizing, the final results presented in this paper are from a dynamic PVSA model.

5.3 Results and discussions

5.3.1 Limits for US-DOE targets:

In order to compare various technologies, it is important their performance is compared only under conditions where the US-DOE targets are met. One of the continuing questions concerning PVSA processes is the low-pressure (P_{L}) required to achieve these targets. Most studies in the literature that have considered flue gas from coal, i.e., $y_{\mathrm{F}} \approx 0.12 - 0.15$, and have focused on vacuum swing adsorption (VSA), i.e., $P_{\mathrm{H}} = 1$, since pressurizing the flue gas, that consists mainly of N_2, was considered to be expensive. Those that have performed rigorous modelling, and experimentation, indicate that extremely low pressures, i.e., < 0.05 bar, are required to meet the US-DOE target [15, 71]. Quite a few articles have rightfully questioned the feasibility of scaling-up such operations [40]. Most industrial adsorption processes operate at pressures > 0.1 bar; vacuum pump efficiencies deteriorate below this value, and the volumetric flow-rates increase requiring very large piping, valves and equipment. Some studies have suggested that this can be either overcome by pressurizing the flue gas [19] or by using multiple stages [145]. It is also generally believed that the challenge of requiring low vacuum pressures can be overcome by designing an appropriate adsorbent.

In order to explore the question "*If we were able to design a hypothetical mate-*

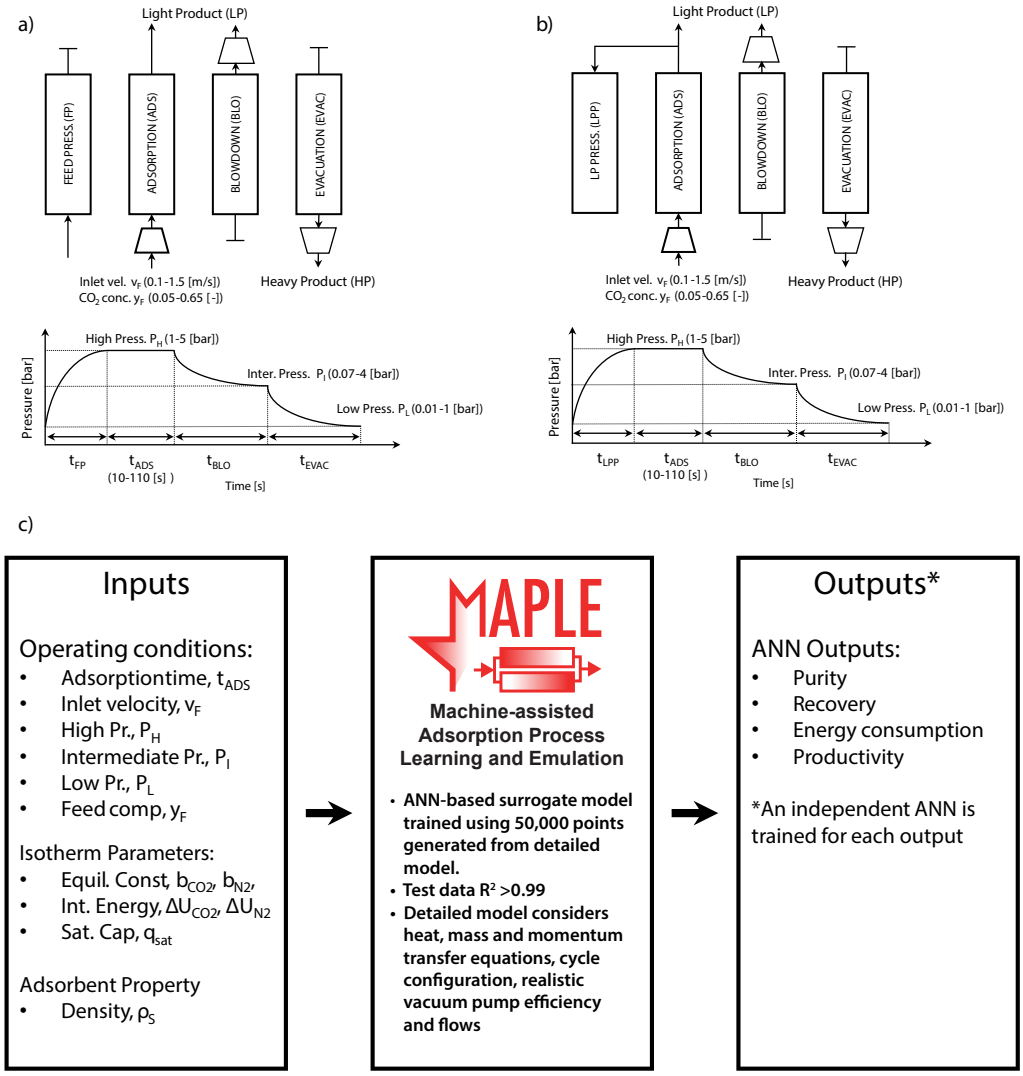

Figure 5.1: Process cycles used in this study a) 4-step with feed pressurization (FP), b) 4-step with light-product pressurization (LPP). c) The key components of the MAPLE framework.

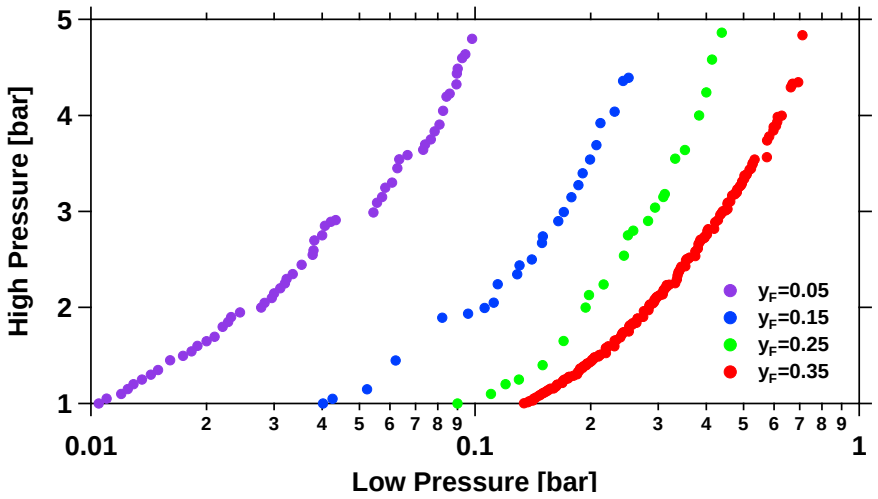

Figure 5.2: Pareto curves obtained from a multi-objective optimization for maximizing low-pressure (P_{L}) and minimizing high-pressure (P_{H}) to achieve US-DOE targets (CO_2 purity $> 95\%$ and recovery $\geq 90\%$)for various feed compositions using the 4-step with LPP cycle. Both operating and isotherm parameters were used as decision variables. The region to the right of each curve is infeasible.

rial, what will be the maximum value of P_{L} *that will allow us to achieve the US-DOE target?*" a series of optimization runs were performed for various values of y_{F} using the 4-step with LPP cycle. For these runs, $Pu_{\mathrm{CO_2}} \geq 95\%$, and $Re_{\mathrm{CO_2}} \geq 90\%$, were considered as constraints. Multi-objective optimization to simultaneously maximize P_{L}, and minimize P_{H} was performed for a variety of y_{F} for the 4 step with LPP process. All material and process variables used for training were considered as decision variables. The resulting Pareto curves are shown in Fig. 5.2. The region towards the right of the Pareto curve is infeasible. For instance, for $y_{\mathrm{F}} = 0.15$, in order to achieve US-DOE targets, a maximum P_{L} of ≈ 0.04 bar is required to be operated as a VSA process. Further if the lowest P_{L} allowed is 0.1 bar, the feed has to be pressurized at-least a value of 1.8 bar. If operation at a higher value of P_{L} is expected, a different cycle should be adopted or an adsorbent whose isotherms are markedly different from a Langmuir form is required. For instance, Khurana and Farooq considered a more complex dual-reflux cycle configuration that could achieve the DOE-Targets at higher P_{L}, albeit at the cost of significantly higher energy [91]. The figure also shows that

even if the flue gas is pressurized upto 5 bar pressure, a vacuum pressure of ≈ 0.2 bar is required to barely satisfy the US-DOE target. This indicates that pressurizing the flue gas should be considered and it might be difficult to avoid vacuum operations. As expected dilute feeds require lower values of P_{L} at any given P_{H}. This study indicates that PVSA processes, merely from the requirement of avoiding deep vacuum, are unfavourable for dilute feeds.

5.3.2 Process limits:

Four case studies were considered to identify the practically achievable performance limits and the results are plotted in Fig 5.3 as a function of y_{F}. Typical ranges of y_{F} (CO_2 composition in the feed stream) for flue gases from natural gas combined cycle (NGCC), coal, cement and steel plants are also highlighted for convenience [146]. For case study 1, the key question posed was "*If one can synthesize ideal hypothetical adsorbents, what are the limits of minimum energy and maximum productivity while satisfying the constraints imposed by US-DOE targets*". Hence, for this study, the optimizer considers all the operating conditions and adsorbent properties, described earlier, as decision variables with an aim to either minimize energy or maximize productivity, with $Pu_{\mathrm{CO_2}}$ and $Re_{\mathrm{CO_2}}$ as constraints. The results are shown in Fig. 5.3 (a) and (b). Each curve in this figure is associated with a label and parameters of the power-law expression fitted to these curves are provided in Table 5.2. Figure 5.3 (a) shows the results of the minimum energy for four different cases: the thermodynamic minimum based on the free-energy of mixing (E1) [147]; the minimum energy for a four-step with LPP with the assumption that vacuum pumps and compressors operate at 100% isentropic efficiency (E2); the minimum energy with the assumption that vacuum pumps and compressors operate with a pressure-dependent efficiency for the cases of a four-step with LPP (E3) and four-step with FP (E4) process configurations. It is important to point out for E2, E3, and E4, each point on the Pareto curves represents a unique combination of adsorbent property and process configu-

ration. As expected, the minimum energy reduces with the increase in y_F. The gap between the thermodynamic minimum and the 100% efficiency gives the limit that can be achieved with the 4-step LPP processes. It is worth noting that at low values of y_F, the ratio of the achievable minimum energy for the 4-step LPP process, and the thermodynamic minimum is significantly larger as compared to the ratio at higher values of y_F. This result demonstrates that PVSA is energetically unfavourable at low y_F, *even if the ideal adsorbent is deployed*. This arises from the need to deploy very low vacuum levels in order to achieve the desired purity and recovery constraints, i.e., a result that is fully consistent with the observation in Fig. 5.2. The gap between curves E2 and E3 indicates the impact of finite prime-mover efficiency. Over the entire range of y_F, the average efficiency of the pumps and compressors varies between $\approx$ 45 to 60%. Finally, the difference between curves E3 and E4 indicates the impact of changing the cycle configuration by just one step. This highlights why a combined search of best process configuration and adsorbent is critical. For the sake of comparison, the reboiler duty of 2.3 GJ/tonne CO_2 captured (at $Pu = 99.8\%$ and $Re = 90\%$) for a commercial absorption process, i.e., CanSOLV, is provided [148]. A reasonable thermal to electrical conversion factor of 40% is used to represent the equivalent energy in electrical units. It can be seen that for $y_F < 0.12$, the PVSA process cannot compete with the CanSOLV process even if the ideal adsorbent can be made. Again, it is important to point out that the energy value of absorption was obtained from an experimental pilot-scale system, whereas all the values for the PVSA processes are considering the "best-possible" scenarios. If pressure drops in the lines, valves are considered, each of the PVSA curves will shift up, and the y_F value at which PVSA can be competitive with absorption will increase. The results of the productivity maximization problem are shown in Fig. 5.3 (b). Since there are no theoretical limits, akin to the thermodynamic minimum, there is no reference to compare the productivity values. Nevertheless, it is interesting to see that the maximum productivity curve corresponding to the 4-step with LPP process (P3) and that

of the FP process (P4) are close to each other at very low values of y_F but show a modest difference at higher feed compositions.

The values of the decision variables corresponding to curves E3 and P3 for a selected set of y_F are shown in Fig 5.4 a) and b), respectively, as a radar plot. Each line on the radar plot represents a unique set of decision variables for the different feed compositions for E3 and P3 shown in the legends. The relative position of the lines on each spoke/radii represents the magnitude/value of that decision variable. For the case of energy minimization, the P_H value remains low, compared to the range over which the optimizer could have chosen. This relates to the fact that pressurizing the feed any more than what is required to meet the US-DOE targets results in higher energy consumption. The values of P_L again are low enough. The feed velocity has converged to a value that is not close to either bound. Increasing the velocity any further results in increased pressure drop in the adsorption step resulting in additional energy consumption. With respect to the material properties, the optimizer converged on values of q_{sat} that were not close to either bound. The N_2 affinity parameter, b_{N_2}, has converged to very low values, reiterating that negligible N_2 adsorption favours lower energy consumption [132, 141]. The CO_2 affinity parameter also puts the isotherms closer to in a linear region. These are also confirmed by the ΔU values that have both converged to the lower bounds. Fig 5.4 b) shows the spider plot for P3. Some salient differences compared to Fig 5.4 a) can be noticed. The P_H values converged at the upper bound, while the P_L values did not go to their minimum. The behaviour of the P_H values is rather understandable as the optimizer tends to maximize the so-called working capacity. However, the behaviour of P_L values highlights a subtle aspect that is associated with the dynamics of the vacuum pump. Since we have assumed a constant volumetric flow of the pump, it is understandable that the pump would need to run longer in order to evacuate a given amount (moles) of the product compared to operation at higher pressures. This results in longer cycle times that act to reduce productivity. The v_F in all cases has now converged at its maxi-

mum limit in-order to increase productivity. It is also worth noting that q_{sat} values have hit the upper bound as the optimizer tries to maximize the working capacity. The corresponding ΔU values consistently converge to their lower bound. The corresponding CO_2 and isotherms are plotted, along with the isotherms of the three real adsorbents, in Fig. 5.4. Since the N_2 affinity in all cases was negligible, its isotherms are not shown. It can be seen that all isotherms are closer to being linear and the capacities for P3 are larger than those for E3. This clearly points to the fact that very nonlinear isotherms are not desired as they adversely affect processes that require low vacuum pressures. These observations are consistent with other studies [91].

In Case study 2, the key question posed was, "*How does the performance of real adsorbents compare to the limits determined in Case study 1?*". Three adsorbents were considered, namely, zeolite 13X (the current benchmark material), IISERP-MOF2, a MOF that was found to provide the minimum energy from an extensive search of the literature [129], UTSA-16, another well-studied MOF that has been known to provide low energy consumption. Each of these materials was fitted to a Langmuir isotherm and was used in the optimization (see Table S3 for parameters). Since the material properties are fixed, only process variables were chosen as decision variables for these optimization runs. Figure 5.3 (c) compares the performance of these three materials with the achievable limit (E3). Of the three, IISERP-MOF2 (E5) performs the best, followed by UTSA-16 (E6) and Zeolite 13X (E7). From the perspective of minimum energy, the difference between the two MOFs is rather marginal. This trend confirms earlier studies that have attributed the superior performance of the two MOFs to their lower N_2 affinities. [129]. The gap between E3 and E5 can be considered as the innovation gap for material development. Within the range $y_{\text{F}} = 0.1$ to $y_{\text{F}} = 0.45$, the difference between the curves E5 and E3 reduces from $\approx 20\%$ to 2.5%. This is an interesting result that shows that in the range of operating conditions at which PVSA may be favourable, i.e., at high y_{F}, the material innovation-gap is very small, indicating that further improvements in material development can be very challenging,

and the focus will need to be on other attributes such as stability, sensitivity to moisture, cost, etc. Figure 5.3 (d) shows maximum achievable productivity for the three materials. The productivity achievable using Zeolite 13X (P7) is very low compared to the others. Unlike the case of energy, where the higher N_2 affinity contributed to the higher energy consumption, in the case of productivity, the impeding factor is the higher non-linearity of the CO_2 isotherm. Vacuum pumps take a longer time to evacuate columns filled with materials that have a nonlinear isotherm and this leads to lower productivity. This is highlighted in Fig. 5.4 d). Further, the innovation gap in terms of productivity shows the opposite trend compared to energy. In other words, at lower values of y_F, IISERP is close to the achievable target, but at higher values of y_F, there seems to be some opportunity to innovate.

In Case study 3, the key question posed was "*How does the recovery constraint affect the achievable limits?*". The CO_2 recovery is a key constraint that can have a major impact on the performance [70]. In this case, the assumption is that all the feed enters the adsorption column, but the process operating conditions can be altered such that the target CO_2 recovery can be achieved. The typical US-DOE requirement is 90%, while for deep-decarbonization scenarios, higher recoveries are desired and if the goal is to reduce the cost of CO_2 capture, lower recoveries might be tolerated. In this case study, the recovery constraint was set at 70, 80 and 95% while maintaining $Pu_{CO_2} \geq 95\%$. The difference between the 95% case (E10) and the 90% case (E3) is much larger than the difference between the 90% (E3) and 80% (E9). This trend is consistent with previous studies which showed that the energy consumption increases exponentially with the recovery [70]. It is also interesting to note that at 95% recovery, the minimum energy limit corresponding to $y_F = 0.15$, i.e., corresponding to flue gas from coal plants is comparable to that of absorption. The productivity limits are shown in Fig. 5.3 (f). The trends are similar to the energy values. High productivity gains can be achieved when the recovery constraint is relaxed from 95 to 90%. Below that, the gains are modest.

In Fig. 5.2, we explored the pressure ranges that will satisfy US-DOE targets. In case study 4, we move a step further and ask "*How does the low pressure affect the performance?*". The achievable energy limits are shown in Fig. 5.3 (g). For this study, we considered three additional lower bounds for the low-pressure, namely, 0.1 bar (E11), 0.25 bar (E12) and 0.4 bar (E13). There is a significant difference between E3 and E11. This arises from the fact that in order to achieve the US-DOE targets, the flue gas has to be pressurized, and the energy consumption for that step is quite high. It is worth pointing out that if we are restricted to $P_{\mathrm{L}} \geq 0.1$ bar, the achievable energy, corresponding to $y_{\mathrm{F}} = 0.18$, exceeds the reboiler energy in absorption. This clearly indicates that PVSA is unlikely to compete with absorption processes for coal-based flue gas, even if the best adsorbent can be synthesized. For the same limit of P_{L}, the maximum achievable productivity (P11) is not markedly different compared to P3. However, constraining P_{L} to even higher values has a marked impact on productivity. The mapping of key decision variables for each case study is provided in the supporting information, along with an MS Excel file with the numerical values.

5.3.3 Adsorbent limits:

The previous sections explored the practically achievable limits, where we solved the inverse problem. In this section, we attempt to explore the forward problem, i.e., how materials properties map to process performance, specifically using the 4-step with LPP cycle. Within the materials properties, we focus our attention on the isotherms of CO_2 and N_2. As seen earlier, the Langmuir isotherms for two components can be described using five parameters. For ease of visualization, we fix three of them. From the inverse problem solutions, we observed that the $|\Delta U|$ for both components reached its minimum limit, and accordingly, we fix them to $|\Delta U_{\mathrm{CO_2}}|$=7 kJ/mol and $|\Delta U_{\mathrm{N_2}}|$=3 kJ/mol. We also fix the q_{sat} values for both components to 6 mol/kg (comparable to those of Zeolite 13X). In this context, the isotherms of the two components can be completely specified by the Henry constants of the two components, $H_{\mathrm{CO_2}}$ and $H_{\mathrm{N_2}}$.

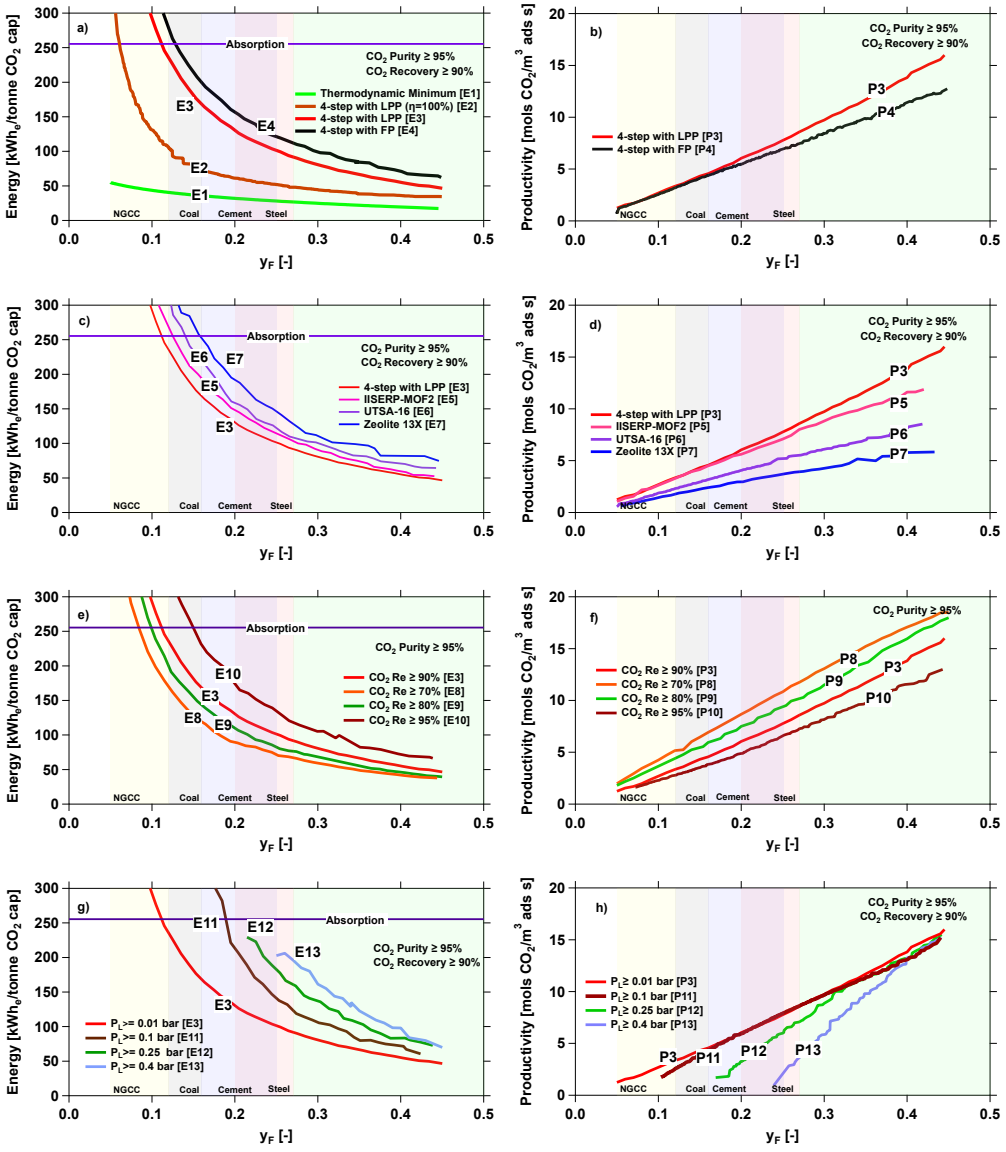

Figure 5.3: Practically achievable performance limits for a variety of case studies. The figures in the left column refer to minimum energy, while those on the right indicate maximum productivity case studies. a) and b) are results from case study 1, where both isotherm and process operating parameters are used as decision variables. c) and d) are results from case study 2, where the aim was to evaluate the performance of some real adsorbents with the 4-step LPP process. Here only operating parameters are used as decision variables. e) and f) are results from case study 3 that explored the impact of CO_2 recovery on the achievable limits with the 4-step LPP process. Here both isotherm and operating parameters were treated as decision variables. g) and h) are results from case study 4 that explored the impact of the low pressure with the 4-step LPP process. Here both isotherm and operating parameters were treated as decision variables. The reboiler duty for adsorption was obtained from the literature [148] and a 40% efficiency was used to convert from thermal to electrical units. Note: 100 kWh_e/tonne CO_2 cap = 0.36 GJ/tonne, 10 mol_{CO_2}/m^3 ads s = 38 tonne CO_2/m^3 ads day

At this point, several combinations of H_{CO_2} and H_{N_2} can be generated and each pair represents a hypothetical material, whose isotherms can be fully reconstructed using the five isotherm parameters. The plot of H_{CO_2} vs. H_{N_2} is called the nonlinearity plot (NLP) as it denotes the nonlinearity of the isotherms [141]. Since the q_{sat} value is fixed, a low value of H_i represents a linear isotherm and a high value denotes a nonlinear isotherm. Note that in the NLP, since CO_2 is considered as the stronger component, only the region above the diagonal is feasible. Further, any line parallel to the diagonal represents hypothetical materials with identical selectivities ($\alpha = H_{CO_2}/H_{N_2}$). As expected, the diagonal represents $\alpha = 1$.

Case study 5 concerns the question *"For a fixed composition, what is the practically achievable minimum energy and maximum productivity for each hypothetical material?"*. In this case study, for each material, i.e., a combination of H_{CO_2} and H_{N_2}, the process variables were treated as decision variables, and the objective functions were set to either minimize energy or maximize productivity, both subject to US-DOE targets. The results are depicted in the NLP, as shown in Fig. 5.5 (a) and (b) for $y_F = 0.15$. The region denoted by the grey dots was explored, but the optimizer was not able to fulfil the US-DOE constraints. Within the range of values where feasible conditions were found, many interesting observations can be made. First, materials with fixed values of α do not result in identical performance. For instance, consider materials with $\alpha = 1000$. At the bottom left, we have a region where the US-DOE targets are not met, then we pass through a region where the separation is feasible, but the energy consumption is high, then a region where energy consumption reduces, and then another region where the energy increases. Finally, we are back in a region where the US-DOE targets are not met. A very similar trend is observed when considering productivity values. This clearly indicates that the selectivity, which is often used as a parameter to screen materials, does not provide a good correlation to the process performance. Second, the behaviour described here can be rationalized by understanding that in the bottom left of the NLP, it is not possible to achieve separa-

tion because of the low CO_2 affinity and at the top right of the figure, the limitation comes from the high N_2 affinity. Hence, it is clear that, even at a fixed value of α, there is an optimal value of H_{CO_2} and H_{N_2} where the energy is minimized (or the productivity is maximized). Now, let us consider traversing along a path where H_{N_2} is fixed, say at $H_{N_2} = 10^{-4}$ m^3/kg. Close to the diagonal, there is a region where the targets are not achieved. As we move up, i.e., as H_{CO_2} increases, we traverse through a region where the energy is first high, then decreases, and finally increases again. In other words, the energy goes through a minimum with H_{CO_2}. Similarly, when considering Fig. 5.5 b, the productivity goes through a maximum. At lower values of H_{CO_2}, the separation is challenging and hence very high values of energy need to be spent. Beyond the minimum, as the Henry constant increases, the isotherm becomes more nonlinear, and since the operating pressure range is fixed (as it would be in a real process), the working capacity decreases. This translates into poorer performance. Finally, let us consider points that lie on a constant H_{CO_2} value. As we move from higher values of H_{N_2} to lower values, the performance improves. This observation is consistent with previous observations that pointed to the fact improvement of the performance of materials can be achieved by aiming to reduce N_2 adsorption. Finally, it is also worth noting that within the region where the DOE targets are met, there is a wide variation in the energy consumption, i.e., between $\approx$ 150 to 400 kWh$_e$/tonne CO_2 cap. with the minimum around $\alpha = 1000$ and $H_{CO_2} \approx 0.033$m^3/kg. Interestingly, this region also corresponds to where the maximum productivity is achieved. Hence, from both the energy and productivity perspectives, this region appears to be optimal for $y_F = 0.15$. Note that the IISERP-MOF2 and UTSA-16 are closer to this region, while Zeolite 13X is further away. Comparing their relative performances from Fig. 5.3, the trends seem consistent.

In case study 6, the key question was, *"How does the NLP vary when the feed composition is changed?"*. Hence, the optimization reported in Fig. 5.5 (a) and (b) was repeated, now for feed compositions of 0.25. The results are shown in Fig. 5.5 (c)

and (d). All the qualitative trends observed in Fig. 5.5 (a) and (b) are also observed when the feed composition is increased. However, it is worth noting that the region of feasible separation is now, understandably, enlarged. Note that the energy values are much lower, and the productivity values are higher compared to the results for $y_F = 0.15$. Finally, the energy and productivity landscape seems to be much shallower compared to the case of $y_F = 0.15$. In other words, a much broader range of H_{CO_2} and H_{N_2} values result in comparable values of energy (or productivity) than the case of $y_F = 0.15$. The corresponding values of P_H and P_L, for each hypothetical adsorbent is provided in Figs. S5 and S6 of the supporting information.

5.3.4 Perspective:

This study shows that it will be challenging for PVSA processes to out-compete established absorption-based processes when CO_2 composition in the feed is below $y_F = 0.15$. At higher feed compositions, PVSA seems to have a clear opportunity to offer lower energy consumption compared to absorption, with the possibility of operating at practical vacuum conditions. However, in this range, the innovation gap between existing materials to the hypothetical best in terms of energy is marginal. It is worth noting that this study considers PVSA processes using beaded adsorbents that follow a Langmuir isotherm. While these can be considered as limitations, it is worth pointing out that most current work on material development can be reasonably captured within these assumptions. Hence, we argue that the results of this study can have broad implications for both adsorbent and process development. It is also important to note that the ability of an adsorbent is not just dependent on its ability to concentrate CO_2 from N_2. Other factors, including, but not limited to, stability, inertness to impurities and moisture, and structurability, play a critical role, and the optimal adsorbent is often a compromise of many parameters. Nevertheless, this work provides broad guidelines on what practical limitations exist and where future research could be focused on. While we have considered only performance metrics in

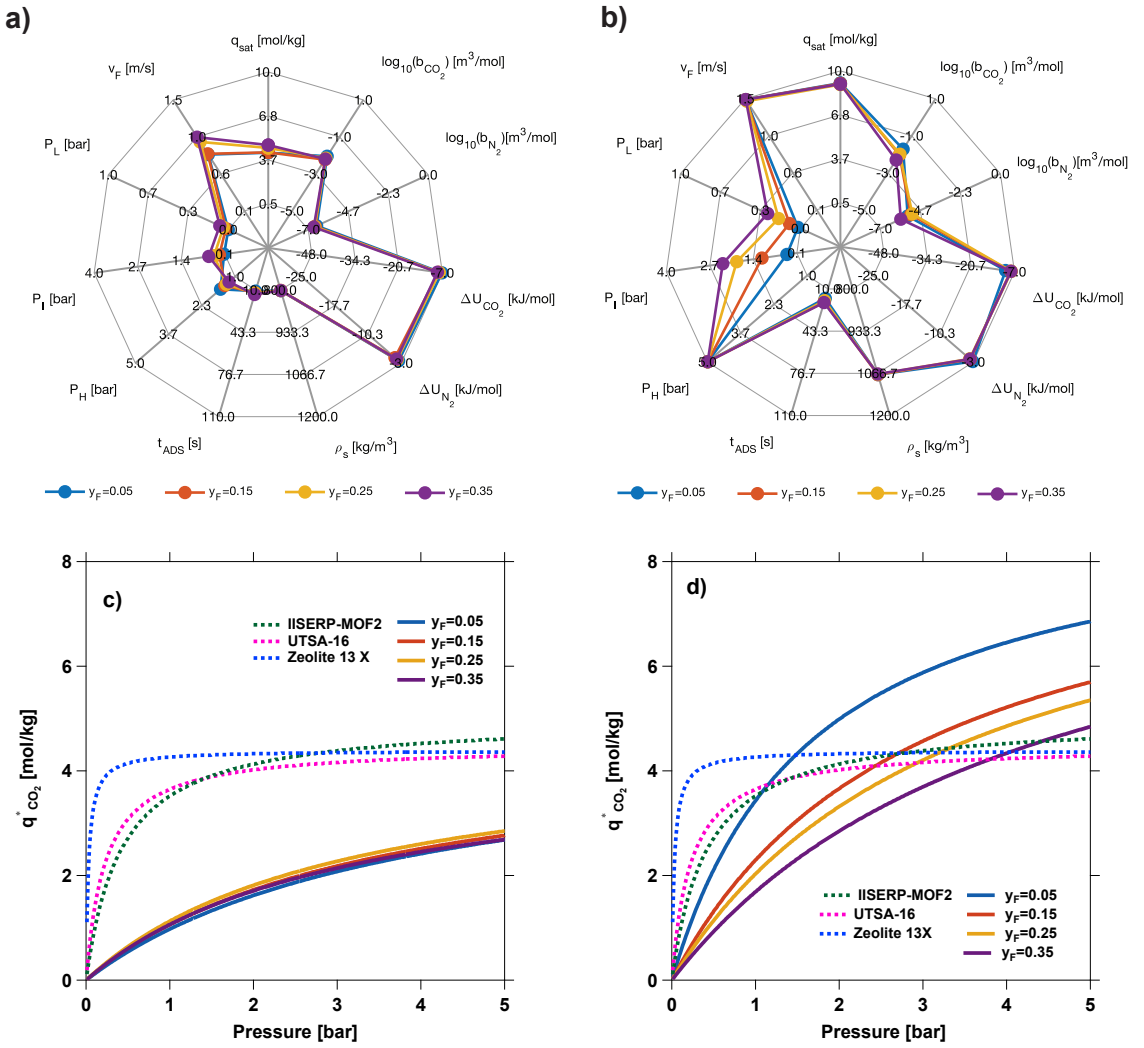

Figure 5.4: Mapping of decision variables corresponding to curves E3 and P3in Fig. 5.3. a) Radar plot of decision variables corresponding to minimum energy (i.e., curve E3 in Fig 5.3), and b) Radar plot of decision variables corresponding to maximum productivity (i.e., curve P3 in Fig 5.3). c) and d) show the isotherms of CO_2 (and N_2, its very low) corresponding to isotherm parameters shown in a) and b). The plot of the isotherms shown in a) and b) along with those of the three real adsorbents studied are shown in sub-figures c) and d), respectively.

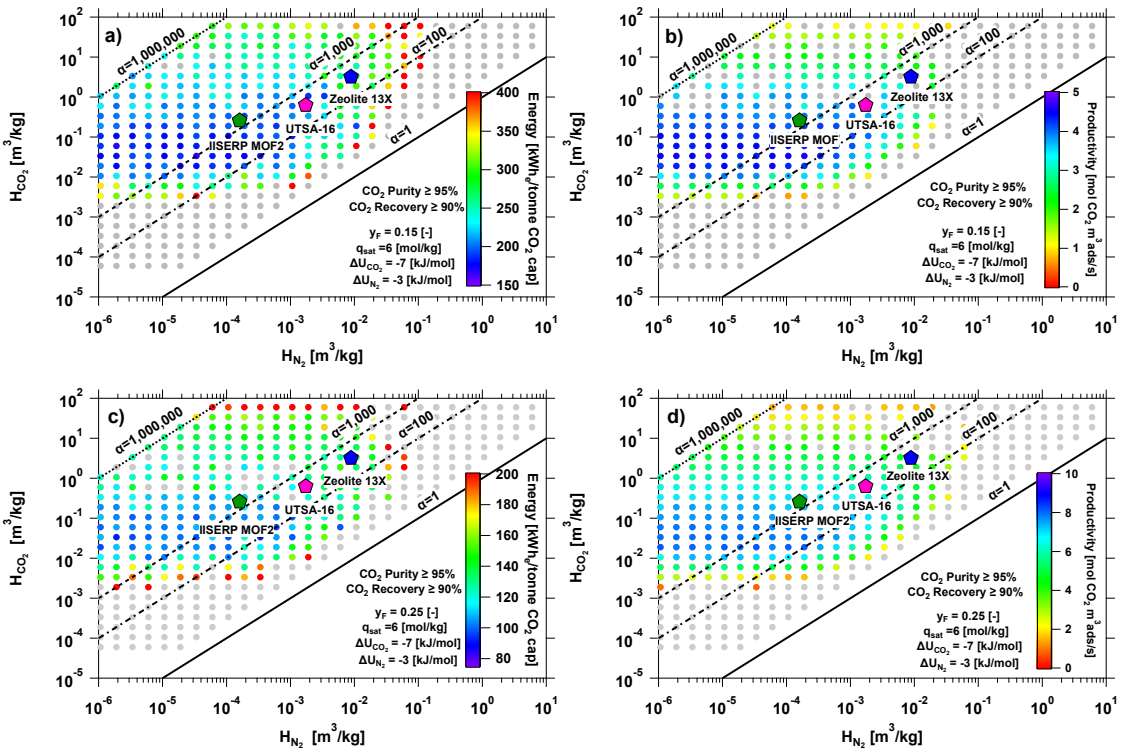

Figure 5.5: The impact of adsorption isotherm on process performance. The subplots a) and c) show minimized energy, while b) and d) show maximized productivity of the 4-step with LPP cycle. For each combination of $H_{\mathrm{CO_2}}$ and $H_{\mathrm{N_2}}$, the process operating conditions are optimized to either minimize energy or maximize productivity. The diagonal lines on the plot represent the lines of constant selectivity, the symbols correspond to the adsorbents used in this study as a reference. Note that the isotherm parameters for these materials are provided in the supporting information. The results are shown for two different feed compositions $y_{\mathrm{F}} = 0.15$ (top row), $y_{\mathrm{F}} = 0.25$ (bottom row)

this work, challenges in scaling-up the processes especially for treating large flue gas volumes should not be underestimated [143]. We have to caution the reader not to extrapolate the conclusions made here for other adsorption separation processes, e.g., TSA, since they operate on very different principles. Finally, the study reiterates the need for synergistic development of processes and materials and highlights the possibilities that could arise through the use of machine learning tools.

Parameter	Type	Value
Column properties		
Bed length, L [m]	Fixed	1.0
Column inner radius, r_{in} [m]	Fixed	0.14
Column outer radius, r_{out} [m]	Fixed	0.16
Particle voidage, ϵ_{p} [-]	Fixed	0.35
Particle radius, r_{p} [m]	Fixed	1×10^{-3}
Density of the column wall, ρ_{w} [kg m^{-3}]	Fixed	7,800.00
Bed voidage, ϵ [-]	Fixed	0.37
Tortuosity factor, τ [-]	Fixed	3.00
Fluid properties		
Effective heat conduction coefficient, K_{z} [J m^{-1} s^{-1} K^{-1}]	Fixed	9.03×10^{-2}
Thermal conductivity of the wall, K_{w} [W m^{-1} K^{-1}]	Fixed	16.00
Inside heat transfer coefficient, h_{in} [W m^{-2} K^{-1}]	Fixed	0.00
Outside heat transfer coefficient, h_{out} [W m^{-2} K^{-1}]	Fixed	0.00
Gas specific heat capacity, $C_{\text{p,g}}$[J kg^{-1} K^{-1}]	Fixed	1010.60
Adsorbed phase specific heat capacity, $C_{\text{p,a}}$ [J kg^{-1} K^{-1}]	Fixed	1010.60
Adiabatic constant, γ [-]	Fixed	1.40
Universal gas constant, R_g [m^3 Pa mol^{-1} K^{-1}]	Fixed	8.314
Fluid viscosity, μ [kg m^{-1} s^{-1}]	Fixed	1.72×10^{-5}
Molecular diffusivity, D_{M} [m^2 s^{-1}]	Fixed	1.60×10^{-5}
Adsorbent properties		
Adsorbent specific heat capacity, $C_{\text{p,s}}$ [J kg^{-1} K^{-1}]	Fixed	1070.00
Density of the solid particle, ρ_{s} [kg m^{-3}]	Variable	800.00-1200.00
Adsorption saturation capacity, q_{sat} [mol kg^{-1}]	Variable	0.50 to 10.00
Adsorption equilibrium constant of CO_2, b_{0,CO_2} [m^3 mol^{-1}]	Variable	10^{-12} to 10^{-1}
Adsorption equilibrium constant of N_2, b_{0,N_2} [m^3 mol^{-1}]	Variable	10^{-11} to 10^{-1}
Internal energy of adsorption of CO_2, ΔU_{CO_2} [kJ mol^{-1}]	Variable	-7.00 to -47.00
Internal energy of adsorption of N_2, ΔU_{N_2} [kJ mol^{-1}]	Variable	-3.00 to -25.00
Process properties		
Feed temperature, T_{F} [K]	Fixed	298.15
Blowdown step vacuum pump flow-rate, v_{BLO} [m s^{-1}]	Fixed	0.59
Evacuation step vacuum pump flow-rate, v_{EVAC} [m s^{-1}]	Fixed	0.90
Pressurization step exponential pressure history term, α_{PRESS} [s]	Fixed	0.50
Vacuum pump efficiency, η [%]	Variable	$\frac{15.84P}{1+19.8P}$
Adsorption step time, t_{ADS} [s]	Variable	10.00 to 110.00
High pressure, P_{H} [bar]	Variable	1.00 to 5.00
Intermediate pressure, P_{I} [bar]	Variable	0.07 to 4.00
Evacuation pressure, P_{L} [bar]	Variable	0.01 to 1.00
Feed rate, v_{F} [m s^{-1}]	Variable	0.10 to 1.50
CO_2 feed composition, y_{F} [-]	Variable	0.05 to 0.65

Table 5.1: Parameters used for detailed model simulations. Those indicated as variable are used for training the MAPLE framework and used as decision variables.

Curve #	**Constraints** $[Pu_{CO_2}/Re_{CO_2}]$	α	β
E1	95/90	14.590	-0.458
E2	95/90	11.669	-1.078
E3	95/90	19.594	-1.182
E4	95/90	21.723	-1.186
E5	95/90	20.301	-1.235
E6	95/90	23.645	-1.119
E7	95/90	25.097	-1.262
E8	95/70	14.286	-1.170
E9	95/80	15.013	-1.230
E10	95/95	22.046	-1.297
E11	95/90	16.725	-1.554
E12	95/90	19.096	-1.616
E13	95/90	15.896	-1.923
P3	95/90	40.185	1.159
P4	95/90	32.633	1.115
P5	95/90	33.760	1.136
P6	95/90	21.734	1.257
P7	95/90	15.388	1.040
P8	95/70	43.780	1.014
P9	95/80	42.668	1.089
P10	95/95	33.558	1.186
P11	95/90	47.347	1.335
P12	95/90	72.070	1.799
P13	95/90	152.800	2.694

Table 5.2: The data from the fitting of the various optimizations cases discussed in Fig. 5.3 to performance indicator (PI), PI $= \alpha e^{\beta y_F}$. Energy values are in (kWh_e/tonne CO_2 cap) and productivity values are in (mol_{CO_2}/m^3 ads s). These fits are valid for values of y_F between 0.05 and 0.45. However for the cases of E11, E12, E13, P11, P12, P13, the applicable ranges are provided in Fig. 5.3

.

Chapter 6

Experimental validation of MAPLE: an adsorbent agnostic neural network VSA model

6.1 Introduction

Modelling adsorption processes accurately and predicting process performance at steady-state conditions is computationally expensive due to its inherent cyclic nature. Hence simulating these processes *in-silico* or in-process optimization or screening large databases of adsorbents is a challenge [40, 135]. To understand gaps in knowledge, such as how adsorption equilibria affect the final performance, or identifying the optimum operating conditions for a given adsorbent using detailed process models becomes computationally challenging. In this work, we exploit recent innovations in machine learning to accelerate adsorption process simulations [72, 73, 135].

Recently, a generalized data-driven surrogate model based on a deep neural network: the machine-assisted adsorption process learning and emulation (MAPLE) framework, was shown to fully emulate an adsorption process cyclic steady state [142]. The training data was generated using a detailed 1D finite volume model with inputs generated by using a Latin Hypercube (LHC) sampling. The model has multiple inputs such as step times, pressures, Langmuir parameters, particle density and can predict outputs such as product purity, recovery, energy, and productivity. As such,

the model is trained to be adsorbent agnostic so that it can predict the performance of the cycle for a set of arbitrary adsorbent and process parameters [142]. The main advantage of this approach is that once trained. It can be used for applications such as adsorbent screening, predictive control, targeted optimizations, etc. In previous studies, we have validated the framework using numerical simulations and demonstrate its advantages [142, 149]. In this work, we provide the experimental validation for the concentration of O_2 from air.

Traditional large-scale air separation processes in the chemical industry are based on the cryogenic distillation process [2, 94, 150]. At a smaller scale range, where the need is only O_2 at purities above 90%, air separation is performed using PVSA processes. They can separate O_2 at relatively wide range, from small scales ranging from 5 LPM personal O_2 concentrators to 300 TPDO O_2 generation units [17]. The current benchmark adsorbent for this separation is zeolite-based such as LiX, CaX, and 13X. The process cycle used to perform this separation is usually a Skarstrom cycle or some modification of the same [2, 17, 94, 151].

In this work, the MAPLE model is trained for a Skarstorm cycle suitable for raffinate purification in a VSA process. To test the efficacy of the model, a case study of air separation to produce high purity O_2 is considered. Two commercial adsorbents, JLOX LiX and UOP−HP Zeolite 13X were chosen for validation. A series of characterization experiments allowed the description of the isotherms of N_2, O_2 and Ar on these adsorbents. Their Langmuir isotherm parameters were taken as the input to the MAPLE model. Multi-objective optimizations to maximize purity, recovery, the productivity of the process for each of these adsorbents were performed by coupling MAPLE with an optimizer [144]. Several points on the Pareto curves were chosen, and the corresponding operating parameters were translated into experiments on a two-column lab-scale PSA rig [36]. This study paves the path for the reliable use of the MAPLE framework for process optimization, predictive control and screening adsorption performance.

6.2 Adsorbent Equilibria

Two commercial adsorbents: JLOX 103, which included lithium exchanged zeolite manufactured by JALON corporation, China and a zeolite 13X sorbent UOP HP was used. As a first step, the adsorption equilibria of the adsorbents for the three gases considered were measured using a Micrometrics ASAP 2020C volumetric system for N_2, O_2, and Ar. The detailed measurement procedure can be found in our previous work [110]. In this study, we use a constant-selectivity single-site Langmuir (SSL) isotherm to describe the competitive adsorption equilibrium:

$$q_i^* = \frac{q_{\text{sat}} b_i C_i}{1 + \Sigma_i b_{\text{i}} C_i} = \frac{H_i C_i}{1 + \Sigma_i b_{\text{i}} C_i}, , \ i = \text{N}_2, \text{O}_2, \text{Ar} \tag{6.1}$$

Here q_{sat} is the saturation capacity of the adsorbing gas, b_i is the equilibrium constant for component i, and q_i^* is the equilibrium solid phase loading. The product of q_{sat} and b_i is the Henry constant, H_i. The temperature dependence of the equilibrium constant is described by:

$$b_i = b_{0,i} e^{\frac{-\Delta U_i}{R_g T}} \tag{6.2}$$

Here ΔU_i is the internal energy of adsorption for component i, R_g is the universal gas constant and, T is the temperature. For the three components, the SSL isotherm comprises of seven parameters, namely, q_{sat}, b_{0,O_2}, b_{0,N_2}, $b_{0,\text{Ar}}$, ΔU_{O_2}, ΔU_{N_2}, and ΔU_{Ar}. These parameters were fitted to the experimental measured data using non-linear regression. The q_{sat} values are fit to the strongest of the three component, namely, N_2, and was fixed to be a constant for O_2, and Ar. The equilibrium data along with the fitted isotherms are shown in Fig. 6.1. The SSL shows an excellent fit of the experimental data. The fitted isotherm parameters are provided in Table 6.1. A quick estimate of the the N_2/O_2 defined as:

$$\alpha_{i,j} = \frac{H_i}{H_j} \tag{6.3}$$

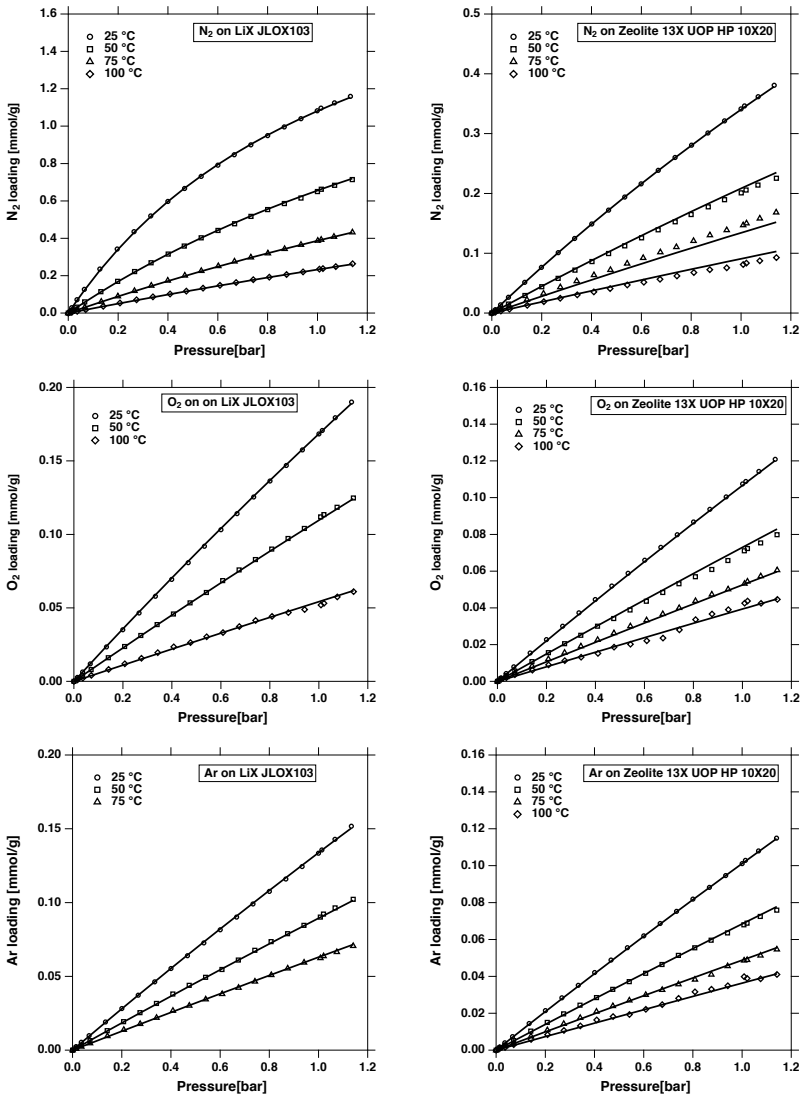

Figure 6.1: Characterization of adsorption equilibria. The left column are the isotherms for LiX, and the right column are the isotherms for 13X. The symbols are experimentally measured values and the lines are the SSL fit.

shows that LiX, to be a superior adsorbent when compared to 13X, an observation that is well documented in the literature. for instance $\alpha_{N_2,O_2}|_{LiX} \approx 12$ and $\alpha_{N_2,O_2}|_{13X} \approx 3$

6.3 Experimental System and process cycle

In this work, VSA experiments were carried out in a two-bed lab-scale system, the process schematic of which is shown in Fig. 6.2 a). It consists of two 300 cc stainless steel columns ($\approx$ 18 cm length and 2.52 cm diameter). Each column was packed with $\approx$ 200 g of adsorbent. The bed voidages for the LiX case was estimated to be $\approx$ 0.42, and 13X = 0.41. The average particle size (r_p) of the LiX $\approx 1.5 \times 10^{-3}$, 13X $\approx 0.8 \times 10^{-3}$[m]. The particle density used in the study for LiX is 1100 [kg/m^3], 13X: 1050 [kg m^{-3}]. The particle voidage, (ρ_P) for LiX was assumed to be 0.65, and 13X = 0.5. A vacuum pump (Pfeiffer Vacuum MVP 040-2, Germany) was used to operate the unit at sub-ambient pressures. Appropriate flow meters and flow controllers (Alicat Scientific, Tucson, AZ, USA) were used to measure and control the gas flows, and the mass-flow controllers have a maximum flowrate rating of 10 SCCM. An oxygen analyzer (Quantek Instruments, Model 906A, USA) was used to measure the outlet O_2 composition. The composition of the extract product is measured using a mass spectrometer (MS, Pfeiffer Vacuum OmniStar GSD 320, Asslar, Germany). One thermocouple located at 16 cm from the column inlet was used to obtain the transient temperature histories. A metering valve (MV-1) is placed between the light reflux line to maintain the pressure of the donor column in the coupled light-reflux step. The VSA experiments were conducted using certified premixed cylinders containing air consisting of 20.5 mol% O_2, 78.5 mol% N_2, and 1 mol% N_2. The VSA experimental rig includes O_2 sensors to collect O_2 composition at the raffinate ($z = L$) and extract ($z = 0$) end of the column. All experiments were run for 100 cycles, although the cyclic steady state was reached, $\approx$ 25 cycles.

6.4 Process cycle

The VSA process used in this study, A 4-step cycle with light product reflux (LR) and feed pressurization (FP), is shown in Fig. 6.2 b). This is popularly known as the Skarstrom cycle and consists of the following steps:

- An adsorption step, where the feed mixture consisting of synthetic dry air is introduced at the feed end ($z = 0$) of the column with an interstitial feed velocity v_{F} and pressure P_{ATM}, for a period of t_{ADS}. The light product, which is predominantly O_2, is collected at the outlet end ($z = L$).

- A light reflux donor (D) step, where the outlet stream from the adsorption step, is used to purge the column in the light reflux receiver (R) step.

- An evacuation step, where a vacuum pump reduces the pressure to a value, P_{L} at the feed end ($z = 0$) and column is regenerated to remove the adsorbed N_2.

- A light reflux(R) step, where a portion of the product from the light reflux donor (D) step is directed to purge the column, which is maintained at P_{L}. This step helps to remove the N_2 adsorbed on the bed and keep the product end of the column filled with high purity O_2.

- A pressurization step, where the pressure of the column is brought back from the P_{L} to P_{ATM} using the feed stream (FP) at the same flowrate as the adsorption and light reflux (D) steps.

Zeolite Type	Gas	q_{sat} [mol/kg]			b_0 [m^3/mol]			ΔU [kJ/mol]		
		Value	95%-	95%+	Value	95%-	95%+	Value	95%-	95%+
13X	N_2	2.471	2.051	2.871	9.35×10^{-6}	1.19×10^{-5}	7.38×10^{-6}	-14.96	-15.59	-14.34
LiX	N_2	2.279	2.247	2.311	1.44×10^{-6}	1.60×10^{-6}	1.30×10^{-6}	-23.85	-24.13	-23.57
13X	O_2	2.471	2.051	2.871	2.02×10^{-5}	2.21×10^{-5}	1.84×10^{-5}	-9.92	-10.16	-9.675
LiX	O_2	2.279	2.247	2.311	1.69×10^{-5}	1.77×10^{-5}	1.61×10^{-5}	-11.71	-11.84	-11.58
13X	Ar	2.471	2.051	2.871	1.67×10^{-5}	1.78×10^{-5}	1.57×10^{-5}	-10.25	-10.41	-10.09
LiX	Ar	2.279	2.247	2.311	6.38×10^{-5}	7.01×10^{-5}	5.79×10^{-5}	-7.801	-8.043	-7.56

Table 6.1: Single site Langmuir isotherm model fitting parameters for three gases, namely, N_2, O_2, and Ar along with the 95% confidence interval from the isotherm fitting.

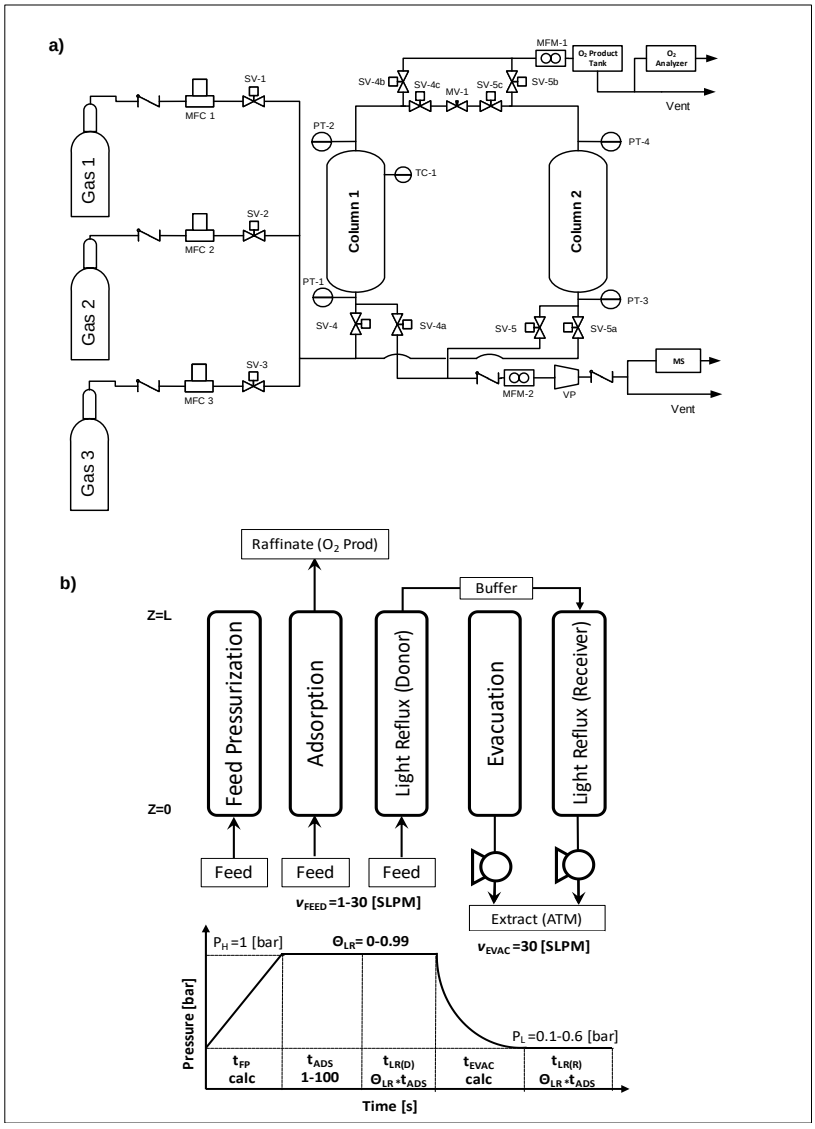

Figure 6.2: Experimental set-up and cycle studied (a) Schematic diagram of the bench-scale VSA test apparatus. (b) Illustration of the 4-step cycle with LPP. Note that the thermocouple TC-1 is at 17 cm from the column inlet.

6.5 Performance Indicators

At a process scale, four performance indicators, O_2 purity (Pu_{O_2}), O_2 recovery (Re_{O_2}), and process productivity Pr, are considered. The experimental purity was calculated as the moles of O_2 in the product tank over the total number of moles in the product tank. The experimental recovery was calculated as the number of moles of O_2 in the product tank over the total number of moles feed into the bed in the pressurization,

adsorption, and light reflux steps. The experimental productivity was calculated as the moles of O_2 collected each cycle over the volume of the bed. The cycle-time used to calculate productivity is the sum of the duration of the four steps. The evacuation step has a dedicated vacuum pump that operates at a constant volumetric flow rate, the flow rate of which is fixed at 30 SLPM. This means that the duration of the evacuation (t_{EVAC}) is dependent on the flow rate. This study considers the size of the vacuum pump, and the column dimensions are fixed to be consistent with the experimental rig. Note that the flow rate of the vacuum pump varies with the low pressure. However, it is considered to be fixed for modelling purposes. Finally, the pressure drops in the lines can be detrimental to energy consumption for systems working under vacuum conditions. The pressure drop can result in increased energy consumption and slower evacuation, which will worsen the process performance. In this study, such pressure drops, external to the columns, are considered to be negligible. It is important to consider the results in light of these assumptions.

6.6 VSA Process Modelling

Modelling an adsorbent-based separation process requires a detailed description of mass and heat transfer and fluid dynamics inside the adsorption bed. Since these adsorptive processes are inherently cyclic, the equations describing each step are iteratively solved until a cyclic steady state (CSS). In this study, we fix the column dimensions and the sizes of fluid movers fixed to match the scale of a lab-scale VSA testing rig first described in Perez *et al.*[36]. The model has the following key assumptions: 1. The ideal gas law; 2. An axially dispersed plug flow model describes the flow in the adsorption bed, meaning there are no radial effects; 3. The solid and fluid phases are in thermal equilibrium; 4. Mass transfer is described by a linear-driving force (LDF) model, assuming that the molecular diffusion in macropores controls the mass transfer; 5. Darcy's law is used to describe the pressure drop in the column. It has been shown that this assumption is sufficient for the testing rig used in this

work and for the operating conditions studied. The column mass and energy balances result in a system of partial differential equations (PDEs). The PDEs are reduced to ordinary differential equations (ODEs) systems using a finite-volume scheme. They are solved using *ode23s*, an inbuilt solver in MATLAB. Boundary conditions for the different steps are applied as appropriate. Model equations and boundary conditions are provided in the supporting information. Properties associated with the column are provided in Table 6.2. The entire simulation strategy is detailed in a previous work [19] and validated experimentally both at lab-scale [36] and pilot-scales [75].

6.7 MAPLE Sampling and Training

The MAPLE modelling framework is a data-driven surrogate model trained to emulate an adsorbent process using supervised machine learning [142]. This model is trained for a generalized with both adsorbent and process-related inputs. Once trained, this model can predict VSA process performance instantaneously.

Meaningful constraints while generating the samples were applied such as, N_2 is always the strongly adsorbed gas, i.e. $b_{N_2} \geq b_{O_2} + 0.5$ [m^3/mol]. The heat of adsorption of N_2 is always greater than O_2, i.e., $|\Delta U_{N_2}| \geq |\Delta U_{O_2}| + 1$ [kJ/mol]. The adsorption step duration is longer than the Light reflux duration, i.e., $t_{ADS} \geq t_{LR} + 1[s]$. The purge to feed ratio Θ is defined as the ratio of t_{LR}/t_{ADS}. For the sake of simplicity, the isotherm inputs for Ar are assumed to be the same as that of O_2. While we acknowledge that this can be a limitation, it is worth pointing out that in several adsorbents, as can been seen here, have very similar equilibria for O_2 and Ar. The selectivity of the adsorbent, $\alpha = H_{N_2}/H_{O_2}$, is in the range of $3 \leq \alpha \leq 10^6$. In this study, a hypothetical adsorbent can be defined by any random combination of the five SSL parameters. The inputs and their training ranges are shown in Fig: 6.2 b) and the ranges are provided in Table 6.2.

The trained variables consist of five SSL parameters, the low pressure (P_L), the duration of the adsorption step (t_{ADS}), inlet feed flowrate (v_F), the light reflux step

Parameter	Type	Value
Column properties		
Bed length, L [m]	Measured	0.18
Column inner radius, r_{in} [m]	Measured	0.025
Column outer radius, r_{out} [m]	Measured	0.027
Density of the column wall, ρ_{w} [kg m^{-3}]	Fixed	7,800.00
Tortuosity factor, τ [-]	Fixed	3.00 [31]
Fluid properties		
Effective heat conduction coefficient, K_{z} [J m^{-1} s^{-1} K^{-1}]	Fixed	9.03 $\times 10^{-2}$ [31]
Thermal conductivity of the wall, K_{w} [W m^{-1} K^{-1}]	Fixed	16.00 [31]
Inside heat transfer coefficient, h_{in} [W m^{-2} K^{-1}]	Fitted	8.20
Outside heat transfer coefficient, h_{out} [W m^{-2} K^{-1}]	Fitted	3.00
Gas specific heat capacity, $C_{\text{p,g}}$[J kg^{-1} K^{-1}]	Fixed	1010.60 [31]
Adsorbed phase specific heat capacity, $C_{\text{p,a}}$ [J kg^{-1} K^{-1}]	Fixed	1010.60 [31]
Adiabatic constant, γ [-]	Fixed	1.40
Universal gas constant, R_g [m^3 Pa mol^{-1} K^{-1}]	Fixed	8.314
Fluid viscosity, μ [kg m^{-1} s^{-1}]	Fixed	1.72×10^{-5}
Molecular diffusivity, D_{M} [m^2 s^{-1}]	Fixed	1.60×10^{-5}
Adsorbent properties		
Adsorbent specific heat capacity, $C_{\text{p,s}}$ [J kg^{-1} K^{-1}]	Fixed	1070.00 [31]
Particle radius, r_{p} [m]	Variable	0.25×10^{-3}-2.5×10^{-3}
Bed voidage, ϵ [-]	Variable	0.35-0.45
Density of the solid particle, ρ_{s} [kg m^{-3}]	Variable	800.00-1200.00
Particle voidage, ϵ_{p} [-]	Variable	0.35-0.7
Adsorption saturation capacity, q_{sat} [mol kg^{-1}]	Variable	0.50 to 10.00
Adsorption equilibrium constant of CO_2, b_{0,CO_2} [m^3 mol^{-1}]	Variable	10^{-12} to 10^{-1}
Adsorption equilibrium constant of O_2, b_{0,O_2} [m^3 mol^{-1}]	Variable	10^{-11} to 10^{-1}
Internal energy of adsorption of N_2, ΔU_{N_2} [kJ mol^{-1}]	Variable	-7.00 to -30.00
Internal energy of adsorption of O_2, ΔU_{O_2} [kJ mol^{-1}]	Variable	-3.00 to -25.00
Process properties		
Feed temperature, T_{F} [K]	Fixed	298.15
High pressure, P_{H} [bar]	Fixed	1.00
Evacuation step vacuum pump flow-rate, v_{EVAC} [SLPM]	Fixed	30
Adsorption step time, t_{ADS} [s]	Variable	10.00 to 110.00
Evacuation pressure, P_{L} [bar]	Variable	0.1 to 0.6
Feed flowrate, v_{F} [SLPM]	Variable	1 to 30

Table 6.2: Parameters used for detailed model simulations. Those indicated as variable are used for training the air separation MAPLE framework and used as decision variables.

(t_{LR}), the particle morphology, such as the particle diameters (R_{P}), particle voidage (ϵ_{P}), bed voidage (ϵ_{B}), and adsorbent particle density (ρ_{ADS}). Recent studies have pointed out that performance gains can be obtained by also varying particle sizes and porosities [33, 128]. In this study, we settle for conservative ranges of these parameters based on commercially available materials. The dataset consisting of 20,000 samples was run in the detailed model. This data was then split into a training and testing ratio of 90:10, and the model accuracy was evaluated using the R^2_{Adj} of the test-set. A network consisting of 3 hidden layers with 20 neuron layers was chosen. A test $R^2_{\mathrm{Adj}} \geq 0.99$ was obtained for all the performance indicators, signifying high prediction accuracy. The testing and validation results are shown as a parity plot for the various KPIs in Fig. 6.3. The results from the MAPLE model are comparable with a high degree of accuracy with the detailed model. The MAPLE model is then coupled with a genetic algorithm optimization tool non-dominated sorting genetic algorithm (NSGA-2), available in MATLAB for performing all the case studies described below. We call this optimization framework MAPLE-Opt. [142, 144]. For each optimization, an initial population of $96 \times 4 = 384$ was chosen and was run for 50 generations. The optimization was repeated multiple times by varying the initial populations to avoid local minima and stochastic variations in the final result. The optimized decision variables obtained from MAPLE-Opt. are then re-run in the detailed model and the experimental set-up until cyclic steady state (CSS). This increases the reliability of the entire process. Hence, thus results shown in this work are indeed from the detailed model.

6.8 Results and Discussion

Once trained and tested, the MAPLE neural network model will predict the performance of any adsorbent that agrees with a Langmuir isotherm function in the process. In this study, we are considering two commercial zeolite-based adsorbents, namely, 13X and LiX. The objective is to use the trained model in an optimization framework

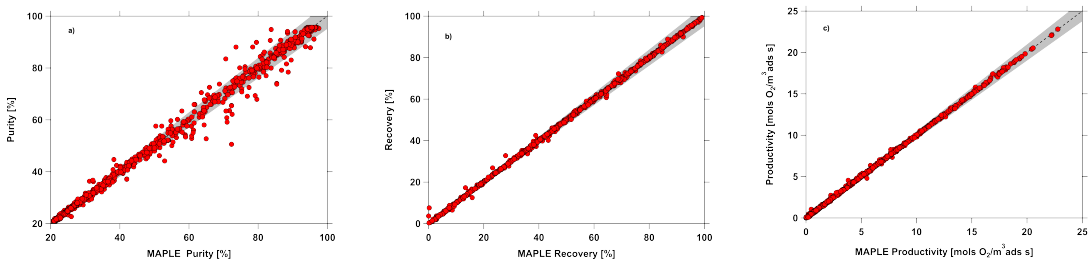

Figure 6.3: The parity plots of the prediction from MAPLE for different performance indicators against those obtained from the detailed model for a test-set of 1000 samples as inputs for the Skarstrom cycle. a) Purity, b) Recovery, c) Productivity. The shaded area indicates a 5% deviation from the diagonal.

to obtain trade-offs of various performance indicators and process variables. The operating conditions obtained from such case studies can be used to target performance in the lab-scale VSA rig described in the previous section. The isotherm inputs for the model are the operating conditions and particle morphology, and the values are provided in Table 6.2.

6.8.1 Purity-Recovery Optimization

One of the vital trade-off when designing an adsorption process are the countering objectives of process purity and recovery. In this case study, we run the optimization to maximize these objectives. The resulting optimization routine (MAPLE-Opt) is run with fixed isotherm and particle parameters to the values of the two adsorbents shown in Table 6.2. The range of the operating parameters like step times, low pressure, and feed rate are also provided in Table 6.2. The resulting Pareto curves for the two materials are shown in Figure 6.4 as solid lines. This curve represents the best possible purity and recovery obtained for the two adsorbents in the given range of operating conditions. The region to the top right of the curves is infeasible for the said adsorbent, and the area below is sub-optimal. The small sample of the operating conditions obtained from the MAPLE Opt was re-run in the detailed model to ensure the accuracy of prediction. It is clear from the plots that the MAPLE model and the detailed model are in excellent agreement with minor deviation in the high purity

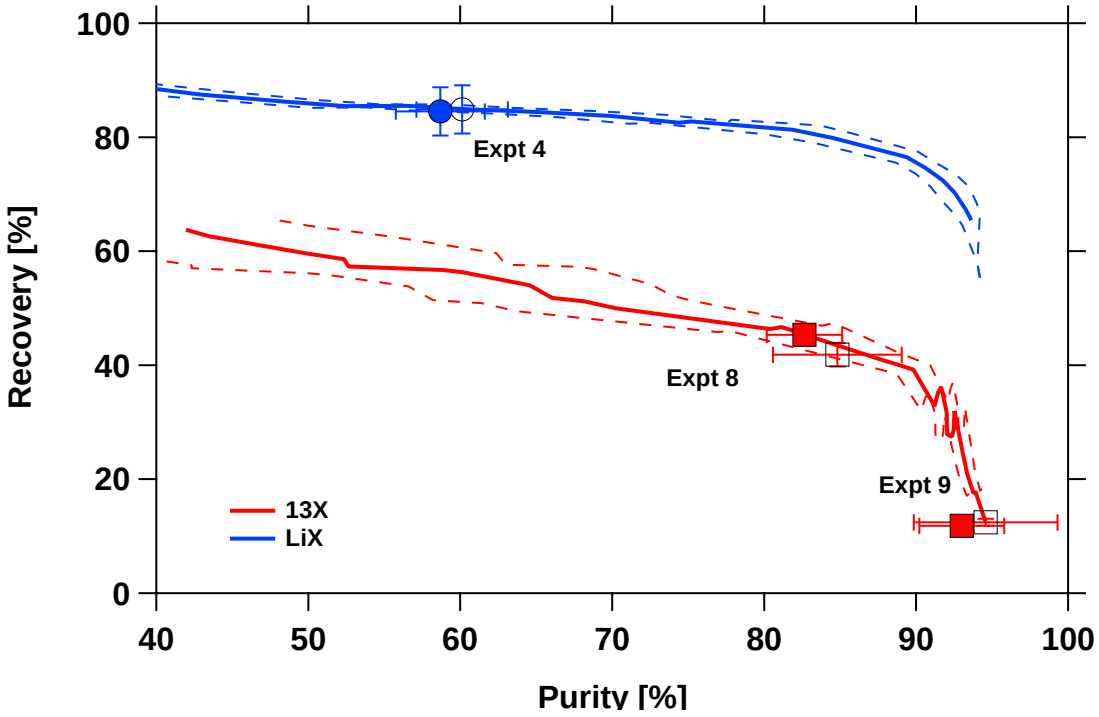

Figure 6.4: Pareto fronts for the multi-objective optimization of purity and recovery of the four-step Skarstrom VSA cycle for the two adsorbents. The solid blue line corresponds to LiX, and the red line corresponds to 13X. The closed symbols represent the purity and recovery obtained from running operating conditions in the experimental rig, and the open symbols the results from the same operating conditions in the MAPLE model. The dashed lines indicate the 95% confidence interval for isotherm parameters.

region. The LiX sorbent outperforms 13X, for a purity $\geq$90% the 13X adsorbent provides the best recovery of 35%, while the LiX sorbent yields 75%.

6.8.2 Purity-Productivity Optimization

The performance indicator, recovery only provides the highest amount of O_2 we can recover and as such only provides us with a potential for separation and may not provide the best conditions to operate the process. To run the process, in reality, one must optimize its productivity, which by definition offers the highest amount of product gas that can be collected per unit adsorbent mass and for unit time. Hence for the second case, we optimize the productivity and purity trade-off. Figure 6.5 shows

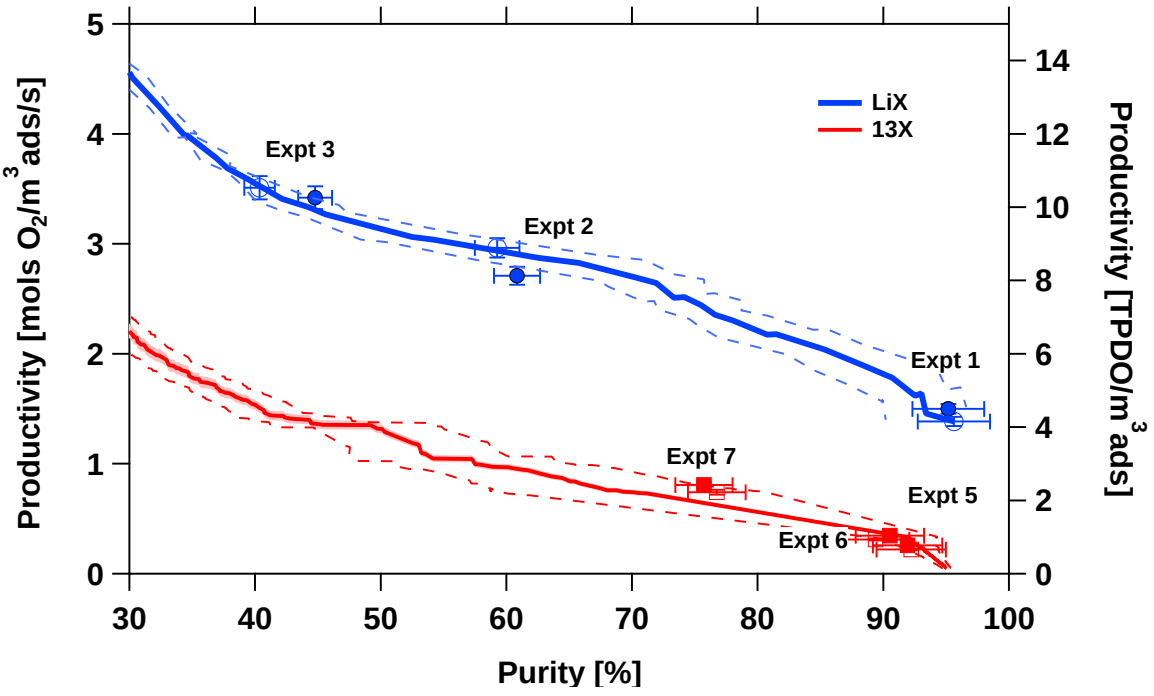

Figure 6.5: Pareto fronts for the multi-objective optimization of purity and productivity of the Skarstrom VSA cycle for the two adsorbents are shown. The solid blue line corresponds to LiX, and the solid red line corresponds to 13X. The closed markers represent the purity and productivity and the open markers the results from the same operating conditions in the MAPLE model. The dashed lines indicate the 95% confidence interval for isotherm parameters

the Pareto curves for the performance indicators of purity and productivity for the two different adsorbents. The trend is very similar to the previous case; however, it is clear from the figure that LiX performs far better than the 13X when considering the process productivity. In fact, in the high purity region, LiX has $\approx 2\times$ the productivity offered by 13X. This trend is again explained by the higher selectivity offered by LiX compared to 13X. The higher loading of N_2 on the LiX allows for the processing of more feed and hence can obtain higher O_2 production capacity. In the previous case study, the inlet flow rate is limited to 10 SLPM in the optimizations since this is the limiting flow rate for the flow controllers in the lab-scale rig. Hence the performance shown in this work is not necessarily the best that the adsorbents can offer, but what can be achieved in the lab-scale rig.

A sensitivity analysis on the Pareto curves was carried out to obtain a 95% confidence interval for the predictions. In this study, the effect of the isotherm fitting parameters was analyzed. To do this, the DVs from the Pareto curves were varied and re-ran as inputs in the MAPLE model. In the first case, only the isotherm inputs were changed to the upper and lower values of the 95% confidence of the SSL fit. The values are provided in Table 6.1. The results were analyzed, and a $\pm 2\sigma$ is plotted around the Pareto curves as dashed lines.

6.8.3 Experimental Validation

This study aims to verify the validity of the MAPLE framework experimentally. This study aims to validate the MAPLE model at different performance regions and to check if the model is truly general and adsorbent agnostic. To this effect, we choose operating conditions obtained from the various cases. Here, the outputs of the optimizer, namely, the decision variables, i.e., the low-pressure values, are programmed into the control system. The inlet flow rate is set in the flowmeter (MFC-2), and was kept the same for the pressurization, adsorption and light reflux(D) steps. Before the start of the experiment, the bed was saturated with the feed composition. The cycle was repeated for 100 iterations for both beds. The outlet flows, and composition was recorded along with the dynamic bed pressure and temperature histories. Integrating the inlet and outlet flows along with provided the purity, recovery, and productivity values.

The resulting experimental performance for the different experimental runs is summarized in Table 6.3. The first four experiments shown are for the LiX adsorbent, and the next five are for the 13X adsorbent system. Expt 1-3 are obtained from the purity productivity optimization for the LiX adsorbent and are shown in figure 6.5 and filled squares. Expt 5-7 are for the 13X adsorbent purity productivity optimizations and are shown as filled circles. The open symbols show the MAPLE model predictions for the same operating conditions. Experiments 4, 8, 9 are obtained from purity recovery

optimizations, Expt 4 is for LiX adsorbent, and Expt 8 and 9 are for 13X adsorbent are shown in figure 6.4. The experimental performance for all three experimental KPIs are in good agreement with the MAPLE model predictions. The results can be visualized with the Pareto curves in Fig 6.4 - 6.5. Variations in performance are expected due to practical challenges and operational variations. The results show an excellent match between the predictions of the MAPLE model and the experiment.

The experimental conditions were simulated in the detailed model to analyze, and the process was simulated dynamically to a cyclic steady state—the simulation results were plotted alongside the experimentally obtained transients. Figure 6.6 a) shows the pressure history over one cycle for all the experiments conducted in Table 6.3, the symbols from experiments, and the solid lines are obtained from the detailed dynamic model. Note that the idle steps needed to schedule the two-bed VSA process are removed in the figure 6.6 to match the simulation. The feed flowrate in the adsorption step, light reflux step, and pressurization step are kept the same in the simulation. The pressure history for the evacuation step is predicted based on a constant volumetric boundary condition and has been shown in previous modelling works [143, 149]. The bottom two panels show the adsorption product outlet flow measured in MFM-1 and the evacuation flow rate measured in MFM-2. Figure 6.7 shows the experimentally obtained purity and recovery are plotted as a function of the number of cycles along with the detailed model predictions for the same. The results show good agreement between the two quantities over the entire duration of the experiment, particularly at CSS. This further validates the detailed model and MAPLE model. The general observation is that the detailed model results and the experimental histories agree with each other.

Adsorbent	Expt	Operating conditions				Experiment			MAPLE Model			Detailed model		
		T_{ads}	T_{LR}	P_L	V_F	Purity	Recovery	Prod	Purity	Recovery	Prod	Purity	Recovery	Prod
		[s]	[s]	[bar]	[SLPM]	[%]	[%]	*	[%]	[%]	*	[%]	[%]	*
LiX	1	11.0	3.0	0.1	9.7	95.2	64.2	1.5	95.6	61.6	1.4	95.2	60.2	1.5
	2	11.0	4.0	0.4	9.8	60.9	65.9	2.7	59.3	69.8	3.0	62.4	70.6	3.2
	3	15.0	4.0	0.4	9.8	44.8	71.3	3.4	40.4	71.6	3.5	44.1	72.4	3.5
	4	23.0	0.0	0.1	6.0	58.7	84.5	1.0	60.1	84.9	0.9	60.6	84.9	1.0
13X		6.0	4.0	0.3	4.5	91.9	27.5	0.3	92.2	26.7	0.2	93.9	27.1	0.4
	6	7.0	5.0	0.3	5.5	90.5	31.3	0.3	89.4	26.2	0.3	93.2	30.5	0.6
	7	6.0	4.0	0.4	6.9	75.7	32.8	0.8	76.8	32.5	0.7	82.3	35.9	1.0
	8	6.0	5.0	0.4	4.3	93.7	12.6	0.1	94.6	12.4	0.1	95.3	12.1	0.2
	9	6.0	3.0	0.2	5.8	82.7	45.3	0.5	84.8	41.9	0.5	85.3	44.0	0.8

Table 6.3: Optimal operating conditions and the measured performance of the VSA experiments, shown alongside the MAPLE model predictions for the same conditions. * the units of productivity are mol_{O_2} / m^3 ads /s.

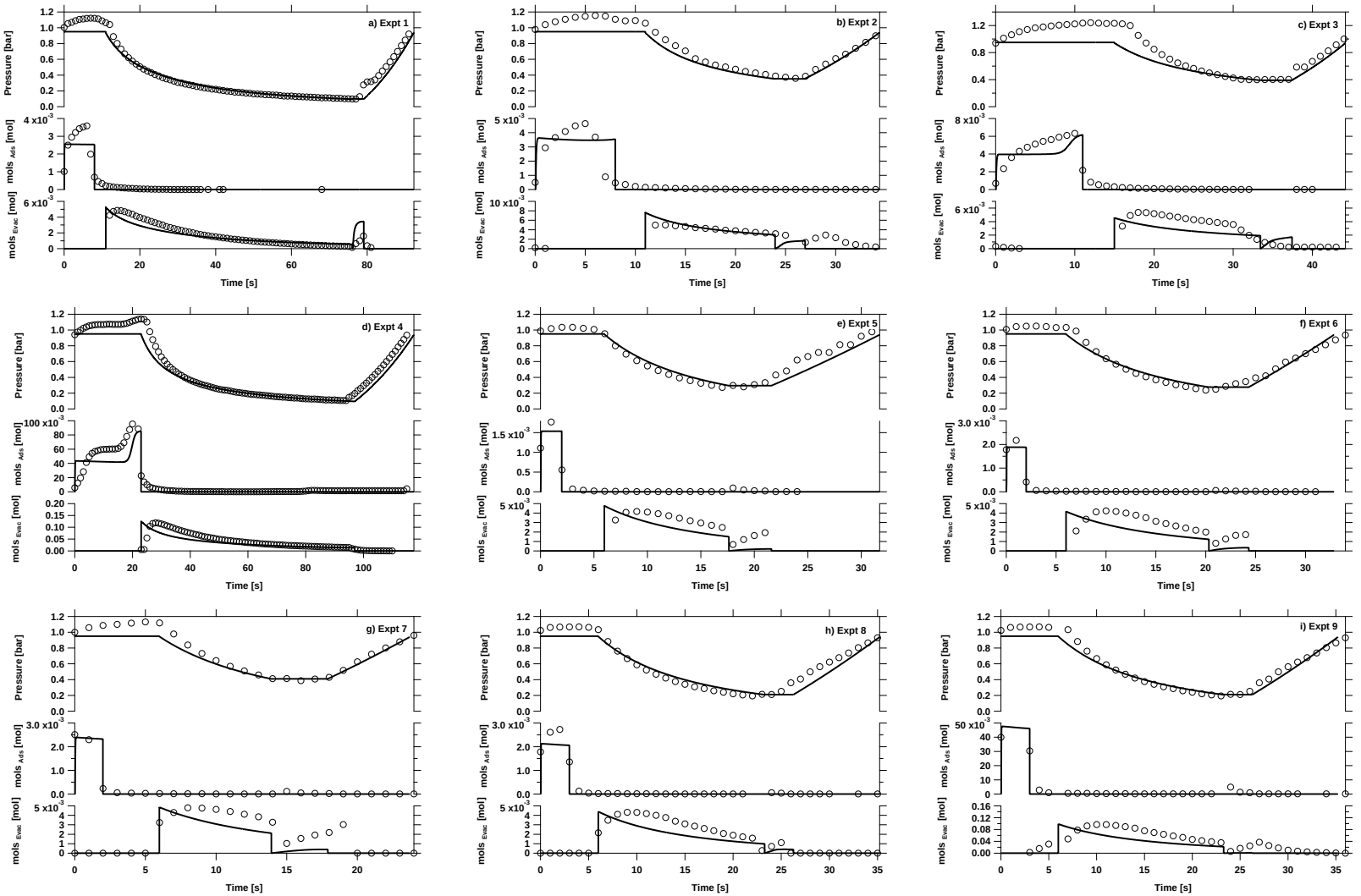

Figure 6.6: Comparison of experimental and simulated transients for the experimental runs. The pressure history for one cycle is shown along with the detailed model results for the same inputs. The middle row and bottom row in each sub figure shows the outlet flow rate of the raffinate and extract product step, respectively. The symbols are from the experimental measurement and the line is obtained from the detailed simulations.

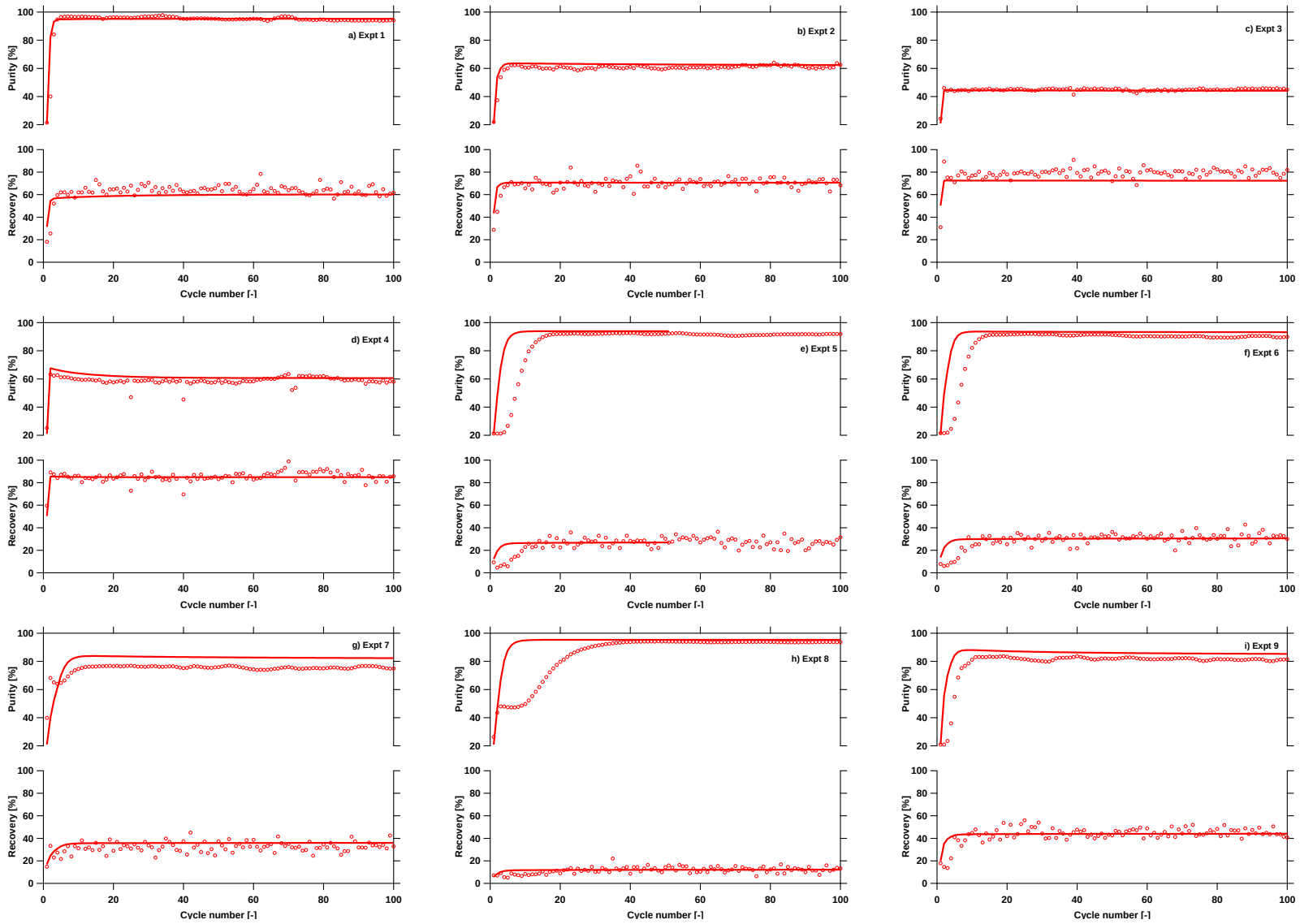

Figure 6.7: Comparison of experimental and simulated values of purity and recovery over 100 cycles for the Skarstrom cycle from dry air. Open markers represent the experimental purity and recovery at each cycle, and solid lines is from the detailed model simulation.

6.9 Conclusions

In this study, the machine-assisted process learner and emulation framework (MAPLE) was trained to learn from data obtained from a detailed model. The detailed model simulated the performance of a lab-scale VSA rig, and the adsorbent inputs were parametrized. A Latin Hypercube sampling strategy was used to sample input data, including operating conditions and hypothetical adsorbent inputs. The trained model is now adsorbent agnostic as it can predict the performance of any given adsorbent at a given operating condition at a cyclic steady state. This was tested by carrying out multi-objective optimizations for various performance objectives for two commercially available adsorbents. The resulting optimized operating conditions for both adsorbents were used as inputs to the experimental lab-scale rig to confirm the predictions. A sensitivity analysis was carried out on the MAPLE model predictions by varying the isotherm fitting parameters and particle morphology—the results were used to construct confidence intervals for the MAPLE model. The experimental profiles were also compared to the detailed model results and fit the histories satisfactorily. Additionally, the experimental performance was matched with the detailed model and MAPLE model results and was comparable.

This study aimed to verify if the adsorbent agnostic model trained with only hypothetical adsorbents could predict, with sufficient accuracy, the performance of a commercial adsorbent. This was shown to be the case for various objectives and at optimized conditions. This study shows that neural network models such as this one can not only be used to predict the performance *in-silico* but can also be used to target specific performance. This work shows an alternative approach to performing expensive and time-consuming experimental runs currently used to optimize process performance. Since these models can be trained for different input conditions such as feed composition or feed temperature etc., coupled with instantaneous prediction, these models can also be used for predictive control in the future.

Chapter 7

Conclusions, Recommendations, & Future Work

7.1 Conclusions

This thesis investigated various aspects of adsorption process design using analytical data-driven techniques such as machine learning and artificial intelligence. The surrogate models obtained from such studies were used to predict, optimize, validate both experimentally and using detailed simulations. In chapter 2, an extensive database of adsorbents was screened, first using GCMC based in-silico prediction of equilibrium characteristics on the adsorbents for CO_2 and N_2 gas. The predictions fit a Langmuir isotherm model and were used as inputs to a detailed experimentally validated finite volume-based model to predict adsorbent performance in a benchmark VSA process. The study required over 32 million core years of computation to optimize and screen over 1500 materials for the case of CO_2 capture from post-combustion flue gas accurately. In addition to this, the data obtained were analyzed using various data-driven techniques to find underlying trends and to find a suitable screening model. A model based on decision trees was shown to have high accuracy in predicting the better adsorbents from the database. A list of twenty-nice adsorption metrics and geometric parameters traditionally reported in the literature of adsorbent screening and showcasing potential in adsorbents was analyzed for predictive capability. It was found that non of the simplified metrics individually or in tandem did not predict the VSA

performance with sufficient accuracy. It was shown that the energy consumption or productivity of CO_2capture with solid sorbents within a VSA system could not be accurately predicted from equilibrium adsorption metrics alone and that full process simulations are required.

In chapter 3, machine learning techniques were tested to accelerate full process simulations and validated with experimental results. In this work, a slew of machine learning and AI algorithms were evaluated for their ability to be used as predictive surrogate models for full VSA simulations. In addition to this, an artificial neural network model was trained to learn the internal bed profiles at cyclic steady-state conditions. This trained model was used to predict the approximate cyclic steady state in an optimization framework to accelerate full model performance. Both the surrogate Opt. and CSS Opt. where shown to decrease the optimization load by a factor of 25×, and 6×, respectively. Additionally, both the surrogate model predictions and the internal bed profiles were validated with lab-scale experimental data.

In chapter 4, an adsorbent agnostic framework was developed using artificial neural networks to emulate a full PVSA process model. This was called the machine-assisted process learner and emulator (MAPLE). The effect of the ANN architecture on prediction accuracy was analyzed to find the best architecture. The accuracy of the trained model was first tested using real-world adsorbents such as Zeolite 13X detailed process simulations. The model was then used in an optimization framework to perform constrained and unconstrained multi-objective process optimizations. The results of MAPLE-based optimizations (MAPLE Opt.) were tested against detailed model-based optimization for various case studies. The modelling and optimization framework was validated using external literature. The modelling framework was shown to learn from data derived from a purely hypothetical set of isotherm and operating conditions and then predict the performance of actual real work adsorbents. This tool can find its application in unsteady processes in nature to simulate, optimize, and screen adsorbents for adsorption-driven processes. This model can also find

applications in dynamic process control and model predictive control of adsorption-driven processes.

In chapter 5, the machine-assisted process learner and emulator (MAPLE) framework to find the practical limits of PVSA based carbon capture. A machine learning-based model was trained to emulate a dynamic PVSA process model. The results highlighted the various gaps in research for PVSA based carbon capture. The study showed that PVSAs need to focus on higher feed compositions for practical implementation and realistic advantages over current benchmarks. The study also optimized the hypothetical best adsorbents for different feed compositions and different constraints, such as recovery and pressures. The results also showed regions on the adsorbent Henry's constant space where the optimum adsorbents lay and showed their isotherm characteristics.

In chapter 6, the experimental validation of the machine-assisted process learner and emulator (MAPLE) framework was tested using a O_2 generation process as a case study. The detailed model was used to generate data using a sampled set of inputs containing hypothetical isotherm inputs and operating conditions for a 4 step with Light reflux and feed pressurization cycle. Two different adsorbents, namely LiX and 13X, were considered for this study. A series of process optimizations were carried out for different objectives for both materials. The optimization results were consolidated, and the operating conditions were used to drive the experimental campaigns. The experimental results obtained were a close match to the generalized MAPLE model predictions. The neural network model was used in an interpretive manner for the first time in literature to visualize the performance landscape of VSA performance for the two adsorbents. The results showed that the adsorbent agnostic MAPLE model is very well suited to target required performance.

7.2 Future Work

In addition, the material databases almost include more than 500,000 structures (both experimental and hypothetical) that can be evaluated for different gas mixtures. Such huge databases can be screened for best performers using machine learning models such as MAPLE. Unsupervised/semi-supervised learning methods can be applied to classify the databases' materials into different clusters and know the underlying patterns/distributions within the databases.

Further, supervised learning techniques can be used to map the structures and material properties without the associated computational burdens of solving physical models. Models like MAPLE can generate computationally cheap process data that allows the process designer to investigate the structure to process performance relationship. A large amount of data generated during the process design is hard to analyze since it is unstructured and unbalanced. Semi-supervised/unsupervised algorithms can be utilized on unlabeled, unstructured data to find causal relationships between the inputs and the final performance. Clustering algorithms can reduce the high dimensionality of the inputs to reduce human intervention during sampling. Large-scale adsorbent screening requires robust and fast optimization algorithms to overcome issues such as local minima, etc. An area of further exploration could be to test various optimization algorithms such as coordinate search or PSO to find a more robust framework. The adsorbent agnostic framework can also be used in steady-state process models to perform plant-wide optimization and explore hybrid concepts, which were previously computationally restrictive.

In adsorption-driven carbon capture, the presence of water and other impurities may affect the final process performance. Thus, the inclusion of water and other gases in models becomes very important. Modelling water in detailed process models increases the computations load of the detailed models. Models like MAPLE and CSS Opt. can reduce the computational load of such complex simulations. With a

fast CSS initialized detailed modelled, these studies could be carried out with relative ease and with a high degree of accuracy. The identification and prediction of cyclic steady-state profiles can predict new process cycles if sufficient data is collected. Learning from bed profiles and hybrid AI modes also leads to the possibility of cycle agnostic neural networks that create new and novel cycle sequences. Finally, neural networks could correctly target optimized conditions to avoid expensive experimental campaigns to optimize the process. This leads to the possibility of digital twinning of the PSA process and predictive model control of unsteady-state processes.

Bibliography

[1] D. M. Ruthven, *Principles of adsorption and adsorption processes*. New York: John Wiley, 1984.

[2] S. Sircar, "Pressure swing adsorption," *Ind. Eng. Chem. Res.*, vol. 41, no. 6, pp. 1389–1392, 2002.

[3] D. M. Ruthven, S. Farooq, and K. S. Knaebel, *Pressure swing adsorption*. New York: VCH Publishers, 1994, ISBN: 1560815175.

[4] S. Sircar, "Basic research needs for design of adsorptive gas separation processes," *Ind. Eng. Chem. Res.*, vol. 45, no. 16, pp. 5435–5448, 2006.

[5] M. Hefti, L. Joss, Z. Bjelobrk, and M. Mazzotti, "On the potential of phase-change adsorbents for CO_2 capture by temperature swing adsorption," *Faraday Discuss.*, vol. 192, pp. 153–179, 2016.

[6] L. Joss, M. Gazzani, M. Hefti, D. Marx, and M. Mazzotti, "Temperature swing adsorption for the recovery of the heavy component: An equilibrium-based shortcut model," *Ind. Eng. Chem. Res.*, vol. 54, no. 11, pp. 3027–3038, 2015.

[7] K. Chue, J. Kim, Y. Yoo, S. Cho, and R. Yang, "Comparison of activated carbon and zeolite 13x for CO_2 recovery from flue gas by pressure swing adsorption," *Ind. Eng. Chem. Res.*, vol. 34, no. 2, pp. 591–598, 1995.

[8] A. Meisen and X. Shuai, "Research and development issues in CO_2 capture," *Energy Convers. Manage.*, vol. 38, S37–S42, 1997.

[9] IPCC, *Climate change 2014: mitigation of climate change*. Cambridge University Press, 2015, vol. 3.

[10] N. Stern, "The economics of climate change," *Am. Econ. Rev.*, vol. 98, no. 2, pp. 1–37, 2008.

[11] I. P. on Climate Change, *Climate change 2014: mitigation of climate change*. Cambridge University Press, 2015, vol. 3.

[12] D. S. Sholl and R. P. Lively, "Seven chemical separations: To change the world: Purifying mixtures without using heat would lower global energy use, emissions and pollution–and open up new routes to resources," *Nature*, vol. 532, no. 7600, pp. 435–438, 2016.

[13] M. Bui, C. S. Adjiman, A. Bardow, E. J. Anthony, A. Boston, S. Brown, P. S. Fennell, S. Fuss, A. Galindo, L. A. Hackett, J. P. Hallett, H. J. Herzog, G. Jackson, J. Kemper, S. Krevor, G. C. Maitland, M. Matuszewski, I. S. Metcalfe, C. Petit, G. Puxty, J. Reimer, D. M. Reiner, E. S. Rubin, S. A. Scott, N. Shah, B. Smit, J. P. M. Trusler, P. Webley, J. Wilcox, and N. Mac Dowell, "Carbon capture and storage (CCS): The way forward," *Energ. Environ. Sci.*, vol. 11, no. 5, pp. 1062–1176, 5 2018. DOI: 10.1039/C7EE02342A. [Online]. Available: 10.1039/C7EE02342A.

[14] H. J. Herzog, *Carbon Capture*. MIT Press, 2018.

[15] M. Khurana and S. Farooq, "Adsorbent screening for postcombustion CO_2 capture: A method relating equilibrium isotherm characteristics to an optimum vacuum swing adsorption process performance," *Ind. Eng. Chem. Res.*, vol. 55, no. 8, pp. 2447–2460, 2016. DOI: 10.1021/acs.iecr.5b04531.

[16] A. H. Farmahini, S. Krishnamurthy, D. Friedrich, S. Brandani, and L. Sarkisov, *Performance-based screening of porous materials for carbon capture*, 2020. arXiv: 2009.12289 [cond-mat.mtrl-sci].

[17] M. W. Ackley, "Medical oxygen concentrators: A review of progress in air separation technology," *Adsorption*, vol. 25, no. 8, pp. 1437–1474, 2019.

[18] Y. J. Colón and R. Q. Snurr, "High-throughput computational screening of metal–organic frameworks," *Chemical Society Reviews*, vol. 43, no. 16, pp. 5735–5749, 2014.

[19] R. Haghpanah, R. Nilam, A. Rajendran, S. Farooq, and I. A. Karimi, "Cycle synthesis and optimization of a vsa process for postcombustion CO_2 capture," *AIChE J.*, vol. 59, no. 12, pp. 4735–4748, 2013. DOI: 10.1002/aic.14192.

[20] M. Khurana and S. Farooq, "Simulation and optimization of a 6-step dual-reflux vsa cycle for post-combustion CO_2 capture," *Chem. Eng. Sci*, vol. 152, pp. 507–515, 2016.

[21] P. A. Webley, A. Qader, A. Ntiamoah, J. Ling, P. Xiao, and Y. Zhai, "A new multi-bed vacuum swing adsorption cycle for CO_2 capture from flue gas streams," *Energy Procedia*, vol. 114, pp. 2467–2480, 2017.

[22] J. Ritter, A. Ebner, S. R. H. Du, and A. Mehrotra, "New adsorption cycles for carbon dioxide capture and concentration," University of South Carolina, Tech. Rep., 2008.

[23] S. P. Reynolds, A. D. Ebner, and J. A. Ritter, "Stripping psa cycles for CO_2 recovery from flue gas at high temperature using a hydrotalcite-like adsorbent," *Ind. Eng. Chem. Res.*, vol. 45, no. 12, pp. 4278–4294, 2006.

[24] L. Erden, A. D. Ebner, and J. A. Ritter, "Separation of landfill gas CH_4 from N_2 using pressure vacuum swing adsorption cycles with heavy reflux," *Energy & Fuels*, vol. 32, no. 3, pp. 3488–3498, 2018.

[25] S. P. Reynolds, A. Mehrotra, A. D. Ebner, and J. A. Ritter, "Heavy reflux psa cycles for co 2 recovery from flue gas: Part i. performance evaluation," *Adsorption*, vol. 14, no. 2-3, pp. 399–413, 2008.

[26] L.-C. Lin, A. H. Berger, R. L. Martin, J. Kim, J. A. Swisher, K. Jariwala, C. H. Rycroft, A. S. Bhown, M. W. Deem, M. Haranczyk, *et al.*, "In silico screening of carbon-capture materials," *Nat. Mater.*, vol. 11, no. 7, p. 633, 2012. DOI: 10.1038/nmat3336.

[27] R. Vaidhyanathan, S. S. Iremonger, G. K. Shimizu, P. G. Boyd, S. Alavi, and T. K. Woo, "Direct observation and quantification of CO_2 binding within an amine-functionalized nanoporous solid," *Science*, vol. 330, no. 6004, pp. 650–653, 2010.

[28] K. Adil, P. M. Bhatt, Y. Belmabkhout, S. M. T. Abtab, H. Jiang, A. H. Assen, A. Mallick, A. Cadiau, J. Aqil, and M. Eddaoudi, "Valuing metal–organic frameworks for postcombustion carbon capture: A benchmark study for evaluating physical adsorbents," *Adv. Mater.*, vol. 29, no. 39, p. 1 702 953, 2017.

[29] A. K. Rajagopalan, A. M. Avila, and A. Rajendran, "Do adsorbent screening metrics predict process performance? a process optimisation based study for post-combustion capture of CO_2," *Int. J. Greenh. Gas Con.*, vol. 46, pp. 76–85, 2016. DOI: 10.1016/j.ijggc.2015.12.033.

[30] J. Park, H. O. Rubiera Landa, Y. Kawajiri, M. J. Realff, R. P. Lively, and D. S. Sholl, "How well do approximate models of adsorption-aased CO_2 capture processes predict results of detailed process models?" *Ind. Engg. Chem. Res.*, vol. 59, no. 15, pp. 7097–7108, 2019. DOI: 10.1021/acs.iecr.9b05363.

[31] R. Haghpanah, A. Majumder, R. Nilam, A. Rajendran, S. Farooq, I. A. Karimi, and M. Amanullah, "Multiobjective optimization of a four-step adsorption process for postcombustion CO_2 capture via finite volume simulation," *Ind. Eng. Chem. Res.*, vol. 52, pp. 4249–4265, 2013.

[32] K. T. Leperi, Y. G. Chung, F. You, and R. Q. Snurr, "Development of a general evaluation metric for rapid screening of adsorbent materials for postcombustion CO_2 capture," *ACS Sus. Chem. Engg.*, vol. 7, no. 13, pp. 11 529–11 539, 2019. DOI: 10.1021/acssuschemeng.9b01418.

[33] A. H. Farmahini, S. Krishnamurthy, D. Friedrich, S. Brandani, and L. Sarkisov, "From crystal to adsorption column: Challenges in multiscale computational screening of materials for adsorption separation processes," *Ind. Engg. Chem. Res.*, vol. 57, no. 45, pp. 15 491–15 511, 2018. DOI: 10.1021/acs.iecr.8b03065.

[34] D. Ko, R. Siriwardane, and L. T. Biegler, "Optimization of pressure swing adsorption and fractionated vacuum pressure swing adsorption processes for CO_2 capture," *Ind. Eng. Chem. Res.*, no. 44, pp. 8084–8094, 2005.

[35] L. Joss, F. Capra, M. Gazzani, M. Mazzotti, and E. Martelli, "Mo-mcs: An efficient multi-objective optimization algorithm for the optimization of temperature/pressure swing adsorption cycles," in *Comput. Chem. Eng.* Vol. 38, Elsevier, 2016, pp. 1467–1472.

[36] L. E. Perez, P. Sarkar, and A. Rajendran, "Experimental validation of multi-objective optimization techniques for design of vacuum swing adsorption processes," *Sep. Purif. Technol.*, vol. 224, pp. 553–563, 2019. DOI: 10.1016/j.seppur.2019.05.039.

[37] C. Altintas, I. Erucar, and S. Keskin, "High-throughput computational screening of the metal organic framework database for CH_4/H_2 separations," *ACS Appl Mater Interfaces.*, vol. 10, no. 4, pp. 3668–3679, 2018.

[38] V. Subramanian Balashankar, A. K. Rajagopalan, R. de Pauw, A. M. Avila, and A. Rajendran, "Analysis of a batch adsorber analogue for rapid screening of adsorbents for postcombustion CO_2 capture," *Ind. Engg. Chem. Res.*, vol. 58, no. 8, pp. 3314–3328, 2019.

[39] D. Ko, R. Siriwardane, and L. T. Biegler, "Optimization of a pressure-swing adsorption process using zeolite 13x for CO_2 sequestration," *Ind. Eng. Chem. Res.*, vol. 42, no. 2, pp. 339–348, 2003. DOI: 10.1021/ie0204540. eprint: http://dx.doi.org/10.1021/ie0204540. [Online]. Available: http://dx.doi.org/10.1021/ie0204540.

[40] S. Brandani, A. H. Farmahini, D. Friedrich, S. Krishnamurthy, and L. Sarkisov, "Performance-based screening of porous materials for carbon capture," *arXiv (cond-mat.mtrl-sci)*, vol. 2009.12289, 2020. [Online]. Available: https://arxiv.org/abs/2009.12289.

[41] C. E. Wilmer, M. Leaf, C. Lee, O. K. Farha, D. Hauser, J. T. Hupp, and R. Q. Snurr, "Large-scale screening of hypothetical metal–organic frameworks," *Nat. Chem.*, vol. 4, no. 2, p. 83, 2012.

[42] P. Z. Moghadam, A. Li, S. B. Wiggin, A. Tao, A. G. Maloney, P. A. Wood, S. C. Ward, and D. Fairen-Jimenez, "Development of a cambridge structural database subset: A collection of metal–organic frameworks for past, present, and future," *Chemistry of Materials*, vol. 29, no. 7, pp. 2618–2625, 2017.

[43] P. G. Boyd and T. K. Woo, "A generalized method for constructing hypothetical nanoporous materials of any net topology from graph theory," *CrystEngComm*, vol. 18, no. 21, pp. 3777–3792, 2016.

[44] Y. J. Colón, D. A. Gomez-Gualdron, and R. Q. Snurr, "Topologically guided, automated construction of metal–organic frameworks and their evaluation for energy-related applications," *Crystal Growth & Design*, vol. 17, no. 11, pp. 5801–5810, 2017.

[45] C. R. Groom, I. J. Bruno, M. P. Lightfoot, and S. C. Ward, "The cambridge structural database," *Acta Crystallographica Section B: Structural Science, Crystal Engineering and Materials*, vol. 72, no. 2, pp. 171–179, 2016.

[46] Y. G. Chung, E. Haldoupis, B. J. Bucior, M. Haranczyk, S. Lee, H. Zhang, K. D. Vogiatzis, M. Milisavljevic, S. Ling, J. S. Camp, *et al.*, "Advances, updates, and analytics for the computation-ready, experimental metal–organic framework database: Core mof 2019," *Journal of Chemical & Engineering Data*, vol. 64, no. 12, pp. 5985–5998, 2019.

[47] R. Pophale, P. A. Cheeseman, and M. W. Deem, "A database of new zeolite-like materials," *Physical Chemistry Chemical Physics*, vol. 13, no. 27, pp. 12 407–12 412, 2011.

[48] B. S. Gelfand, R. P. Huynh, S. P. Collins, T. K. Woo, and G. K. Shimizu, "Computational and experimental assessment of CO_2 uptake in phosphonate monoester metal–organic frameworks," *Chem. Mater.*, vol. 29, no. 24, pp. 10 469–10 477, 2017.

[49] A. Goj, D. S. Sholl, E. D. Akten, and D. Kohen, "Atomistic simulations of CO_2 and N_2 adsorption in silica zeolites: The impact of pore size and shape," *J. Phys. Chem. B*, vol. 106, no. 33, pp. 8367–8375, 2002.

[50] I. C. Change, "Synthesis report. contribution of working groups i," *II and III to the fifth assessment report of the intergovernmental panel on climate change*, vol. 151, no. 10.1017, 2014.

[51] J. Rogelj, D. Shindell, K. Jiang, S. Fifita, P. Forster, V. Ginzburg, C. Handa, H. Kheshgi, S. Kobayashi, E. Kriegler, *et al.*, "Mitigation pathways compatible with 1.5 c in the context of sustainable development," in *Global warming of 1.5° C*, Intergovernmental Panel on Climate Change, 2018, pp. 93–174.

[52] D. M. D'Alessandro, B. Smit, and J. R. Long, "Carbon dioxide capture: Prospects for new materials," *Angewandte Chemie International Edition*, vol. 49, no. 35, pp. 6058–6082, 2010.

[53] H.-C. Zhou, J. R. Long, and O. M. Yaghi, "Introduction to metal–organic frameworks," *Chemical reviews*, vol. 112, no. 2, pp. 673–674, 2012.

[54] H. Furukawa, K. E. Cordova, M. O'Keeffe, and O. M. Yaghi, "The chemistry and applications of metal-organic frameworks," *Science*, vol. 341, no. 6149, 2013.

[55] P. Nugent, Y. Belmabkhout, S. D. Burd, A. J. Cairns, R. Luebke, K. Forrest, T. Pham, S. Ma, B. Space, L. Wojtas, *et al.*, "Porous materials with optimal adsorption thermodynamics and kinetics for co 2 separation," *Nature*, vol. 495, no. 7439, pp. 80–84, 2013.

[56] L. Liang, C. Liu, F. Jiang, Q. Chen, L. Zhang, H. Xue, H.-L. Jiang, J. Qian, D. Yuan, and M. Hong, "Carbon dioxide capture and conversion by an acid-base resistant metal-organic framework," *Nature communications*, vol. 8, no. 1, pp. 1–10, 2017.

[57] J. Jiang, Z. Lu, M. Zhang, J. Duan, W. Zhang, Y. Pan, and J. Bai, "Higher symmetry multinuclear clusters of metal–organic frameworks for highly selective CO_2 capture," *Journal of the American Chemical Society*, vol. 140, no. 51, pp. 17 825–17 829, 2018.

[58] T. M. McDonald, J. A. Mason, X. Kong, E. D. Bloch, D. Gygi, A. Dani, V. Crocella, F. Giordanino, S. O. Odoh, W. S. Drisdell, *et al.*, "Cooperative insertion of co 2 in diamine-appended metal-organic frameworks," *Nature*, vol. 519, no. 7543, pp. 303–308, 2015.

[59] J. Yu, L.-H. Xie, J.-R. Li, Y. Ma, J. M. Seminario, and P. B. Balbuena, "CO_2 capture and separations using mofs: Computational and experimental studies," *Chemical reviews*, vol. 117, no. 14, pp. 9674–9754, 2017.

[60] M. Fernandez, P. G. Boyd, T. D. Daff, M. Z. Aghaji, and T. K. Woo, "Rapid and accurate machine learning recognition of high performing metal organic frameworks for CO_2 capture," *J. Phys. Chem. Letters*, vol. 5, no. 17, pp. 3056–3060, 2014.

[61] M. Fernandez, N. R. Trefiak, and T. K. Woo, "Atomic property weighted radial distribution functions descriptors of metal–organic frameworks for the prediction of gas uptake capacity," *The Journal of Physical Chemistry C*, vol. 117, no. 27, pp. 14 095–14 105, 2013.

[62] J. M. Huck, L.-C. Lin, A. H. Berger, M. N. Shahrak, R. L. Martin, A. S. Bhown, M. Haranczyk, K. Reuter, and B. Smit, "Evaluating different classes of porous materials for carbon capture," *Energy & Environmental Science*, vol. 7, no. 12, pp. 4132–4146, 2014.

[63] S. Nandi, S. Collins, D. Chakraborty, D. Banerjee, P. K. Thallapally, T. K. Woo, and R. Vaidhyanathan, "Ultralow parasitic energy for postcombustion CO_2 capture realized in a nickel isonicotinate metal–organic framework with excellent moisture stability," *Journal of the American Chemical Society*, vol. 139, no. 5, pp. 1734–1737, 2017.

[64] S. A. Freeman, R. Dugas, D. H. Van Wagener, T. Nguyen, and G. T. Rochelle, "Carbon dioxide capture with concentrated, aqueous piperazine," *International Journal of Greenhouse Gas Control*, vol. 4, no. 2, pp. 119–124, 2010.

[65] M. K. Verma, *Fundamentals of carbon dioxide-enhanced oil recovery (CO2-EOR): A supporting document of the assessment methodology for hydrocarbon recovery using CO2-EOR associated with carbon sequestration*. US Department of the Interior, US Geological Survey Washington, DC, 2015.

[66] K. S. Walton and D. S. Sholl, "Research challenges in avoiding "showstoppers" in developing materials for large-scale energy applications," *Joule*, vol. 1, no. 2, pp. 208–211, 2017.

[67] M. F. Hasan, E. L. First, and C. A. Floudas, "Cost-effective CO_2 capture based on in silico screening of zeolites and process optimization," *Phys. Chem. Chem. Phys.*, vol. 15, no. 40, pp. 17 601–17 618, 2013.

[68] A. Hajiahmadi Farmahini, S. Krishnamurthy, D. Friedrich, S. Brandani, and L. Sarkisov, "From crystal to adsorption column: Challenges in multiscale computational screening of materials for adsorption separation processes," *Ind. Eng. Chem. Res.*, 2018.

[69] G. N. Nikolaidis, E. S. Kikkinides, and M. C. Georgiadis, "A model-based approach for the evaluation of new zeolite 13x-based adsorbents for the efficient post-combustion CO_2 capture using p/vsa processes," *Chem. Eng. Res. Des.*, vol. 131, pp. 362–374, 2018.

[70] R. T. Maruyama, K. N. Pai, S. G. Subraveti, and A. Rajendran, "Improving the performance of vacuum swing adsorption based CO_2 capture under reduced recovery requirements," *Int. J. Greenh. Gas Control.*, vol. 93, p. 102 902, 2020. DOI: 10.1016/j.ijggc.2019.102902.

[71] K. Pai, J. Baboolal, D. Sharp, and A. Rajendran, "Evaluation of diamine-appended metal-organic frameworks for post-combustion CO_2 capture by vacuum swing adsorption," *Sep. Purif. Technol.*, vol. 211, pp. 540–550, 2019. DOI: 10.1016/j.seppur.2018.10.015.

[72] K. T. Leperi, D. Yancy-Caballero, R. Q. Snurr, and F. You, "110th anniversary: Surrogate models based on artificial neural networks to simulate and optimize pressure swing adsorption cycles for CO_2 capture," *Ind. Engg. Chem. Res.*, vol. 58, no. 39, pp. 18 241–18 252, 2019. DOI: 10.1021/acs.iecr.9b02383.

[73] M. Khurana and S. Farooq, "Integrated adsorbent process optimization for minimum cost of electricity including carbon capture by a vsa process," *AIChE J.*, vol. 65, no. 1, pp. 184–195, 2019. DOI: 10.1002/aic.16362.

[74] Y. G. Chung, J. Camp, M. Haranczyk, B. J. Sikora, W. Bury, V. Krungleviciute, T. Yildirim, O. K. Farha, D. S. Sholl, and R. Q. Snurr, "Computation-ready, experimental metal–organic frameworks: A tool to enable high-throughput screening of nanoporous crystals," *Chemistry of Materials*, vol. 26, no. 21, pp. 6185–6192, 2014.

[75] S. Krishnamurthy, V. R. Rao, S. Guntuka, P. Sharratt, R. Haghpanah, A. Rajendran, M. Amanullah, I. A. Karimi, and S. Farooq, "CO_2 capture from dry flue gas by vacuum swing adsorption: A pilot plant study," *AIChE J.*, vol. 60, no. 5, pp. 1830–1842, 2014.

[76] T.-H. Bae, M. R. Hudson, J. A. Mason, W. L. Queen, J. J. Dutton, K. Sumida, K. J. Micklash, S. S. Kaye, C. M. Brown, and J. R. Long, "Evaluation of cation-exchanged zeolite adsorbents for post-combustion carbon dioxide capture," *Energy & Environmental Science*, vol. 6, no. 1, pp. 128–138, 2013.

[77] S. Cavenati, C. A. Grade, and A. E. Rodrigues, "Adsorption equilibrium of methane, carbon dioxide, and nitrogen on zeolite 13x at high pressures," *J. Chem. Eng. Data*, 2004.

[78] A. Zoelle, D. Keairns, M. J. Turner, M. Woods, N. Kuehn, V. Shah, V. Chou, L. L. Pinkerton, and T. Fout, "Cost and performance baseline for fossil energy plants volume 1b: Bituminous coal (igcc) to electricity revision 2b–year dollar update," NETL, Tech. Rep., 2015.

[79] D. M. Ruthven, "CO_2 capture: Value functions, separative work and process economics," *Chemical Engineering Science*, vol. 114, pp. 128–133, 2014.

[80] S. U. Rege and R. T. Yang, "A simple parameter for selecting an adsorbent for gas separation by pressure swing adsorption," *Sep. Sci. Technol.*, vol. 36, no. 15, pp. 3355–3365, 2001. DOI: 10.1081/SS-100107907. eprint: http://www.tandfonline.com/doi/pdf/10.1081/SS-100107907. [Online]. Available: http://www.tandfonline.com/doi/abs/10.1081/SS-100107907.

[81] Y. G. Chung, D. A. Gómez-Gualdrón, P. Li, K. T. Leperi, P. Deria, H. Zhang, N. A. Vermeulen, J. F. Stoddart, F. You, J. T. Hupp, *et al.*, "In silico discovery of metal-organic frameworks for precombustion CO_2 capture using a genetic algorithm," *Science advances*, vol. 2, no. 10, e1600909, 2016.

[82] R. Krishna, "Screening metal–organic frameworks for mixture separations in fixed-bed adsorbers using a combined selectivity/capacity metric," *RSC advances*, vol. 7, no. 57, pp. 35 724–35 737, 2017.

[83] Y. Basdogan, K. B. Sezginel, and S. Keskin, "Identifying highly selective metal organic frameworks for ch4/h2 separations using computational tools," *Industrial & Engineering Chemistry Research*, vol. 54, no. 34, pp. 8479–8491, 2015.

[84] A. D. Wiersum, J.-S. Chang, C. Serre, and P. L. Llewellyn, "An adsorbent performance indicator as a first step evaluation of novel sorbents for gas separations: Application to metal–organic frameworks," *Langmuir*, vol. 29, no. 10, pp. 3301–3309, 2013.

[85] F. Notaro, J. T. Mullhaupt, F. W. Leavitt, and M. W. Ackley, *Adsorption process and system using multilayer adsorbent beds*, US Patent 5,674,311, 1997.

[86] M. W. Ackley, A. B. Stewart, G. W. Henzler, F. W. Leavitt, F. Notaro, and M. S. Kane, *Psa apparatus and process using adsorbent mixtures*, US Patent 6,027,548, 2000.

[87] S. Krishnamurthy, R. Haghpanah, A. Rajendran, and S. Farooq, "Simulation and optimization of a dual-adsorbent, two-bed vacuum swing adsorption process for CO_2 capture from wet flue gas.," *Ind. Eng. Chem. Res.*, vol. 53, 14462 âˆ'–14 473, 2014.

[88] J. Charnell, "Gel growth of large crystals of sodium a and sodium x zeolites," *Journal of Crystal Growth*, vol. 8, no. 3, pp. 291–294, 1971.

[89] S. M. Auerbach, K. A. Carrado, and P. K. Dutta, *Handbook of zeolite science and technology*. CRC press, 2003.

[90] N. Chanut, S. Bourrelly, B. Kuchta, C. Serre, J.-S. Chang, P. A. Wright, and P. L. Llewellyn, "Screening the effect of water vapour on gas adsorption performance: Application to CO_2 capture from flue gas in metal–organic frameworks," *ChemSusChem*, vol. 10, no. 7, pp. 1543–1553, 2017.

[91] M. Khurana and S. Farooq, "Integrated adsorbent-process optimization for carbon capture and concentration using vacuum swing adsorption cycles," *AIChE J.*, vol. 63, no. 7, pp. 2987–2995, 2017. DOI: 10.1002/aic.15602.

[92] H. Daglar and S. Keskin, "Computational screening of metal–organic frameworks for membrane-based co2/n2/h2o separations: Best materials for flue gas separation," *The Journal of Physical Chemistry C*, vol. 122, no. 30, pp. 17 347–17 357, 2018.

[93] S. Krishnamurthy, R. Haghpanah, A. Rajendran, and S. Farooq, "Simulation and optimization of a dual-adsorbent, two-bed vacuum swing adsorption process for CO_2 capture from wet flue gas," *Ind. Engg. Chem. Res.*, vol. 53, no. 37, pp. 14 462–14 473, 2014.

[94] S. Sircar, "Air fractionation by adsorption," *Sep. Sci. Technol.*, vol. 23, no. 14-15, pp. 2379–2396, 1988.

[95] S Sircar and T. Golden, "Purification of hydrogen by pressure swing adsorption," *Sep. Sci. Technol.*, vol. 35, no. 5, pp. 667–687, 2000.

[96] R. T. Yang, *Gas separation by adsorption processes*, ser. Series on chemical engineering: v. 1. London: London: Imperial College Press, 1997, ISBN: 1860940471.

[97] H. Dureckova, M. Krykunov, M. Z. Aghaji, and T. K. Woo, "Robust machine learning models for predicting high CO_2 working capacity and CO_2/H_2 selectivity of gas adsorption in metal organic frameworks for pre combustion carbon capture," *J. Phys. Chem. C*, vol. 123, no. 7, pp. 4133–4139, 2019.

[98] S. Kitagawa, "Metal–organic frameworks (MOFs)," *Chem. Soc. Rev.*, vol. 43, no. 16, pp. 5415–5418, 2014.

[99] P. A. Webley and J. He, "Fast solution-adaptive finite volume method for psa/vsa cycle simulation; 1 single step simulation," *Comp. Chem. Engg.*, vol. 23, no. 11-12, pp. 1701–1712, 2000.

[100] Y. Wang, A. W. Dowling, C. Krieft, A. Walther, and L. T. Biegler, "Pressure swing adsorption optimization strategies for CO_2 capture," in *Comput. Aided Chem. Eng.* Vol. 36, Elsevier, 2015, pp. 197–223.

[101] S. Effendy, S. Farooq, and D. M. Ruthven, "A rigorous criterion for approach to cyclic steady-state in psa simulations," *Chem. Engg. Sci.*, vol. 160, pp. 313–320, 2017.

[102] S. Nilchan and C. Pantelides, "On the optimisation of periodic adsorption processes," *Adsorption*, vol. 4, no. 2, pp. 113–147, 1998.

[103] Y. Ding and M. D. LeVan, "Periodic states of adsorption cycles iii. convergence acceleration for direct determination," *Chem. Engg. Sci*, vol. 56, no. 17, pp. 5217–5230, 2001.

[104] A. Forrester, A. Sobester, and A. Keane, *Engineering design via surrogate modelling: a practical guide*. John Wiley & Sons, 2008.

[105] M. F. Hasan, I. Karimi, S Farooq, A Rajendran, and M Amanullah, "Surrogate-based VSA process optimization for post-combustion CO_2 capture," in *Comput. Aided Chem. Eng.* Vol. 29, Elsevier, 2011, pp. 402–406.

[106] J. Beck, D. Friedrich, S. Brandani, and E. S. Fraga, "Multi-objective optimisation using surrogate models for the design of VPSA systems," *Comput. Aided Chem. Eng.*, vol. 82, pp. 318–329, 2015.

[107] S. G. Subraveti, Z. Li, V. Prasad, and A. Rajendran, "Machine learning-based multiobjective optimization of pressure swing adsorption," *Ind. Engg. Chem. Res.*, vol. 58, no. 44, pp. 20 412–20 422, 2019.

[108] P. A. Webley, "Adsorption technology for CO_2 separation and capture: A perspective," *Adsorption*, vol. 20, pp. 225–231, 2014.

[109] S. P. Reynolds, A. D. Ebner, and J. A. Ritter, "New pressure swing adsorption cycles for carbon dioxide sequestration," *Adsorption*, vol. 11, no. 1, pp. 531–536, 2005.

[110] N. Wilkins and A. Rajendran, "Measurement of competitive CO_2 and N_2 adsorption on Zeolite 13X for post-combustion CO_2 capture," *Adsorption*, vol. 25, no. 2, pp. 115–133, 2019.

[111] G. Li, P. Xiao, P. Webley, J. Zhang, R. Singh, and M. Marshall, "Capture of CO_2 from high humidity flue gas by vacuum swing adsorption with zeolite 13x," *Adsorption*, vol. 14, no. 2-3, pp. 415–422, 2008.

[112] L. Wang, Y. Yang, W. Shen, X. Kong, P. Li, J. Yu, and A. E. Rodrigues, "CO_2 capture from flue gas in an existing coal-fired power plant by two successive pilot-scale vpsa units," *Ind. Eng. Chem. Res.*, vol. 52, pp. 7947–7955, 2013.

[113] P. Xiao, J. Zhang, P. Webley, G. Li, R. Singh, and R. Todd, "Capture of CO_2 from flue gas streams with zeolite 13X by vacuum-pressure swing adsorption," *Adsorption*, vol. 14, no. 4-5, pp. 575–582, 2008.

[114] X. Hu, E. Mangano, D. Friedrich, H. Ahn, and S. Brandani, "Diffusion mechanism of co 2 in 13X zeolite beads," *Adsorption*, vol. 20, no. 1, pp. 121–135, 2014.

[115] R. T. Maruyama, K. N. Pai, S. G. Subraveti, and A. Rajendran, "Improving the performance of vacuum swing adsorption based CO_2 capture under reduced recovery requirements," *Int. J. Greenh. Gas. Con.*, vol. in Press, 2019.

[116] G. Fiandaca, E. S. Fraga, and S. Brandani, "A multi-objective genetic algorithm for the design of pressure swing adsorption," *Eng. Optim.*, vol. 41, no. 9, pp. 833–854, 2009.

[117] W.-Y. Loh and Y.-S. Shih, "Split selection methods for classification trees," *Stat. Sin.*, pp. 815–840, 1997.

[118] L. Breiman, "Bagging predictors," *Mach. Learn.*, vol. 24, no. 2, pp. 123–140, 1996.

[119] L. Breiman, "Random forests," *Mach. Learn.*, vol. 45, no. 1, pp. 5–32, 2001.

[120] A. J. Smola and B. Schölkopf, "A tutorial on support vector regression," *Stat. Comput.*, vol. 14, no. 3, pp. 199–222, 2004.

[121] D. J. MacKay, "Bayesian interpolation," *Neural computation*, vol. 4, no. 3, pp. 415–447, 1992.

[122] C. K. Williams and C. E. Rasmussen, *Gaussian processes for machine learning*, 3. MIT Press Cambridge, MA, 2006, vol. 2.

[123] R. Haghpanah, A. Majumder, R. Nilam, A. Rajendran, S. Farooq, I. A. Karimi, and M. Amanullah, "Multi-objective optimization of a 4-step adsorption process for post-combustion CO_2 capture using finite volume technique," *Ind. Eng. Chem. Res.*, vol. 52, pp. 4249–4265, 2013.

[124] N. Casas, J. Schell, L. Joss, and M. Mazzotti, "A parametric study of a psa process for pre-combustion CO_2 capture," *Sep. Purif. Technol.*, vol. 104, pp. 183–192, 2013.

[125] F. Capra, M. Gazzani, L. Joss, M. Mazzotti, and E. Martelli, "Mo-mcs, a derivative-free algorithm for the multiobjective optimization of adsorption processes," *Ind. Engg. Chem. Res.*, vol. 57, no. 30, pp. 9977–9993, 2018.

[126] A. Agarwal, L. T. Biegler, and S. E. Zitney, "Superstructure-based optimal synthesis of pressure swing adsorption cycles for precombustion CO_2 capture," *Ind. Eng. Chem. Res.*, vol. 49, no. 11, pp. 5066–5079, 2009. [Online]. Available: http://pubs.acs.org/doi/abs/10.1021/ie900873j.

[127] K. T. Leperi, R. Q. Snurr, and F. You, "Optimization of two-stage pressure/-vacuum swing adsorption with variable dehydration level for postcombustion carbon capture," *Ind. Eng. Chem. Res.*, vol. 55, no. 12, pp. 3338–3350, 2015.

[128] A. H. Farmahini, D. Friedrich, S. Brandani, and L. Sarkisov, "Exploring new sources of efficiency in process-driven materials screening for post-combustion carbon capture," *Ener. Envi. Sci.*, vol. 13, no. 3, pp. 1018–1037, 2020. DOI: 10.1039/C9EE03977E.

[129] T. D. Burns, K. N. Pai, S. G. Subraveti, S. P. Collins, M. Krykunov, A. Rajendran, and T. K. Woo, "Prediction of mof performance in vacuum swing adsorption systems for postcombustion CO_2 capture based on integrated molecular simulations, process optimizations, and machine learning models," *Env. Sci. Technol.*, vol. 54, no. 7, pp. 4536–4544, 2020. DOI: 10.1021/acs.est.9b07407.

[130] B. J. Maring and P. A. Webley, "A new simplified pressure/vacuum swing adsorption model for rapid adsorbent screening for CO_2 capture applications," *Int. J. Greenh. Gas Con.*, vol. 15, pp. 16–31, 2013. DOI: 10.1016/j.ijggc.2013.01.009.

[131] V. Subramanian Balashankar and A. Rajendran, "Process optimization-based screening of zeolites for post-combustion CO_2 capture by vacuum swing adsorption," *ACS Sus. Chem. Engg.*, vol. 7, no. 21, pp. 17 747–17 755, 2019. DOI: 10.1021/acssuschemeng.9b04124.

[132] D. Danaci, M. Bui, N. Mac Dowell, and C. Petit, "Exploring the limits of adsorption-based CO_2 capture using mofs with pvsa–from molecular design to process economics," *Mol. Syst. Des. Engg.*, vol. 5, no. 1, pp. 212–231, 2020. DOI: 10.1039/C9ME00102F.

[133] A. Ajenifuja, L. Joss, and M. Jobson, "A new equilibrium shortcut temperature swing adsorption model for fast adsorbent screening," *Ind. Engg. Chem. Res.*, vol. 59, no. 8, pp. 3485–3497, 2020.

[134] J. Beck, D. Friedrich, S. Brandani, S. Guillas, and E. S. Fraga, "Surrogate based optimisation for design of pressure swing adsorption systems," in *Comput. Aided Chem. Eng.* Vol. 30, Elsevier, 2012, pp. 1217–1221.

[135] K. N. Pai, V. Prasad, and A. Rajendran, "Experimentally validated machine learning frameworks for accelerated prediction of cyclic steady state and optimization of pressure swing adsorption processes," *Sep. Purif. Technol.*, vol. 241, p. 116 651, 2020. DOI: 10.1016/j.seppur.2020.116651.

[136] J. A. Ritter, K. C. Bumiller, K. J. Tynan, and A. D. Ebner, "On the use of the dual process langmuir model for binary gas mixture components that exhibit single process or linear isotherms," *Adsorption*, vol. 25, no. 8, pp. 1511–1523, 2019. DOI: 10.1021/la104965w.

[137] K. Maik Jablonka, D. Ongari, S. Mohamad Moosavi, and B. Smit, "Big-data science in porous materials: Materials genomics and machine learning," *arXiv*, arXiv–2001, 2020.

[138] IPCC, *Global warming of 1.5° c. an ipcc special report on the impacts of global warming of 1.5° c above pre-industrial levels and related global greenhouse gas emission pathways, in the context of strengthening the global response to the threat of climate change, sustainable development, and efforts to eradicate poverty*, 2018.

[139] A. Samanta, A. Zhao, G. K. Shimizu, P. Sarkar, and R. Gupta, "Post-combustion CO_2 capture using solid sorbents: A review," *Ind. Eng. Chem. Res.*, vol. 51, no. 4, pp. 1438–1463, 2011. DOI: 10.1021/ie200686q. [Online]. Available: http://pubs.acs.org/doi/abs/10.1021/ie200686q.

[140] D. Yancy-Caballero, K. T. Leperi, B. J. Bucior, R. K. Richardson, T. Islamoglu, O. K. Farha, F. You, and R. Q. Snurr, "Process-level modelling and optimization to evaluate metal–organic frameworks for post-combustion capture of CO_2," *Mol. Syst. Des. Eng.*, vol. 5, no. 7, pp. 1205–1218, 2020. DOI: 10.1039/D0ME00060D.

[141] A. Rajagopalan and A. Rajendran, "The effect of nitrogen adsorption on vacuum swing adsorption based post-combustion CO_2 capture," *Int. J. Greenh. Gas Con.*, vol. 78, pp. 437–447, 2018. DOI: 10.1016/j.ijggc.2018.09.002.

[142] K. N. Pai, V. Prasad, and A. Rajendran, "Generalized, adsorbent-agnostic, artificial neural network framework for rapid simulation, optimization, and adsorbent screening of adsorption processes," *Ind. Eng. Chem. Res.*, vol. 59, no. 38, pp. 16 730–16 740, 2020. DOI: 10.1021/acs.iecr.0c02339.

[143] S. G. Subraveti, S. Roussanaly, R. Anantharaman, L. Riboldi, and A. Rajendran, "Techno-economic assessment of optimised vacuum swing adsorption for post-combustion CO_2 capture from steam-methane reformer flue gas," *Sep. Purif. Technol.*, vol. 256, p. 117 832, 2020. DOI: 10.1016/j.seppur.2020.117832.

[144] K. Deb, A. Pratap, S. Agarwal, and T. Meyarivan, "A fast and elitist multiobjective genetic algorithm: Nsga-ii," *IEEE Trans. Evol. Comput.*, vol. 6, no. 2, pp. 182–197, 2002. DOI: 10.1109/4235.996017.

[145] G. N. Nikolaidis, E. S. Kikkinides, and M. C. Georgiadis, "An integrated two-stage p/vsa process for postcombustion CO_2 capture using combinations of adsorbents zeolite 13x and mg-mof-74," *Ind. Eng. Chem. Res.*, vol. 56, no. 4, pp. 974–988, 2017. DOI: 10.1021/acs.iecr.6b04270.

[146] J. Husebye, A. L. Brunsvold, S. Roussanaly, and X. Zhang, "Techno economic evaluation of amine based CO_2 capture: Impact of CO_2 concentration and steam supply," *Energy Procedia*, vol. 23, pp. 381–390, 2012, The 6th Trondheim Conference on CO_2 Capture, Transport and Storage, ISSN: 1876-6102. DOI: 10.1016/j.egypro.2012.06.053.

[147] S. Brandani, "Carbon dioxide capture from air: A simple analysis," *Energy & Environ.*, vol. 23, no. 2-3, pp. 319–328, 2012. DOI: 10.1260/0958-305X.23.2-3.319.

[148] A. Singh and K. Stéphenne, "Shell cansolv CO_2 capture technology: Achievement from first commercial plant," *Energy Procedia*, vol. 63, pp. 1678–1685, 2014. DOI: 10.1016/j.egypro.2014.11.177.

[149] K. N. Pai, V. Prasad, and A. Rajendran, "Practically achievable process performance limits for pressure-vacuum swing adsorption-based postcombustion CO_2 capture," *ACS Sustainable Chemistry & Engineering*, vol. 9, no. 10, pp. 3838–3849, 2021.

[150] D. M. Ruthven, *Principles of Adsorption and Adsorption Processes*. John Wiley & Sons, 1984.

[151] S. Sircar and J. W. Zondlo, *Fractionation of air by adsorption*, US Patent 4,013,429, 1977.

[152] W Smith and T. Forester, "Dl_poly_2. 0: A general-purpose parallel molecular dynamics simulation package," *Journal of molecular graphics*, vol. 14, no. 3, pp. 136–141, 1996.

[153] W Smith, T. Forester, and I. Todorov, "The dl poly classic user manual," *STFC, STFC Daresbury Laboratory, Daresbury, Warrington, Cheshire, WA4 4AD, United Kingdom, version*, vol. 1, 2012.

[154] S. L. Mayo, B. D. Olafson, and W. A. Goddard, "Dreiding: A generic force field for molecular simulations," *Journal of Physical chemistry*, vol. 94, no. 26, pp. 8897–8909, 1990.

[155] A. K. Rappé, C. J. Casewit, K. Colwell, W. A. Goddard III, and W. M. Skiff, "Uff, a full periodic table force field for molecular mechanics and molecular dynamics simulations," *Journal of the American chemical society*, vol. 114, no. 25, pp. 10 024–10 035, 1992.

[156] C. Campañá, B. Mussard, and T. K. Woo, "Electrostatic potential derived atomic charges for periodic systems using a modified error functional," *Journal of Chemical Theory and Computation*, vol. 5, no. 10, pp. 2866–2878, 2009.

[157] G. Kresse and J. Furthmüller, "Efficient iterative schemes for ab initio total-energy calculations using a plane-wave basis set.," *Phys. Rev. B.*, vol. 54, pp. 11 169–11 186, 1996.

[158] G. Kresse and M. Marsman, "Vasp manual (2014)," *VASP manual.*, 2014.

[159] J. P. Perdew, K. Burke, and M. Ernzerhof, "Generalized gradient approximation made simple," *Physical review letters*, vol. 77, no. 18, p. 3865, 1996.

[160] J. P. Perdew, M. Ernzerhof, and K. Burke, "Rationale for mixing exact exchange with density functional approximations," *The Journal of chemical physics*, vol. 105, no. 22, pp. 9982–9985, 1996.

[161] A. Garcia-Sanchez, C. O. Ania, J. B. Parra, D. Dubbeldam, T. J. Vlugt, R. Krishna, and S. Calero, "Transferable force field for carbon dioxide adsorption in zeolites," *The Journal of Physical Chemistry C*, vol. 113, no. 20, pp. 8814–8820, 2009.

[162] D.-Y. Peng and D. B. Robinson, "A new two-constant equation of state," *Industrial & Engineering Chemistry Fundamentals*, vol. 15, no. 1, pp. 59–64, 1976.

[163] T. F. Willems, C. H. Rycroft, M. Kazi, J. C. Meza, and M. Haranczyk, "Algorithms and tools for high-throughput geometry-based analysis of crystalline porous materials," *Microporous and Mesoporous Materials*, vol. 149, no. 1, pp. 134–141, 2012.

[164] M. Ramezan, T. J. Skone, N. Nsakala, G. Liljedahl, L. Gearhart, R Hestermann, and B Rederstorff, "Carbon dioxide capture from existing coal-fired power plants," *National Energy Technology Laboratory, DOE/NETL Report*, vol. 401, p. 110 907, 2007.

[165] D. Jansen, M. Gazzani, G. Manzolini, E. van Dijk, and M. Carbo, "Pre-combustion CO_2 capture," *International Journal of Greenhouse Gas Control*, vol. 40, pp. 167–187, 2015.

[166] R Anantharaman, O Bolland, N Booth, E van Dorst, C Ekstrom, E. Fernandes, F Franco, E Macchi, G Manzolini, D Nikolic, *et al.*, "Decarbit: European best practice guidelines for assessment of CO_2 capture technologies," *Norwegian University of Science and Technology: Trondheim, Norway*, 2011.

Appendix A: Supporting information for: Prediction of MOF performance in vacuum swing adsorption systems for post-combustion CO_2 capture based on integrated molecular simulations, process optimizations, and machine learning models.

A.1 Grand Canonical Monte Carlo Simulations

Grand Canonical Monte Carlo (GCMC) simulations were performed with an in-house developed code [152] based on the DL POLY Classic code [153]. The material is represented with a 3×3×3 super cell with 3-dimensional boundary conditions. Interactions between the gas molecules and the MOF framework are calculated as the sum of atom pair Lennard-Jones and Coulomb potentials. The Lennard-Jones parameters for the framework atoms were taken from the DREIDING [154] and when such parameters were not available the Universal Force Field (UFF) [155] parameters were used. The charges on the framework atoms were calculated using the REPEAT method, [156] which fits partial atomic charges to best match a quantum mechanical (QM) electrostatic potential (ESP). The QM ESPs were calculated using the Vienna Ab Initio Simulation Package (VASP) [157, 158] using the PBE functional [159, 160] with a plane-wave cutoff of 400 eV. To model the guest molecules, we used Garcia-Sanchez parameters for CO_2, [161] and an in-house parameters for N_2 which have been optimized to reproduce N_2 adsorption isotherms of MOFs. [162] The N_2 parameters are presented Table A.1. Single componentCO_2 and N_2 isotherms were calculated at 298 K with 18 pressures between 0.01 and 1.20 bar. All simulations were performed using the Peng-Robinson Equation of State [163]. These calculations were performed using 30,000 cycles equilibration cycles and 30,000 production cycle. A cycle consists of N Monte Carlo steps where N is the number of guest molecules present at any given point. For example, if a system adsorbed 100 guest molecules at equilibrium, 3 million MC steps would be performed. This methodology has been shown to accurately reproduce experimental isotherms [26, 67, 164].

Atom	bl ($\mathring{A}^a$)	q(e)	$/k_b$ (K)	ρ ($\mathring{A}$)
N	0.5500	-0.4820	39.966	2.4549
COM	0.0000	0.9640	0.000	0.0000

Table A.1: N_2 potential parameters used in GCMC simulations. ^{a}bl is the distance of the atom to the molecular centre of mass (COM)

A.2 Validation of Competitive Isotherm Model

The VSA simulation code relies on inputs of dual-site Langmuir (DSL) isotherm and uses a competitive DSL model to calculate competitive adsorption. The competitive loadings for each guest are given by the equation A.1, which assumes that the stronger binding sites for each guest will compete for the same binding sites. This assumption was validated by comparing the competitive isotherms generated by this competitive DSL model to isotherms generated using GCMC simulations with both gases. Figure A.1 shows the comparison between the competitive DSL model and these binary simulations for a few of the top performing MOFs. The GCMC simulations and the competitive DSL generated isotherms in good agreement with one another.

$$q_i^* = \frac{q_{\mathrm{sb},i} b_i P_i}{1 + \Sigma b_i P_i} + \frac{q_{\mathrm{sd},i} d_i P_i}{1 + \Sigma d_i P_i} \tag{A.1}$$

$$b_i = b_{0,i} e^{-\Delta H_{\mathrm{b},i}/RT} \tag{A.2}$$

$$d_i = d_{0,i} e^{-\Delta H_{\mathrm{d},i}/RT} \tag{A.3}$$

Where:

- $q_{\mathrm{sb},i}$ = saturation uptake for site 1
- b and d = Langmuir constants
- b_0 and d_0 = Temperature independent Langmuir Constant
- P_x = Partial Pressure of component x
- ΔH_{ads} = Isosteric Heat of adsorption
- ΔU = Change in internal energy
- R = Gas Constant
- T = Temperature

A.3 Removal of Toxic and Rare Atom Types

To reduce the set of materials being studied, a decision was made to remove elements with high toxicity, such as mercury, as well as expensive and rare elements such as platinum. The atom types considered in this study are: H, Li, B, C, N, O, F, Na, Mg, Al, Si, P, S, Cl, K, Ca, Ti, V, Mn, Fe, Co, Ni, Cu, Zn, Br, Zr, C, Sn, and I.

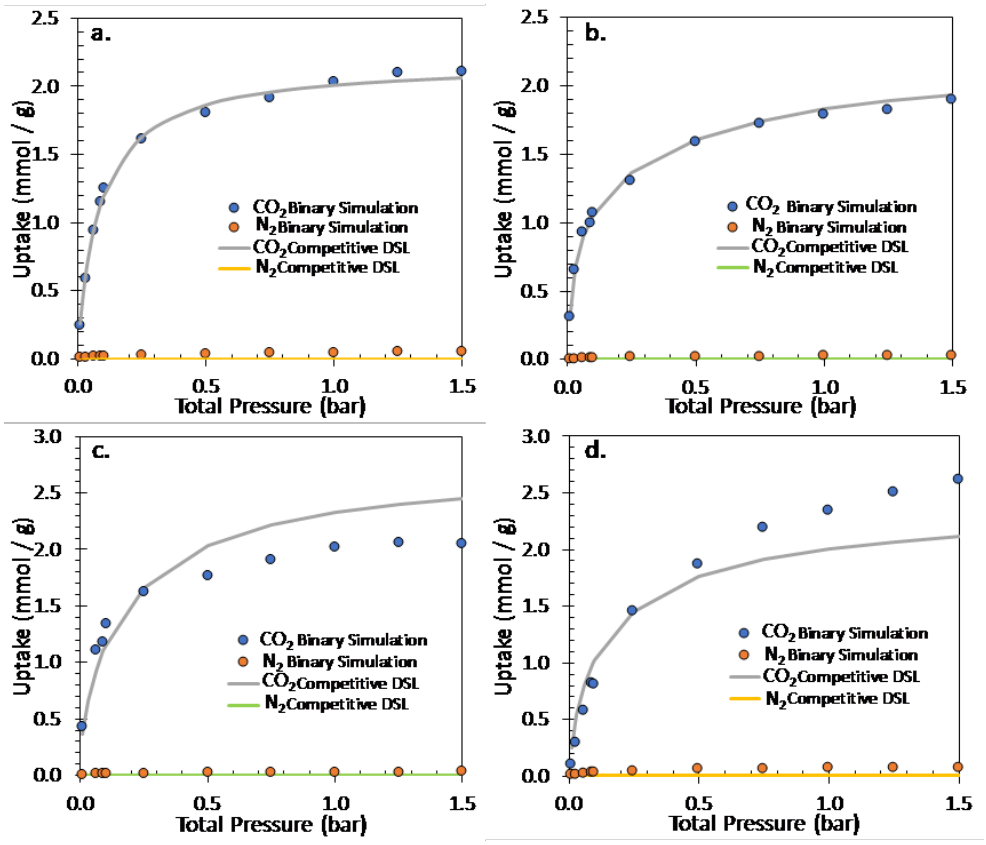

Figure A.1: Loading as a function of the total pressure for a 15% CO2/85% N2 mixture for binary GCMC simulations (circles) and the competitive dual-site Langmuir isotherms (lines) fit using single component GCMC for a. PESTUD, b. LABGAY, c. OPENON, and d. UFUMUD02.

Model equations	
Overall mass balance	$\frac{1}{P}\frac{\partial P}{\partial t} - \frac{1}{T}\frac{\partial T}{\partial t} = -\frac{T}{P}\frac{\partial}{\partial z}\left(\frac{P}{T}v\right) - \frac{1-\epsilon}{\epsilon}\frac{RT}{P}\sum_{i=1}^{n_{\text{comp}}}\frac{\partial q_i}{\partial t}$
Component mass balance	$\frac{\partial y_i}{\partial t} + \frac{y_i}{P}\frac{\partial P}{\partial t} - \frac{y_i}{T}\frac{\partial T}{\partial t} = \frac{T}{P}D_L\frac{\partial}{\partial z}\left(\frac{P}{T}\frac{\partial y_i}{\partial z}\right) - \frac{T}{P}\frac{\partial}{\partial z}\left(\frac{y_i P}{T}v\right) - \frac{RT}{P}\frac{1-\epsilon}{\epsilon}\frac{\partial q_i}{\partial t}$
Mass transfer rate	$\frac{\partial q_i}{\partial t} = k_i\left(q_i^* - q_i\right);\ k_i = \frac{C_i}{q_i^*}\frac{15\epsilon_{\text{P}}D_{\text{P}}}{r_{\text{P}}^2}\ ;\ D_{\text{P}} = \frac{D_{\text{M}}}{\tau}$
Pressure drop	$-\frac{\partial P}{\partial z} = \frac{150}{4}\frac{1}{r_{\text{p}}^2}\left(\frac{1-\epsilon}{\epsilon}\right)^2\mu v$
Column energy balance	$\left[\frac{1-\epsilon}{\epsilon}\left(\rho_{\text{s}}C_{\text{p,s}} + C_{\text{p,a}}\sum_{i=1}^{n_{\text{comp}}}q_i\right)\right]\frac{\partial T}{\partial t} = \frac{K_z}{\epsilon}\frac{\partial^2 T}{\partial z^2} - \frac{C_{\text{p,g}}}{R}\frac{\partial}{\partial z}(vP) - \frac{C_{\text{p,g}}}{R}\frac{\partial P}{\partial t} - \frac{1-\epsilon}{\epsilon}C_{\text{p,a}}T\sum_{i=1}^{n_{\text{comp}}}\frac{\partial q_i}{\partial t} + \frac{1-\epsilon}{\epsilon}\sum_{i=1}^{n_{\text{comp}}}\left(\left(-\Delta H_i\right)\frac{\partial q_i}{\partial t}\right) - \frac{2h_{\text{in}}}{\epsilon r_{\text{in}}}\left(T - T_{\text{w}}\right)$
Wall energy balance	$\rho_{\text{w}}C_{\text{p,w}}\frac{\partial T_{\text{w}}}{\partial t} = K_{\text{w}}\frac{\partial^2 T_{\text{w}}}{\partial z^2} + \frac{2r_{\text{in}}h_{\text{in}}}{r_{\text{out}}^2 - r_{\text{in}}^2}\left(T - T_{\text{w}}\right) - \frac{2r_{\text{out}}h_{\text{out}}}{r_{\text{out}}^2 - r_{\text{in}}^2}\left(T_{\text{w}} - T_{\text{a}}\right)$

Table A.2: Equations for modeling adsorption column dynamics.

A.4 Geometric Property Calculations

All geometric properties of the materials reported in this study were calculated using the zeo++ software package [165].

A.5 VSA Simulator

The constitutive transport equations were obtained based on the following assumptions:

- Axially dispersed plug flow model was employed to represent the bulk gas flow
- The gas-phase obeys ideal gas law
- Particle size was assumed to be constant for all the MOFs
- The solid-phase mass transfer was described using a linear driving force (LDF) model. Just as is the case for Zeolite 13X pellets, The mass transfer in the crystals are assumed to be fast and resistance is controlled by molecular diffusion in macropores.
- No radial gradients for concentration, temperature and pressure along the column
- Darcy's law accounts for frictional pressure drop along the column in the axial direction
- Thermal equilibrium exists between the gas-phase and solid-phase inside the column
- The outer surface of the column is maintained at a constant temperature and heat transfer occurs across the column wall
- The particle properties and bed voidage are uniform across the column

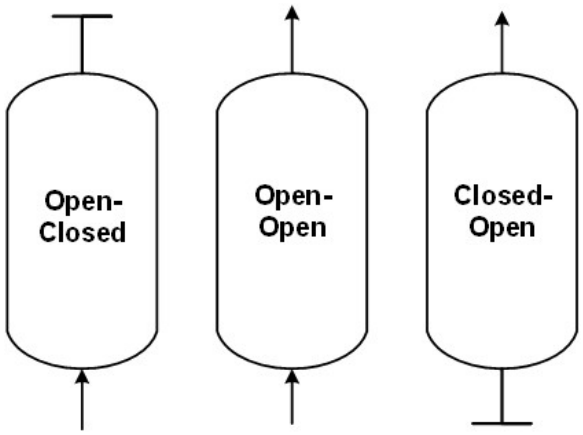

Figure A.2: Typical operating configurations of the constituent steps in a P/VSA cycle

Step	z=0	z=L
OPEN-CLOSED	$P\|_{\mathrm{z=0}} = P_{\mathrm{L}} + (P_{\mathrm{H}} - P_{\mathrm{L}})e^{(-\alpha_{\mathrm{PRESS}}t)}$	$\frac{\partial y_i}{\partial \mathrm{z}}\big\|_{\mathrm{z=L}} = 0$
	$D_L \frac{\partial y_i}{\partial z}\big\|_{\mathrm{z=0}} = -v\|_{\mathrm{z=0}} (y_{i,\mathrm{F}} - y_i\|_{\mathrm{z=0}})$	$\frac{\partial P}{\partial \mathrm{z}}\big\|_{\mathrm{z=L}} = 0$
	$\frac{\partial \mathrm{T}}{\partial \mathrm{z}}\big\|_{\mathrm{z=0}} = -\epsilon\, v\|_{\mathrm{z=0}}\, \rho_{\mathrm{g}} \mathrm{C}_{\mathrm{p,g}(\mathrm{T_F} - \mathrm{T}\|_{\mathrm{z=0}})}$	$\frac{\partial \mathrm{T}}{\partial \mathrm{z}}\big\|_{\mathrm{z=L}} = 0$
	$T_{\mathrm{w}}\|_{\mathrm{z=0}} = T_{\mathrm{a}}$	$T_{\mathrm{w}}\|_{\mathrm{z=L}} = T_{\mathrm{a}}$
OPEN-OPEN	$v\|_{\mathrm{z=0}} = v_{\mathrm{F}}$	$P\|_{\mathrm{z=L}} = P_{\mathrm{H}}$
	$D_L \frac{\partial y_i}{\partial z}\big\|_{\mathrm{z=0}} = -v\|_{\mathrm{z=0}} (y_{i,\mathrm{F}} - y_i\|_{\mathrm{z=0}})$	$\frac{\partial y_i}{\partial z}\big\|_{\mathrm{z=L}} = 0$
	$\frac{\partial T}{\partial z}\big\|_{\mathrm{z=0}} = -\epsilon\, v\|_{\mathrm{z=0}}\, \rho_g C_{p,\mathrm{g}}(T_F - T\|_{\mathrm{z=0}})$	$\frac{\partial T}{\partial z}\big\|_{\mathrm{z=L}} = 0$
	$T_{\mathrm{w}}\|_{\mathrm{z=0}} = T_{\mathrm{a}}$	$T_{\mathrm{w}}\|_{\mathrm{z=L}} = T_{\mathrm{a}}$
CLOSED-OPEN (BLO)	$v\|_{\mathrm{z=0}} = 0$	$P\|_{\mathrm{z=L}} = P_{\mathrm{H}} + (P_{\mathrm{INT}} - P_{\mathrm{H}})e^{(-\alpha_{\mathrm{BLO}}t)}$;
	$\frac{\partial y_i}{\partial z}\big\|_{\mathrm{z=0}} = 0$	$\frac{\partial y_i}{\partial z}\big\|_{\mathrm{z=L}} = 0$
	$\frac{\partial T}{\partial z}\big\|_{\mathrm{z=0}} = 0$	$\frac{\partial T}{\partial z}\big\|_{\mathrm{z=L}} = 0$
	$\frac{\partial P}{\partial z}\big\|_{\mathrm{z=0}} = 0$	$T_{\mathrm{w}}\|_{\mathrm{z=L}} = T_{\mathrm{a}}$
CLOSED-OPEN (EVAC)	$P\|_{\mathrm{z=0}} = P_{\mathrm{INT}} + (P_{\mathrm{L}} - P_{\mathrm{INT}})e^{(-\alpha_{\mathrm{EVAC}}t)}$;	$v\|_{\mathrm{z=L}} = 0$
	$\frac{\partial y_i}{\partial z}\big\|_{\mathrm{z=0}} = 0$	$\frac{\partial y_i}{\partial z}\big\|_{\mathrm{z=L}} = 0$
	$\frac{\partial T}{\partial z}\big\|_{\mathrm{z=0}} = 0$	$\frac{\partial T}{\partial z}\big\|_{\mathrm{z=L}} = 0$
	$T_{\mathrm{w}}\|_{\mathrm{z=0}} = T_{\mathrm{a}}$	$\frac{\partial P}{\partial z}\big\|_{\mathrm{z=L}} = 0$

Table A.3: Boundary conditions for the typical steps in a cyclic adsorption process.

Key Performance indicators	
$\text{Energy}\left[\frac{\text{kWh}_\text{e}}{\text{tonne CO}_2\text{ captured}}\right]$	$\frac{E_{\text{ADS}} + E_{\text{BLO}} + E_{\text{EVAC}}}{\text{Mass of CO}_2\text{ in evacuation product}}$
E_{ADS}	$\frac{1}{\eta}\epsilon\pi r_{\text{in}}^2 \frac{\gamma}{\gamma-1} \int_{t=0}^{t=t_{\text{ADS}}} (vP(t)) \left[\left(\frac{P(t)}{P_{\text{atm}}}\right)^{\frac{\gamma-1}{\gamma}} - 1\right] dt$
E_{BLO}	$\frac{1}{\eta}\epsilon\pi r_{\text{in}}^2 \frac{\gamma}{\gamma-1} \int_{t=0}^{t=t_{\text{BLO}}} (vP(t)) \left[\left(\frac{P_{\text{atm}}}{P(t)}\right)^{\frac{\gamma-1}{\gamma}} - 1\right] dt$
E_{EVAC}	$\frac{1}{\eta}\epsilon\pi r_{\text{in}}^2 \frac{\gamma}{\gamma-1} \int_{t=0}^{t=t_{\text{EVAC}}} (vP(t)) \left[\left(\frac{P_{\text{atm}}}{P(t)}\right)^{\frac{\gamma-1}{\gamma}} - 1\right] dt$

Table A.4: Equations for the key performance indicators.

A.6 Parasitic Energy

A.6.1 VSA Energy

E_i represents the energy consumption in step i. The energy consumption E_i for blowdown and evacuation steps represent the vacuum pump energy consumption with a delivery pressure of 1 bar. In the above equation, a vacuum pump efficiency of 72% was used.

A.6.2 Compression Energy Contribution

An additional compression term was added to the VSA simulator to include the energetic requirement of compressing the outlet gas to 150 bar [26, 67, 165] for transportation. An approach proposed in the literature is followed to compute energy contribution towards multi-stage compression. The compression term is split into two components (equation A.4): the energy required ($E_{\text{Compressor}}$) to compressCO_2 in multiple stages up to 80 bar [166], and the energy required (E_{Pump}) to run the pump to deliverCO_2 at 150 bar and 313.15 K.

$$Energy_{\text{Compression}} = Energy_{\text{Compressor}} + Energy_{\text{Pump}} \tag{A.4}$$

In equation A.4, S represents the number of compression stages required to compress CO_2 to pressure of 80 bar from an initial pressure of 1 bar. The value of S can be calculated using equation A.5.

$$E_{comp} = S\frac{n_{total}RT}{\eta_{comp}}\frac{\gamma-1}{\gamma}[Y^{\frac{\gamma-1}{\gamma}} - 1]dt \tag{A.5}$$

$$S = \frac{lnr_{\text{T}}}{lnr_{\text{i}}} \tag{A.6}$$

$$r_{\text{i}} = \frac{P_{\text{High}}}{P_{\text{Low}}} \tag{A.7}$$

The variables r_T and r_i are the total compression ratio and the maximum compression ratio achievable in a single stage. A single stage compressor is set to provide

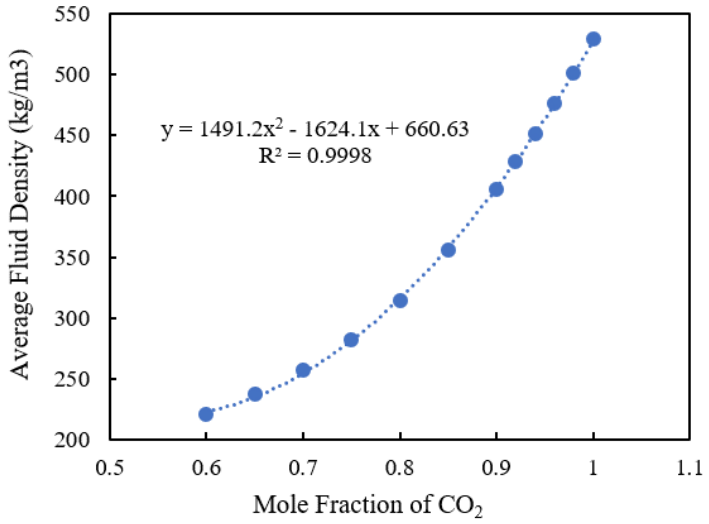

Figure A.3: Fitted plot of the average fluid density of CO_2/N_2 mixture as a function of the mole fraction of CO_2. Points represent the NIST values and the dotted line represents the fit.

a maximum compression ratio of 2.518. A compressor efficiency of 85% was used in this work. The second term in equation A.4 is calculated using,

$$E_{Pump} = \frac{\Delta P m_{tot}}{\eta_{pump}\rho} \tag{A.8}$$

The variables m_{tot} and η pump are the mass flow rate and pump efficiency. The pump efficiency used for this calculation was 75% [19]. The ΔP term is the change in pressure resulting from the use of the pump. The density of the supercritical fluid, ρ, is the average density of the fluid in kg/m^3 over the change in pressure and is defined below as a function ofCO_2 purity. The density of the supercritical fluid (ρ) in equation A.8, can be calculated as a function of CO_2 purity. To accurately determine the average fluid density over the pressure ranges being tested, a quadratic equation was fit to density values obtained from the NIST Standard Reference Database (equation A.8). The values in the equation being used were fit specifically for the defined pressure range at 313.15 K. The fit is representative of a range of CO_2 molar ratios from 0.6 to 1 and is presented in Figure A.3. If any of these properties are altered, fitting to an appropriate set of data would be required to calculate accurate fluid densities.

A.7 Simulation Methodology

The column was initially saturated withN_2 at 1 bar pressure and 25 °C. The partial differential equations (PDEs) shown above were converted to ordinary differential equations (ODEs) in time by discretizing the spatial terms using finite volume methods. The resulting ODEs were solved in MATLAB using ode23s solver. The cycles were simulated until the system has reached a cyclic steady state (CSS). The process was considered to attain CSS if the mass balance error for five consecutive cycles was less than or equal to 0.5%. The parameters used for VSA simulations are given in Table A.5.

Parameter	Type	Value
Column properties		
Bed length, L [m]	Fixed	1.0
Column inner radius, r_{in} [m]	Fixed	0.1445
Column outer radius, r_{out} [m]	Fixed	0.1620
Particle voidage, ϵ_{p} [-]	Fixed	0.35
Particle radius, r_{p} [m]	Fixed	1×10^{-3}
Density of the column wall, ρ_{w} [kg m^{-3}]	Fixed	7,800
Bed voidage, ϵ [-]	Fixed	0.37
Tortuosity factor, τ [-]	Fixed	3.0
Properties and Constants		
Effective heat conduction coefficient, K_{z} [J m^{-1} s^{-1} K^{-1}]	Fixed	0.0903
Thermal conductivity of the wall, K_{w} [W m^{-1} K^{-1}]	Fixed	16.0
Inside heat transfer coefficient, h_{in} [W m^{-2} K^{-1}]	Fixed	8.6
Outside heat transfer coefficient, h_{out} [W m^{-2} K^{-1}]	Fixed	2.5
Gas specific heat capacity, $C_{\text{p,g}}$[J kg^{-1} K^{-1}]	Fixed	1010.6
Adsorbed phase specific heat capacity, $C_{\text{p,a}}$ [J kg^{-1} K^{-1}]	Fixed	1010.6
Wall specific heat capacity, $C_{\text{p,w}}$ [J kg^{-1} K^{-1}]	Fixed	502.0
Adiabatic constant, γ [-]	Fixed	1.4
Universal gas constant, R [m^3 Pa mol^{-1} K^{-1}]	Fixed	8.314
Fluid viscosity, μ [kg m^{-1} s^{-1}]	Fixed	1.72×10^{-5}
Molecular diffusivity, D_{M} [m^2 s^{-1}]	Fixed	1.60×10^{-5}
Adsorbent specific heat capacity, $C_{\text{p,s}}$ [J kg^{-1} K^{-1}]	Fixed	1070
Operating Conditions		
Heat of adsorption of CO_2, ΔU_{CO_2} [kJ mol^{-1}]	Variable	-20 to -42
Heat of adsorption of N_2, ΔU_{N_2} [kJ mol^{-1}]	Variable	-5 to -18

Table A.5: Simulation parameters for VSA simulations

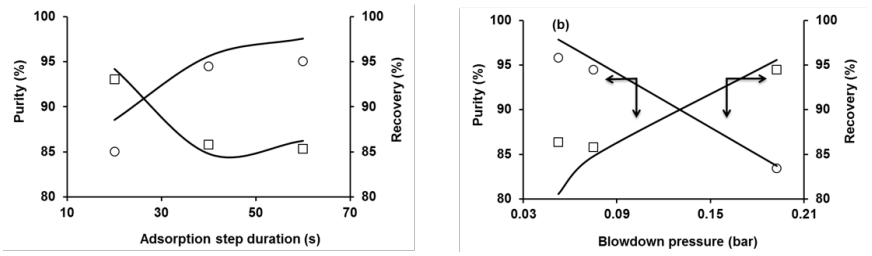

Figure A.4: Effect of (a) adsorption step time (b) blowdown pressure on purity and recovery. Symbols represent the pilot plant experiments while the lines represent the model predictions. [75]

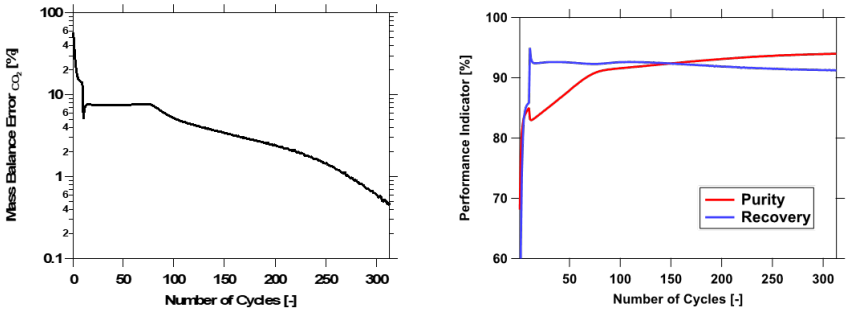

Figure A.5: Convergence of (a) mass balance error (b) CO_2 purity and recovery after the VSA process has reached CSS. LABGAY MOF with isotherm shown in Fig.A.1 (b) was used for this case study.

A.7.1 Validation of VSA model

The VSA model used in this work was validated using pilot-scale experiments. Figure A.4 represents the effect of adsorption time and blowdown pressure on the purity and recovery of the CO_2. As it can be seen from the figure, the model predictions are matched well with the experimental CO_2 purities and recoveries [75].

The VSA process is said to attain CSS when the mass balance error is less than 0.5% for five consecutive cycles and there are no changes in column state variables. The criteria for stopping the simulation is attaining the CSS. The performance indicators for the VSA process viz. Purity, Recovery, Energy and Productivity are calculated after CSS. For LABGAY MOF with isotherm shown in Fig. A.4 (b), the convergence of mass balance error, purity and recovery as calculated by the model are shown in Fig. A.5 and the operating parameters used were: t_{press} =20 s, t_{ads} =126 s, t_{bd} =21 s, t_{evac} =91 s, P_I =0.15 bar, P_L =0.02 bar. The axial profiles of CO_2 solid phase concentration, gas phase concentration and temperature across the column at the end of each step in the VSA process after CSS condition was attained are shown in Fig. A.6.

A.7.2 Grid-Search of Process Conditions

To provide an estimate of a material's performance and allow for the identification of high-performing materials without a full optimization of the process conditions, a grid-search was performed on 3 of the process variables. A total of 1000 process points were calculated for each material. The process parameters tested during this grid-search are given in Table A.6.

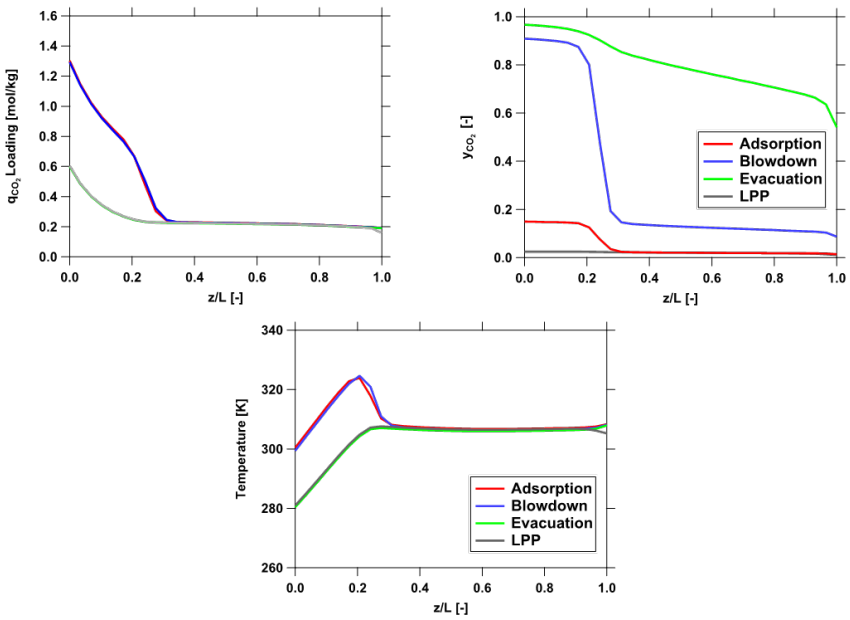

Figure A.6: Axial profiles of (a) CO_2 solid phase concentration (b) CO_2 gas phase concentration (c) Temperature across the column at the end of each step in the VSA process after the system reached CSS. LABGAY MOF with isotherm shown in Fig. A.1 (b) was used for this case study.

Parameter	Minimum	Maximum	Interval
Adsorption Time (t_{ads}), s	30	120	10
Blowdown Time (t_{blow}), s	30		Fixed
Evacuation Time (t_{evac}), s	tads + 10		Fixed
Blowdown Pressure (P_{blow}), bar	0.06	0.15	0.01
Evacuation Pressure (P_{evac}), bar	0.03		Fixed
Feed Velocity (v_0), ms^{-1}	0.1	1	0.1

Table A.6: Values and ranges used in the grid-search

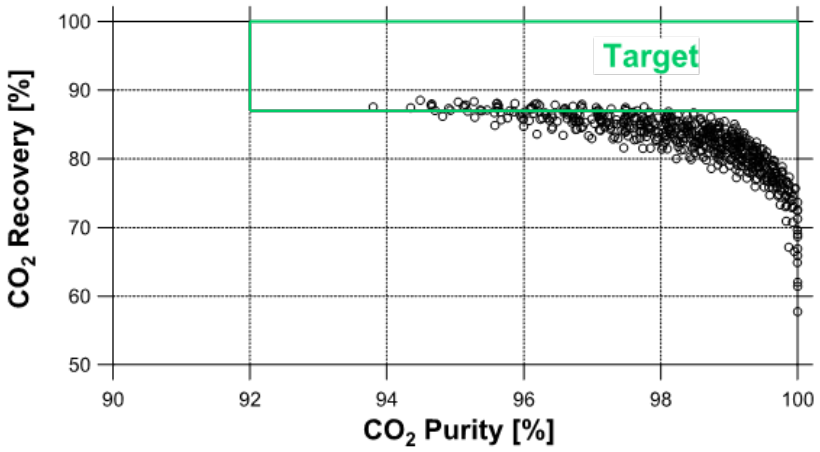

Figure A.7: CO_2 purity vs recovery obtained for LABGAY MOF during grid-search simulations.

Parameter	Minimum	Maximum
Adsorption Time (t_{ads})), s	20	200
Blowdown Time (t_{blow})), s	20	50
Evacuation Time (tevac), s	20	200
Blowdown Pressure (Pblow), bar	0.03	0.15
Evacuation Pressure (P_{evac}), bar	0.01	0.06
Feed Velocity (v0)), ms^{-1}	0.1	2.0
Feed Temperature, K	293.15	328.15

Table A.7: Process parameter ranges allowed during the GA optimization.

A.7.3 Genetic Algorithm (GA)

A genetic algorithm (GA) was used to optimize all 7 process parameters to maximize a material's productivity, minimize the parasitic energy, and attain the minimum DoE purity-recovery target (PRT) requirement of 95/90. GA is a powerful optimization technique based off Darwinian evolution used for optimization in high dimensional search spaces. These optimizations involve the generation and mating of individuals, with the 7 process parameters (Table A.7) acting as optimization values, or 'genes'. Fitness values are calculated for each member in the population, and the most fit individuals are carried forward to the next generation, whereas the remainder of the next generation is generated by combining the genes of the high performers. To ensure sampling of the whole search space, random mutations are also introduced after the mating process.

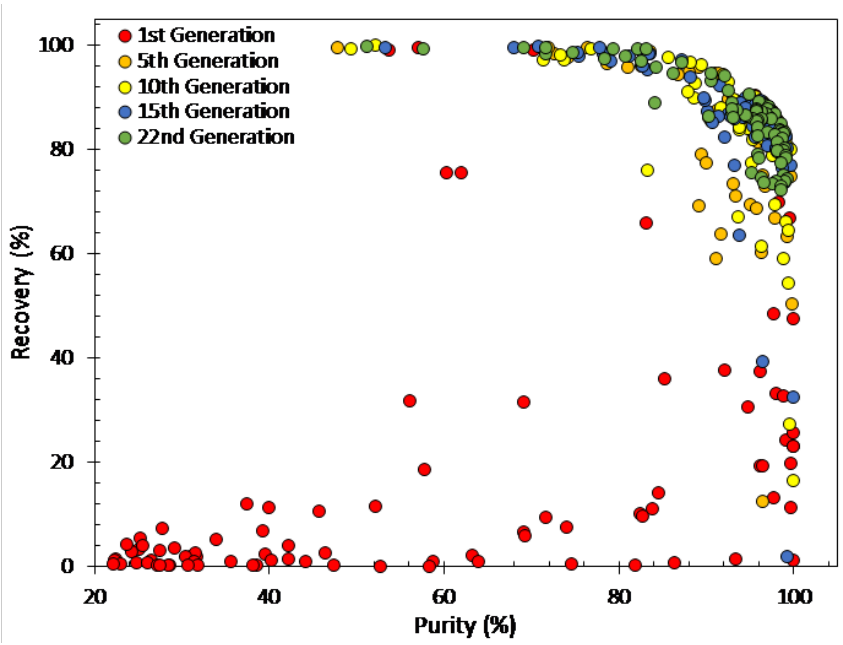

Figure A.8: CO_2 recovery vs purity obtained for LABGAY MOF for 5 generations of a genetic algorithm optimization.

Seeding is used in the GA where 10 candidate solutions (CSs) are selected randomly, where CSs with lower fitness values are more likely to be selected. The rest of the GA's initial population was generated using Latin Hypercube Sampling23 selecting CSs within the ranges described in Table S5. A population size of 100 was used. To generate subsequent generations elitism was used where the top 5 most fit CSs from the previous generation are passed unchanged into the new generation. The remaining CSs are created by using a mating procedure where the parents are selected using a roulette wheel selection based on their fitness function. Each parameter has a value randomly selected that lies between each of the parents' parameter values. After that mutations are applied where each 'gene' has a 20% chance to be mutated. If a gene is chosen to be mutated, its value can change up to 20% of the total range for that value, shown in Table A.7 (i.e. up to 18 s if the value is the adsorption time). The new generation is tested using the PSA simulator, at which point the procedure repeats. This process continues until the top performing structure remains constant for 10 consecutive generations. Each material had GA optimization performed a minimum 3 times to ensure the search space is well sampled by the GA. The effectiveness of this optimization procedure is demonstrated in Figure A.14, where the purity and recovery values of each generation show a marked improvement as the number of generations tested is increased. The poorest distribution of purity/recovery values is seen in the 1st generation compared to the high purity/recovery values predicted by the 22nd generation.

A.7.4 Objective Function

To achieve a multi-objective optimization a fitness function needed to be devised to appropriately scale all target variables. The GA begins by optimizing the purity and recovery while ignoring the productivity and parasitic energies. This step was found to be essential during this study, as GAs attempted without this initial optimization had great difficulty meeting the DoE requirements. The fitness function for this initial optimization is calculated using a scaled distance function:

Parameter	Minimum	Target	Unit
Purity	95	100	%
Recovery	90	100	%
Parasitic Energy	250	135	kWh/t
Productivity	0.5	3.5	mol/m^{3}s

Table A.8: Values used in the fitness function to scale the performance parameters.

$$Fitness = \sqrt{\frac{P_{Target} - P_i}{P_{Target} - P_{DOE}}^2 + \frac{R_{Target} - R_i}{R_{Target} - R_{DOE}}^2} \tag{A.9}$$

P_i = purity at point i
R_i = recovery at point i
target = 100 %
DoE = Minimum value set by DoE

Once 20% of a generation's population has met the DoE PRT, the GA switches to a constrained energy/productivity optimization, with a penalty function for any individuals in the population which do not meet the DoE targets. The new fitness function used is:

$$\text{Fitness}=\sqrt{\frac{\text{E}_{\text{Target}}-\text{E}_{\text{i}}}{\text{E}_{\text{Target}}-\text{E}_{\text{DOE}}}^2 + \frac{\text{Pr}_{\text{Target}}-\text{Pr}_{\text{i}}}{\text{Pr}_{\text{Target}}-\text{Pr}_{\text{DOE}}}^2 + \text{P}_{\text{Err}} + \text{R}_{\text{Err}}}$$

$$P_{Err} = \{if P_i \leq P_{DoE}, 10,000 \times (P_{DoE} - P_i) P_{Err} = \{if P_i \geq P_{DoE}, 0) \tag{A.10}$$

$$R_{Err} = \{if R_i \leq R_{DoE}, 10,000 \times (R_{DoE} - R_i)$$

$$\text{R}_{Err} = \{if R_i \geq R_{DoE}, 0) \tag{A.11}$$

E_i = parasitic energy at point i
Pr_i = productivity at point i
target = best possible energy/productivity
min = minimum value chosen to balance the fitness function

These fitness functions are distance functions which the GA attempts to minimize, with the ideal value being 0. The denominators in the fitness function act to scale each individual target variable to ensure that no one variable dominates the fitness function. The error functions introduced in the Energy/Productivity optimization's fitness function act to constrain the fitness function so that points below the DoE PRT are heavily penalized and therefore get rejected by the GA. The behavior of the fitness values as a function of GA population is shown in Figure S8 for the LABGAY MOF material. This figure shows a distinct improvement in the average fitness of the population as the number of generations increases. The best candidate solution for each generation (shown in blue diamonds) shows only minor improvement. This can be explained by the seeding of the initial population providing a good guess of the global minimum value, and therefore only minor improvement is made to those candidate solutions over the course of the optimization.

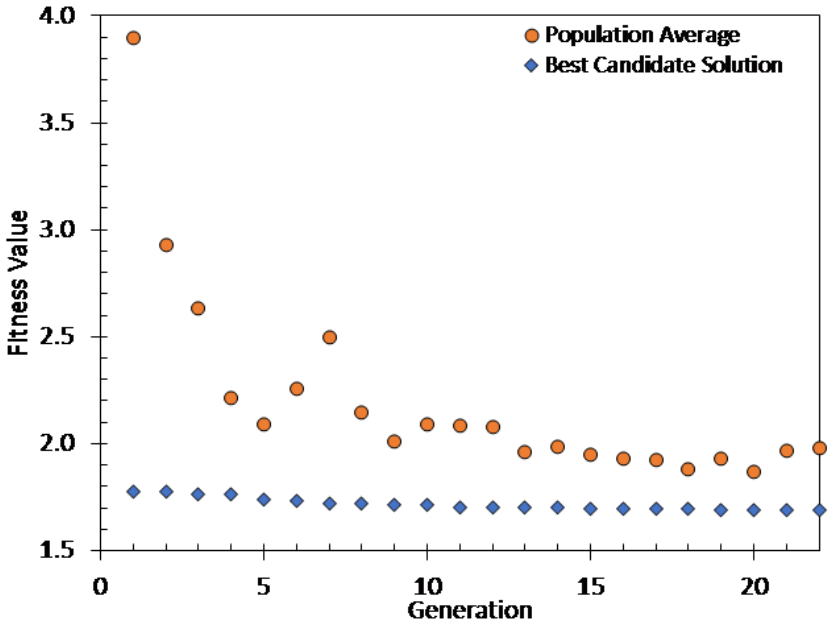

Figure A.9: The average population fitness value (green circles) and the best candidate solution fitness values (blue diamonds) as a function of generation over the course of a single optimization of LABGAY MOF.

Parameter	Minimum	Target	Unit
Parasitic Energy	300	200	kWh/t
Productivity	1.0	3.0	$mol/m^3/s$

Table A.9: Values used in the fitness function to scale the performance parameters.

A.7.5 Top 12 Materials

Table 1 of the main text describes balanced process points selected for each of the top 12 materials. The balanced points were those process points which met the 95/90-PRT while having PE values below 250 kWh/MT CO_2 and productivities greater than Zeolite-13X (1.1 $molCO_2$ m^{-3} s^{-1}). The points were selected based on the fitness function described by equation S41 with slightly modified boundaries. The boundaries were updated once the GA's were completed and reflect a better balance of PE and productivity. These new boundaries are given in Table A.9.

A.7.6 Random Forest Decision Tree Modelling

Random forest models were built using decision trees generated with the scikit-learn decision tree package in python 2.7.17 For these fittings, 2 classifications were used: 1) MOFs which are able to meet the DoE Purity/Recovery Target (PRT) and 2) MOFs which fail the DoE PRT. This target is the bare minimum requirement for material to be a viable candidate for use in this separation and therefore the ability to predict this property is crucial for the materials discovery process. All classifications were performed using a rigid cut-off of 95% purity and 90% recovery was used. The data

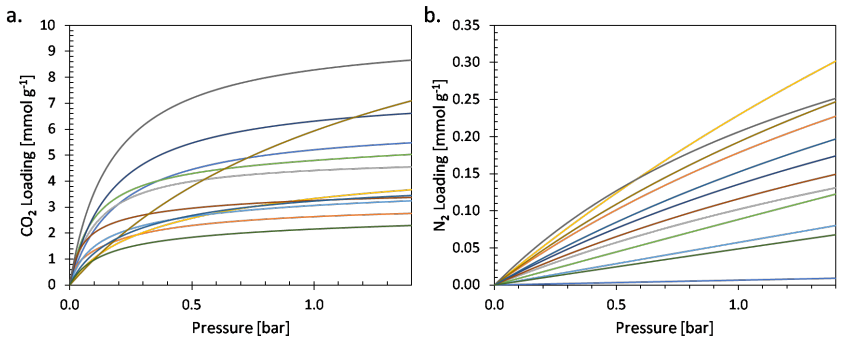

Figure A.10: Single component a) CO_2 isotherms and b) N_2 isotherms for the 12 materials in Table 2.1.

set consisted of 1632 MOF structures which had undergone a full grid-search or GA optimization. Out of the total 1632 MOFs, only 392 materials met the DoE PRT. This means that if one were to randomly select a material there is a 24.0% chance it can meet the DoE PRT. These models were fit using the geometric descriptors used are presented in Table A.10 as well as the conventional metrics fittings were performed using the descriptors listed in Table 2.2 For each random forest model fitting, the data set was randomized with 90% of the MOFs selected for training and the remaining 10% set aside for validation. Each forest contained 21 decision trees, each of which were fit at depths from 1 to 10. Selection of the depth used in the model for each individual tree was done by selecting the depth which returned the highest Matthews correlation coefficient (MCC) value given by equation S47 from a five-fold cross validation. The decision to use MCC over other performance metrics because it is designed for imbalanced datasets such the one used in the study. Once each tree is fit to the optimal depth, the random forest model is then assembled, and the validation set is tested. Each individual MOF in the validation set passes through each tree in the forest and therefore gets classified 21 times. The random forest model then considers the results of the 21 classifications and returns the classification that appears most frequently for that MOF. For example, a MOF is fed into the random forest and 8 of the 21 trees return a pass whereas the remaining 13 trees return a fail. The model therefore determines that this material will fail the DoE PRT. Several accuracy metrics can be used to measure the effectiveness of this classifier, all of which give a different view of the data. Precision determined using equation S43, is a representation percentage of materials classified as DoE materials using the decision tree which can meet the DoE PRT. For example, a precision of 50% would mean that only half of the materials the decision tree classifies as a DoE material will be able to meet the PRT. Negative Predictive Value (NPV), given by equation S44, is analogous the precision but considers the fraction of materials classified as failing to meet the DoE PRT which are true negative values. Recall, given by equation S45, is a measure of how accurately the decision tree model can find true positive values, or values which meet the DoE. Overall accuracy given in equation S46 is a representation of the model's ability to correctly classify all materials. Finally the Matthews correlation coefficient (MCC), given by equation S47, is an overall representation of the model's effectiveness, where a value of -1 means that the model is completely inaccurate, 1 means the model is perfectly accurate, and a value of 0 is returned when all points are either assigned to a "pass" state or a "failed" state (for example TP + FP = 0 or TN + FN = 0).

$$Precision = \frac{TP}{(TP + FP)} \times 100\% \tag{A.12}$$

Geometric Descriptors	Units
Maximum Accessible Pore Diameter	$\mathring{A}$
Maximum Channel Diameter	$\mathring{A}$
Maximum Pore Diameter	$\mathring{A}$
Gravimetric Surface Area	m^2/g
Volumetric Surface Area	m^2/cm^3
Void Fraction	[-]
Free Volume	cm^3/g
Crystal Density	kg/m3

Table A.10: List of all geometric descriptors used in decision tree fittings.

$$NVP = \frac{TN}{(TN + FN)} \times 100\% \tag{A.13}$$

$$Recall = \frac{TP + TN}{(TP + FN)} \times 100\% \tag{A.14}$$

$$Overallaccuracy = \frac{TP}{TN + FN + TP + FP} \times 100\% \tag{A.15}$$

$$MCC = \frac{((TP \times TN) - (FP \times FN))}{\sqrt{((TP + FP)(TP + FN)(TN + FP)(TN + FN))}} \tag{A.16}$$

A.7.7 Univariate Analysis

In this section, statistical analysis was performed for all the MOFs that were considered for grid-search simulations. The univariate probability distributions based on different metrics and structural properties were obtained to identify the characteristics of different classes of materials i.e. 1) Top 150 (coded in black); 2) DOE (coded in blue) and; 3) Non-DOE (coded in red). Fig. S10 compares the univariate probability distributions of different metrics for three classes of materials. The univariate probability distributions are obtained using kernel (Gaussian) density estimation in MATLAB.18 The kernel density estimator is given by:

$$\hat{f_h}(x) = \frac{1}{nh} \Sigma_{j=1}^{n} K \frac{x - x_i}{h} \tag{A.17}$$

Where x_1, x_2, x_3..x_n are the data samples from an unknown distribution, n is the sample size and K is the normal (Gaussian) kernel smoothing function employed in this analysis; h is the default bandwidth which is theoretically optimal for estimating normal distribution densities.19 The black shaded area represents the Top 150 MOFs; blue shaded area represents the MOFs that met 95/90 PRT requirements; and the red shaded area represents the MOFs that did not meet 95/90 PRT requirements. As it can be seen from the Fig. A.11, all the three curves overlap for most of the metrics,

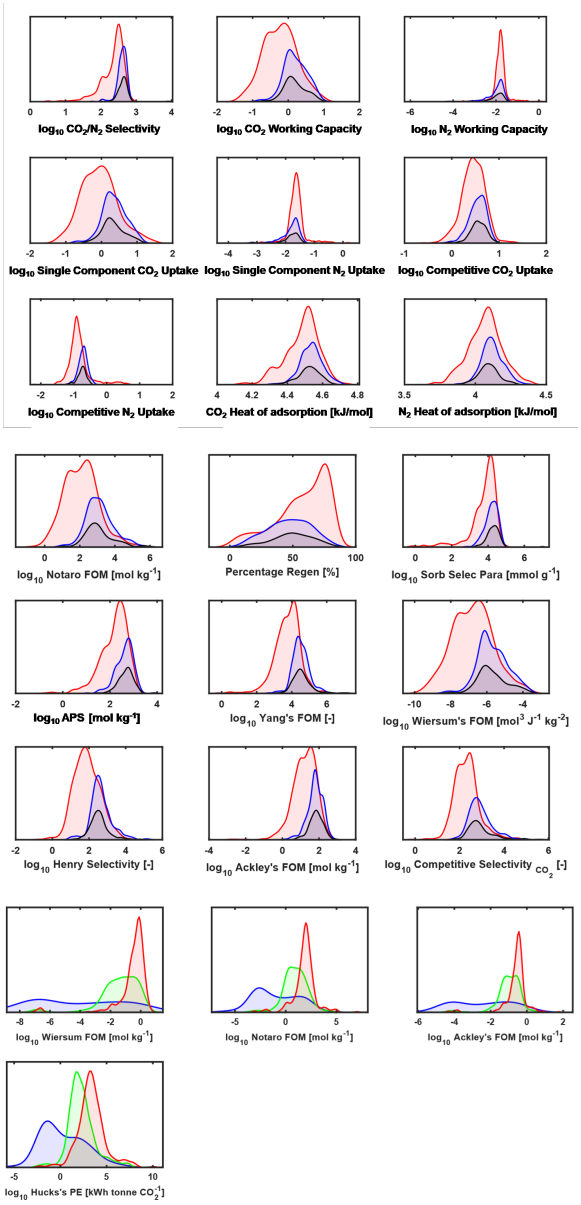

Figure A.11: Comparison of univariate probability distributions of different metrics for three classes of materials, i.e. 1) Top 150 (shaded in black) 2) DOE (shaded in blue) 3) Non-DOE (shaded in red)

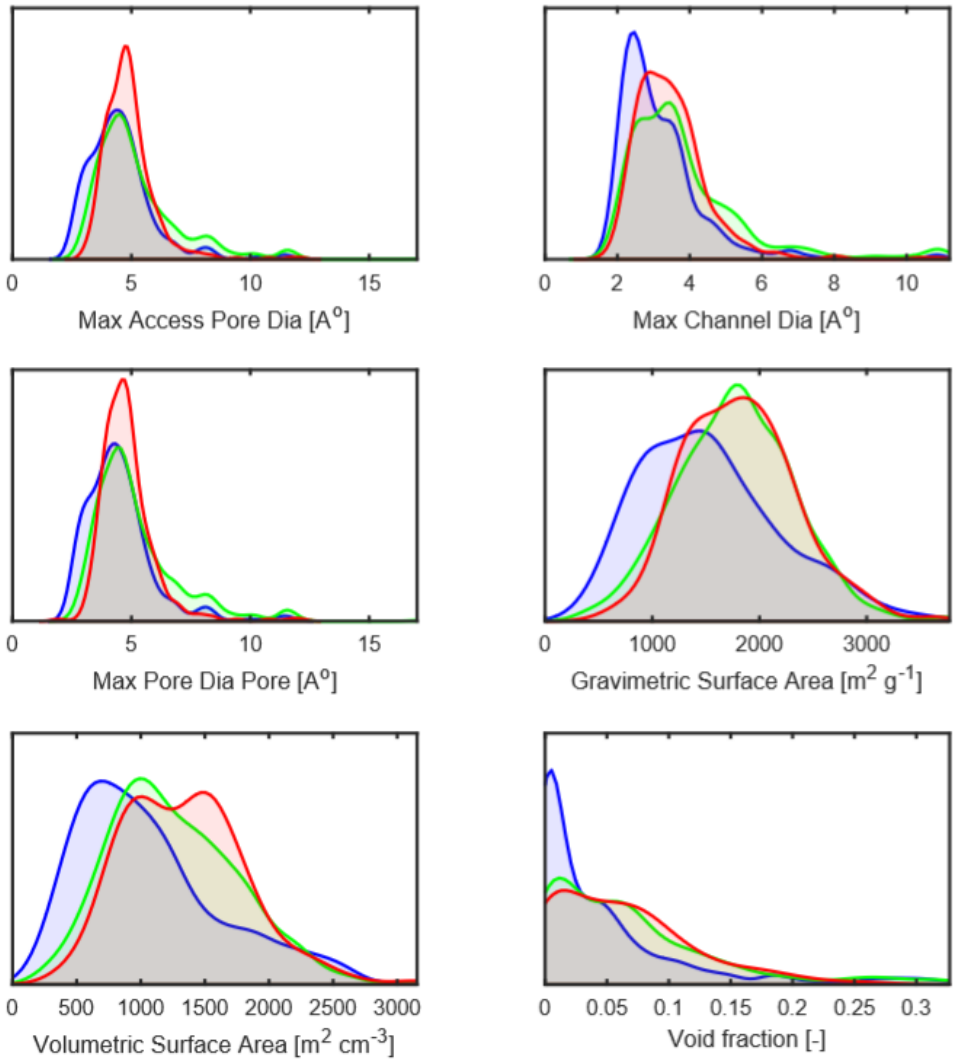

Figure A.12: Comparison of univariate probability distributions of structural properties for three classes of materials, i.e. 1) Top 150 (shaded in black), 2) DOE (shaded in blue), 3) Non-DOE (shaded in red)

indicating that there is no clear distinction for these three classes of materials. Some of the metrics like Separation potential and Notaro show targeted regions for achieving good MOFs but cannot guarantee because the targeted regions are contaminated with poor performing MOFs as well.

Figure A.12 represents the univariate probability distributions of structural properties for the three classes of materials. Similar to Fig. S10, there is no clear distinction among the curves indicating that the desired characteristics cannot be targeted during the synthesis.

A.7.8 Linear Discriminant Analysis (LDA)

Linear discriminant analysis was performed on up to 2 metrics listed in Table 1. The goal of the classifications was to attempt the prediction of whether a material can meet the DoE PRT using the data gathered from the grid-search. This analysis was

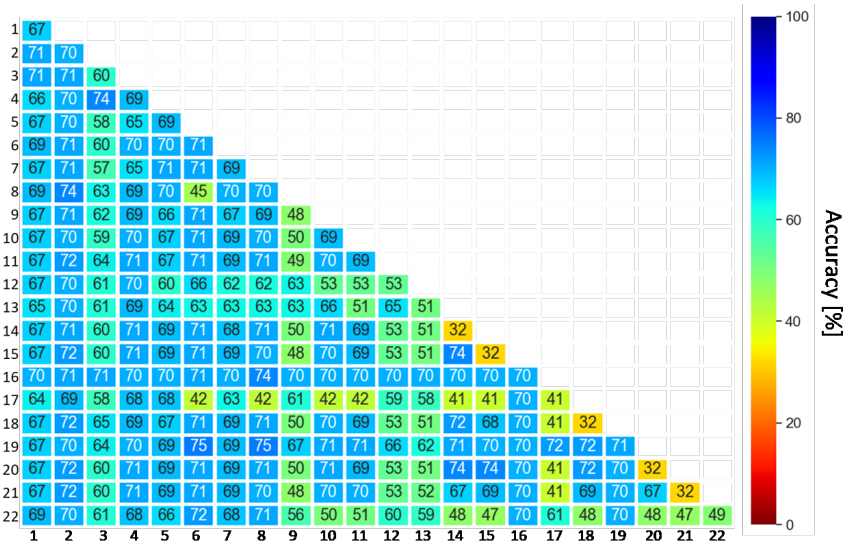

Figure A.13: Best accuracy points from LDA analysis for all 22 performance metrics, with the numbers on the axes corresponding to the metrics in Table1. The diagonal on these matrices contain the 1-dimensional LDA results for each parameter and the off-diagonal entries contain the 2-dimensional LDA model results.

performed on 1632 materials in which 370 (22.7%) met the DoE PRT. Since 77.3% of the data set failed the DoE PRT, there was a data imbalance which would cause the LDA to always set every material to fail, resulting in an overall accuracy of 77.3%. To improve the classification of these models, a cost of misclassification was added to the "pass" cases to optimize the Matthews correlation coefficient (MCC) instead of the overall accuracy. The cost was varied from 0 to 1, and the value with the highest MCC was chosen for each metric, or combination of metrics. This improved the models, allowing for a more balanced and representative separation in the data. Figure A.13 shows all accuracy values for LDAs consisting of a single metric along the diagonal, and the combinations of metrics in the off-diagonal region of the matrix. Figure A.14 shows MCC values, Figure S14 shows the precision values, and Figure S15 show the recall values for those same metrics at the best MCC point. Figure S16a, b, c, and d present the, accuracies, MCC values, precision values, and the recall values for the geometric properties, respectively.

A.7.9 Principal Component Analysis (PCA)

Kernel Principal Component Analysis (PCA) allows us to eliminate some of the features from the descriptor matrix that have a very small variance, and thus are not very important for the description of a given dataset. Moreover, PCA can be used for clear and more understandable visual representation, because it is very convenient to visualize data in two dimensions. Thus, we have performed PCA of the process simulation data described by a set of 24 parameters (the features) and collected for 1550 (number of samples) experimental Metal Organic Frameworks (MOFs). Note that none of the geometrical descriptors have been included in that set of 24 parameters. Further, all MOFs in our data set belong to one of the three classes: MOFs that do not meet the 95/90 purity-recovery requirements, MOFs that meet 95/90 purity-recovery targets but whose parasitic energy is above 257 kWh/t CO_2 or 925.2 kJ/kg CO_2, and MOFs that meet 95/90 purity-recovery targets whose parasitic energy is

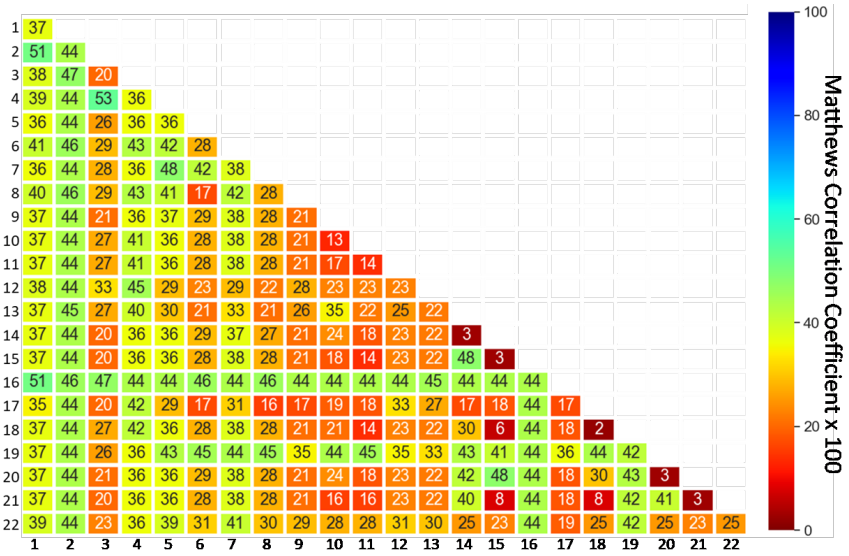

Figure A.14: Best MCC points from LDA analysis for all 22 performance metrics, with the numbers on the axes corresponding to the metrics in Table1. The diagonal on these matrices contain the 1-dimensional LDA results for each parameter and the off-diagonal entries contain the 2-dimensional LDA model results.

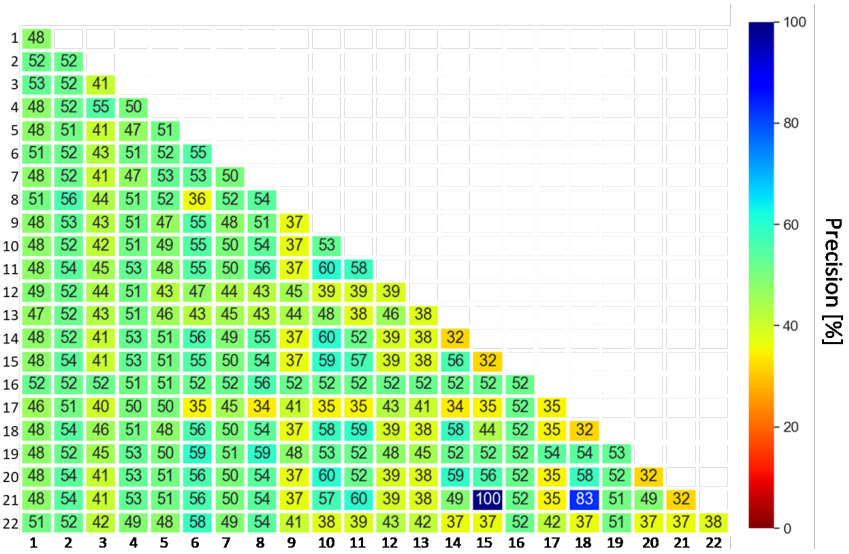

Figure A.15: Precision for the best MCC points from LDA analysis for all 22 performance metrics, with the numbers on the axes corresponding to the metrics in Table1. The diagonal on these matrices contain the 1-dimensional LDA results for each parameter and the off-diagonal entries contain the 2-dimensional LDA model results.

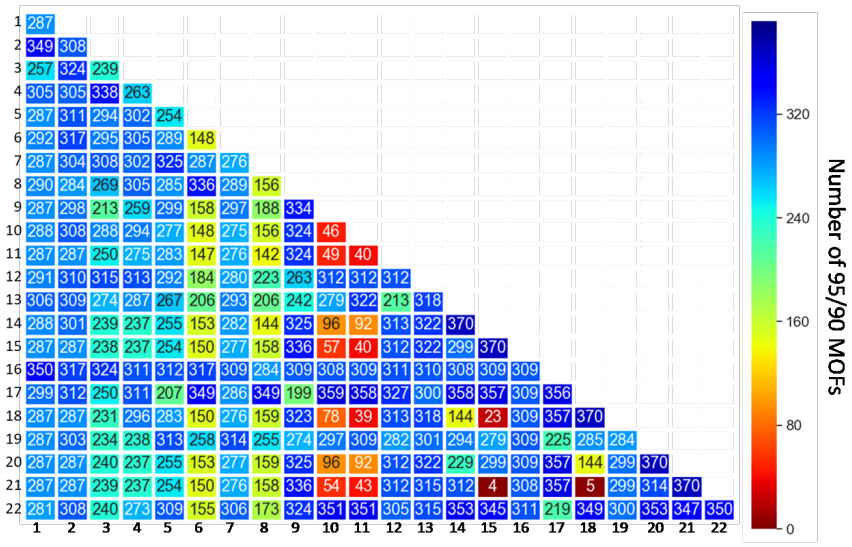

Figure A.16: Number of 95/90-PRT MOFs identified out of 392 for the best MCC points from LDA analysis for all 22 performance metrics, with the numbers on the axes corresponding to the metrics in Table1. The diagonal on these matrices contain the 1-dimensional LDA results for each parameter and the off-diagonal entries contain the 2-dimensional LDA model results.

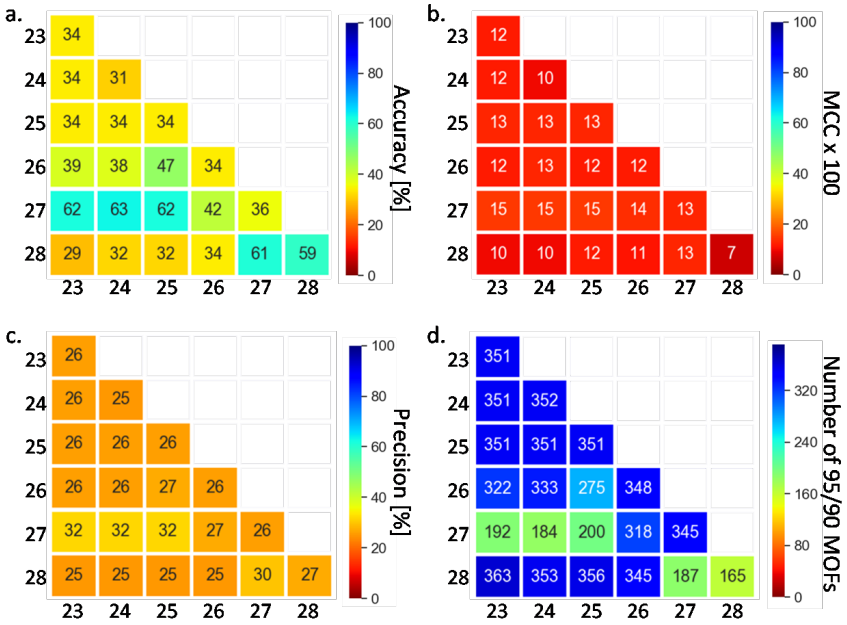

Figure A.17: Results from the 1 and 2-dimensional LDA analysis for the 6 structural properties. The metric numbers correspond to the metrics in Table 1. These plots present a) the overall accuracy [%] of the models, b) the MCC × 100 values of the models, c) the precision [%] of the models, and d) the recall [%] of the models. The diagonal on these matrices contain the 1-dimensional LDA results for each parameter and the off-diagonal entries contain the 2-dimensional LDA model results.

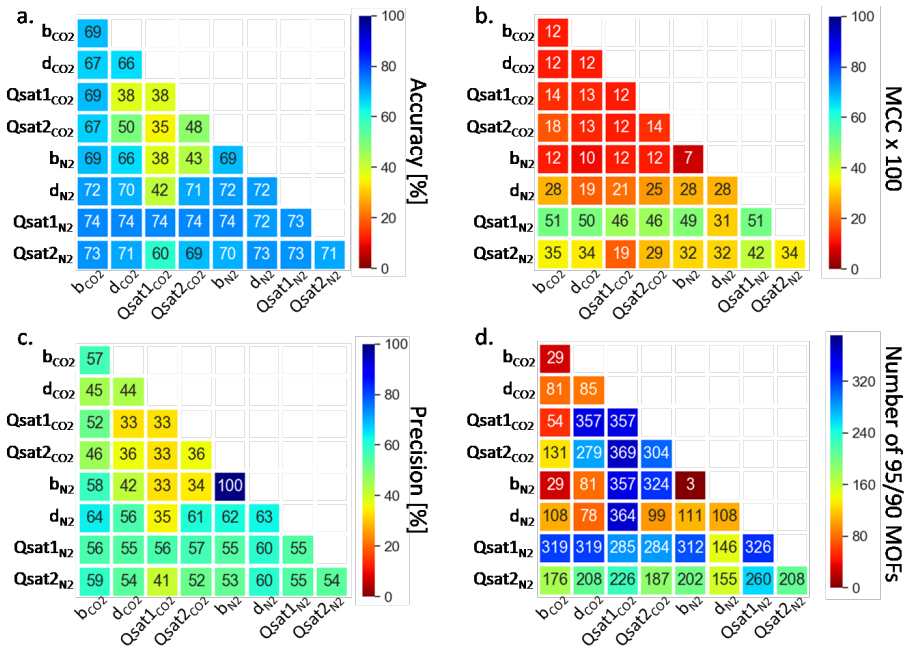

Figure A.18: Results from the 1 and 2-dimensional LDA analysis for isotherm parameters showing a) the overall accuracy of the models, b) the MCC of the models, c) the Precision of the models, and d) the number of 95/90 PRT MOFs identified by the models. The diagonal on these matrices contain the 1-dimensional LDA results for each parameter and the off-diagonal entries contain the 2-dimensional LDA model results.

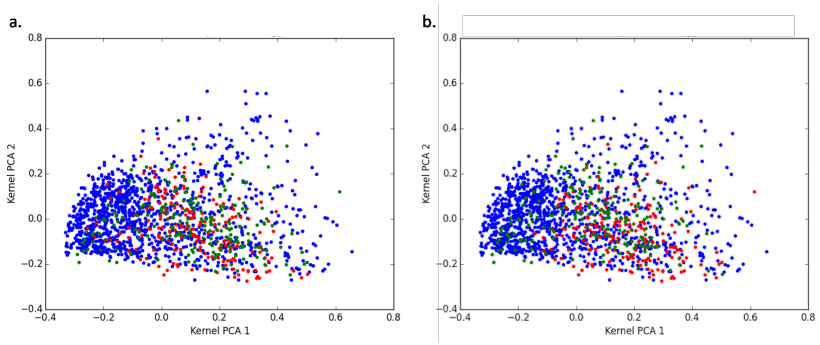

Figure A.19: Kernel PCA plots for materials separated by a) parasitic energy, and b) productivity where blue points represent MOFs which failed the DoE PRT, red points are materials which meet the PRT and the best points are worse than the Pe/Prod median value, and green are materials which meet the PRT and whose best points outperform the median value.

below 257 kWh/t CO_2. The mentioned classes are shown in Figure S18 as blue, red and green circles, respectively, in the space of the first two principal components. The PCA features are dimensionless and constructed from linear combinations of all metrics.

As we can see, the three classes of MOFs are not distinguishable and are on top of each other. To investigate further, the PCA was performed on one the materials which met the DoE PRT to determine whether this method could distinguish the two remaining classes of materials. This analysis was performed for both the Parasitic Energy, the results of which are shown in Figure 3c, and for the Productivity shown in Figure A.20. For both the parasitic energy and the productivity, this analysis showed that the PCA is not able to distinguish between the two classes, indicating that the set of descriptors used in this analysis are not suitable for use in predicting these two valuable industrial performance metrics.

A.7.10 Machine Learning Models for Parasitic Energy and Productivity

The objective of this work was to determine whether the parasitic energies or productivities of the MOF materials optimized for post-combustion PSA capture could be predicted using conventional metrics and isotherm parameters. This was attempted using three different techniques: support vector regression (SVR), gradient boosted decision tree regression (GBR), and an artificial neural network regression (NNR). The scikit-learn python package was used for all three methods.

The data set for this work was pulled from the original set used in the fitting of our random forest classifiers for the prediction of a material's ability to meet the DoE-PRT. The full list of descriptors used can be found in Table 1, lifted verbatim from the paper's manuscript, with the addition of the Dual-Site Langmuir parameters for CO_2 and N_2 for each material. Among the 1022 materials which have been fully optimized, 482 were able to meet the DoE-PRT. Of those 482 materials, 47 were removed since they were materials whose isotherm parameters were found in literature and whose cifs we do not have and as a result no geometric descriptors were available for these structures. The fittings were therefore performed on the remaining materials, with the best energy and best productivities selected given the DoE constraints. The data was randomly shuffled and split into training and test sets with 75% of the data being

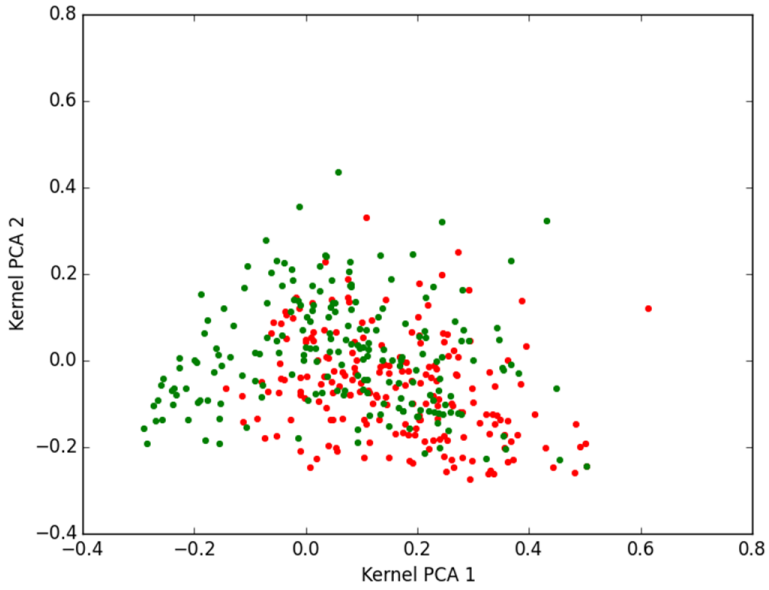

Figure A.20: Kernel PCA plots for materials separated by productivity where red points are materials which meet the PRT and the best points are worse than the Pe/Prod median value, and green are materials which meet the PRT and whose best points outperform the median value.

used for training. The data was shuffled once upon the code's import of the data sets, however each time the code is rerun the data is re-shuffled.

5-Fold Cross Validation

A 5-fold cross validation was implemented for optimizing the hyper parameters of the SVR and GBR fittings. This was done by splitting the training set into 5 equal sets. One of the sets was then put aside for validation and the model was fit using the remaining 4 parts. This process was then repeated 5 times, allowing each of the 5 sets to be used once as the validation set. The reported cross validation scores are the averages of the 5 fittings, and the error bars represent the standard deviations of those scores. This method was used to select the best hyperparameters for the model. Once the parameters with the highest R2 in the cross-validation were identified, the model was then re-fit using those hyperparameters on the full training set.

Support Vector Regression Fitting

The support vector regression was performed using the scikit-learn SVR package. Fittings were attempted with all available pre-programmed kernels (rbf, polynomial, linear, and sigmoid) with two key hyperparameters: Gamma and tolerance. The 'auto' function for selecting the Gamma parameter was used. The tolerance parameter was then tested over a range of 1.0×10^{-10} to $\times10^{5}$, calculating the Pearson R^2 value for the training set, the test set, and the 5-fold cross validation. The highest R^2 values for the Parasitic Energy and was 0.12 whereas productivity did not exceed 0.1, both utilizing the rbf kernel.

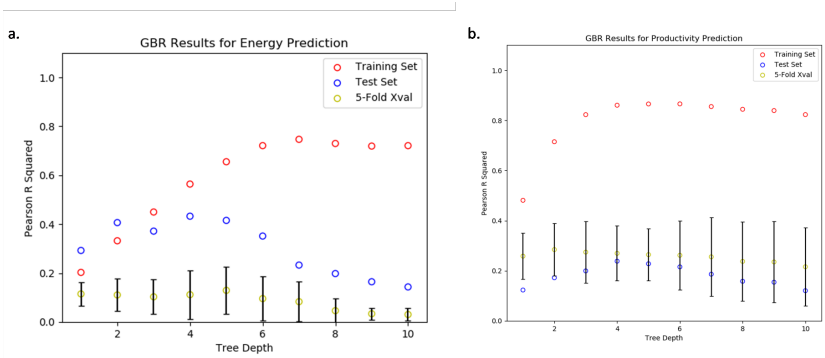

Figure A.21: The GBR performance results showing the 5-fold cross-validation Pearson R2 (green), the test set R^2 values (blue), and the Training Set R^2 (red) for a) the Parasitic Energy using a min sample size of 4 and a learning rate of 0.01, and b) the productivity using the min sample size of 4 and a learning rate of 0.1.

Gradient Boosted Decision Tree Regression

Training of the GBR models was performed in a similar fashion to the SVR models and was attempted using all four pre-programmed loss function. Out of the available loss functions, the best results were obtained using the Huber loss function. For the GBR models, three hyperparameters were varied: min sample split, learning rate, and maximum tree depth. The min sample split, which is defined as the minimum number of samples on a node of the decision tree needed for any splitting to be attempted, was ranged from 2 to 10 with the best results obtained at a value of 4. A value of 4 for this hyperparameters means that if there are fewer that 4 samples on a node of the decision tree, the GBR code will not attempt to further separate those samples and the branch of that tree will end. The learning rate, which determines the size of the step of the along the gradient the optimizer takes, was varied from a value of 1 to $1.0\times1^{0-5}$ with the best results obtained at 0.01. The third hyperparameter, the maximum depth was ranged from 1 to 10, with the best results obtained between 4 and 6. The best model fit for the PE based on the 5-fold cross-validation had a test set R^2 of approximately 0.41. For the productivity, the best model obtained yielded a test set R^2 of approximately 0.18.

Artificial Neural Network Regression

The sklearn NNR models were tested using all pre-programmed optimizers, including the Adam optimizer, as well as all pre-programmed activation functions. The learning rate was set to constant with a validation fraction of 0.1 and the batch-size was set to auto. The best results obtained from these fittings was a test set R^2 value of 0.1, using the Adam optimizer, the Relu activation function, and a learning rate of 0.01.

Effect of the Diffusion Coefficient

Industrial PSA units require a constant flow of gas through the column. As a result, the separations are dependant on the kinetics of adsorption. The rate limiting step of these kinetics is the macropore diffusion in structured Zeolite-13X [114]. Since the formation of these macropores is a result of the pelletization of nanoporous materials using a binder, it was assumed that all materials studied here-in undergo a comparable pelletization process. This assumption was made due to a lack of experimental data relating to macropore diffusion in structured MOFs. The diffusion coefficient

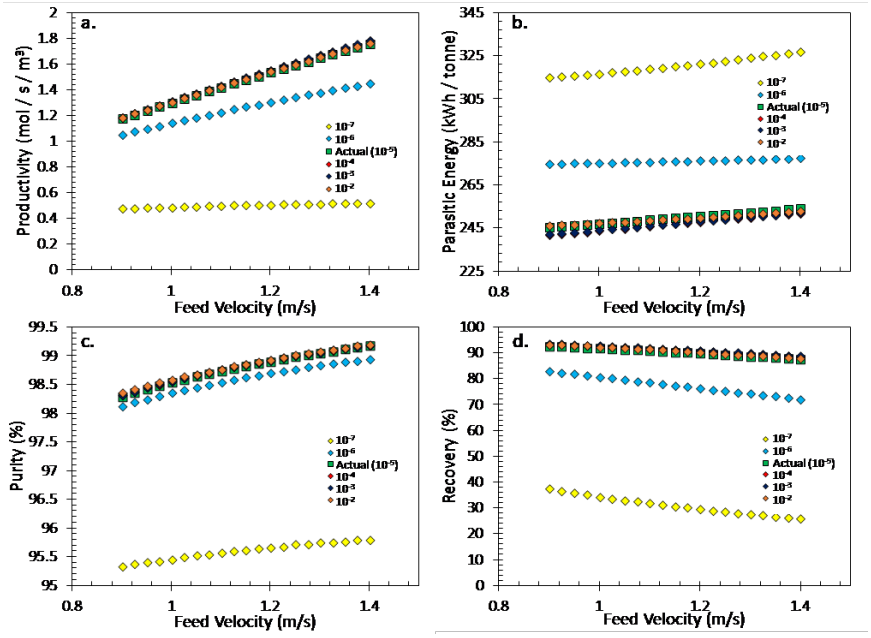

Figure A.22: Plots of the a) Productivity, b) Parasitic Energy, c) Purity, and d) Recovery as a function of feed velocity for different orders of magnitude of the macropore diffusion coefficient.

controlling the rate limiting step was calculated using the concentration of the gas components in each section of the column. This coefficient based on a molecular diffusivity of $1.2{\times}1^{0-5}$ m^2/s in Zeolite-13X [114]. To validate this approximation, a sensitivity analysis was performed on IISERP-MOF2. Although no data is available relating to the macropore diffusion in IISERP-MOF2, the micropore diffusion coefficient has been found to be 2 orders of magnitude larger than that of Zeolite-13X. The diffusion coefficient was tested across 6 orders of magnitude and a one-dimensional search was performed using the best parasitic energy process point, varying only the feed velocity from 0.9 to 1.4 m/s. Based on the results of this sensitivity analysis presented in Figure A.21, we see a minimal effect on the results when the diffusion coefficient is increased, and we see a dramatic drop in performance when this value is decreased. This indicates that using the diffusion coefficient of Zeolite-13X is a valid approximation provided the material being tested has a macropore diffusion coefficient with the same order of magnitude as that used Zeolite-13X or greater.

A.8 Vacuum Pump Efficiencies

The vacuum pump efficiency used in our simulations was 72%. This value is on the higher end of the range of commercially available vacuum pumps, which range in efficiency from 50% to 80%. Changing this efficiency has a direct impact on the PSA Work term in the parasitic energy, as this is the step which utilizes vacuum pumps. As such, changing this efficiency will impact on our genetic algorithm optimization which may result in different optimal process points. To test this, we re-ran GA optimizations on IISERP-MOF2 using an efficiency of 50%. The results of this optimization yielded a different set of best process points. This means that to ensure a material's top performance, these process points would require re-optimization if the vacuum pump efficiencies differ.

Appendix B: Supporting information for: Experimentally validated machine learning frameworks for accelerated prediction of cyclic steady state and optimization of pressure swing adsorption processes.

B.1 Process Modeling

B.1.1 Model Equations

Model equations	
Overall mass balance	$\frac{1}{P}\frac{\partial P}{\partial t} - \frac{1}{T}\frac{\partial T}{\partial t} = -\frac{T}{P}\frac{\partial}{\partial z}\left(\frac{P}{T}v\right) - \frac{1-\epsilon}{\epsilon}\frac{RT}{P}\sum_{i=1}^{n_{\text{comp}}}\frac{\partial q_i}{\partial t}$
Component mass balance	$\frac{\partial y_i}{\partial t} + \frac{y_i}{P}\frac{\partial P}{\partial t} - \frac{y_i}{T}\frac{\partial T}{\partial t} = \frac{T}{P}D_{\text{L}}\frac{\partial}{\partial z}\left(\frac{P}{T}\frac{\partial y_i}{\partial z}\right) - \frac{T}{P}\frac{\partial}{\partial z}\left(\frac{y_i P}{T}v\right) - \frac{RT}{P}\frac{1-\epsilon}{\epsilon}\frac{\partial q_i}{\partial t}$
Mass transfer rate	$\frac{\partial q_i}{\partial t} = k_i\left(q_i^* - q_i\right);\ k_i = \frac{c_i}{q_i^*}\frac{15\epsilon_{\text{P}}D_{\text{P}}}{r_{\text{P}}^2}$
Pressure drop	$-\frac{\partial P}{\partial z} = \frac{150}{4}\frac{1}{r_{\text{p}}^2}\left(\frac{1-\epsilon}{\epsilon}\right)^2\mu v$
Column energy balance	$\left[\frac{1-\epsilon}{\epsilon}\left(\rho_{\text{s}}C_{\text{p,s}} + C_{\text{p,a}}\sum_{i=1}^{n_{\text{comp}}}q_i\right)\right]\frac{\partial T}{\partial t} = \frac{K_z}{\epsilon}\frac{\partial^2 T}{\partial z^2} - \frac{C_{\text{p,g}}}{R}\frac{\partial}{\partial z}(vp) - \frac{C_{\text{p,g}}}{R}\frac{\partial P}{\partial t} - \frac{1-\epsilon}{\epsilon}C_{\text{p,a}}T\sum_{i=1}^{n_{\text{comp}}}\frac{\partial q_i}{\partial t} + \frac{1-\epsilon}{\epsilon}\sum_{i=1}^{n_{\text{comp}}}\left(\left(-\Delta \text{H}_{\text{i}}\right)\frac{\partial q_i}{\partial t}\right) - \frac{2h_{\text{in}}}{\epsilon r_{\text{in}}}\left(T - T_{\text{w}}\right)$
Wall energy balance	$\rho w C_{\text{p,w}}\frac{\partial T_{\text{w}}}{\partial t} = K_w\frac{\partial^2 T_{\text{w}}}{\partial z^2} + \frac{2r_{\text{in}}h_{\text{in}}}{r_{\text{out}}^2 - r_{\text{in}}^2}\left(T - T_{\text{w}}\right) - \frac{2r_{\text{out}}h_{\text{out}}}{r_{\text{out}}^2 - r_{\text{in}}^2}\left(T_{\text{w}} - T_{\text{a}}\right)$

Table B.1: Equations for modeling adsorption column dynamics.

B.1.2 Boundary Conditions

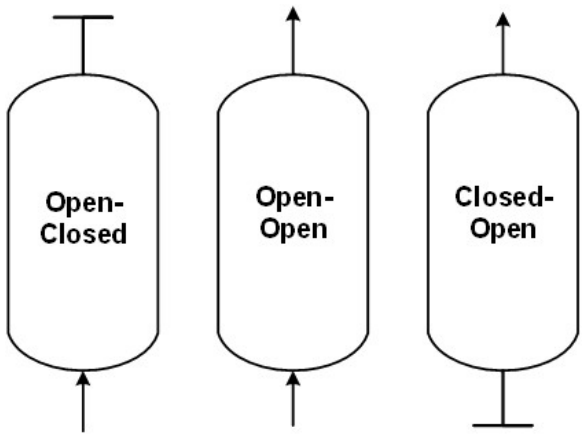

Figure B.1: Typical operating configurations of the constituent steps in a PSA cycle

Step	z=0	z=L
OPEN-CLOSED	$P\|_{\mathrm{z=0}} = P_2 + (P_1 - P_2)e^{(-\alpha_p t)}$	$\frac{\partial y_i}{\partial z}\big\|_{\mathrm{z=L}} = 0$
	$D_{\mathrm{L}}\ \frac{\partial y_i}{\partial z}\big\|_{\mathrm{z=0}} = -v\|_{\mathrm{z=0}}\,(y_{i,\mathrm{feed}} - y_i\|_{\mathrm{z=0}})$	$\frac{\partial P}{\partial z}\big\|_{\mathrm{z=L}} = 0$
	$\frac{\partial \mathrm{T}}{\partial z}\big\|_{\mathrm{z=0}} = -\epsilon\ v\|_{\mathrm{z=0}}\,\rho_g C_{pg}(T_{\mathrm{feed}} - T\|_{\mathrm{z=0}})$	$\frac{\partial \mathrm{T}}{\partial z}\big\|_{\mathrm{z=L}} = 0$
	$T_{\mathrm{w}}\|_{\mathrm{z=0}} = T_{\mathrm{a}}$	$T_{\mathrm{w}}\|_{\mathrm{z=L}} = T_{\mathrm{a}}$
OPEN-OPEN	$v\|_{\mathrm{z=0}} = v_{\mathrm{feed}}$	$P\|_{\mathrm{z=L}} = P_2$
	$D_{\mathrm{L}}\ \frac{\partial y_i}{\partial z}\big\|_{\mathrm{z=0}} = -v\|_{\mathrm{z=0}}\,(y_{i,\mathrm{feed}} - y_i\|_{\mathrm{z=0}})$	$\frac{\partial y_i}{\partial z}\big\|_{\mathrm{z=L}} = 0$
	$\frac{\partial T}{\partial z}\big\|_{\mathrm{z=0}} = -\epsilon\ v\|_{\mathrm{z=0}}\,\rho_g C_{p,\mathrm{g}}(T_{feed} - T\|_{\mathrm{z=0}})$	$\frac{\partial T}{\partial z}\big\|_{\mathrm{z=L}} = 0$
	$T_{\mathrm{w}}\|_{\mathrm{z=0}} = T_{\mathrm{a}}$	$T_{\mathrm{w}}\|_{\mathrm{z=L}} = T_{\mathrm{a}}$
CLOSED-OPEN	$v\|_{\mathrm{z=0}} = 0$	$P\|_{\mathrm{z=L}} = P_1 + (P_2 - P_1)e^{(-\alpha_p t)}$
	$\frac{\partial y_i}{\partial z}\big\|_{\mathrm{z=0}} = 0$	$\frac{\partial y_i}{\partial z}\big\|_{\mathrm{z=L}} = 0$
	$\frac{\partial T}{\partial z}\big\|_{\mathrm{z=0}} = 0$	$\frac{\partial T}{\partial z}\big\|_{\mathrm{z=L}} = 0$
	$\frac{\partial P}{\partial z}\big\|_{\mathrm{z=0}} = 0$	$T_{\mathrm{w}}\|_{\mathrm{z=L}} = T_{\mathrm{a}}$

Table B.2: Boundary conditions for the typical steps in a cyclic adsorption process.

B.1.3 Simulation Parameters

Isotherm parameter	CO_2	N_2
b_0 [m^3 mol^{-1}]	3.93×10^{-7}	3.13×10^{-6}
d_0 [m^3 mol^{-1}]	1.25×10^{-7}	3.13×10^{-6}
ΔU_b [J mol^{-1}]	-40,981	-15,715
ΔU_d [J mol^{-1}]	-34,188	-15,715
q_{s_b} [mol m^{-3}]	2,768	2,768
q_{s_d} [mol m^{-3}]	2,758	2,768

Table B.3: Dual-site Langmuir isotherm parameters for CO_2 and N_2 on Zeochem Zeolite 13X [36]

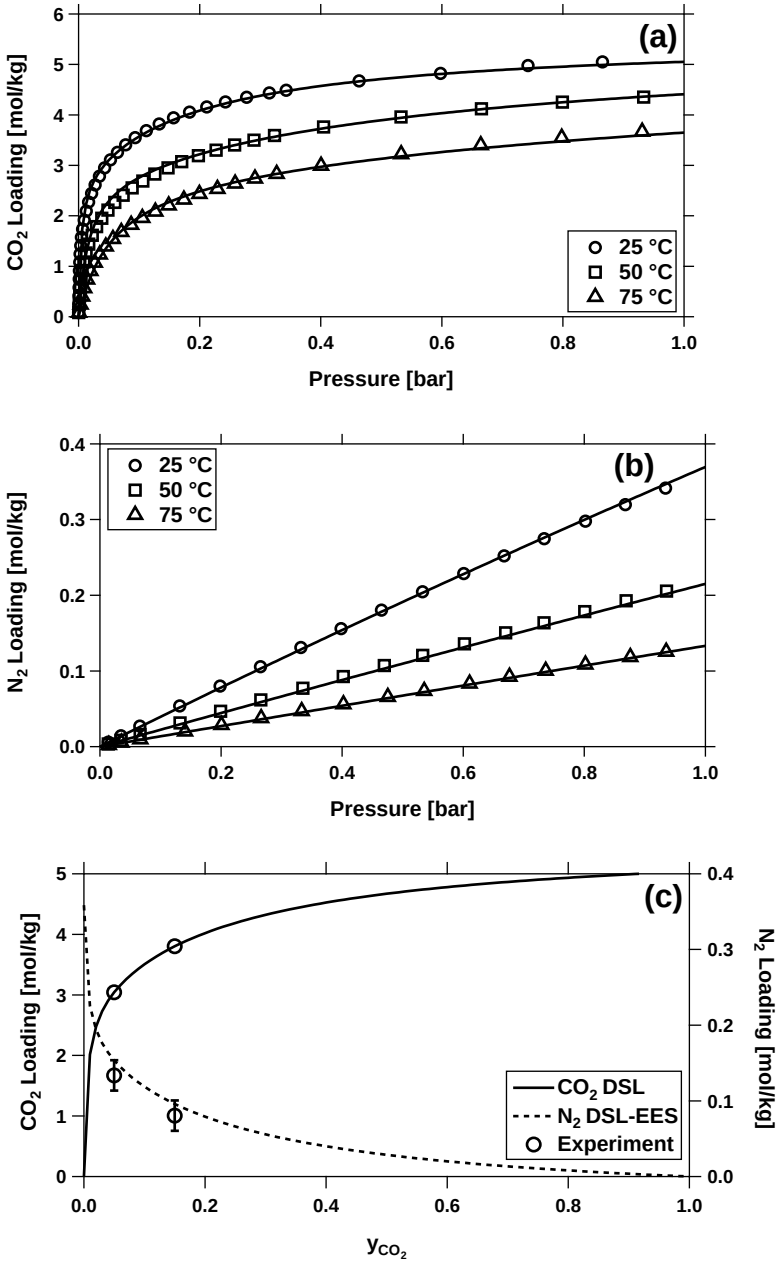

Figure B.2: Characterization of adsorption equilibria. a) CO_2 isotherms with symbols representing experimentally measured values and the lines showing the DSL fit. b) N_2 isotherms with symbols being experimentally measured values and the lines showing the DSL-EES fit. c)Competitive equilibria of CO_2 and N_2 at 1.01 bar and 22°C. The symbols were measured from DCB experiments. The lines show the calculated values from the DSL-EES isotherm. Reproduced from Perez *et al.* [36]

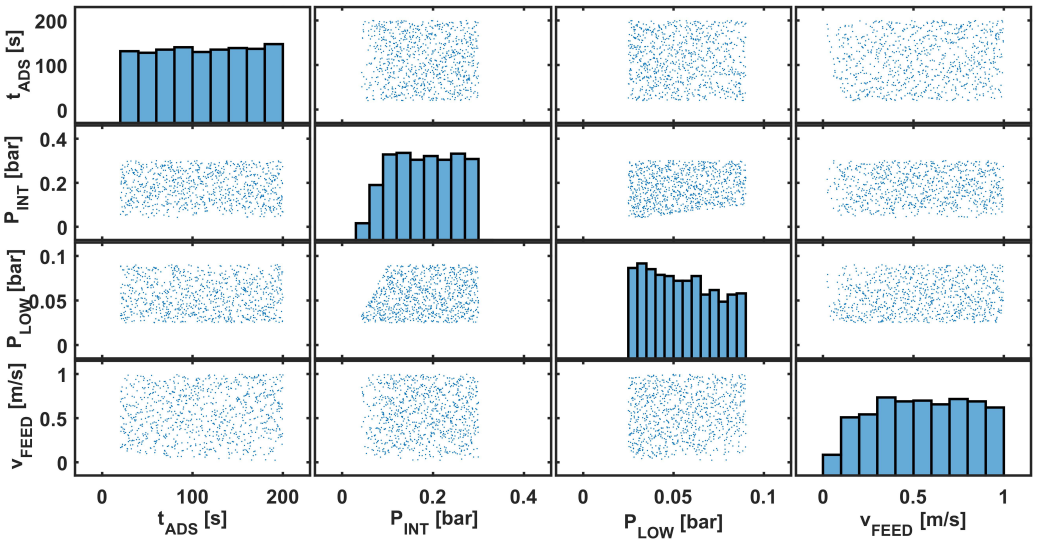

Figure B.3: The input sample distribution of the different unique operating conditions, namely, t_{ADS}, P_{INT}, P_{LOW}, and v_{FEED}, for the 4-step cycle with LPP

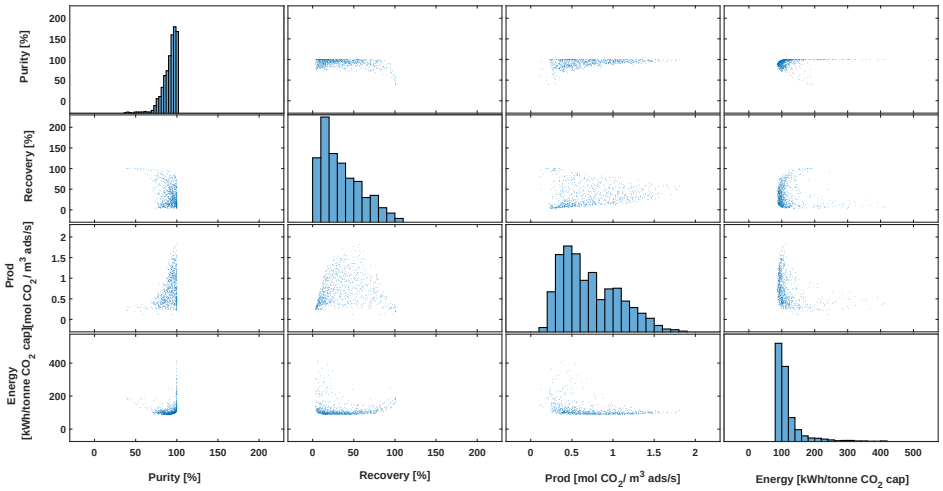

Figure B.4: The output distribution of the key performance indicators for the 4-step cycle with LPP obtained from the LHC sampling from Fig. B.3, i.e. Purity, Recovery, Productivity, and Energy. Note that the sub-plots in the diagonal are the univariate distributions for the key performance indicators.

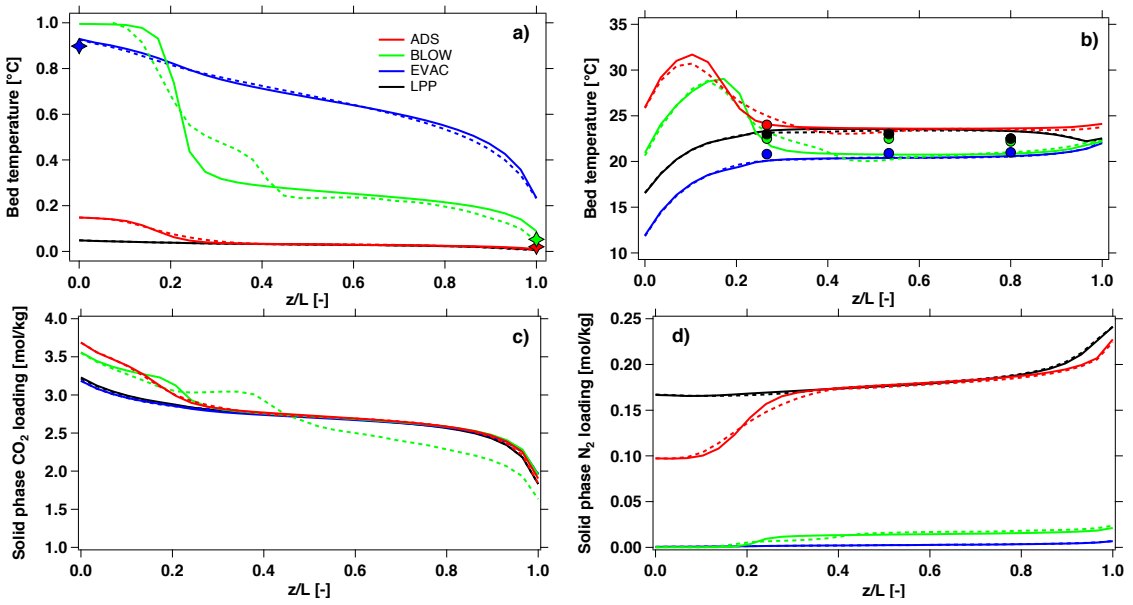

Figure B.5: Cyclic steady state profiles of the state variables at the end of the cycle steps for the experimental run B from Table 3; the dashed lines are predictions from the ANN surrogate model and the solid lines are the detailed model simulations. a) CSS profiles of the gas phase composition of CO_2, the symbols are the CO_2 concentrations measured at the$Z = 0$ and $Z = L$ end of the column at the end of each cycle step. b) CSS profiles for the solid state loading for CO_2 d) CSS profiles for the solid state loading for N_2. d) CSS profiles for the bed temperature, the symbols are the temperatures measured at TC-1, TC-2, TC-3 along the column at the end of each step averaged over the last 5 cycles.

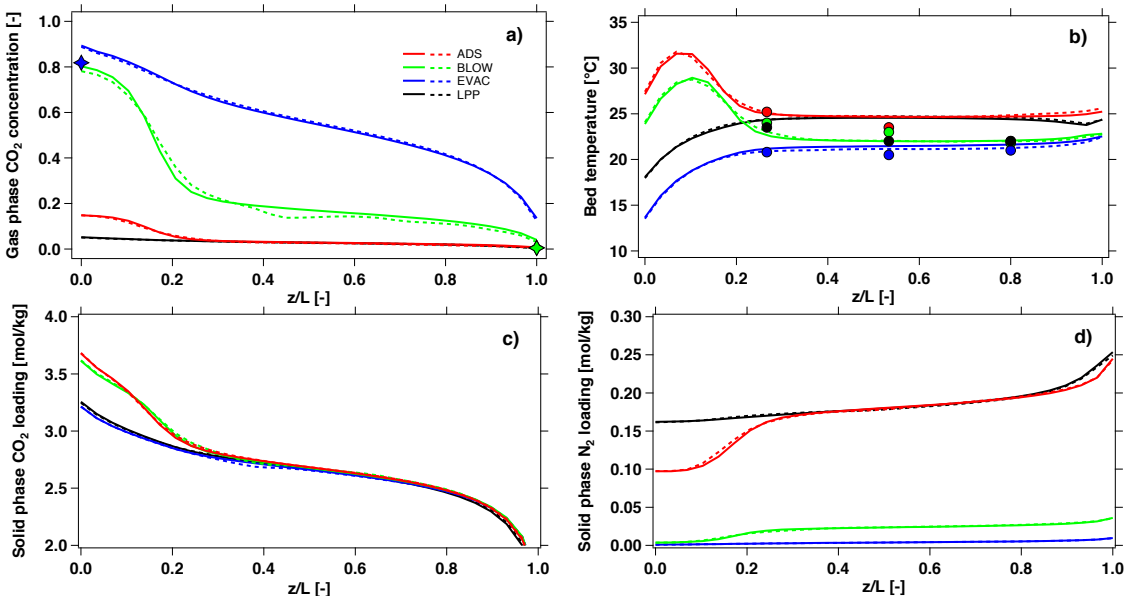

Figure B.6: Cyclic steady state profiles of the state variables at the end of the cycle steps for the experimental run C from Table 3; the dashed lines are predictions from the ANN surrogate model and the solid lines are the detailed model simulations. a) CSS profiles of the gas phase composition of CO_2, the symbols are the CO_2 concentrations measured at the$Z = 0$ and $Z = L$ end of the column at the end of each cycle step. b) CSS profiles for the solid state loading for CO_2 d) CSS profiles for the solid state loading for N_2. d) CSS profiles for the bed temperature, the symbols are the temperatures measured at TC-1, TC-2, TC-3 along the column at the end of each step averaged over the last 5 cycles.

Appendix C: Supporting information for: Generalized, Adsorbent-agnostic, artificial neural network framework for rapid simulation, optimization, and adsorbent screening of adsorption processes

C.1 Process Modeling

C.1.1 Model Equations

Model equations	
Overall mass balance	$\frac{1}{P}\frac{\partial P}{\partial t} - \frac{1}{T}\frac{\partial T}{\partial t} = -\frac{T}{P}\frac{\partial}{\partial z}\left(\frac{P}{T}v\right) - \frac{1-\epsilon}{\epsilon}\frac{RT}{P}\sum_{i=1}^{n_{\text{comp}}}\frac{\partial q_i}{\partial t}$
Component mass balance	$\frac{\partial y_i}{\partial t} + \frac{y_i}{P}\frac{\partial P}{\partial t} - \frac{y_i}{T}\frac{\partial T}{\partial t} = \frac{T}{P}D_L\frac{\partial}{\partial z}\left(\frac{P}{T}\frac{\partial y_i}{\partial z}\right) - \frac{T}{P}\frac{\partial}{\partial z}\left(\frac{y_i P}{T}v\right) - \frac{RT}{P}\frac{1-\epsilon}{\epsilon}\frac{\partial q_i}{\partial t}$
Mass transfer rate	$\frac{\partial q_i}{\partial t} = k_i\left(q_i^* - q_i\right);\ k_i = \frac{C_i}{q_i^*}\frac{15\epsilon_{\text{P}}D_{\text{P}}}{r_{\text{P}}^2}\ ;\ D_{\text{P}} = \frac{D_{\text{M}}}{\tau}$
Pressure drop	$-\frac{\partial P}{\partial z} = \frac{150}{4}\frac{1}{r_{\text{p}}^2}\left(\frac{1-\epsilon}{\epsilon}\right)^2\mu v$
Column energy balance	$\left[\frac{1-\epsilon}{\epsilon}\left(\rho_{\text{s}}C_{\text{p,s}} + C_{\text{p,a}}\sum_{i=1}^{n_{\text{comp}}}q_i\right)\right]\frac{\partial T}{\partial t} = \frac{K_{\text{z}}}{\epsilon}\frac{\partial^2 T}{\partial z^2} - \frac{C_{\text{p,g}}}{R}\frac{\partial}{\partial z}(vP) - \frac{C_{\text{p,g}}}{R}\frac{\partial P}{\partial t} - \frac{1-\epsilon}{\epsilon}C_{\text{p,a}}T\sum_{i=1}^{n_{\text{comp}}}\frac{\partial q_i}{\partial t} + \frac{1-\epsilon}{\epsilon}\sum_{i=1}^{n_{\text{comp}}}\left(\left(-\Delta H_i\right)\frac{\partial q_i}{\partial t}\right) - \frac{2h_{\text{in}}}{\epsilon r_{\text{in}}}\left(T - T_{\text{w}}\right)$
Wall energy balance	$\rho_{\text{w}}C_{\text{p,w}}\frac{\partial T_{\text{w}}}{\partial t} = K_{\text{w}}\frac{\partial^2 T_{\text{w}}}{\partial z^2} + \frac{2r_{\text{in}}h_{\text{in}}}{r_{\text{out}}^2 - r_{\text{in}}^2}\left(T - T_{\text{w}}\right) - \frac{2r_{\text{out}}h_{\text{out}}}{r_{\text{out}}^2 - r_{\text{in}}^2}\left(T_{\text{w}} - T_{\text{a}}\right)$

Table C.1: Equations for modeling adsorption column dynamics.

C.1.2 Boundary Conditions

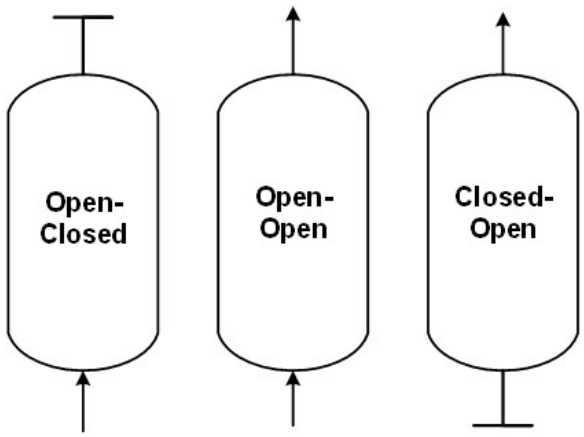

Figure C.1: Typical operating configurations of the constituent steps in a P/VSA cycle

Step	z=0	z=L
OPEN-CLOSED	$P\|_{\mathrm{z=0}} = P_{\mathrm{L}} + (P_{\mathrm{H}} - P_{\mathrm{L}})e^{(-\alpha_{\mathrm{PRESS}}t)}$	$\frac{\partial y_i}{\partial z}\Big\|_{\mathrm{z=L}} = 0$
	$D_L \frac{\partial y_i}{\partial z}\Big\|_{\mathrm{z=0}} = -v\|_{\mathrm{z=0}} (y_{i,\mathrm{F}} - y_i\|_{\mathrm{z=0}})$	$\frac{\partial P}{\partial z}\Big\|_{\mathrm{z=L}} = 0$
	$\frac{\partial \mathrm{T}}{\partial z}\Big\|_{\mathrm{z=0}} = -\epsilon\, v\|_{\mathrm{z=0}}\, \rho_{\mathrm{g}} \mathrm{C}_{\mathrm{p,g}(\mathrm{T_F} - \mathrm{T}\|_{\mathrm{z=0}})}$	$\frac{\partial \mathrm{T}}{\partial z}\Big\|_{\mathrm{z=L}} = 0$
	$T_{\mathrm{w}}\|_{\mathrm{z=0}} = T_{\mathrm{a}}$	$T_{\mathrm{w}}\|_{\mathrm{z=L}} = T_{\mathrm{a}}$
OPEN-OPEN	$v\|_{\mathrm{z=0}} = v_{\mathrm{F}}$	$P\|_{\mathrm{z=L}} = P_{\mathrm{H}}$
	$D_L \frac{\partial y_i}{\partial z}\Big\|_{\mathrm{z=0}} = -v\|_{\mathrm{z=0}} (y_{i,\mathrm{F}} - y_i\|_{\mathrm{z=0}})$	$\frac{\partial y_i}{\partial z}\Big\|_{\mathrm{z=L}} = 0$
	$\frac{\partial T}{\partial z}\Big\|_{\mathrm{z=0}} = -\epsilon\, v\|_{\mathrm{z=0}}\, \rho_g C_{p,\mathrm{g}} (T_F - T\|_{\mathrm{z=0}})$	$\frac{\partial T}{\partial z}\Big\|_{\mathrm{z=L}} = 0$
	$T_{\mathrm{w}}\|_{\mathrm{z=0}} = T_{\mathrm{a}}$	$T_{\mathrm{w}}\|_{\mathrm{z=L}} = T_{\mathrm{a}}$
CLOSED-OPEN (BLO)	$v\|_{\mathrm{z=0}} = 0$	$P\|_{\mathrm{z=L}} = P_{\mathrm{H}} + (P_{\mathrm{INT}} - P_{\mathrm{H}})e^{(-\alpha_{\mathrm{BLO}}t)}$;
	$\frac{\partial y_i}{\partial z}\Big\|_{\mathrm{z=0}} = 0$	$\frac{\partial y_i}{\partial z}\Big\|_{\mathrm{z=L}} = 0$
	$\frac{\partial T}{\partial z}\Big\|_{\mathrm{z=0}} = 0$	$\frac{\partial T}{\partial z}\Big\|_{\mathrm{z=L}} = 0$
	$\frac{\partial P}{\partial z}\Big\|_{\mathrm{z=0}} = 0$	$T_{\mathrm{w}}\|_{\mathrm{z=L}} = T_{\mathrm{a}}$
CLOSED-OPEN (EVAC)	$P\|_{\mathrm{z=0}} = P_{\mathrm{INT}} + (P_{\mathrm{L}} - P_{\mathrm{INT}})e^{(-\alpha_{\mathrm{EVAC}}t)}$;	$v\|_{\mathrm{z=L}} = 0$
	$\frac{\partial y_i}{\partial z}\Big\|_{\mathrm{z=0}} = 0$	$\frac{\partial y_i}{\partial z}\Big\|_{\mathrm{z=L}} = 0$
	$\frac{\partial T}{\partial z}\Big\|_{\mathrm{z=0}} = 0$	$\frac{\partial T}{\partial z}\Big\|_{\mathrm{z=L}} = 0$
	$T_{\mathrm{w}}\|_{\mathrm{z=0}} = T_{\mathrm{a}}$	$\frac{\partial P}{\partial z}\Big\|_{\mathrm{z=L}} = 0$

Table C.2: Boundary conditions for the typical steps in a cyclic adsorption process.

C.1.3 Key process performance indicators (PIs)

Key Performance indicators	
Purity [%]	$\frac{n_{CO_2}^{EVAC}}{n_{CO_2}^{EVAC}+n_{N_2}^{EVAC}} \times 100$
Recovery [%]	$\frac{n_{CO_2}^{EVAC}}{n_{CO_2}^{F}} \times 100$
Productivity $\left[\frac{\text{mol } CO_2}{\text{m}^3 \text{ ads s}}\right]$	$\frac{n_{CO_2}^{EVAC}}{(\text{ Vol of ads }) (\text{Cycle time })}$
Energy $\left[\frac{\text{kWh}_e}{\text{tonne } CO_2 \text{ captured}}\right]$	$\frac{E_{ADS} + E_{BLO} + E_{EVAC}}{\text{Mass of } CO_2 \text{ in evacuation product}}$
E_{ADS}	$\frac{1}{\eta}\epsilon\pi r_{in}^2 \frac{\gamma}{\gamma-1} \int_{t=0}^{t=t_{ADS}} (vP(t)) \left[\left(\frac{P(t)}{P_{atm}}\right)^{\frac{\gamma-1}{\gamma}} - 1\right] dt$
E_{BLO}	$\frac{1}{\eta}\epsilon\pi r_{in}^2 \frac{\gamma}{\gamma-1} \int_{t=0}^{t=t_{BLO}} (vP(t)) \left[\left(\frac{P_{atm}}{P(t)}\right)^{\frac{\gamma-1}{\gamma}} - 1\right] dt$
E_{EVAC}	$\frac{1}{\eta}\epsilon\pi r_{in}^2 \frac{\gamma}{\gamma-1} \int_{t=0}^{t=t_{EVAC}} (vP(t)) \left[\left(\frac{P_{atm}}{P(t)}\right)^{\frac{\gamma-1}{\gamma}} - 1\right] dt$

Table C.3: Equations for the key performance indicators.

Table C.4: Single Site Langmuir (SSL) isotherm parameters for the adsorbents in the literature [15]. Only those adsorbents that met the criteria for representation by an SSL isotherm are provided here. Some duplicate occurences refer to different data sources reported in the original paper.

Adsorbent	q_{sat} [mol m^{-3}]	b_{0,CO_2} [m^3 mol^{-1}]	b_{0,N_2} [m^3 mol^{-1}]	$-\Delta U_{CO_2}$ [kJ mol^{-1}]	$-\Delta U_{N_2}$ [kJ mol^{-1}]
MgMOF-74	5331.29	6.38×10^{-7}	2.06×10^{-6}	33.73	18.32
UTSA-16	8385.87	6.15×10^{-7}	2.06×10^{-6}	30.57	9.91
Zeolite 13X	4960.70	2.50×10^{-6}	2.70×10^{-6}	31.19	16.38
MOF-177	800.00	4.66×10^{-6}	1.27×10^{-4}	20.00	8.00
NAB	7477.28	2.53×10^{-7}	5.94×10^{-6}	25.71	8.55
h8291835	5278.94	5.98×10^{-7}	1.46×10^{-5}	24.03	8.00
h8155527	4300.50	2.13×10^{-7}	1.17×10^{-5}	30.67	8.00
CaX	7745.77	6.52×10^{-7}	8.50×10^{-5}	32.52	8.00
MgX	8026.19	2.15×10^{-7}	3.27×10^{-7}	33.80	20.00
NaA	5112.23	3.09×10^{-6}	2.83×10^{-5}	27.59	8.00

Table C.4 continued from previous page

Adsorbent	q_{sat} [mol m^{-3}]	b_{0,CO_2} [m^3 mol^{-1}]	b_{0,N_2} [m^3 mol^{-1}]	$-\Delta U_{CO_2}$ [kJ mol^{-1}]	$-\Delta U_{N_2}$ [kJ mol^{-1}]
NaX	8125.71	2.82×10^{-7}	1.04×10^{-5}	35.88	12.65
PS-MFI	6322.72	2.08×10^{-6}	5.12×10^{-7}	23.71	19.74
Zn-MOF-74	12000.00	4.07×10^{-6}	1.00×10^{-5}	23.02	10.94
Co-MOF-74	10223.22	1.19×10^{-7}	3.82×10^{-5}	34.02	9.88
Ni-MOF-74	8510.18	4.63×10^{-6}	1.54×10^{-6}	25.20	20.00
MOF-177	880.55	5.07×10^{-6}	7.22×10^{-5}	20.00	8.74
CuBTC	11342.63	2.87×10^{-7}	3.65×10^{-6}	27.27	12.60
mmen-CuBTTri	5242.98	1.18×10^{-8}	4.28×10^{-7}	40.39	17.72
ZIF-68	5126.00	1.79×10^{-6}	3.16×10^{-6}	21.58	12.86
ZIF-69	5850.63	3.76×10^{-6}	8.48×10^{-6}	20.01	10.68
ZIF-70	2452.20	4.90×10^{-6}	1.03×10^{-5}	20.00	11.45
ZIF-78	3654.30	3.04×10^{-6}	1.78×10^{-5}	24.11	10.75
ZIF-79	3339.58	1.49×10^{-6}	6.78×10^{-6}	23.46	12.06
ZIF-81	4359.92	1.88×10^{-6}	7.90×10^{-6}	23.00	11.50
ZIF-82	4033.62	2.87×10^{-6}	9.17×10^{-6}	22.40	11.15
PPN-4	800.00	4.38×10^{-6}	1.24×10^{-4}	20.00	8.00
PPN-6-SO3H	3852.00	1.39×10^{-6}	3.01×10^{-5}	25.30	8.00
ZIF-36-CAG	2970.81	3.21×10^{-7}	3.84×10^{-6}	45.00	20.00
ZIF-39-DIA	9811.80	1.00×10^{-7}	5.80×10^{-7}	26.51	13.82
ZIF-39-ZNI	2111.13	8.01×10^{-8}	6.80×10^{-7}	27.14	19.76
ZIF-116-MER	10718.71	1.89×10^{-6}	1.33×10^{-5}	20.16	9.02
HMOF-MOF-5	875.51	7.86×10^{-6}	1.52×10^{-4}	20.02	8.00
HMOF-16	11762.36	1.13×10^{-6}	9.68×10^{-6}	21.35	8.00
HMOF-27	845.91	5.57×10^{-6}	1.73×10^{-4}	20.00	8.00
HMOF-96	906.68	6.17×10^{-6}	1.67×10^{-3}	20.00	8.00
HMOF-602	2605.99	3.50×10^{-6}	5.93×10^{-5}	20.05	8.00
HMOF-972	848.34	7.02×10^{-6}	1.64×10^{-4}	20.00	8.00

Table C.4 continued from previous page

Adsorbent	q_{sat} [mol m^{-3}]	b_{0,CO_2} [m^3 mol^{-1}]	b_{0,N_2} [m^3 mol^{-1}]	$-\Delta U_{CO_2}$ [kJ mol^{-1}]	$-\Delta U_{N_2}$ [kJ mol^{-1}]
HMOF-992	6894.91	1.62×10^{-6}	1.52×10^{-5}	20.00	8.00
HMOF-1041	855.48	7.34×10^{-6}	1.38×10^{-4}	20.00	8.00

Table C.5: Comparison of DOE classification and minimum energy calculations of MAPLE with those from Khurana and Farooq . [15]. A flag of "1" represents that the material can satisfy DOE target, while a"0" indicates that it cannot. Note that the Detailed model results from Khurana and Farooq use a dual-site Langmuir isotherm to describe the equilibria, whereas the MAPLE-Opt. uses a single-site Langmuir fitted to the the data generated using the dual-site Langmuir parameters provided by Khurana and Farooq.

Adsorbent	MAPLE-Opt.		Detailed-Opt.	
	DOE [1 0]	Energy [kWh$_e$/tonne CO_2 cap]	DOE [1 0]	Energy [kWh$_e$/tonne CO_2 cap]
MOF-177	0	0	0	1
NAB	1	124.24	1	123.41
h8291835	1	138.36	1	136.76
h8155527	1	121.6	1	117.44
CaX	1	192.6	1	189.21
MgX	1	158.32	1	156.61
NaA	1	133.17	1	13N.51
NaX	1	176.16	1	173.73
PS-MFI	1	183.4	1	216.57
Zn-MOF-74	1	168.71	1	162.14
Co-MOF-74	0	0	0	1
Ni-MOF-74	0	0	0	1
MOF-177	0	0	0	1
CuBTC	1	177.45	1	161.11

Table C.5 continued from previous page

Adsorbent	MAPLE-Opt.		Results from the literature [15]	
	DOE	Energy	DOE	Energy
	[1 0]	[kWh_e/tonne CO_2 cap]	[1 0]	[kWh_e/tonne CO_2 cap]
mmen-CuBTTri	1	0	1	131.65
ZIF-68	1	153.6	1	155.26
ZIF-69	1	156.74		158.27
ZIF-7N	0	0	1	181.31
ZIF-78	1	152.3	1	146.64
ZIF-79	1	158.17	1	151.51
ZIF-81	1	154.49	1	148.54
ZIF-82	1	149.16	1	141.17
PPN-4	0	0	0	0
PPN-6-SO3H	0	0	1	129.63
ZIF-36-CAG	1	217.17	1	188.44
ZIF-39-DIA	1	157.12	1	136.23
ZIF-39-ZNI	0	0	0	0
ZIF-116-MER	1	189.53	1	218.57
HMOF-MOF-5	0	0	0	0
HMOF-16	1	218.14	1	139.84
HMOF-27	0	0	0	0
HMOF-96	0	0	0	0
HMOF-6N2	0	0	0	0
HMOF-972	0	0	0	0
HMOF-992	1	164.79	1	195.89
HMOF-1N41	0	0	0	0

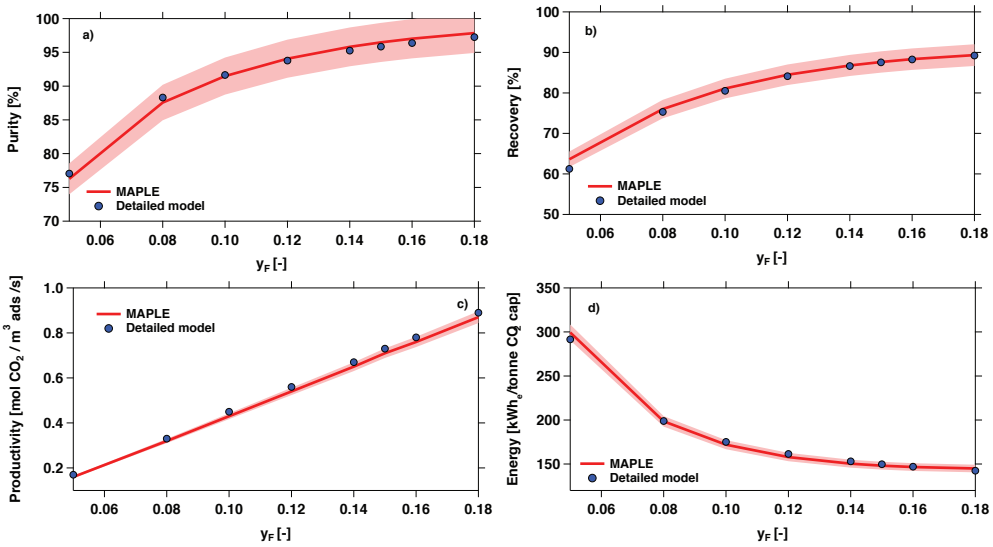

Figure C.2: Parametric study showing the variation of key performance indicators a) CO_2 Purity b) CO_2 Recovery c) Productivity d) Energy for Zeolite 13X as a function of intermediate pressure y_F. Operating parameters t_{ADS}[s]: 92.4, P_{INT}[bar]: 0.08, P_L[bar]: 0.03, v_F[m s^{-1}]: 0.64. Solid lines show the results from MAPLE surrogate framework and symbols correspond to the detailed model results, the shaded area represents a 2% error band.

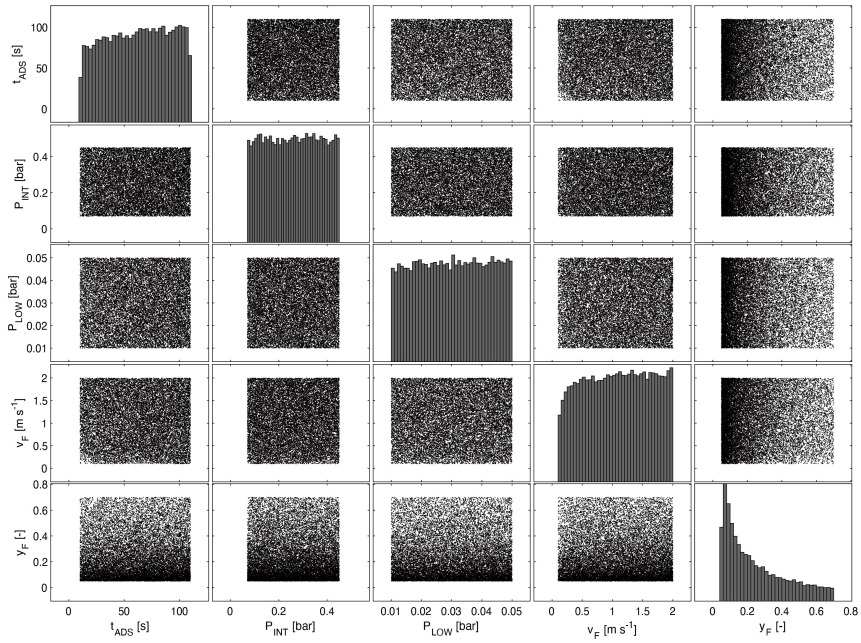

Figure C.3: Distribution of operating conditions used in the training set. A total of 21000 sample's are shown here.

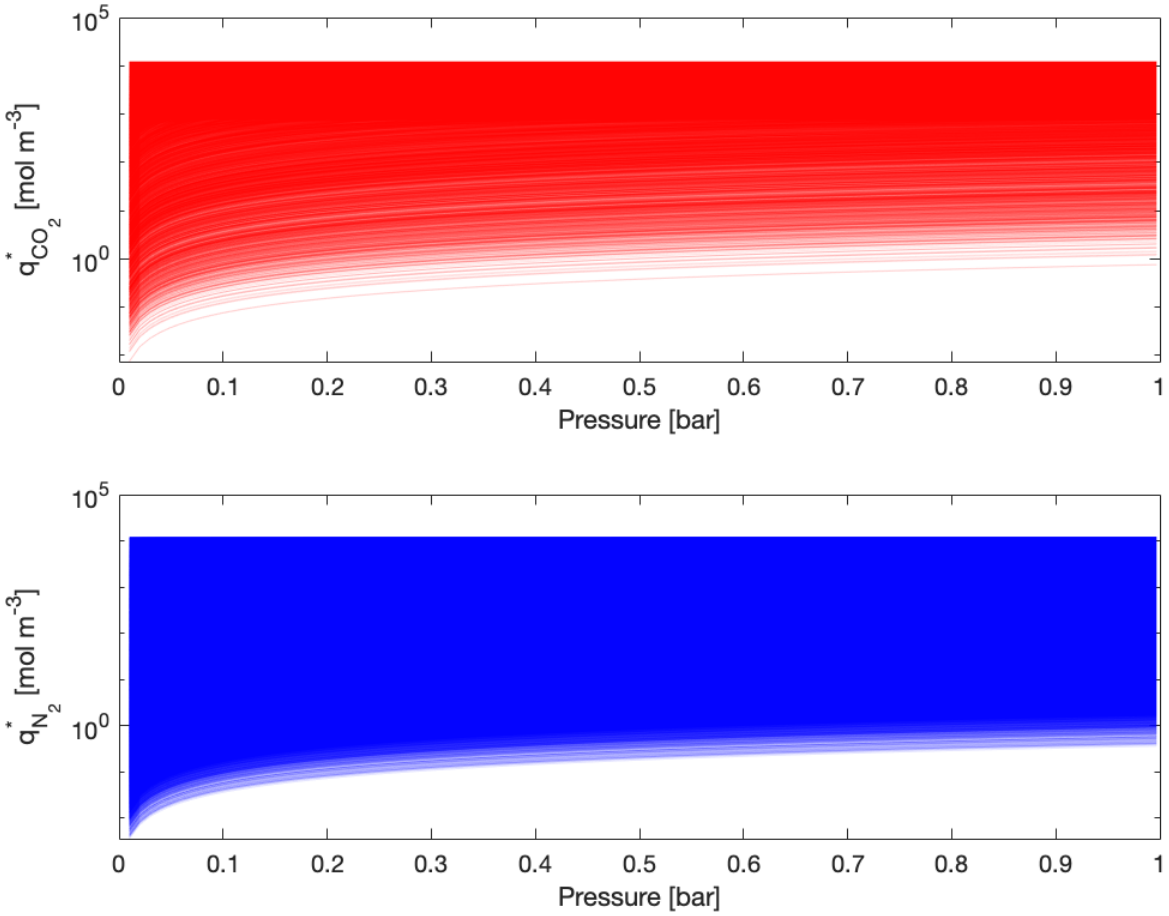

Figure C.4: Distribution of CO_2 (top) and N_2 (bottom) isotherms used in the training set.

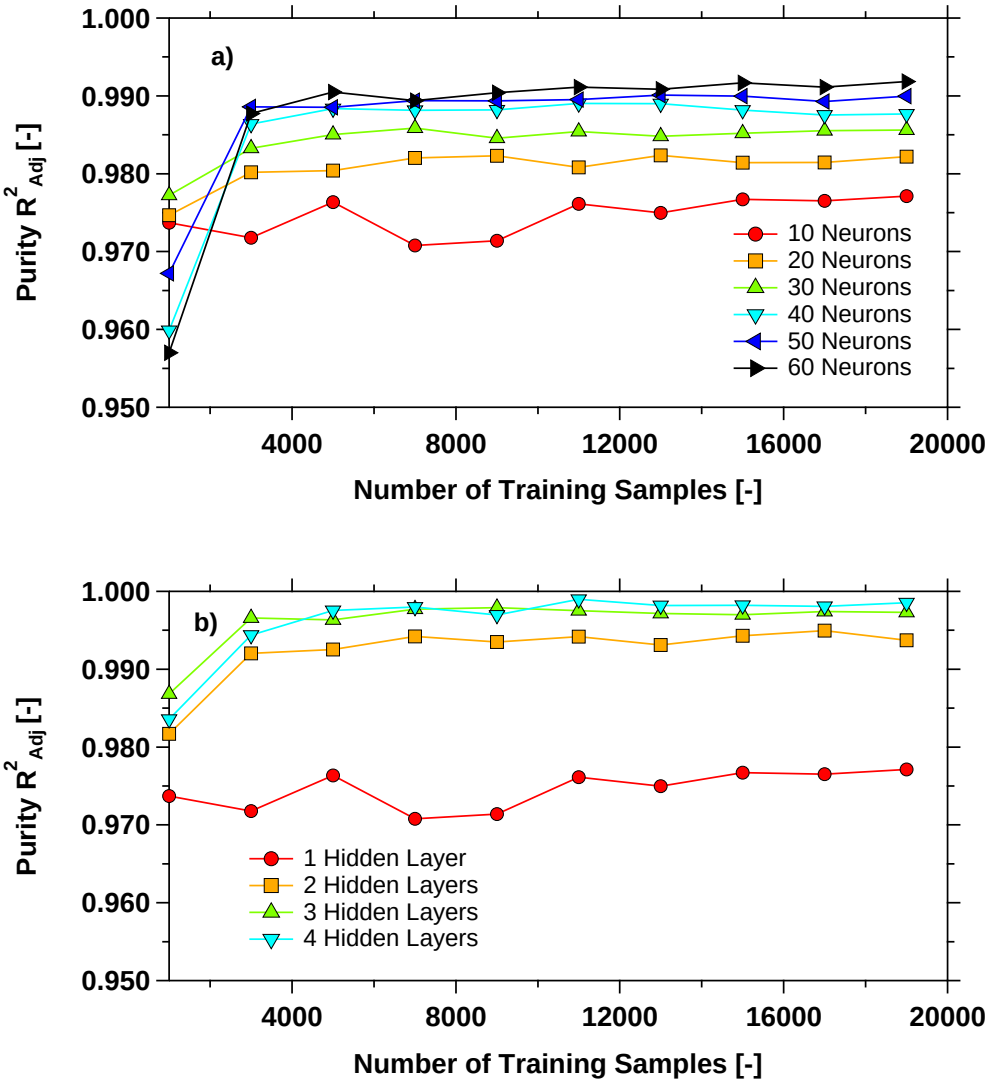

Figure C.5: The effect of neural network architecture on model prediction accuracy: Test R^2_{Adj} for Purity is shown as a function of the training-set size a) The effect of number of neurons and training samples on R^2_{Adj} b) The effect of number of hidden layers. Ten neurons were used in each hidden layer. The test-set contains 1000 samples.

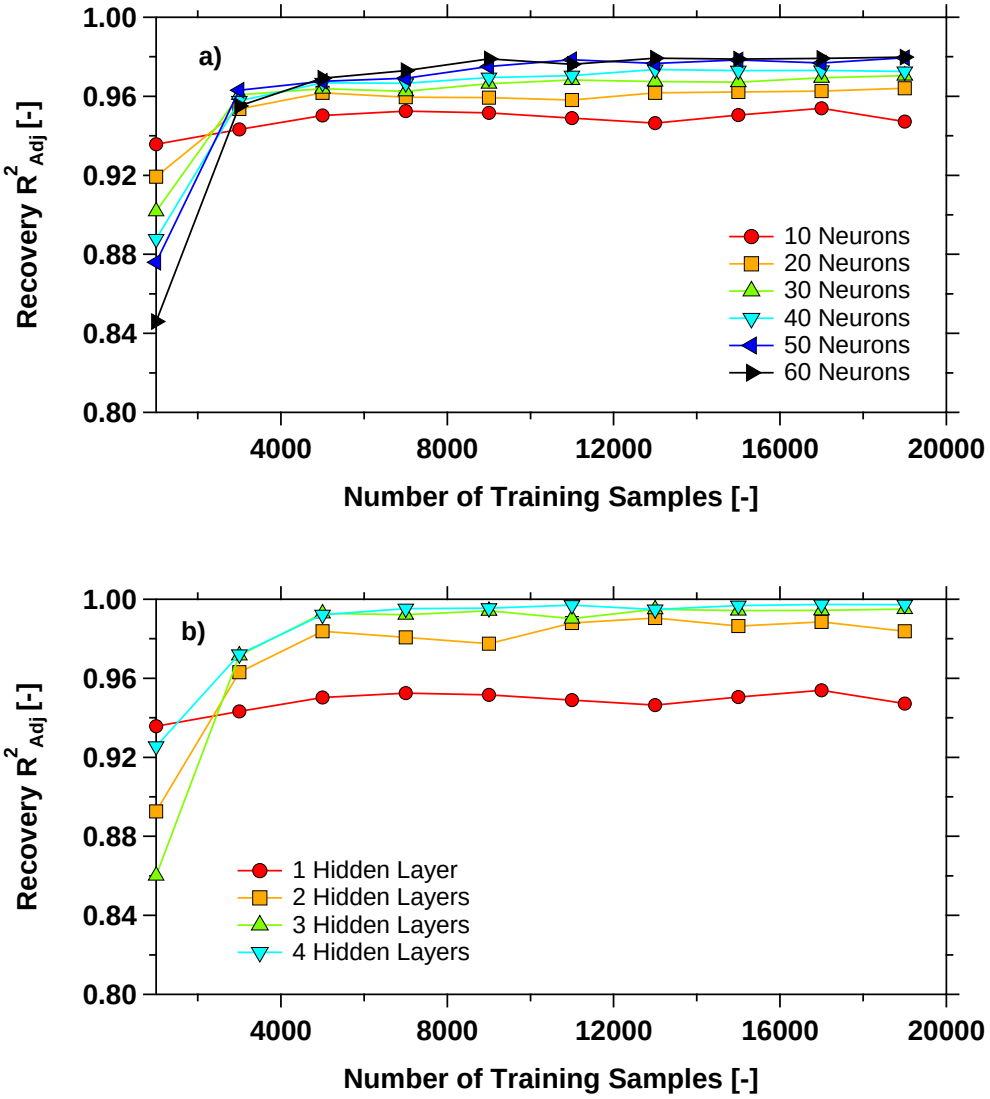

Figure C.6: The effect of neural network architecture on model prediction accuracy: Test R^2_{Adj} for Recovery is shown as a function of the training-set size a) The effect of number of neurons and training samples on R^2_{Adj} b) The effect of number of hidden layers. Ten neurons were used in each hidden layer. The test-set contains 1000 samples.

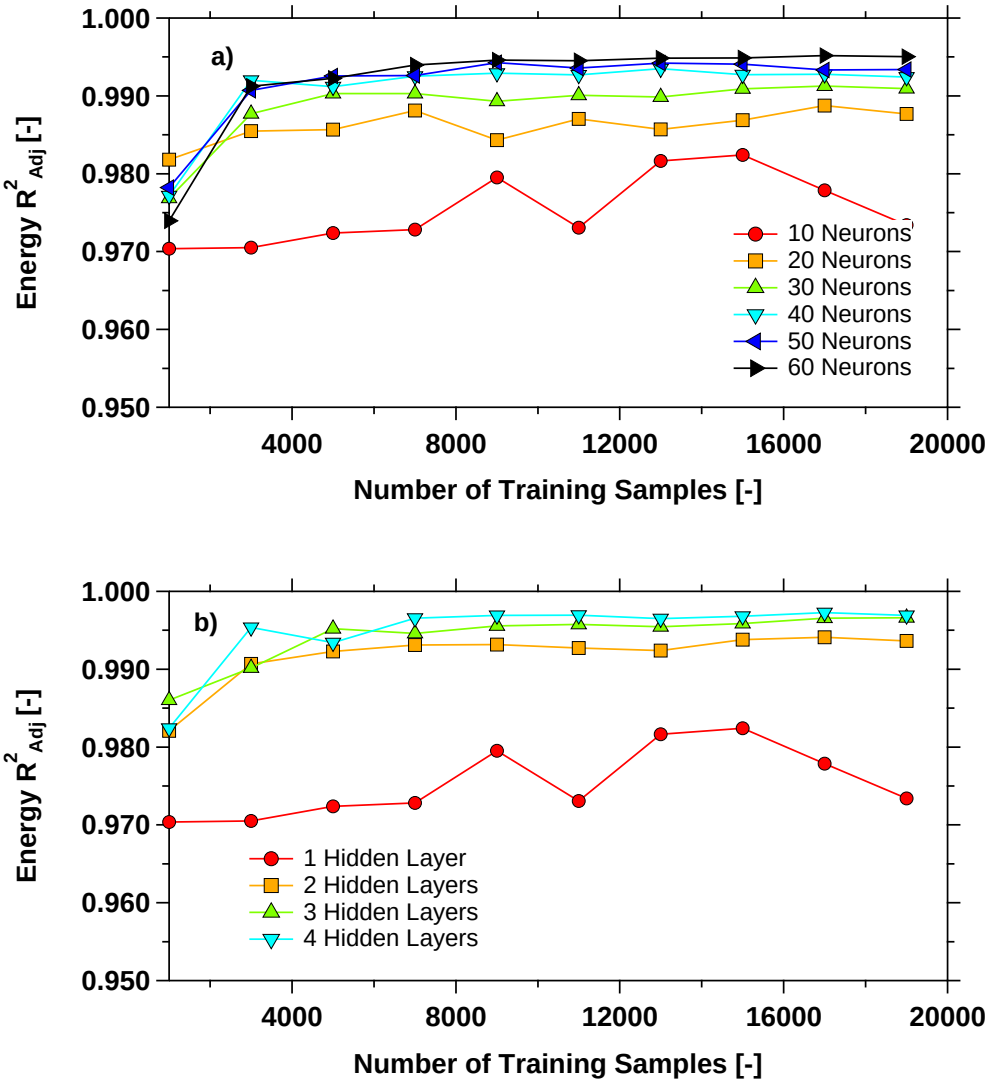

Figure C.7: The effect of neural network architecture on model prediction accuracy: Test R^2_{Adj} for Energy is shown as a function of the training-set size a) The effect of number of neurons and training samples on R^2_{Adj} b) The effect of number of hidden layers. Ten neurons were used in each hidden layer. The test-set contains 1000 samples.

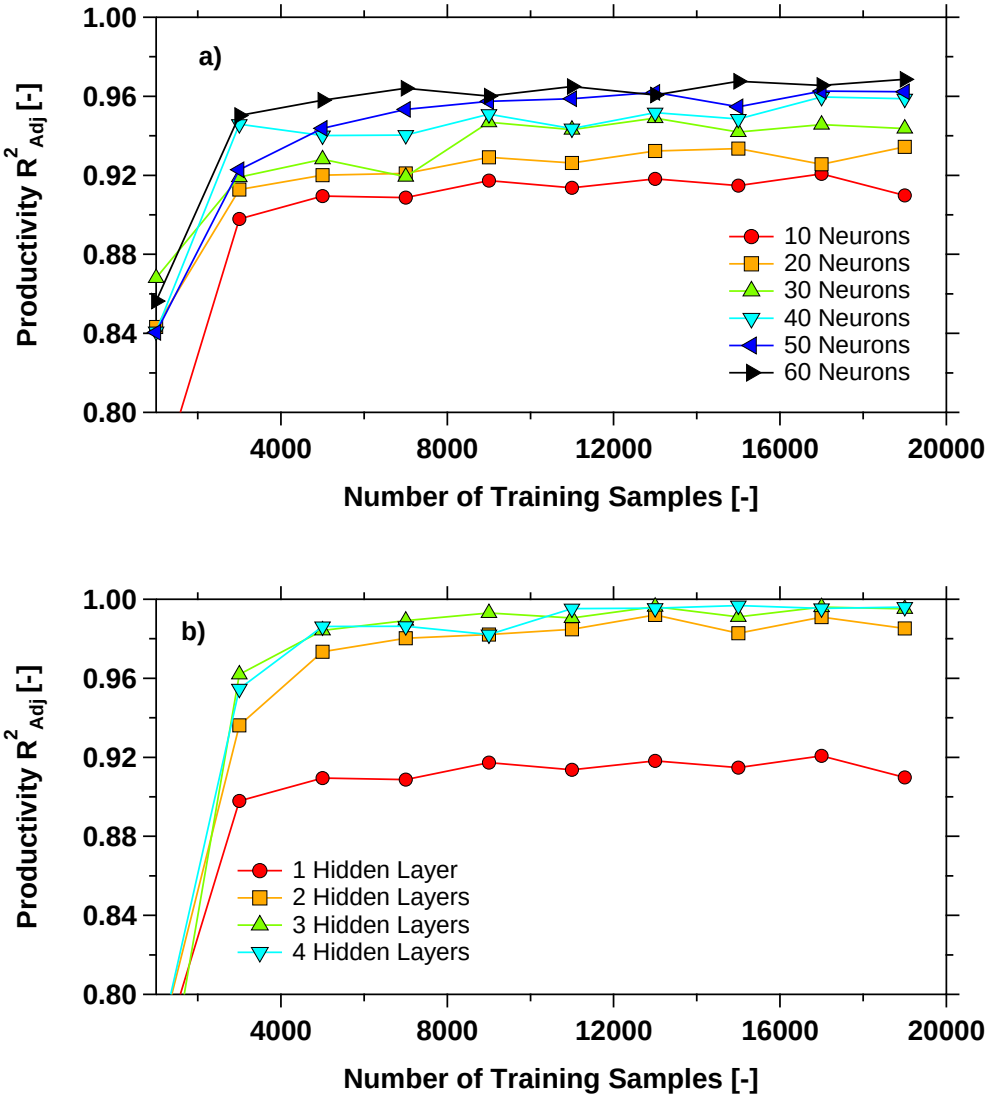

Figure C.8: The effect of neural network architecture on model prediction accuracy: Test R^2_{Adj} for Productivity is shown as a function of the training-set size a) The effect of number of neurons and training samples on R^2_{Adj} b) The effect of number of hidden layers. Ten neurons were used in each hidden layer. The test-set contains 1000 samples.

Appendix D: Supporting information for: Practically Achievable Process Performance Limits for Pressure-Vacuum Swing Adsorption-Based Post-combustion CO_2 Capture.

D.1 Process Modeling

D.1.1 Model Equations

Overall mass balance:

$$\frac{1}{P}\frac{\partial P}{\partial t} - \frac{1}{T}\frac{\partial T}{\partial t} = -\frac{T}{P}\frac{\partial}{\partial z}\left(\frac{P}{T}v\right) - \frac{1-\epsilon}{\epsilon}\frac{RT}{P}\sum_{i=1}^{n_{\text{comp}}}\frac{\partial q_i}{\partial t} \tag{D.1}$$

Component mass balance:

$$\frac{\partial y_i}{\partial t} + \frac{y_i}{P}\frac{\partial P}{\partial t} - \frac{y_i}{T}\frac{\partial T}{\partial t} = \frac{T}{P}D_L\frac{\partial}{\partial z}\left(\frac{P}{T}\frac{\partial y_i}{\partial z}\right) - \frac{T}{P}\frac{\partial}{\partial z}\left(\frac{y_i P}{T}v\right) - \frac{RT}{P}\frac{1-\epsilon}{\epsilon}\frac{\partial q_i}{\partial t} \tag{D.2}$$

Mass transfer rate:

$$\frac{\partial q_i}{\partial t} = k_i\left(q_i^* - q_i\right); k_i = \frac{C_i}{q_i^*}\frac{15\epsilon_{\text{P}}D_{\text{P}}}{r_{\text{P}}^2}; D_{\text{P}} = \frac{D_{\text{M}}}{\tau} \tag{D.3}$$

Pressure drop:

$$-\frac{\partial P}{\partial z} = \frac{150}{4}\frac{1}{r_{\text{p}}^2}\left(\frac{1-\epsilon}{\epsilon}\right)^2\mu v \tag{D.4}$$

Column energy balance:

$$\begin{aligned}&\left[\tfrac{1-\epsilon}{\epsilon}\left(\rho_{\text{s}}C_{\text{p,s}} + C_{\text{p,a}}\sum_{i=1}^{n_{\text{comp}}}q_i\right)\right]\tfrac{\partial T}{\partial t} = \tfrac{K_{\text{z}}}{\epsilon}\tfrac{\partial^2 T}{\partial z^2} - \tfrac{C_{\text{p,g}}}{R}\tfrac{\partial}{\partial z}(vP) - \tfrac{C_{\text{p,g}}}{R}\tfrac{\partial P}{\partial t} - \\ &\tfrac{1-\epsilon}{\epsilon}C_{\text{p,a}}T\sum_{i=1}^{n_{\text{comp}}}\tfrac{\partial q_i}{\partial t} + \tfrac{1-\epsilon}{\epsilon}\sum_{i=1}^{n_{\text{comp}}}\left(\left(-\Delta H_i\right)\tfrac{\partial q_i}{\partial t}\right)\end{aligned} \tag{D.5}$$

Step	z=0	z=L
OPEN-CLOSED (FP)	$P\|_{\mathrm{z=0}} = P_{\mathrm{L}} + (P_{\mathrm{H}} - P_{\mathrm{L}})e^{(-\alpha_{\mathrm{PRESS}}t)}$	$\frac{\partial y_i}{\partial z}\big\|_{\mathrm{z=L}} = 0$
	$D_L \frac{\partial y_i}{\partial z}\big\|_{\mathrm{z=0}} = -v\|_{\mathrm{z=0}} (y_{i,\mathrm{F}} - y_i\|_{\mathrm{z=0}})$	$\frac{\partial P}{\partial z}\big\|_{\mathrm{z=L}} = 0$
	$\frac{\partial \mathrm{T}}{\partial z}\big\|_{\mathrm{z}} = 0 = -\epsilon\, v\|_{\mathrm{z}} = 0 \rho_{\mathrm{g}} C_{\mathrm{p,g}} (T_{\mathrm{F}} - T\|_{\mathrm{z}} = 0)$	$\frac{\partial \mathrm{T}}{\partial z}\big\|_{\mathrm{z=L}} = 0$
OPEN-CLOSED (LPP)	$\frac{\partial y_i}{\partial z}\big\|_{\mathrm{z=0}} = 0$	$v\|_{\mathrm{z=L}} = \frac{v_{\mathrm{ADS}} P_{\mathrm{ADS}}\|_{\mathrm{z=L}}}{P\|_{\mathrm{z=L}}}$
	$\frac{\partial P}{\partial z}\big\|_{\mathrm{z=0}} = 0$	$D_L \frac{\partial y_i}{\partial z}\big\|_{\mathrm{z=L}} = -v\|_{\mathrm{z=L}} (y_{i,\mathrm{F}} - y_i\|_{\mathrm{z=L}})$
	$\frac{\partial \mathrm{T}}{\partial z}\big\|_{\mathrm{z=0}} = 0$	$\frac{\partial \mathrm{T}}{\partial z}\big\|_{\mathrm{z}} = \mathrm{L} = -\epsilon\, v\|_{\mathrm{z}} = \mathrm{L} \rho_{\mathrm{g}} C_{\mathrm{p,g}} (T_{\mathrm{F}} - T\|_{\mathrm{z}} = \mathrm{L})$
OPEN-OPEN (ADS)	$v\|_{\mathrm{z=0}} = v_{\mathrm{F}}$	$P\|_{\mathrm{z=L}} = P_{\mathrm{H}}$
	$D_L \frac{\partial y_i}{\partial z}\big\|_{\mathrm{z=0}} = -v\|_{\mathrm{z=0}} (y_{i,\mathrm{F}} - y_i\|_{\mathrm{z=0}})$	$\frac{\partial y_i}{\partial z}\big\|_{\mathrm{z=L}} = 0$
	$\frac{\partial, T}{\partial z}\big\|_{\mathrm{z=0}} = -\epsilon\, v\|_{\mathrm{z=0}} \rho_g C_{p,\mathrm{g}} (T_F - T\|_{\mathrm{z=0}})$	$\frac{\partial T}{\partial z}\big\|_{\mathrm{z=L}} = 0$
CLOSED-OPEN (BLO)	$v\|_{\mathrm{z=0}} = 0$	$v\|_{\mathrm{z=L}} = v_{\mathrm{BLO}}$
	$\frac{\partial y_i}{\partial z}\big\|_{\mathrm{z=0}} = 0$	$\frac{\partial y_i}{\partial z}\big\|_{\mathrm{z=L}} = 0$
	$\frac{\partial T}{\partial z}\big\|_{\mathrm{z=0}} = 0$	$\frac{\partial T}{\partial z}\big\|_{\mathrm{z=L}} = 0$
	$\frac{\partial P}{\partial z}\big\|_{\mathrm{z=0}} = 0$	
CLOSED-OPEN (EVAC)	$v\|_{\mathrm{z=0}} = v_{\mathrm{EVAC}}$	$v\|_{\mathrm{z=L}} = 0$
	$\frac{\partial y_i}{\partial z}\big\|_{\mathrm{z=0}} = 0$	$\frac{\partial y_i}{\partial z}\big\|_{\mathrm{z=L}} = 0$
	$\frac{\partial T}{\partial z}\big\|_{\mathrm{z=0}} = 0$	$\frac{\partial T}{\partial z}\big\|_{\mathrm{z=L}} = 0$
		$\frac{\partial P}{\partial z}\big\|_{\mathrm{z=L}} = 0$

Table D.1: Boundary conditions for the typical steps in a cyclic adsorption process.

D.1.2 Boundary Conditions

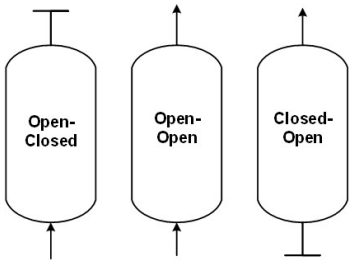

Figure D.1: Typical operating configurations of the constituent steps in a P/VSA cycle

D.1.3 Key process performance indicators (PIs)

$$Pu_{\mathrm{CO_2}} = \frac{n^{\mathrm{EVAC}}_{\mathrm{CO_2}}}{n^{\mathrm{EVAC}}_{\mathrm{CO_2}} + n^{\mathrm{EVAC}}_{\mathrm{N_2}}} \times 100 \tag{D.6}$$

$$Re_{\mathrm{CO_2}} = \frac{n^{\mathrm{EVAC}}_{\mathrm{CO_2}}}{n^{\mathrm{F}}_{\mathrm{CO_2}}} \times 100 \tag{D.7}$$

$$Pr = \frac{n^{\mathrm{EVAC}}_{\mathrm{CO_2}}}{(\text{ Vol of ads. }) (t_{\mathrm{ADS}} + t_{\mathrm{BLO}} + t_{\mathrm{EVAC}} + t_{\mathrm{LPP/PRESS}})} \tag{D.8}$$

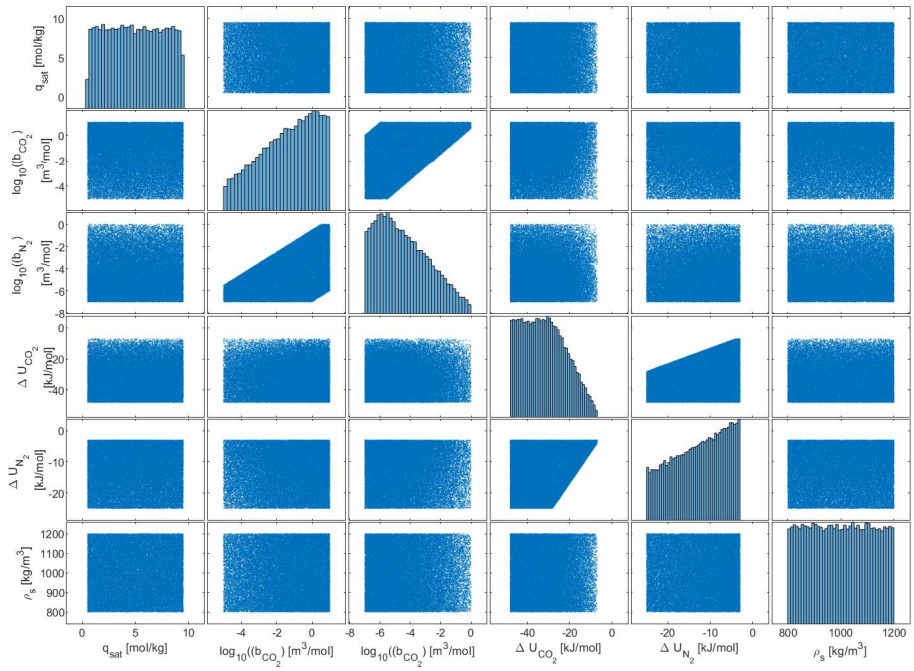

Figure D.2: Training sample distributions of the SSL isotherm parameters. A total of 50000 sample's are shown here.

$$En = \frac{E_{\text{ADS}} + E_{\text{BLO}} + E_{\text{EVAC}} + E_{\text{PRESS}}}{\text{Mass of } CO_2 \text{ in evacuation product}} \tag{D.9}$$

$$E_{\text{ADS}} = \frac{1}{\eta}\epsilon\pi r_{\text{in}}^2 \frac{\gamma}{\gamma-1}\int_{t=0}^{t=t_{\text{ADS}}} (vP(t))\left[\left(\frac{P(t)}{P_{\text{atm}}}\right)^{\frac{\gamma-1}{\gamma}} - 1\right] dt \tag{D.10}$$

$$E_{\text{BLO}} = \frac{1}{\eta}\epsilon\pi r_{\text{in}}^2 \frac{\gamma}{\gamma-1}\int_{t=0}^{t=t_{\text{BLO}}} (vP(t))\left[\left(\frac{P_{\text{atm}}}{P(t)}\right)^{\frac{\gamma-1}{\gamma}} - 1\right] dt \tag{D.11}$$

$$E_{\text{EVAC}} = \frac{1}{\eta}\epsilon\pi r_{\text{in}}^2 \frac{\gamma}{\gamma-1}\int_{t=0}^{t=t_{\text{EVAC}}} (vP(t))\left[\left(\frac{P_{\text{atm}}}{P(t)}\right)^{\frac{\gamma-1}{\gamma}} - 1\right] dt \tag{D.12}$$

$$E_{\text{PRESS}} = \frac{1}{\eta}\epsilon\pi r_{\text{in}}^2 \frac{\gamma}{\gamma-1}\int_{t=0}^{t=t_{\text{ADS}}} (vP(t))\left[\left(\frac{P(t)}{P_{\text{atm}}}\right)^{\frac{\gamma-1}{\gamma}} - 1\right] dt \tag{D.13}$$

Note that E_{PRESS}=0 for the case of the 4 step with LPP cycle.

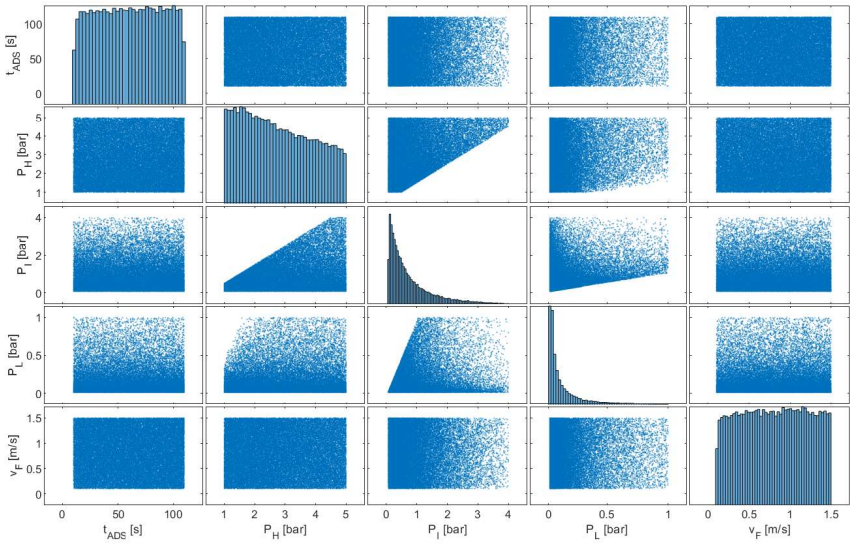

Figure D.3: Training sample distributions of the cycle specific operating parameters. A total of 50000 sample's are shown here.

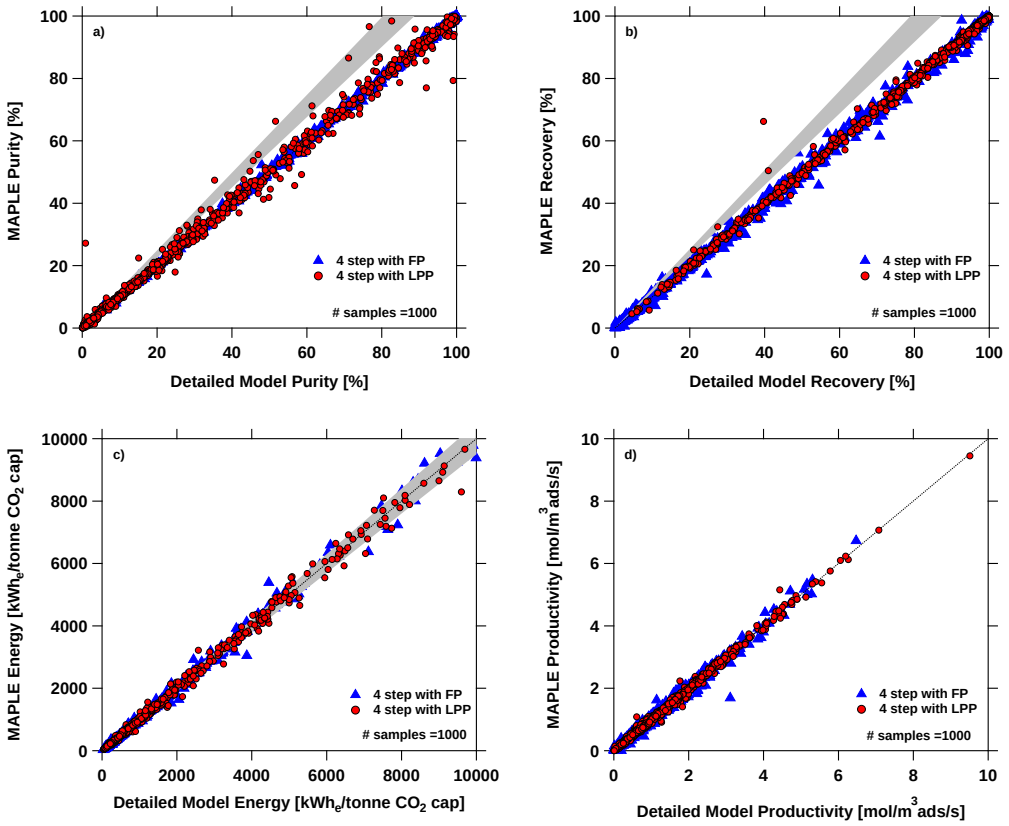

Figure D.4: The parity plots of the prediction from MAPLE for different performance indicator against those obtained from the detailed model for a test-set of 1000 samples as inputs for the 4 step with LPP cycle. a) Purity, b) Recovery, c) Energy, d) Productivity. The shaded area indicates a 5% deviation from the diagonal.

Table D.2: Single site Langmuir (SSL) isotherm parameters for the adsorbents used in this study.

Adsorbent	q_{sat}	b_{0,CO_2}	b_{0,N_2}	$-\Delta U_{CO_2}$	$-\Delta U_{N_2}$	ρ_s
	$[mol\,kg^{-1}]$	$[m^3\,mol^{-1}]$	$[m^3\,mol^{-1}]$	$[kJ\,mol^{-1}]$	$[kJ\,mol^{-1}]$	$[kg\,m^{-3}]$
UTSA-16	4.478	4.70×10^{-7}	1.400×10^{-6}	30.57	9.91	1000
Zeolite 13X	4.390	2.50×10^{-6}	2.70×10^{-6}	31.19	16.38	1130
IISERP-MOF2	5.000	2.02×10^{-7}	2.64×10^{-7}	31.13	11.89	1000

Appendix E: Supporting information for: Experimental validation of MAPLE: an adsorbent agnostic neural network VSA mode

E.1 Process Modeling

E.1.1 Model Equations

Overall mass balance:

$$\frac{1}{P}\frac{\partial P}{\partial t} - \frac{1}{T}\frac{\partial T}{\partial t} = -\frac{T}{P}\frac{\partial}{\partial z}\left(\frac{P}{T}v\right) - \frac{1-\epsilon}{\epsilon}\frac{RT}{P}\sum_{i=1}^{n_{\text{comp}}}\frac{\partial q_i}{\partial t} \tag{E.1}$$

Component mass balance:

$$\frac{\partial y_i}{\partial t} + \frac{y_i}{P}\frac{\partial P}{\partial t} - \frac{y_i}{T}\frac{\partial T}{\partial t} = \frac{T}{P}D_L\frac{\partial}{\partial z}\left(\frac{P}{T}\frac{\partial y_i}{\partial z}\right) - \frac{T}{P}\frac{\partial}{\partial z}\left(\frac{y_i P}{T}v\right) - \frac{RT}{P}\frac{1-\epsilon}{\epsilon}\frac{\partial q_i}{\partial t} \tag{E.2}$$

Mass transfer rate:

$$\frac{\partial q_i}{\partial t} = k_i\left(q_i^* - q_i\right); k_i = \frac{C_i}{q_i^*}\frac{15\epsilon_{\text{P}}D_{\text{P}}}{r_{\text{P}}^2}; D_{\text{P}} = \frac{D_{\text{M}}}{\tau} \tag{E.3}$$

Pressure drop:

$$-\frac{\partial P}{\partial z} = \frac{150}{4}\frac{1}{r_{\text{p}}^2}\left(\frac{1-\epsilon}{\epsilon}\right)^2\mu v \tag{E.4}$$

Column energy balance:

$$\begin{aligned}&\left[\tfrac{1-\epsilon}{\epsilon}\left(\rho_{\text{s}}C_{\text{p,s}} + C_{\text{p,a}}\sum_{i=1}^{n_{\text{comp}}}q_i\right)\right]\tfrac{\partial T}{\partial t} = \tfrac{K_{\text{z}}}{\epsilon}\tfrac{\partial^2 T}{\partial z^2} - \tfrac{C_{\text{p,g}}}{R}\tfrac{\partial}{\partial z}(vP) - \tfrac{C_{\text{p,g}}}{R}\tfrac{\partial P}{\partial t} - \\ &\tfrac{1-\epsilon}{\epsilon}C_{\text{p,a}}T\sum_{i=1}^{n_{\text{comp}}}\tfrac{\partial q_i}{\partial t} + \tfrac{1-\epsilon}{\epsilon}\sum_{i=1}^{n_{\text{comp}}}\left(\left(-\Delta H_i\right)\tfrac{\partial q_i}{\partial t}\right)\end{aligned} \tag{E.5}$$

Step	z=0	z=L
OPEN-CLOSED (FP)	$\frac{\partial y_i}{\partial z}\big\vert_{z=0} = 0$ $\frac{\partial P}{\partial z}\big\vert_{z=0} = 0$ $\frac{\partial T}{\partial z}\big\vert_{z=0} = 0$	$v\vert_{z=L} = \frac{v_{FEED} P_{FEED}\vert_{z=L}}{P\vert_{z=L}}$ $D_L \frac{\partial y_i}{\partial z}\big\vert_{z=L} = -v\vert_{z=L}\,(y_{i,F} - y_i\vert_{z=L})$ $\frac{\partial T}{\partial z}\big\vert_{z} = L = -\epsilon\, v\big\vert_{z} = L \rho_g C_{p,g}(T_F - T\big\vert_{z} = L)$
OPEN-OPEN (ADS/LR)	$v\vert_{z=0} = v_F$ $D_L \frac{\partial y_i}{\partial z}\big\vert_{z=0} = -v\vert_{z=0}\,(y_{i,F} - y_i\vert_{z=0})$ $\frac{\partial T}{\partial z}\big\vert_{z=0} = -\epsilon\, v\vert_{z=0}\, \rho_g C_{p,g}(T_F - T\vert_{z=0})$	$P\vert_{z=L} = P_H$ $\frac{\partial y_i}{\partial z}\big\vert_{z=L} = 0$ $\frac{\partial T}{\partial z}\big\vert_{z=L} = 0$
CLOSED-OPEN (EVAC)	$v\vert_{z=0} = v_{EVAC}$ $\frac{\partial y_i}{\partial z}\big\vert_{z=0} = 0$ $\frac{\partial T}{\partial z}\big\vert_{z=0} = 0$	$v\vert_{z=L} = 0$ $\frac{\partial y_i}{\partial z}\big\vert_{z=L} = 0$ $\frac{\partial T}{\partial z}\big\vert_{z=L} = 0$ $\frac{\partial P}{\partial z}\big\vert_{z=L} = 0$

Table E.1: Boundary conditions for the typical steps in a cyclic adsorption process.

E.1.2 Boundary Conditions

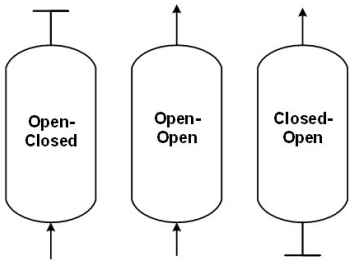

Figure E.1: Typical operating configurations of the constituent steps in a P/VSA cycle

E.1.3 Key process performance indicators (PIs)

$$Pu_{CO_2} = \frac{n_{O_2}^{ADS}}{n_{O_2}^{ADS} + n_{N_2}^{ADS} n_{Ar_2}^{ADS}} \times 100 \tag{E.6}$$

$$Re_{CO_2} = \frac{n_{O_2}^{ADS}}{n_{O_2}^{Feed}} \times 100 \tag{E.7}$$

$$Pr = \frac{n_{O_2}^{ADS}}{(\text{ Vol of ads. }) (t_{ADS} + t_{LR(D)} + t_{LR(R)} + t_{EVAC} + t_{PRESS})} \tag{E.8}$$